Multiaxial Fatigue Characterization and Modeling of AZ31B Magnesium Extrusion

by

Jafar Al Bin Mousa

A thesis
presented to the University of Waterloo
in fulfillment of the
thesis requirement for the degree of
Doctor of Philosophy
in
Mechanical Engineering

Waterloo, Ontario, Canada, 2011

AUTHOR'S DECLARATION

I hereby declare that I am the sole author of this thesis. This is a true copy of the thesis, including any required final revisions, as accepted by my examiners.

I understand that my thesis may be made electronically available to the public.

Jafar Al Bin Mousa

Abstract

The demand for lightweight materials in automobiles has been motivated by two factors: fuel economy and air pollution reduction. One of the first steps taken in automotive vehicle weight reduction was the use of aluminum alloys for both structural and non-structural parts. Although magnesium alloys, that have one fourth the density of steel and one third that of aluminum, have also been used in automobiles, however, their applications were limited to non-structural parts. Recently, interest has been focused on using magnesium alloys as structural materials for automotive load-bearing components. Load-bearing components in automobiles are usually subjected to multiaxial cyclic loading. Fatigue is considered to be a significant cause of ground vehicle component failure. Therefore, for magnesium alloys to be used for these components, an understanding of their fatigue behaviour is necessary. In this study, series of monotonic and cyclic tests were conducted on smooth specimens machined from AZ31B magnesium extrusion section. Two loading modes were considered in this investigation, axial and torsional. Monotonic tensile and compressive tests were performed at three different orientations, longitudinal (LD), i.e., parallel to the extrusion direction, 45° and transverse (TD) directions. Monotonic torsion tests were performed on specimens that were machined along the LD. Similarly, cyclic axial and torsional as well as multiaxial axial-torsional tests were performed on specimens that that were machined along the LD. Three different phase angles were considered for multiaxial tests: in-phase, and 45° and 90° out-of-phase. It was found that monotonic axial stress-strain behaviour is direction dependent due to the different deformation mechanisms involved. Significant yield anisotropy and sigmoidal-type hardening were observed. Twinning-detwinning deformation was considered as the major cause of these behaviours. On the other hand, monotonic torsional stress-strain curve had a linear hardening behaviour. Cyclic axial behaviour was found to be affect by twinning-detwinning deformation. Its most significant characteristics

are: yield asymmetry, power-like hardening in compressive reversal and sigmoidal-type hardening in tensile reversal. This unusual behaviour was attributed to the contribution of three different deformation mechanisms: slip, twinning and detwinning. Due to yield asymmetry, significant positive mean stress was observed especially at LCF. Cyclic hardening was also observed and it was found to be associated with a substantial decrease in plastic strain energy density. Cyclic shear behaviour was symmetric and did not exhibit any of the aforementioned behaviours in cyclic axial loading. Two major observations were made from multiaxial tests. First, additional hardening due to nonproportionality was observed. Second, phase angle has no effect on fatigue life. Three fatigue life models were considered for multiaxial fatigue life prediction: Smith-Watson-Topper, Fatemi-Socie and Jahed-Varvani. The first two models are based on strain and are evaluated on specific critical planes. The third model is based on energy densities calculated from hysteresis loops. Strain- and energy-life curves had knees and pronounced plateaus. Therefore, it was not possible to model the entire fatigue life using Coffin-Manson-Type equations. Low cycle fatigue lives were predicted within $\pm$2x scatter bounds using the Fatemi-Socie and the Jahed-Varvani models for all loading conditions which was not the case with Smith-Watson-Topper model. Total energy, the sum of plastic and positive elastic strain energy densities, was found to correlate fatigue lives for several wrought Mg-alloys under different loading conditions.

Acknowledgements

I would like to express my sincere gratitude to my supervisor, Professor Hamid Jahed and my co-supervisor Professor Steve Lambert for their guidance and expertise. I also wish to thank Professors Tim Topper and Gregory Glinka for their helpful discussion. I am thankful to Andy Barber and Richard Forgett for their technical supports. I would also like to thank John Bonnen from Ford Motor Compnay for his help with the biaxial extensometer.

I would like to thank the members of the fatigue task in the magnesium front end research and development project (MFERD) for their helpful discussion during the past four years. I also wish to thank General Motors for providing the extrusion sections. I am thankful to the members of the solid mechanics group at the University of Waterloo, Seyed Behzad Behravesh, Mohammad Noban, Elfaitori Ibrahim, Amin Eshraghi, Morvarid Karimi Ghovanlou, Arash Tajik and Hassan Mahmoudi, for their support and helpful discussion.

I would like to thank my father, my wife, my brothers, my sisters and my friends who supported and encouraged me throughout this work.

Lastly, I gratefully acknowledge King Fahd University of Petroleum and Mineral (KFUPM) for my PhD scholarship and the Saudi Arabian Cultural Bureau in Ottawa for the administrative support.

To my father and my mother

Husain and Amenah

&

To my wife and my new born daughter

Alaa and Roaa

Table of Contents

List of Tables

List of Figures

Nomenclature

$2c$	Major radius of semi-elliptical crack
α	Observed crack surface angle
$\bar{\sigma}$	von Mises equivalent stress
$\bar{B}$	Material constant
$\bar{C}$	Material constant
β	Material constant
ΔW_{ij}^{p}	Sum of hysteresis loop areas from nine stress components
ΔW_A	Energy due to pure axial loading
ΔW_p	Plastic strain energy density
ΔW_T	Energy due to pure torsional loading
ΔW_t	Total energy density
ΔW_{e+}	Positive elastic energy density

Δ Range

δ_{ij} Kronecker delta

γ Shear strain

$\gamma_f^{'}$ Torsional fatigue ductility coefficient

κ Material constant

ν Poisson's ratio

ω Frequency

ϕ Plane angle

ϕ_n Plane of principal normal stress or strain

ϕ_s Plane of principal shear stress or strain

Ψ Angle of twist

σ True stress

$\sigma_f^{'}$ Axial fatigue strength coefficient

σ_ϕ Normal stress component on an oblique plane with an angle of ϕ

σ_{avg} Center of stress Mohr's circle

$\sigma_{n,max}$ Maximum normal stress at critical plane

τ Shear stress

$\tau_f^{'}$ Torsional fatigue strength coefficient

τ_{ϕ}	Shear stress component on an oblique plane with an angle of ϕ
ε	True sttrain
$\varepsilon_{f}^{'}$	Axial fatigue ductility coefficient
ξ	Observed crack depth angle
m	Material constant
p	Suberscript denotes plastic component
$_{1,2,3}$	Subscripts denotes principal values
$_{a}$	Subscript denotes amplitude
$_{e}$	Subscript denotes elastic component
$_{m}$	Subscript denotes mean value
$_{p}$	Subscript denotes plastic component
$_{x}$	Subscript denotes x-direction
$_{y}$	Subscript denotes y-direction
$_{max}$	Subscript denotes maximum
$_{min}$	Subscript denotes minimum
$_{xy}$	Subscript denotes shear component acting in xy-plane
A	Final cross-sectional area
a	Minor radius of semi-elliptical crack

A_g Material constant

A_o Original area

B Energy-axial fatigue strength exponent

b Axial fatigue strength exponent

B_s Energy-torsional fatigue strength exponent

b_s Torsional fatigue strength exponent

C Energy-axial fatigue toughness exponent

c Axial fatigue ductility exponent

C_s Energy-torsional fatigue toughness exponent

c_s Torsional fatigue ductility exponent

d_i Inner diameter

d_o Outer diameter

E Tensile modulus

$E_e^{'}$ Energy-axial fatigue strength coefficient

$E_f^{'}$ Energy-axial fatigue toughness coefficient

e_{ij} Deviatoric strain

F Force

h Projected crack height

K	Monotonic tensile strength coefficient
k	Material constant
$K^{'}$	Axial fatigue strength coefficient
l_f	Final length
l_o	Original length
m	Material constant
N	Number of cycles
n	Monotonic tensile strain hardening exponent
$n^{'}$	Axial fatigue strain hardening exponent
N_f	Fatigue life
$R_{\sigma,\tau}$	Radius of stress Mohr's circle
S	Engineering stress
S_k	Material constant
s_{ij}	Deviatoric stress
T	Applied torque
t	Time
t_w	Specimen wall thickness
w	Projected crack width

$W_e^{'}$ Energy-torsional fatigue strength coefficient

$W_f^{'}$ Energy-torsional fatigue toughness coefficient

W_d Distortional component of the strain energy density

$K_s^{'}$ Torsional fatigue strength coefficient

$n_s^{'}$ Torsional fatigue strain hardening exponent

Chapter 1

Introduction

1.1 Motivation

Fatigue failure is a phenomenon resulting from the application of cyclic "*repetitive*" loading. Most machines, such as automobiles, operate in a cyclic nature. Therefore, their components are subjected to cyclic loading. Due to the complexity of the operational environment and the geometry, load-bearing components in automobiles are usually subjected to multiaxial cyclic loads. Therefore, multiaxial fatigue analysis becomes an essential design tool for such components. Fatigue is considered to be a significant cause of ground vehicle component failure. A survey of service failures showed that almost 75% were fatigue-related [1]. Other surveys reported that the fatigue failures range from 50 to 90% [2]. A better understanding of fatigue behaviour assists the weight optimization process, which is currently a global quest in the automobile industry. This is because weight directly influences fuel consumption. It is estimated that a 10% decrease in vehicle weight results in 8-10% fuel economy improvement [3]. One of the first steps taken in automotive vehicle

weight reduction was the use of aluminum alloys in 1922. In 1996, a total of about 110 kg of aluminum was used in automobile vehicles and this amount is predicted to increase to 250-340 kg by 2015 [3]. Yet, attentions are currently focused on even lighter materials. Magnesium is one of the lightest metallic elements with abundant resources, and therefore a natural candidate for weight reduction. In fact, magnesium is not a new material to the automotive industry. It was used in early applications in the automotive industry in the 1920s [4]. It is estimated that around 73 and 86 kg of magnesium was used for the 6 and 8 cylinder cars, respectively, between the early 1920s and the late 1930s [4]. After the Second World War and until the 1970s, the *Volkswagen Beetle* was the commercial car that had the single largest application of magnesium alloys, with a total weight of 17 kg [4, 5]. However, once the production of air cooled engines and gearboxes was stopped and the demand for higher performance vehicles increased, the use of magnesium started to decline [4, 6]. Nevertheless, after the mid-1990s the interest in magnesium started to increase again, especially in North America and Europe, due to new regulations to reduce fuel consumption [4, 7]. Magnesium has some shortcomings: insufficient strength and elongation, creep, and corrosion. The problem of atmospheric corrosion can be solved by coating. However, galvanic corrosion of magnesium, whenever it is in contact with another metal, will still be an issue. This can be solved by coating or using compatible aluminum shims or washers [4, 8, 9]. Other shortcomings and the performance of Mg can be improved by alloying. For example, AZ-based Mg alloys are produced by adding aluminum (Al) and zinc (Zn) to pure Mg. Appropriate amounts of additives may improve the strength, castability, workability, corrosion resistance and/or the weldability of these alloys. AZ31C-based alloys have high formability and weldability and ZK60A-based Mg alloys, which are produced by adding zinc (Zn) and zirconium (Zr) to Mg, have a higher hot-workability than other materials. AM series alloys, which are produced by adding aluminum (Al) and man-

ganese (Mn) to Mg, such as AM50A and AM60B have a good combination of strength, ductility, energy absorption properties and castability [8]. Automobile companies have been a major contributor to the research and development of magnesium alloys. Joint programs that are dedicated to the development of Mg alloys are currently established. In the USA, GM, Ford and Chrysler jointly established the United States Council for Automotive Research (USCAR) in 1992 [10]. The Council worked out a plan to strengthening their competitiveness and to address related environmental issues. As a part of this, the Magnesium Powertrain Cast Components Project was started in 2001 under the direction of the United States Automotive Materials Partnership (USAMP). This project aims to increase the use of Mg alloys in motor vehicles to about 100 kg by 2020 [10]. In Japan, the Ministry of Education, Culture, Sports, Science and Technology is funding research which is targeted at the development of new high-performance magnesium alloys. This development and research is aimed to produce new Mg-Zn-, Mg-Al-Ca-, and Mg-Y-Zn-based alloys with high strength, creep resistance and heat resistance [8]. In Europe, a joint research organization was established by automobile manufacturers such as Fiat, Volvo, Daimler-Chrysler, Ford, Volkswagen and BMW. Universities, research organizations and parts suppliers in Europe also participate in this project. One of the common themes of this organization is the development of new heat-resistant Mg alloys. China is now considered as one of the largest magnesium ore producers in the world. While material manufacturing technologies improve with the expansion of markets, in 2001, China initiated a total investment of about 40 million dollars for 5-10 years for R & D projects related to magnesium refining and processing technologies. Foreign automobile manufacturers operating in China as well as Chinese universities and colleges are also involved in these projects [8]. These research and development programs have advanced the application of magnesium alloys in automobiles. For example, instrument panels and steering structures

can be found in Cadillac models, the Opel Vectra, the BMW Mini, and the Rolls-Royce Phantom, as well as seat structures in the SL Roadster from Daimler-Chrysler and the Jaguar X-type [4, 9]. General Motors produced the world's largest magnesium die casting for the instrument panel for the GMC Savana and the Chevrolet Express. This instrument panel weights 12 kg when manufactured from magnesium instead of 18 kg in steel. In addition, it required only 25 magnesium parts instead of 67 steel parts [9]. Powertrain and engine applications have been restricted to low temperature parts. The VW Passat, the A4/A6 Audi and the Chinese Santana use magnesium in manual transmission cases [9]. Recently, BMW introduced the world's lightest and first engine block manufactured from magnesium-aluminum alloys [7]. Still, applications to the car body and chassis are very limited. GM and BMW have been using one piece die cast magnesium for the roof frame and the roof compartment lid in the C-5 Corvette and the BMW 3 Series, respectively [9]. So far, there have been no structural load-bearing components manufactured from magnesium alloys. The requirements for safety, durability and resistance to fatigue represent a great challenge in this area [5]. Recently, research has been conducted to enable the use of magnesium casting and wrought alloys in major automotive structural components. In 2006, a large multi-national US-Canada-China Joint Research & Development Project was launched. The Magnesium Front End Research and Development (MFERD) project is intended to bring magnesium automotive applications from the single component level to the subsystem level. The MFERD project is intended to investigate the applicability of Mg-alloys as lightweight materials for automotive body structures. Fatigue and durability is a key task for this initiative. Participating institutions for fatigue and durability studies are: the University of Waterloo and Ryerson University in Canada; the Institute of Metal Research (IMR) in China; and Mississippi State University, Westmorland Corporation, General Motors, Ford Motor Company and Chrysler Group LLC in the United

States. The present research is part of the MFERD fatigue task sub-project on Design of Magnesium Components Based on Fatigue Performance under contract to Public Works and Government Services Canada, contract no. 23378-070680/001/SQ. As a part of the MFERD project, this research aims to study the multiaxial fatigue behaviour of AZ31B magnesium extrusion. The uniaxial cyclic behaviour of several magnesium extrusions, including the AZ31B, have been investigated in the literature [11–17]. Fig. 1.1 compares monotonic tensile properties of several magnesium extrusions with that of automotive 6000 and 7000 series aluminum extrusions [18]. The properties are expressed as "*specific*" values, i.e., per unit density. In general, it is seen from this figure that the specific properties of magnesium extrusions are comparable, if not better, than those of automotive aluminum alloys. Axial strain-life data for different wrought magnesium alloys are compared with different automotive aluminum alloys in Fig. 1.2 [11, 15, 17, 19–31]. Keeping in mind that the loading capacity of aluminium is higher than that of magnesium, it is seen from this figure that for a given axial strain amplitude the fatigue life of Mg-alloys are generally comparable to that of Al-alloys. Despite the growing research on uniaxial fatigue of magnesium alloys, there are currently no multiaxial fatigue studies on AZ31B extrusion. As far as the mechanical fatigue of automotive structural components, two loading scenarios are of interest: constant and variable amplitude loading. Because of the limited knowledge about the general fatigue behaviour of AZ31B extrusion, only constant amplitude loading was considered in the present work. Also, this study aims to provide necessary experimental results for future cyclic plasticity investigations.

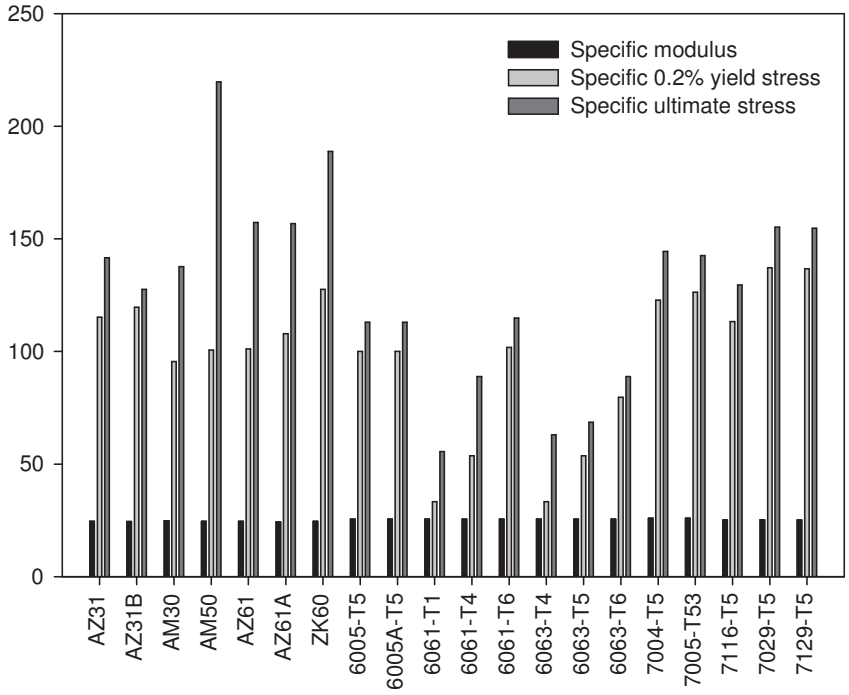

Figure 1.1: Comparison between specific monotonic tensile properties for magnesium extrusions and automotive aluminum extrusions. Specific modulus in (GPa.cm^3/g) and, specific 0.2% yield and specific ultimate strengths in (MPa.cm^3/g), (AT6, 1998).

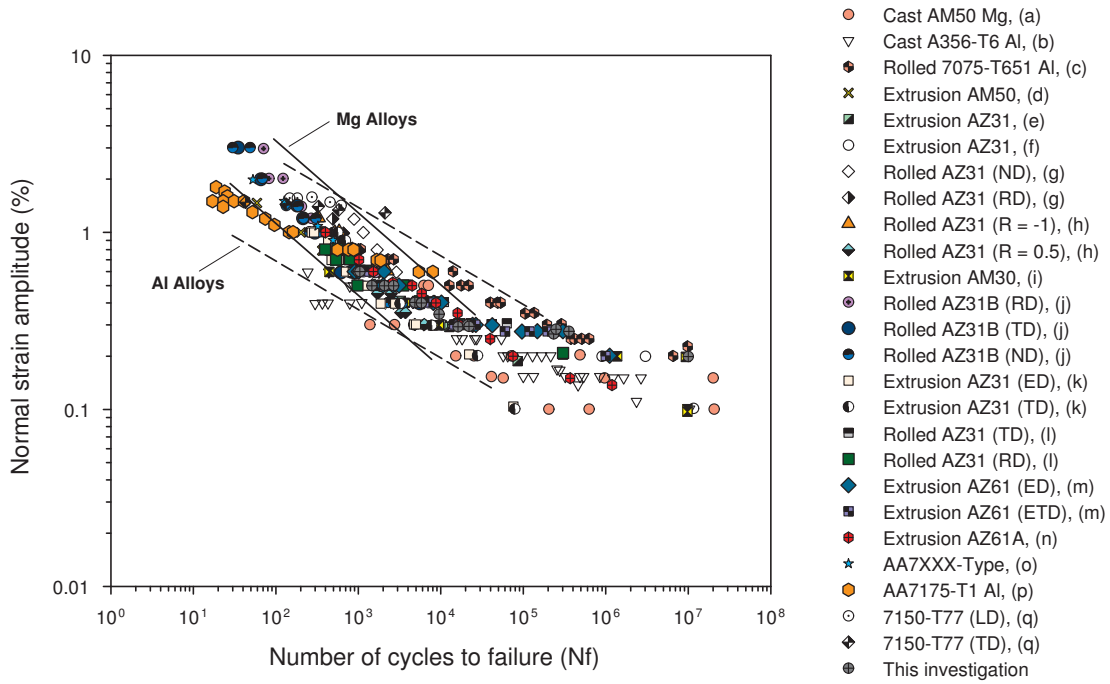

Figure 1.2: Comparison between the axial fatigue life curves for magnesium extrusions and different automotive aluminum alloys. (a)Ref: El Kadiri et al., 2006. (b) Ref: Jordon J.B. et al., 2010. (c) Ref: Xue et al., 2007. (d) Ref: Chen L. et al., 2007. (e) Ref: Hasegawa S. et al., 2007. (f) Ref: Begum S. et al., 2009. (g) Ref: Park SH. et al. 2010. (h) Ref: Hyuk P. et al., 2010. (i) Ref: Luo T.J., 2010. (j) Ref: Wu L. et al., 2010. (k) Ref: Lv F., 2011(I). (l) Ref: Lv F. et al. 2011 (II). (m) Ref: Jordon J.B et al., 2011. (n) Ref: Yu Q. et al., 2011. (o) Ref: Heikkenen H.C. et al. 1981. (p) Ref: Salerno G. et al. 2007. (q) Ref: Srivatsan T.S. 1991.

1.2 Thesis Objectives

This research aims to investigate the multiaxial fatigue behaviour of AZ31B magnesium extrusion. The overall research objectives of this study can be summarized as follows:

1. Characterize the monotonic behaviour under tensile, compressive and torsional loading conditions.
2. Characterize the cyclic behaviour under axial and torsional loading conditions.
3. Investigate the multiaxial cyclic behaviour under proportional and nonproportional axial-torsional loading conditions.
4. Study the fatigue cracking behaviour of the tested specimens under different loading conditions
5. Investigate the applicability of existing fatigue life models in estimating multiaxial fatigue life under pure and multiaxial cyclic loading conditions.

1.3 Thesis Overview

This thesis consists of five chapters. This chapter outlines the importance of this research and states its objectives. The second chapter consists of two parts: analytical and experimental background, and literature review. The analytical and experimental section reviews basic theoretical and experimental methods related to fatigue of engineering materials. The literature review section highlights the ongoing research in three major areas related to fatigue of magnesium alloys: microstructural, macroscopic and mechanistic, and plasticity. The third chapter presents the experimental results and is divided into six parts.

The first and second parts discuss the material and the experimental setup. The third part presents the experimental results for monotonic tension, compression and torsional tests. The fourth part of this chapter focuses on the pseudoelastic behaviour for different loading conditions. Cyclic tests results are presented and discussed in the fifth part. A summary of the major findings is presented in the sixth part. The fourth chapter focuses on fatigue modeling. Cyclic stress-strain curves and fatigue life modeling are discussed in the first and second sections. Then, multiaxial fatigue life prediction models are investigated. Two fatigue modeling approaches are discussed: strain- and energy-based. The last section of chapter four summarizes the major findings about fatigue modeling. Lastly, conclusions and recommendations are presented in chapter five.

Chapter 2

Background

In this chapter, analytical and experimental background related to fatigue is reviewed. This review includes monotonic and cyclic behaviour and fatigue life prediction techniques. In addition, literature review concerning microscopic, macroscopic and plasticity studies on fatigue of magnesium alloys is presented.

2.1 Analytical and Experimental Background

Machine components such as automotive structural parts are usually subjected to repeated loads "*cyclic loads*" resulting in cyclic stresses and strains that can lead microscopic physical damage to the material involved. The American Society for Testing and Materials, hereafter referred to as ASTM, defines fatigue as "*the process of progressive localized permanent structural change occurring in a material subjected to conditions that produce fluctuating stresses and strains at some point or points and that may culminate in cracks or complete fracture after a sufficient number of fluctuations*" [32]. Fatigue design requires an

understanding about the mechanical behaviour of material. There are two standard tests for characterizing a material for fatigue analysis: monotonic and cyclic. Smooth laboratory specimens are machined from the investigated material. Depending on the material and the analysis involved, these specimens can be tested at certain loading, orientations and/or environmental conditions. After that, related mechanical properties can be obtained. These properties can be related to fundamental mechanical parameters, such as stress, strain or energy, for fatigue design analysis. Essentially, the major outcome from fatigue design analysis is the fatigue life. Although constructed based on smooth specimens testing, a successful fatigue design model should have the capability to estimate fatigue life on a component level. Due to the complexity of such analysis, fatigue life estimation for components is usually carried out using finite element analysis. This section provides brief background information about fatigue design analysis. This includes monotonic and cyclic characterizations, experimental techniques and analysis methods.

2.1.1 Monotonic Behaviour

2.1.1.1 Tension and Compression Loading

Monotonic tension or compression tests are performed by monotonically increasing the load until the specimen fails by fracture. The load is applied in the axial direction, i.e., longitudinal direction, of the specimen. If monotonic directional properties are required, specimens should be machined along the desired orientations. As per the ASTM [33], there are three controlling method for monotonic tensile test: rate of straining, rate of stressing and crosshead speed. The recommended rates for crosshead speed are 0.015±0.003 mm/mm/min and 0.05-0.5 mm/mm/min of the reduced section of the specimens for yield strength and ultimate tensile strength determination, respectively. It is a common practice

to determine the yield strength at an offset strain value of 0.2%. This is done by plotting a line that intersects the strain axis at 0.2% with a slope equal to the modulus of elasticity. Usually, extensometers are used to measure the displacement at the gage section. The axial strain is calculated by dividing the incremental displacement, which is measured by the extensometer, over the initial gage length.

2.1.1.2 Torsional Loading

Monotonic torsion test is usually performed by applying torque on cylindrical or tubular specimens such that uniform twisting is applied in the gage section. As per ASTM [34], thin-walled tubular specimens, that obey the thin-walled tube assumption, are recommended because they allow simple determination of shear stress. The specimens should be gripped such that misalignment is avoided to prevent the application of bending moment. Also, the test should be performed in a free-end condition to prevent application of axial forces. Extensometer capable of measuring the angle of twist at the gage section can be used for shear stain measurement.

2.1.2 Analysis Methods for Monotonic Loading

2.1.2.1 Tension and Compression Loading

Two axial stresses and strains can be calculated from monotonic tension or compression tests: engineering and true. Consequently, two stress-strain curves are obtained: engineering and true as shown in Fig. 2.1 [35]. The engineering stress, S, and strain, e, are calculated as in Eqs. 2.1 and 2.2

$$S = \frac{F}{A_o} \tag{2.1}$$

where F is the applied axial force and A_o is the original cross-sectional area of the specimen.

$$e = \frac{l_f - l_o}{l_o} = \frac{\Delta l_o}{l_o} \tag{2.2}$$

where l_o and l_f are the original and the final length of the specimen's gage section. The true stress and strain are calculated using Eq. 2.3 and 2.4

$$\sigma = S(1 + e) \tag{2.3}$$

$$\varepsilon = \ln(1 + e) = \ln \frac{A_o}{A} \tag{2.4}$$

where A is the final cross-sectional area of the specimen.

It should be noted that Eqs. 2.3 and 2.4 are based on the assumption that the volume of the material does not change during tensile or compressive deformation. Usually, monotonic stress-strain curves have two distinct regions: linear and nonlinear. The linear region represents the "*elastic deformation*" while the nonlinear region represents the "*plastic deformation*". In the elastic region, the stress and the strain are related through Hooke's law, Eq. 2.5

$$\sigma = \varepsilon E \tag{2.5}$$

where E is the tensile modulus of elasticity or the Young's modulus which is the slope of the elastic portion in the stress-strain curve. Schematics of engineering and true stress-strain curves for monotonic tensile test are illustrated in Fig. 2.1. The total axial strain

can be divided into two parts, elastic and plastic as in Eq. 2.6

$$\varepsilon = \varepsilon_e + \varepsilon_p \tag{2.6}$$

which can be re-written as

$$\varepsilon = \frac{\sigma}{E} + \left(\frac{\sigma}{K}\right)^{\frac{1}{n}} \tag{2.7}$$

The relation in Eq. 2.7 is called the "*Ramberg-Osgood*" equation. The coefficient "K" and the exponent "n" are called the monotonic strength coefficient and the monotonic strain hardening exponent, respectively. These can be obtained by plotting true stress versus plastic strain from the yield to the ultimate strengths in a *log-log* scale. In this case, the intercept and the slope of the line represent the values of K and n, respectively.

2.1.2.2 Torsion Loading

When a tubular specimen is subjected to torsional loading, the shear stress varies across the thickness. However, as per the ASTM [34, 36] if the specimen satisfies the thin-walled tube assumption then uniform shear stress can be assumed across its thickness. The thin-walled tube assumption states that the mean diameter to wall thickness ratio has to be 10:1 or greater. Mathematically, this assumption can be written as in Eq. 2.8

$$\frac{d_o + d_i}{2t} \geq 10 \tag{2.8}$$

where t, d_o and d_i are the wall thickness, the outer and the inner diameters, respectively. As a result, uniform shear stress, τ, distribution can be calculated using Eq. 2.9

$$\tau = \frac{16T}{\pi(d_o^2 - d_i^2)(d_o + d_i)} \tag{2.9}$$

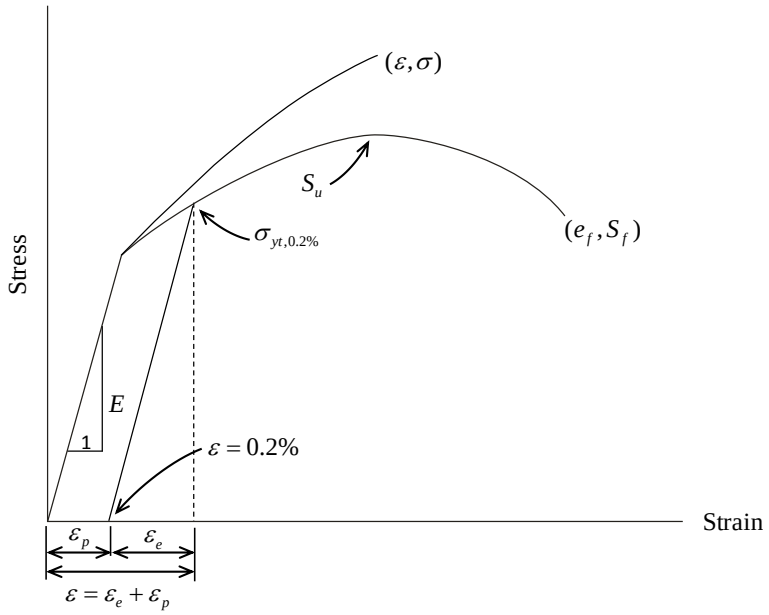

Figure 2.1: A schematic of a typical tensile stress-stress curve for engineering materials. Adopted from Stephens R.I. et al., 2001.

where T is the applied torque. The shear strain, γ, is related to the angle of twist,Ψ, as in Eq. 2.10

$$\gamma = \tan \Psi \tag{2.10}$$

If the angle of twist, measured in radians, is small, Ψ approaches $\tan \Psi$ and γ approaches Ψ. Similar analysis as for Eqs. 2.3 to 2.7 applies to monotonic shear test by replacing σ, ε and E with G, τ, γ and G, respectively.

2.1.3 Cyclic Axial and Torsional Behaviour

While monotonic failure occurs due to monotonically increasing loads, cyclic failure occurs due to the application of an alternating "*repetitive*" loading. Even if the cyclic stress is well below the ultimate strength of the material involved, microscopic cyclic damage accumulates with cycling until it leads to a macroscopic damage that causes failure. The term "*fatigue*" refers to the process of damage and failure due to cyclic loading. There are three approaches in fatigue analysis: stress-, strain- or energy-based. These approaches are classified based on the quantifying parameter of the fatigue damage. Therefore, the fatigue damage parameters for the stress-, the strain- and the energy-based approaches are the stress, the strain and the hysteresis loop energies, respectively. It should be noted that energy-based fatigue damage parameters can also be formulated based on the product of stress and strain components. The cyclic behaviour of a given material can be characterized by performing standard fatigue testing on smooth laboratory specimens. Based on the previous classification of fatigue analysis, there are two standard fatigue testing techniques for stress or strain approaches: stress- and strain-controlled. The energy-based approach uses the hysteresis loop energies obtained from strain-controlled fatigue testing. Strain-based fatigue testing is preferred when plastic deformation is dominant. Although machine

components are usually designed to operate at low stresses, local plasticity usually occurs at stress riser such as notches. As a result, strain-based fatigue analysis offers a tool to study the fatigue behaviour at local sites where plastic deformation is more dominant than elastic deformation. Next, the experimental techniques and the method of analysis for strain-controlled fatigue test are discussed.

2.1.3.1 Experimental Techniques

Cyclic fatigue tests can be performed under axial, torsional or bending loading. However, axial and bending loading creates the same effect on the material because both loading modes produce normal stresses and strains. On the other hand, torsional loading produces state of shear stresses and strains. To some extent, cyclic tests are similar to monotonic tests except that the applied load is alternating with time. There are common aspects in strain-controlled cyclic tests and these are:

1. Waveform
2. Loading
3. Frequency
4. Control mode
5. Test end criteria
6. Number of replicates
7. Specimen preparation
8. Specimen coating

9. Testing conditions

10. PID setting in digital controlled testing machine.

As per ASTM [37], the waveform of the loading can be sinusoidal or triangular. There are two parameters for fatigue loading, the "*amplitude*" and the "*R-ratio*". The amplitude is half the difference of the maximum and the minimum applied load while the R-ratio is the ratio of the maximum to the minimum applied load. Completely reversed loading test has an R-ratio of -1. Cyclic loads can be applied in constant or variable amplitudes. However, cyclic characterization of any material is achieved through constant amplitude testing. The frequency of a test can be decided based on the strain amplitude such that heating of the specimen is avoided. At low strain amplitude levels where plasticity is low, test can be stopped after the load "*force*" or "*torque*" response stabilizes. Then, the test can be run again but under load-controlled condition by applying the stabilized load amplitude. One way to declare failure in fatigue testing is by stopping the test at certain percentage of load drop. ASTM [37] defines 50% of load drop as a failure criteria. If the applied load is low enough such that the specimen does not fail after 10^7 cycles, the test is considered as a "*run-out*" and is stopped. Usually, run-out tests mark the so-called "*fatigue limit*". Depending on the level of scatter, two or three replicates might be needed at each strain level. Because fatigue phenomenon is surface finish dependent, smooth specimens shall be polished such that the maximum surface finish of 0.2 μm is guaranteed [37]. In the case of tubular specimen, the inner surface shall be honed, in addition, tubular specimens should be machined such that the outer and the inner diameters shall be concentric within ± 0.015 of the specimen wall thickness [36]. Because strain-controlled testing is usually performed using extensometer, fatigue specimens shall be coated to prevent the sharp edges of the extensometer from damaging the surface of the specimen. Also, testing conditions such as

temperature and humidity shall all be clearly defined. Digital controlled machines have three control parameters that help adjusting the command based on the feedback. These parameters are proportional, integral and derivative, i.e., "PID". The values of these control parameters shall be adjusted so that the machine can apply the required loading values such as force/torque, displacement/rotation or strain.

Axial Loading

Strain-controlled fatigue tests allow the determination of the axial fatigue properties of the material. Standard results obtained from such test include:

1. Strain life curve
2. Hysteresis loop
3. Fatigue limit
4. Cyclic stress-strain curve
5. Cyclic hardening behaviour
6. Mean stress development

Axial strain-controlled fatigue test can be performed by attaching axial extensometer to the specimen. Usually, axial extensometers have two knife edges that serve two purposes: they mark the gage length of the extensometer and they ensure that attachment of the extensometer during the test such that no slipping can occur. As mentioned previously, coating such as air-drying acrylic coating shall be applied on the surface of the specimen to protect it from the knife edges of the extensometer.

Torsional Loading

Similar to axial fatigue test, cyclic torsional tests allow the determination of the torsional

fatigue properties of the material. Standard results obtained from cyclic torsional test are exactly similar to those for cyclic axial tests. Torsional strain-controlled fatigue test can be performed by attaching an extensometer capable of measuring the angle of twist in the gage section. Standard experimental technique for fatigue testing and cyclic axial tests apply for cyclic torsional tests.

2.1.3.2 Analysis Methods

Axial Loading

From the geometry of the fatigue specimen, the axial stress and the axial strain can be calculated using Eqs. 2.1 and 2.2, respectively. A plot of stress versus strain during one cycle represents the so-called the "*hysteresis loop*" as shown in Fig. 2.2. Usually, half-life hysteresis loop is used for fatigue analysis. A plot of applied axial strain amplitude versus fatigue life represents the so-called "*axial strain life curve*". A standard strain life curve is shown in Fig. 2.3. From Eq. 2.6, the total axial strain amplitude ε_a can be expressed as

$$\varepsilon_a = \frac{\sigma_f^{'}}{E}\Big(2N_f\Big)^b + \varepsilon_f^{'}\Big(2N_f\Big)^c \tag{2.11}$$

where $\sigma_f^{'}$ and $\varepsilon_f^{'}$ are the axial fatigue strength and the axial fatigue ductility coefficients, respectively. The exponents b and c are the axial fatigue strength and the axial ductility exponents. N_f is the fatigue life which is sometime expressed in terms of number of reversals, $2N_f$. E is the tensile modulus of elasticity. Equation 2.11 is known as the "*Coffin-Manson*" equation [38, 39]. The coefficient $\sigma_f^{'}$ and the exponent b in Eq. 2.11 are obtained from axial stress amplitude versus number of reversal curve as shown in Fig. 2.3. On the other hand, the coefficient $\varepsilon_f^{'}$ and the exponent c are obtained from plastic strain amplitude versus number of reversal curve as shown in Fig. 2.3. After performing multiple

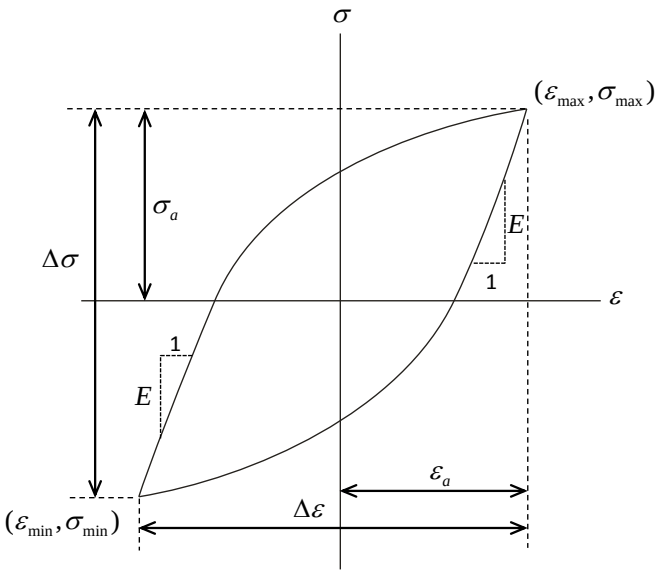

Figure 2.2: Typical hysteresis loop for cyclic loading.

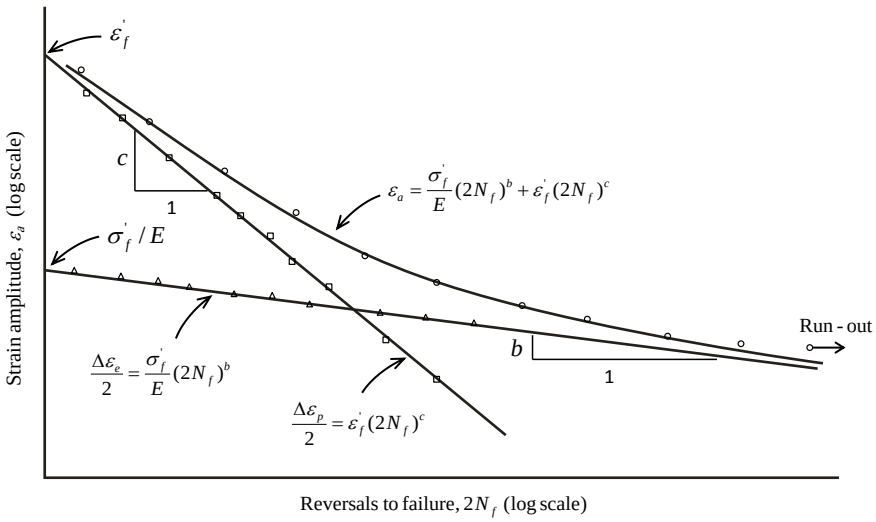

Figure 2.3: Typical strain-life curve for cyclic axial loading.

cyclic tests at different axial strain levels, the maximum points from all hysteresis can be plotted on a single plot with axial stress amplitude in the y-axis and axial strain amplitude in the x-axis. The generated curve from these points represents the so-called "*cyclic axial stress-strain curve*". Similar to monotonic loading, the Ramberg-Osgood relation, Eq. 2.7, can be obtained but for cyclic loading as in Eqs. 2.12 or 2.13

$$\frac{\Delta\varepsilon}{2} = \frac{\Delta\sigma}{2E} + \Big(\frac{\Delta\sigma}{2K'}\Big)^{\frac{1}{n'}} \tag{2.12}$$

or

$$\varepsilon_a = \frac{\sigma_a}{E} + \Big(\frac{\sigma_a}{K'}\Big)^{\frac{1}{n'}} \tag{2.13}$$

where $K^{'}$ and $n^{'}$ are the axial fatigue strength coefficient and the cyclic axial strain hardening exponent, respectively. The same procedure as for Eq. 2.7 is used to obtain the axial cyclic Ramberg-Osgood parameters $K^{'}$ and $n^{'}$. By doubling Eq. 2.12 as in Eq. 2.14, stabilized hysteresis loop can be obtained. Materials that can be described by Eq. 2.14 is said to exhibit "*Masing-type*" behaviour.

$$\Delta\varepsilon = \frac{\Delta\sigma}{E} + 2\Big(\frac{\Delta\sigma}{2K'}\Big)^{\frac{1}{n'}} \tag{2.14}$$

During cyclic tests, materials can develop cyclic hardening or cyclic softening. Some materials may exhibit neither cyclic hardening nor cyclic softening. One way to examine this phenomenon is by plotting the stress amplitude versus the number of cycles or the number of reversals. If the material experiences cyclic hardening, the stress amplitude should increase with cycling. On the other hand, materials that experience cyclic softening show decreasing amplitude as the number of cycles increases. Obviously, materials that show neither hardening nor softening should have constant stress amplitude over the

entire test. An additional cyclic phenomenon related to strain-controlled testing is called "*cyclic-dependent relaxation*". This phenomenon is recognized when a material, which is tested under strain-controlled condition, develops mean stress that decreases with cycling until it reaches zero magnitude.

Torsional Loading

Similar to cyclic axial load, cyclic shear stress and strain can be determined from the geometry of the tested specimen. If tubular specimen that obeys thin-walled tube assumption is used, cyclic shear stress and strain can be calculated from Eqs. 2.9 and 2.10 [36]. Shear hysteresis loop can be represented by plotting shear stress versus shear strain. The shear strain life curve is depicted by plotting applied shear strain versus fatigue life. Analogous to Eq. 2.11 in cyclic axial test, total shear strain amplitude γ_a can be related to fatigue life using the shear form of the Coffin-Manson relation as in Eq. 2.15.

$$\gamma_a = \frac{\tau_f^{'}}{G}\Big(2N_f\Big)^{b_s} + \gamma_f^{'}\Big(2N_f\Big)^{c_s} \tag{2.15}$$

where $\tau_f^{'}$ and $\gamma_f^{'}$ are the torsional fatigue strength and the torsional fatigue ductility coefficients, respectively. The exponents b_s and c_s are the torsional fatigue strength and the torsional ductility exponents. G is the shear modulus. The coefficient and exponents in Eq. 2.15 can be obtained using the similar procedure as for axial loading. The shear form of the Ramberg-Osgood is

$$\gamma_a = \frac{\tau_a}{G} + \Big(\frac{\tau_a}{K_s^{'}}\Big)^{\frac{1}{n_s^{'}}} \tag{2.16}$$

where $K_s^{'}$ and $n_s^{'}$ are the torsional fatigue strength coefficient and the cyclic torsional strain hardening exponent, respectively. Again, the coefficient and the exponent in Eq. 2.16 can be determined using similar procedure as for axial loading. In addition, if the tested material

exhibits Masing behaviour stabilized hysteresis loop can be obtained using Eq. 2.17.

$$\Delta\gamma = \frac{\Delta\tau}{G} + 2\Big(\frac{\Delta\tau}{2K'_s}\Big)^{\frac{1}{n_s}} \tag{2.17}$$

2.1.4 Multiaxial Fatigue Behaviour

In many applications, engineering load-bearing components such as crank shafts, rear axle and suspension arms, operate under multiaxial loads. In fact, multiaxial state is very common such that even uniaxial loading produces multiaxial state of stress and or strain. For example, a simple bar loaded axially is actually under a triaxial state of strain due Poisson's ratio effect. Similarly, the state of stress at notches is usually multiaxial even if the main body is loaded in one direction. Therefore, the term *multiaxial* cyclic loading implies the existences of fluctuating stresses and/or strains on a part such that the components of these stresses and/or strains are applied in different directions. Basically, there are two methods through which multiple loads can be combined. In the first method, different loads are applied independently such that the phase angle between these loads is zero. The amplitudes of these loads may not be the same. This is called *proportional* or *in-phase* loading. The second method is similar to the first one except that the phase angle φ is not zero. This is called *nonproportional* or *out-of-phase* loading. An illustration for proportional and 90° out-of-phase multiaxial loading conditions on tubular specimen is shown in Fig. 2.4. Loading amplitudes in multiaxial fatigue tests can be constant or variable. Although the variability in the loading amplitude increases the complexity of the analysis, however, multiaxial fatigue analysis can get even more complex when the combined loads have different frequencies. It should be noted that this research focuses on sinusoidal constant amplitude multiaxial fatigue loading.

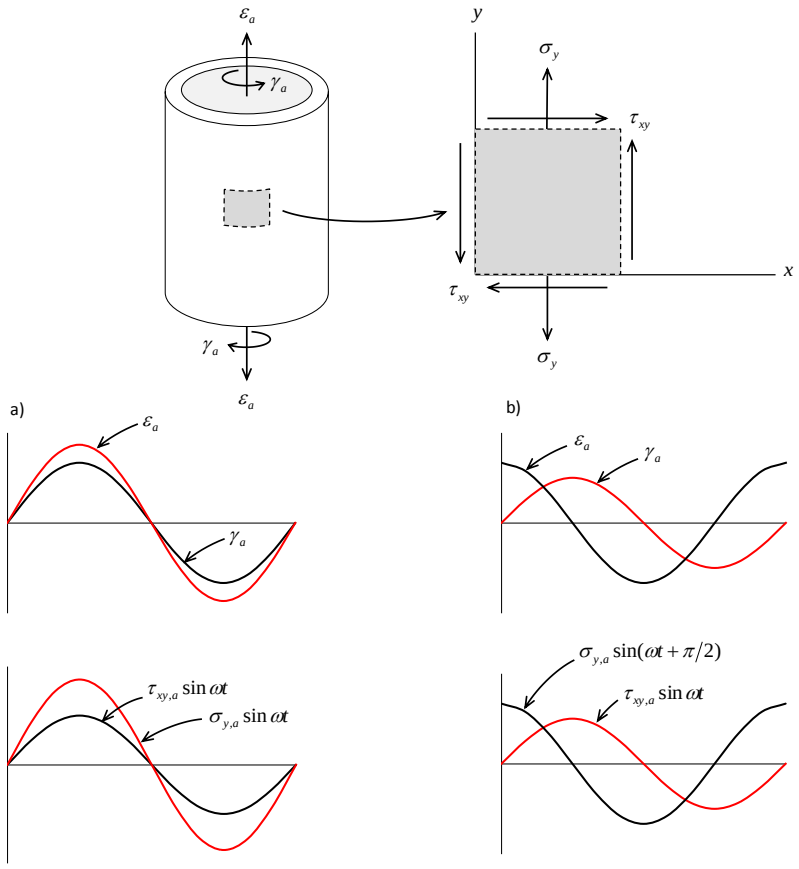

Figure 2.4: Tubular specimen under axial-torsional loading. a) Proportional. b) 90° out-of-phase. Adopted from Stephens R.I. et al., 2001.

2.1.4.1 Experimental Techniques

Multiaxial cyclic test is similar to uniaxial cyclic test except that the former involves application of multiple modes of loading. Strain-controlled multiaxial cyclic test requires strain measurement instruments such as strain gauges/rosettes or extensometers. A biaxial axial-torsional extensometer enables the control of axial and torsional strains. Therefore, biaxial extensometers are usually used in multiaxial axial-torsional tests that involve cylindrical shape specimens. However, as discussed in Section 2.1.2.2 tubular geometry enables simple calculation of torsional stresses and strains. As a result, tubular specimens are favoured in axial-torsional tests. The experimental setup for strain-controlled axial-torsional tests is similar to that in cyclic axial or torsional tests except that multiaxial tests involve the two modes. ASTM [36] developed a standard for strain controlled axial-torsional fatigue tests with thin-walled tubular specimens. The standard specifications were discussed previously for monotonic torsion tests in Section 2.1.1.2. Testing technique and practice for multiaxial tests are similar to those in Section 2.1.3.1.

2.1.4.2 Analysis Methods

In a loaded component, the magnitude and the direction of stresses or strains at a point depends on the orientation of the plane passing through that point. Because there is infinite number of planes, an infinite number of stress and strain combinations are permissible. However, only six components of stresses or strains are enough to fully describe the states of stress or strain. A special case when all nonzero stresses act on a certain plane is called "*plane stress*". Therefore, the states of stress and strains can be determined at any plane using two-dimensional transformation relations. These relations can be represented graphically using the so called Mohr's circle. On the other hand, it is more convenient to deal

with three-dimensional states of stress or strain in a matrix form.

Two dimensional stress and strain states

Strain and stress Mohr's circles can be plotted using stress and strain transformation relations. Considering an arbitrary infinitesimal element on the surface of the specimen's gage section as shown in Fig. 2.5 [40], the normal and shear stress components acting on the oblique plane are

$$\sigma_\phi = \frac{\sigma_x + \sigma_y}{2} + \frac{\sigma_x - \sigma_y}{2}\cos 2\phi + \tau_{xy}\sin 2\phi \tag{2.18}$$

$$\tau_\phi = -\frac{\sigma_x - \sigma_y}{2}\sin 2\phi + \tau_{xy}\cos 2\phi \tag{2.19}$$

The principal normal and shear stresses can be calculated using

$$\sigma_{max}, \sigma_{min} = \frac{\sigma_x + \sigma_y}{2} \pm \sqrt{\left(\frac{\sigma_x - \sigma_y}{2}\right)^2 + \tau_{xy}^2} \tag{2.20}$$

$$\tau_{max}, \tau_{min} = \pm\sqrt{\left(\frac{\sigma_x - \sigma_y}{2}\right)^2 + \tau_{xy}^2} \tag{2.21}$$

The center σ_{avg} and the radius $R_{\sigma,\tau}$ of the circle are calculated from

$$\sigma_{avg} = \frac{\sigma_x + \sigma_y}{2} \tag{2.22}$$

$$R_{\sigma,\tau} = \tau_{max} \tag{2.23}$$

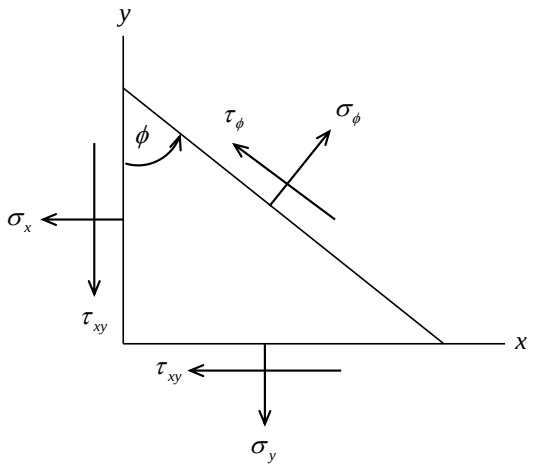

Figure 2.5: Plane stress state. Adopted from Shigley et al., 2003.

The planes of principal normal and shear stresses

$$\tan 2\phi_n = \frac{2\tau_{xy}}{\sigma_x - \sigma_y} \tag{2.24}$$

$$\tan 2\phi_s = -\frac{\sigma_x - \sigma_y}{2\tau_{xy}} \tag{2.25}$$

It should be noted here that counter-clockwise rotation corresponds to a positive ϕ. Also, shear stresses tend to rotate the element clockwise are considered positive. A rotation of 2ϕ in the circle corresponds to a rotation of ϕin the same direction in the material. Similarly, normal and shear strain components on the oblique plane are

$$\varepsilon_\phi = \frac{\varepsilon_x + \varepsilon_y}{2} + \frac{\varepsilon_x - \varepsilon_y}{2}\cos 2\phi + \frac{\gamma_{xy}}{2}\sin 2\phi \tag{2.26}$$

$$\frac{\gamma_\phi}{2} = -\frac{\varepsilon_x - \varepsilon_y}{2}\sin 2\phi + \frac{\gamma_{xy}}{2}\cos 2\phi \tag{2.27}$$

The principal normal and shear strains are

$$\varepsilon_{max}, \varepsilon_{min} = \frac{\varepsilon_x + \varepsilon_y}{2} \pm \sqrt{\left(\frac{\varepsilon_x - \varepsilon_y}{2}\right)^2 + \left(\frac{\gamma_{xy}}{2}\right)^2} \tag{2.28}$$

$$\frac{\gamma_{max}}{2}, \frac{\gamma_{min}}{2} = \pm\sqrt{\left(\frac{\varepsilon_x - \varepsilon_y}{2}\right)^2 + \left(\frac{\gamma_{xy}}{2}\right)^2} = \pm\frac{\varepsilon_{max} - \varepsilon_{min}}{2} \tag{2.29}$$

The center ε_{avg} and the radius $R_{\varepsilon,\gamma}$ of the circle are calculated from

$$\varepsilon_{avg} = \frac{\varepsilon_x + \varepsilon_y}{2} \tag{2.30}$$

$$R_{\varepsilon,\gamma} = \frac{\gamma_{max}}{2} \tag{2.31}$$

and the planes of principal normal and shear strains

$$\tan 2\phi_n = \frac{\gamma_{xy}}{\varepsilon_x - \varepsilon_y} \tag{2.32}$$

$$\tan 2\phi_s = -\frac{\varepsilon_x - \varepsilon_y}{\gamma_{xy}} \tag{2.33}$$

Due to Poisson's effect, transverse axial strain ε_x can be calculated as

$$\varepsilon_x = -\nu\varepsilon_y = -\Big[\nu_e(\varepsilon_y)_e + \nu_p(\varepsilon_y)_p\Big] = \frac{\sigma_y}{E}\big(\nu_p - \nu_e\big) - \nu_p\varepsilon_y \tag{2.34}$$

where ν_e and ν_p are the elastic and plastic Poisson's ratios, respectively.

Cyclic Axial and Torsional Loading: If a tubular specimen is subjected to a strain-controlled sinusoidal cyclic axial loading, the parameters of the stress and strain Mohr's circles during tension reversal can be obtained using Eqs. 2.18-2.34. An example of Mohrs'

circles for cyclic axial loading is shown in Fig. 2.6a. If a tubular specimen is subjected to a sinusoidal strain-controlled cyclic torsional loading, the parameters of stress and strain Mohr's circle can be obtained using Eqs. 2.18-2.34. An example of Mohrs' circle for cyclic torsion is shown in Fig. 2.6b.

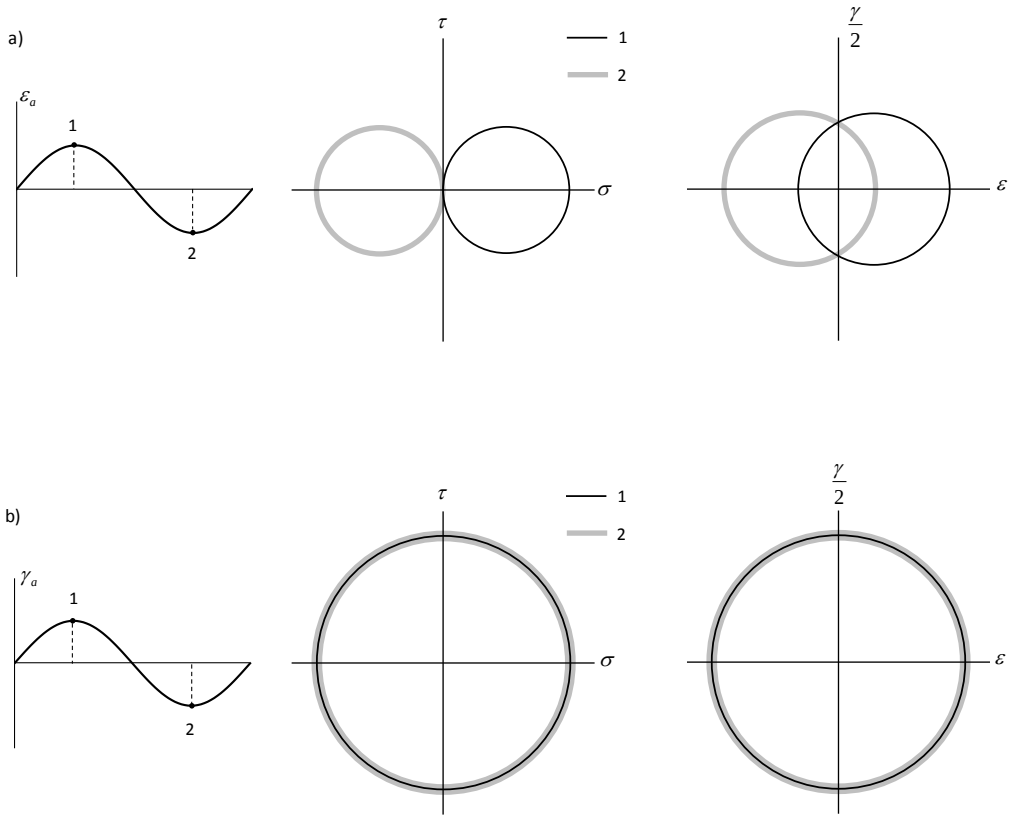

Figure 2.6: Stress and strain Mohrs' circles. a) Cyclic axial loading. b) Cyclic torsional loading.

Combined Axial-Torsional Loading: Similar to previous cases, if a tubular specimen is subjected to a sinusoidal strain-controlled multiaxial axial-torsional cyclic loading, the parameters of stress and strain Mohr's circle can be obtained using Eqs. 2.18-2.34.

Special cases for proportional *"in-phase"* and nonproportional *"out-of-phase"* loading conditions are considered next. An example of Mohrs' circles for two multiaxial loading cases is illustrated in Fig. 2.7. If the applied loads are in-phase, the orientation of the principal axes with respect to the loading axes remains fixed. If a tubular specimen is subjected to

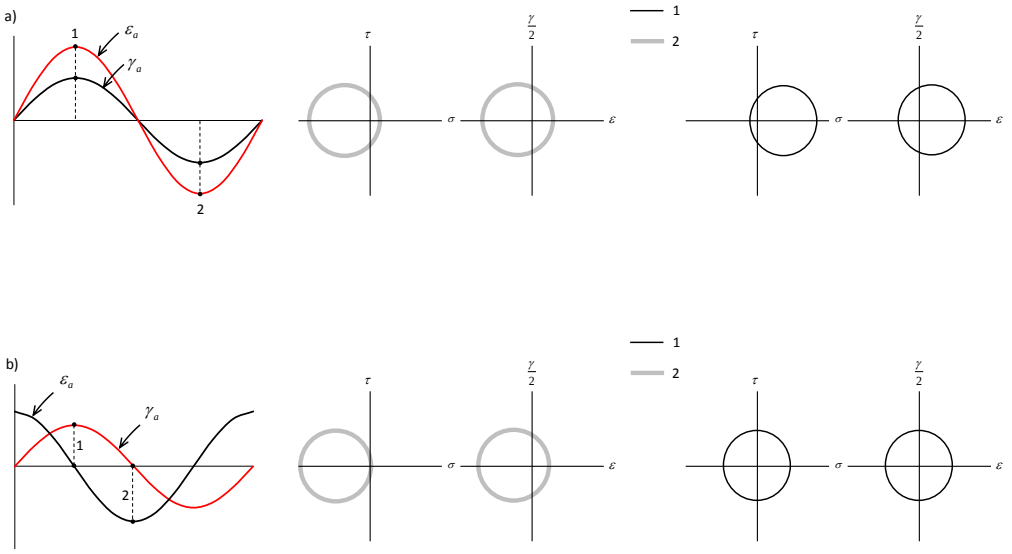

Figure 2.7: Stress and strain Mohrs' circles. a) Proportional loading. b) 90° out-of-phase loading.

a multiaxial sinusoidal axial-torsional strain-controlled loading, then the applied axial and the torsional strains take the following forms:

$$\varepsilon_y = \varepsilon_{y,a} \sin(\omega t + \varphi) \tag{2.35}$$

$$\gamma_{xy} = \gamma_{xy,a} \sin(\omega t) \tag{2.36}$$

where $\varepsilon_{y,a}$ and $\gamma_{xy,a}$ are the axial and torsional applied strain amplitudes, respectively, and

ω and t are the frequency and time, respectively. φ is the phase angle which is equal to zero for in-phase loading. It should be noted here that by adding the phase shift to Eq. 2.35, it is assumed that the axial strain is lagging the torsional strain. The orientations of the principal normal and shear strains can be expressed such as:

$$\phi_n = \frac{1}{2}\arctan\left[\frac{\gamma_{xy,a}\sin\omega t}{(\varepsilon_{x,a}-\varepsilon_{y,a})\sin(\omega t+\varphi)}\right] \tag{2.37}$$

where $\varepsilon_{x,a}$ is the axial strain calculated using Eq. 2.34. From 2.32 and setting $\sigma_y = \sigma_y sin(\omega t+\varphi)$ gives

$$\phi_n = \frac{1}{2}\arctan\left[\frac{\gamma_{xy,a}\sin\omega t}{\left(\frac{\sigma_{yt}}{E}(\nu_p-\nu_e)-(\nu_p+1)\varepsilon_{y,a}\right)\sin(\omega t+\varphi)}\right] \tag{2.38}$$

Knowing that the phase angle $\varphi = 0^\circ$ for proportional loading and the plastic Poisson's ratio $\nu_p = 0.5$ for metals, Eq. 2.38 becomes

$$\phi_n = \frac{1}{2}\arctan\left[\frac{\gamma_{xy,a}}{\left[\frac{\sigma_{yt}}{E}(0.5-\nu_e)-1.5\varepsilon_{y,a}\right]}\right] \tag{2.39}$$

Because the relation between the principal normal and shear orientation can be expressed as

$$2\phi_n = \frac{\pi}{2} - 2\phi_s \tag{2.40}$$

The principal shear strain orientation is given as

$$\phi_s = \frac{\pi}{4} - \frac{1}{2}\arctan\left[\frac{\gamma_{xy,a}}{\left[\frac{\sigma_{yt}}{E}(0.5-\nu_e)-1.5\varepsilon_{y,a}\right]}\right] \tag{2.41}$$

If the phase angle is greater than zero, then the orientation of the principal normal strain

is given by Eq. 2.38. Again, substituting the plastic Poisson's ratio $\nu_p = 0.5$ for metals gives

$$\phi_n = \frac{1}{2} \arctan \left[\frac{\gamma_{xy,a} \sin \omega t}{\left(\frac{\sigma_{yt}}{E}(0.5 - \nu_e) - 1.5\varepsilon_{y,a}\right) \sin(\omega t + \varphi)} \right] \tag{2.42}$$

It is seen from either Eq. 2.42 that the principal orientation ϕ_n is a function of time t. This means that the principal orientation always changes with time. The principal shear orientation can be obtained using Eq. 2.40.

2.2 Fatigue Life Prediction Techniques

Fatigue life prediction requires three aspects: fatigue damage parameter, fatigue life equation and material constants. Usually, fatigue damage parameter is formulated using basic design constituents such as stress, strain or energy. Using material constants that are usually obtained using standard techniques such as monotonic and cyclic tests, fatigue life equation and fatigue damage parameter can be related. Therefore, the three aspects, hereafter, are referred to as *fatigue life prediction model*. A successful fatigue life model should account for different fatigue phenomena such as cyclic hardening and mean stress. In case if uniaxial loading causes local plasticity, stresses, strains or energies can be evaluated using uniaxial elasto-plastic analysis methods such as Neuber [41] or Molski and Glinka [42]. However, using these methods for multiaxial loading state requires converting the multiaxial state into a single equivalent form. Using the well-known von Mises equivalent stress/strain may not be applicable for materials that exhibit anisotropic behaviour. In addition, generalizing these methods to complex multiaxial loading condition, such as nonproportional loading, requires assumptions that are limited to special cases [43–46]. As a result, finite element analysis offers an alternative to performing elasto-plastic analysis

not only for complex loading but for complex geometry as well. Fatigue damage parameters are classified based on the definition of the parameter that quantifies fatigue damage. This can be stress, strain or energy. In a critical plane approach, parameters are evaluated at specific planes; hence, both the fatigue life as well as the crack orientation can be predicted. Selected uniaxial and multiaxial fatigue life prediction methods are discussed next. However, in accordance to the focus of this research only strain- and energy-based parameters are considered.

2.2.1 Uniaxial Fatigue

Here, a brief review of the basic concepts related to strain-based fatigue analysis is presented. In a simple form, the Coffin-Manson relations, Eqs. 2.11 and 2.15, can be used to predict fatigue life for cyclic axial or torsional loading conditions. In this case and considering the cyclic axial loading only, the fatigue damage parameter is the axial strain amplitude ε_a. On the other hand, the fatigue life equation is $\frac{\sigma_f^{'}}{E}(2N_f)^b + \varepsilon_f^{'}(2N_f)^c$. As discussed earlier, this fatigue life equation consists of the *fatigue life* which is N_f, and the *material constants* which are E, $\sigma_f^{'}$, b, c and $\varepsilon_f^{'}$. If mean stress exists, its effect on the fatigue life can be included using methods such as Morrow [47] or Smith-Watson-Topper [48]. For axial cyclic loading, Morrow's mean stress correction is applied to the Coffin-Manson equation as follows

$$\varepsilon_a = \frac{\sigma_f^{'} - \sigma_m}{E}(2N_f)^b + \varepsilon_f^{'}(2N_f)^c \tag{2.43}$$

where σ_m is the mean stress. On the other hand, Smith-Watson-Topper, hereafter referred to as SWT, assumed that for different combinations of strain amplitude ε_a and mean stress σ_m the product $\sigma_{max}\varepsilon_a$ remains constant for a given life. The maximum normal stress is

defined as

$$\sigma_{max} = \sigma_m + \sigma_a \tag{2.44}$$

Basquin [49] suggested a *log-log* relationship between stress amplitude and fatigue life such that

$$\sigma_a = \sigma_f^{'}(2N_f)^b \tag{2.45}$$

In the case when the normal stress amplitude is equal to the maximum normal stress and using Coffin-Manson equation, the SWT mean stress correction is expressed as

$$\sigma_{max}\varepsilon_a E = (\sigma_f^{'})^2(2N_f)^{2b} + \sigma_f^{'}\varepsilon_f^{'}E(2N_f)^{b+c} \tag{2.46}$$

2.2.2 Multiaxial Fatigue

2.2.2.1 Strain-Based Models

Equivalent strain can be used as a fatigue damage parameter. A common equivalent form of strain amplitude $\varepsilon_{eq,a}$ is known as the octahedral shear strain theory and is evaluated as follows

$$\varepsilon_{eq,a} = \frac{\sqrt{(\varepsilon_{1,a} - \varepsilon_{2,a})^2 + (\varepsilon_{2,a} - \varepsilon_{3,a})^2 + (\varepsilon_{3,a} - \varepsilon_{1,a})^2}}{\sqrt{2}(1+\nu)} \tag{2.47}$$

where $\varepsilon_{1,a}$, $\varepsilon_{2,a}$ and $\varepsilon_{3,a}$ are the principal strain amplitudes such that $\varepsilon_{1,a} > \varepsilon_{2,a} > \varepsilon_{3,a}$. Once the equivalent strain amplitude is determined, the can be used in Eq. 2.11 by replacing ε_a with $\varepsilon_{eq,a}$. A major drawback of this method is that it is not suitable for nonproportional loading in which the principal strain axes rotate during cycling.

2.2.2.2 Energy-Based Models

Energy-based parameters use hysteresis energies to quantify fatigue damage. There are two types of energy densities that can be obtained from hysteresis loop: plastic and elastic. These energy densities are illustrated in Fig. 2.8. Ellyin [50] proposed that for an elastic-

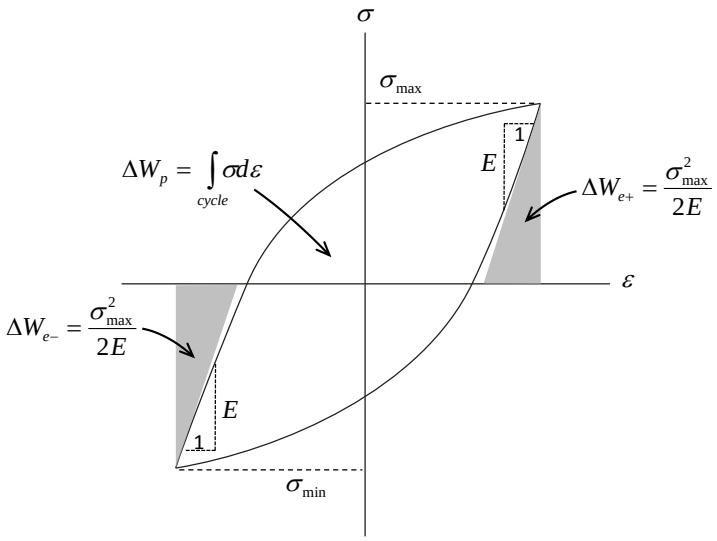

Figure 2.8: Hysteresis loop energy densities.

plastic isotropic material, the von Mises yield condition is equivalent to a constant value of the distortional component of the strain energy density W_d such that

$$W_d = \int_{cycle} s_{ij} de_{ij} = \tag{2.48}$$

where

$$s_{ij} = \sigma_{ij} - \sigma_{kk}\delta_{ij}/3 \tag{2.49}$$

and

$$e_{ij} = \varepsilon_{ij} - \varepsilon_{kk}\delta_{ij}/3 \tag{2.50}$$

s_{ij} and e_{ij} are the deviatoric stress and strain tensors, respectively. Later, Ellyin and Golos [51] suggested that total energy density, sum of plastic and positive elastic strain energy densities, can be used to correlate fatigue damage. The total energy density, ΔW_t is give by

$$\Delta W_t = \Delta W_{e+} + \Delta W_p \tag{2.51}$$

where ΔW_{e+} and ΔW_p are the positive elastic and the plastic strain energy densities, respectively. The addition of positive elastic energy has two advantages. First, it can be considered as a method to include mean stress effect. Second, it helps calculating fatigue damage in the cases when plastic strain energy densities approaches zero such as in HCF. For Masing type materials, the positive elastic strain energy density can be calculated using

$$\Delta W_{e+} = \frac{1+\nu}{3E}(\bar{\sigma}^{max})^2 + \frac{1-2\nu}{6E}(\sigma_{kk}^{max})^2 \tag{2.52}$$

where

$$\bar{\sigma}^2 = \frac{1}{2}[(\sigma_1 - \sigma_2)^2 + (\sigma_2 - \sigma_3)^2 + (\sigma_3 - \sigma_1)^2] = 3J_2 \tag{2.53}$$

where J_2 is the second invariant of the deviatoric stress, Eq. 2.49. On the other hand, the plastic strain energy density for a Masing type material can be calculated using

$$\Delta W_p = \frac{2(1-n')(2K')^{-1/n'}}{1+n'}(\Delta\bar{\sigma})^{(1+n')/n'} \tag{2.54}$$

Finally, fatigue life can be predicted using

$$\Delta W_t = \kappa N_f^m - \bar{B} \tag{2.55}$$

where κ, m and $\bar{B}$ are material constants. Garud [52] proposed an energy model based on the plastic strain energy that is calculated as the sum of energy from all stress components in a cycle such that

$$\Delta W_{ij}^{p} = \int_{cycle} \sigma_{ij} d\varepsilon_{ij}^{p} = A_g N_f^{\beta} \tag{2.56}$$

where ΔW_{ij}^{p} is the sum of hysteresis loop areas from nine stress components, and A_g and β are material constants. σ_{ij} and ε_{ij}^{p} are the stress and the plastic strain components, respectively. If a material that exhibits Masing behaviour is subjected to a multiaxial proportional axial-torsional loading, the plastic strain energy can be calculated using [53,54]

$$\Delta W_p = \Delta\sigma\Delta\varepsilon_p\left(\frac{1-n^{'}}{1+n^{'}}\right) + \Delta\tau\Delta\gamma_p\left(\frac{1-n_s^{'}}{1+n_s^{'}}\right) \tag{2.57}$$

where $n^{'}$ and $n_s^{'}$ are the cyclic axial and the shear strain hardening exponents, respectively. $\Delta\sigma$ and $\Delta\tau$ are the normal and the shear stress ranges, and $\Delta\varepsilon_p$ and $\Delta\gamma_p$ are the normal and the shear plastic strain ranges, respectively. However, during nonproportional loading the shape of the hysteresis is path dependent. Therefore, Garud used incremental theory of plasticity to describe the relation between the cyclic stresses and strains.

Jahed and Varvani [55] proposed an energy parameter based on physical observation of the fatigue cracking mechanisms. These cracking mechanisms are known as case A and case B as shown in Fig. 2.9 [56]. Case A cracks advance along the surface more than the depth, hence, they tend to be shallow and have small aspect ratios. On the other hand, case B cracks grow into the depth. Analogous to Coffin-Manson, two different lives are predicted for multiaxial axial-torsional loading condition such as

$$\Delta W_A = E_e^{'}(N_A)^B + E_f^{'}(N_A)^C \tag{2.58}$$

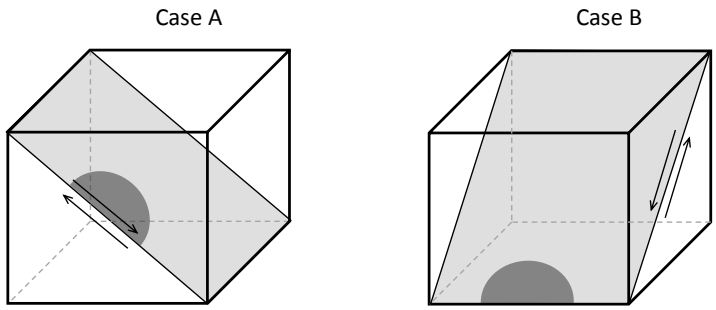

Figure 2.9: Crack growth types. Adapted from Socie and Marquis, 2000.

$$\Delta W_T = W_e^{'}(N_T)^{B_s} + W_f^{'}(N_T)^{C_s} \tag{2.59}$$

where ΔW_A and ΔW_T are the energies due to purely axial and torsional loading, respectively and the coefficients $E_e^{'}$ and $W_e^{'}$ are the energy- axial and torsional fatigue strength coefficients, respectively. $E_f^{'}$ and $W_f^{'}$ are the axial and the torsional fatigue toughness, respectively. The exponents B and B_s are the energy- axial and torsional fatigue strength exponents, respectively, and C and C_s are the axial and the torsional fatigue toughness exponents, respectively. The coefficients and the exponents in Eqs. 2.58 and 2.59 can be obtained similar to Coffin-Manson equations for axial, Eq. 2.11, and torsional loading, Eq. 2.15, but using axial and torsional energy-life curves. Energy-life curve for axial loading is illustrated in Fig. 2.10. Then, the obtained lives, N_A and N_T, are used in Eq. 2.60 for fatigue life prediction.

$$N_f = \frac{\Delta W_A}{\Delta W_t} N_A + \frac{\Delta W_T}{\Delta W_t} N_T \tag{2.60}$$

where ΔW_t is the total energy density.

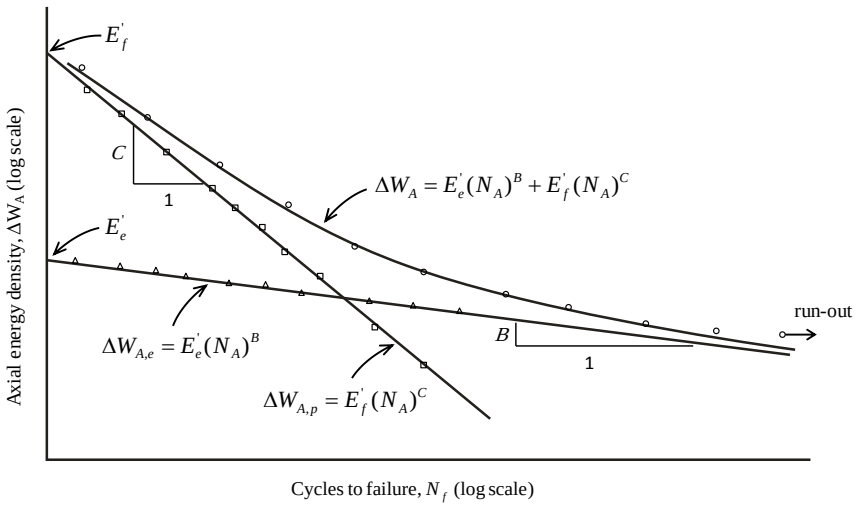

Figure 2.10: A schematic illustrating energy-life curve parameters.

2.2.2.3 Critical Plane Approach

As mentioned previously, critical plane parameters are evaluated at certain planes. Therefore, successful critical planes models should be able to predict the fatigue life as well as the dominant failure plane(s). Similar to classical models, critical plane models can be stress-, strain- or energy-based. Brown and Miller [57] proposed a strain-based parameter that assumes that fatigue life is a non-linear function of strain. The critical plane of this parameter is the plane of maximum shear strain. The general form of Brown and Miller's is

$$\frac{\gamma_{max}}{2} = f(\varepsilon_n) \tag{2.61}$$

where γ_{max} is the maximum shear strain and ε_n is the corresponding normal strain at the critical plane. Later, Kindil et al. [58] suggested a specific form of Brown and Miller's

parameter that is expressed as

$$\frac{\Delta\gamma_{max}}{2} + S_k \Delta\varepsilon_n \tag{2.62}$$

where S_k is a material constant. Socie [59] proposed that by replacing the normal strain amplitude term with the maximum principal strain, SWT parameter in Eq. 2.46 can be used for multiaxial loading. This parameter is evaluated at the plane of maximum normal strain. The SWT multiaxial fatigue model is expressed as

$$\sigma_{n,max}\frac{\Delta\varepsilon_1}{2} = \frac{\sigma_f^{'2}}{E}(2N_f)^{2b} + \sigma_f^{'}\varepsilon_f^{'}(2N_f)^{c+b} \tag{2.63}$$

where $\sigma_{n,max}$ and $\Delta\varepsilon_1$ are the maximum normal stress and the maximum principal strain range at the critical plane. SWT model can be used for proportional and nonproportional loading conditions. A schematic that illustrates the physical basis of SWT parameter is shown in Fig. 2.11a. Fatemi and Socie 1988 [60] proposed a strain-based parameter that considers the plane of maximum shear strain amplitude $\Delta\gamma_{max}/2$ as a critical plane. This parameter can be used for proportional and nonproportional loading conditions. Fatemi-Socie fatigue model is expressed as

$$\frac{\Delta\gamma_{max}}{2}\left(1 + k\frac{\sigma_{n,max}}{S_{yt}}\right) = \frac{\tau_f^{'}}{G}(2N_f)^{b_s} + \gamma_f^{'}(2N_f)^{c_s} \tag{2.64}$$

where k is the Fatemi-Socie constant and σ_{yt} is the monotonic tensile yield strength. The coefficients $\tau_f^{'}$ and $\gamma_f^{'}$ are the torsional fatigue strength and ductility coefficients, respectively. The exponents b_s and c_s are the torsional fatigue strength and ductility exponents, respectively. G is the shear modulus. The physical basis of Fatemi-Socie parameter is shown in Fig. 2.11b. An alternative form of Eq. 2.64 can be achieved using

axial strain-life properties such that

$$\frac{\Delta\gamma_{max}}{2}\left(1+k\frac{\sigma_{n,max}}{S_{yt}}\right)=\left[(1+\nu_e)\frac{\sigma_f^{'}}{E}(2N_f)^b+(1+\nu_p)\varepsilon_f^{'}(2N_f)^c\right]\times\left[1+k\frac{\sigma_f^{'}}{2S_{yt}}(2N_f)^b\right] \quad (2.65)$$

As in Eq. 2.44, the maximum normal stress term in SWT and Fatemi-Socie parameters enable them to include mean or residual normal stresses.

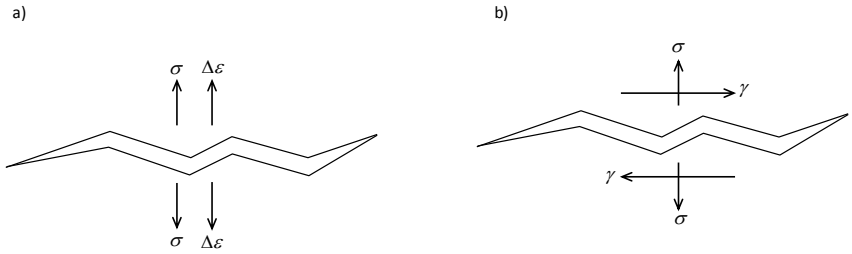

Figure 2.11: Crack growth. a) Tensile crack. b) Effect of normal stress on shear crack. Adopted from Socie and Marquis, 2000.

2.3 Literature Review

Research on magnesium and its alloys has tremendously increased during the past few years due to the wide interest in using magnesium alloys as automotive structural materials. Within the scope of this research, three categories of research have been considered. The first category concerns the fundamental microstructural studies to understand and to characterize magnesium behaviour. The focus of these studies is on the deformation mechanism, twin formation, texture evolution, and grain size, temperature effects and pseudoelasticity. The second category studies macroscopic and mechanistic levels of fatigue modeling. This category focuses on mechanical behaviour under cyclic stress- or

strain-controlled conditions, crack initiation and propagation, fracture properties, and fatigue life prediction models. The third set of studies is on plastic modeling of anisotropic behaviour of Mg alloys through crystal plasticity or continuum mechanics. These studies focus on predictive models for the anisotropic/asymmetric behaviour of Mg alloys and their application in finite element models. The mechanical behaviour of magnesium rolled sheet and extrusion under monotonic and cyclic axial loading in different directions has received considerable attention. Texture orientation and evolution have been mapped to the mechanical behaviour showing the role of twinning in yield asymmetry, the role of detwinning in tension after compression, and the role of slip deformation upon completion of detwinning in tension. Pole figure analyses indicate that extrusion process creates a strong texture in magnesium extrusions such that basal planes are aligned along the extrusion direction with the c-axis perpendicular to it [12, 15, 61–65]. Hexagonal closed packed (HCP) metals, such as magnesium, deform plastically by two mechanisms: slip and twinning [66–68]. Slip and twin planes for HCP metals are illustrated in Fig. 2.12 and Fig. 2.13. Among these systems, the basal slip and the $(10\bar{1}2)$ extension twin are easiest to be activated due to their low critical resolved shear stresses (CRSS). The effect of grain

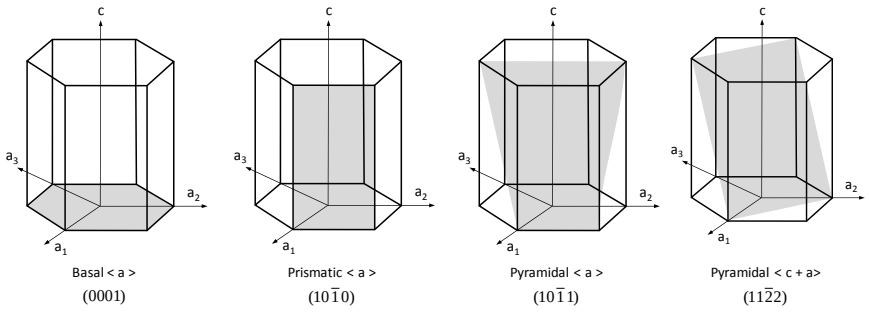

Figure 2.12: Slip planes in HCP metals.

size on the mechanical behaviour of magnesium alloys have been investigated by many

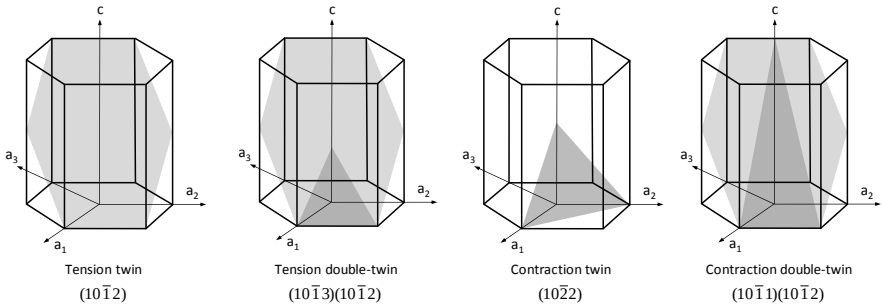

Figure 2.13: Twin planes in HCP metals.

researchers. Koike et al. [69] did monotonic tensile tests on fine-grained AZ31B extrusion with an average grain size of 6.5±0.4 μm and found substantial non-basal slip activities at 2% strain. Uematsu et al. [63] studied the effect of extrusion conditions on grain refinement and fatigue behaviour of several magnesium extrusions. For AZ31B, experiments by Uematsu et al. showed that grain size decreases with decreasing working temperature. They were able to achieve grain size of 2.1 μm at extrusion rates of 67 and outlet temperatures of 625K. Fatigue strength improvement was found to be associated with smaller grain size, especially in the high cycle regime. The fatigue strengths at 10^7 cycles for the samples with grain sizes of 7.2 and 2.1 μm were 90 and 130 MPa, respectively. Like Uematsu et al. [63], Yasumasa et al. [70] observed the same relation between extrusion temperature and grain size. In addition, they found that monotonic tension-compression anisotropy became less pronounced with fine grained samples compared to other samples with larger grain sizes. Zhu et al. [71] performed cyclic tension-compression tests on ultrafine-grained AZ31 extrusion with an average grain size of 5.6 μm and compared it with a conventional one that had an average grain size of 30 μm. Comparisons of the cyclic behaviour showed that, while conventional extrusion exhibits stress-strain asymmetry and cyclic hardening, the ultrafine grained extrusion exhibits symmetric stress-strain behaviour and cyclic soft-

ening. Tang et al. [72] examined the effect of extrusion parameter such as extrusion ratio, temperature and velocity on grain size and texture distribution of AZ31 alloy. They found that extrusion ratio is the most significant parameter for grain refinements while extrusion temperature and velocity have no influence on grain size. Tang et al. measured the (0002) pole intensities at different extrusion conditions and found that maximum intensities increase with decreasing extrusion ratio and increasing velocity. On the other hand, they found that at low extrusion ratio and low velocity the (0002) pole intensities reduce as the extrusion temperature increases. The maximum intensity was not affected by increasing the temperature at high extrusion ratio and high velocity. Experimental investigation of the role of basal and prismatic slips on the tensile elongation of AZ61 rolled sheet was carried out by Koike and Ohyama [73]. They observed that when the basal planes were tilted by more than 16.5° toward the tensile axis, the basal $< a >$ slip was the dominant deformation mechanism and small elongation of 8% was obtained. Otherwise, prismatic $< a >$ slip became the dominant deformation mechanism and elongation that is more than 20% was obtained. Koike and Ohyama found that the critical resolved shear stress ratio of prismatic to basal slip was 1.5-2.0. This ratio is close to the value of 1.1 determined earlier by Koike et al. [69] for fine grained AZ31B that was produced by equal-channel angular extrusion technique. These ratios are interesting because reports on single crystal Mg from the sixties and the early seventies [74–77] suggest a ratio of 100. Agnew and Duygulu [78] investigated plastic anisotropy and the role of non-basal slip in AZ31B sheet. In addition to experiment, they performed polycrystal plasticity simulations to model the texture evolution as well as the observed anisotropy. Agnew and Duygulu validated the measurement of anisotropy and texture by direct observation of the dislocation microstructure. One of the major findings of this investigation is the ratio of the critical resolved shear stress (CRSS) of prismatic to basal slips which is between 2 and 2.5. This value is in agreement with

Koike et al. findings [69, 73]. Agnew and Duygulu [78] suggested that the large difference between the early observations on single crystal studies and the current findings could be due to grain boundaries or grain size. Beer and Barnett [79] investigated the influence of initial microstructure on the hot working flow stress of wrought extruded and as-cast AZ31 alloys. They performed monotonic compression and torsion tests at various temperatures between 300 and 450°C. Beer and Baranett found that high temperature deformation behaviour is sensitive to the deformation condition, the initial microstructure and the deformation mode. Comparing the stress-strain curves, Beer and Baranett found that torsion exhibit much higher strain to peak flow stress than compression. Also, they noticed that the shape of the compression stress-strain curve of wrought material changes significantly as temperature is reduced and strain rate is increased. The authors related this to the enhanced operation of $(10\bar{1}2)$ twinning. Barnett [61] examined the role of twinning in the monotonic behaviour of AZ31 extrusion and found that extension twinning $(10\bar{1}2)$ appears to increase the uniform elongation that is observed in tensile tests. Barnett proposed a constitutive model that successfully described the tensile and compressive flow curves of AZ31 extrusion. This model focuses on the role of crystallographic re-orientation during twinning-detwinning processes to explain the hardening behaviour of the material. Later, Barnett [80] investigated the effect of contraction double twins on the uniform elongation and on the ductile failure of tensile loading. The considered wrought alloys are: AZ31, ZK60 and ZM20. Barnett concluded that the $(10\bar{1}1)-(10\bar{1}2)$ double twinning may decrease uniform elongation and can be responsible for the shear failure of magnesium alloys at low strains. Luo et al. [81] investigated different characteristics of AZ31B sheet alloy. The monotonic tensile results show that the tensile stress strain curve was concave down while the compressive curve was concave up because of twinning deformation. Also, the authors performed the monotonic tests at different orientations, namely longitudinal, transverse

and at an angle of 45°. The results from these different tests indicate that the monotonic behaviour is dependent on the loading orientation. The authors studied the evolution of microstructure under various loading paths and they were able to observe twin formation at different stages. These observations showed that the areal twin fraction reached nearly 72% under compression and then decreased to 6% after subsequent tension. The authors supported this observation by conducting pole figure analysis which clearly indicated that the initial texture is nearly preserved when tension is applied after compression. Lou et al. performed simple shear tests and observed twinning under true shear strain of 5.8% with areal twin fraction of about 12%. Unlike cyclic tension-compression loading, shear hysteresis was symmetric. Brown et al. [12] investigated twinning and detwinning during cyclic deformation of as-extruded AZ31B. Using In-situ Neutron Diffraction, they were able to determine the crystallographic texture during cyclic tension-compression loading with strain amplitude of 1%. Similar to Lou et al. [81], they found that twinning and detwinning was maintained at least until half-life. However, the capacity of the material to reverse the texture was seen to reduce with cycling and some residual twins were observed. Brown et al. argued that the presence of residual twins could explain the increase of hardening during the test. Koike et al. [82] investigated the roles of deformation twinning and slip in the fatigue failure mechanism of AZ31 sheet. They observed tension twins below and above the fatigue limit, which was 70 MPa. Hence, they concluded that tension twins do not directly contribute to fatigue failure. On the other hand, prismatic slip and significant cyclic hardening were only observed above the fatigue limit. Koike et al. attributed the hardening to cross-slip of prismatic dislocations and the interaction between prismatic dislocations and tension twins. Also, $(10\bar{1}1)$-$(10\bar{1}2)$ double twins were also observed under large surface steps. The authors explained that the activation of double twins leads to significant strain incompatibility at the twin/matrix interface causing large

surface steps formation and eventually leading to crack formation, propagation and failure. Pseudoelastic behaviour in hexagonal closed packed (HCP) metals has been observed in different magnesium alloys such as AZ91 casting [83] and AZ31 extrusion [84]. It was found that stress-strain hysteresis loops were forming due to loading-unloading in monotonic tensile and compressive tests. Researchers such as Cáceres et al. [83], Mann et al. [85] and Muránsky et al. [84] attributed such hysteresis effects due to activation of reversal twinning process during loading-unloading. On the other hand, Zhou et al. [86] attributed the hysteresis effect to the formation of fully reversible dislocation-based incipient kink bands.

Fatigue characterization and modeling of magnesium has also grown in recent years. One of the early studies concerning multiaxial fatigue of magnesium alloys was conducted by Bentachfine et al. [87] who performed strain controlled multiaxial tension-torsion tests on a magnesium-lithium alloy. To investigate the phase angle effects, they fixed the strain amplitudes and varied the phase angle. Bentachfine et al. found that fatigue life depends on the phase angle such that the maximum and the minimum fatigue lives were obtained at 0◦ and 90◦ phase angle, respectively. Zenner and Renner [13] investigated the Masing behaviour of AZ91 and AE42 magnesium die casting and AZ31 and AZ80 magnesium extrusions. They found that the die casting alloys show approximately Masing behaviour, which was not observed in the extruded alloys. This was due to the strong anisotropic behaviour in tension and in compression. Zenner and Renner attributed the anisotropic behaviour to deformation twinning. Tokaji et al. [88] investigated fatigue behaviour and fracture mechanisms of rolled AZ31. They performed cyclic tests on smooth and compact-tension specimens. As far as fatigue is concerned, they found that the fatigue strength at 10^7 cycles is 50 MPa. Also, they found that the relationship between fatigue crack propagation and stress intensity factor for large cracks consists of two parts that have two slopes and attributed this to the transition of the operative micromechanisms of fracture, i.e., slip

and twinning. In addition, it was found that cracks initiate at very early stages of fatigue life due to cyclic slip deformation in both transgranular and intergranular modes. Nan et al. [89] used a scanning probe microscope to study crack initiation and propagation near the fatigue limit of AZ31 extrusions. They recognized a very sharp bend in the S-N curve at stress amplitude of 120 MPa. Similar to Tokaji et al. [88], Nan et al. found that cracks initiate in the early stages of fatigue life within the crystal grains. They also observed that initiated cracks propagate in mixed mode (I and III). At stress levels slightly higher than the fatigue limit, Nan et al. observed that the initiated crack were blocked and arrested by the grain boundary. Then, due to cycling, the energy accumulation at the crack tip reaches a critical value allowing the crack to break the grain boundary and then propagate to the adjacent grain. Khan et al. [90] found that fatigue life of AZ31 alloy increases with increasing Mn content up to 0.4 $wt\%$, and was significantly reduced for Mn content of 0.79 $wt\%$. This observation was associated with a decrease in grain size, and an increase in tensile strength and hardness as the Mn content increased up to 0.4 $wt\%$. The authors suggested that Mn contents between 0.4 and 0.6 $wt\%$ should provide a good balance for both mechanical properties and fatigue strength of magnesium alloys. Sonsino and Dieterich [16] performed constant and variable amplitude tests on AZ91HP, AM50HP and AM20HP die casts. Two specimens, notched with $K_t = 2.5$ and unnotched, were tested under stress and strain controlled conditions and at two R ratios: -1 and 0. The authors investigated several fatigue properties and found that the mean stress sensitivity of magnesium alloys is comparable to that of cast aluminum. In addition, they found that the notch sensitivity of magnesium is lower than that of cast-nodular iron or wrought steels under bending. Taking into account that they performed axial tests only, Sonsino and Dieterich concluded that the notch sensitivity of magnesium is even lower since they compared it with data from bending tests. Furthermore, Sonsino and Dieterich evaluated the fatigue

strengths of the three magnesium alloys and compared them with aged cast aluminum alloy G-AlSi7Mg0.6 T6. This comparison shows that the magnesium alloys are comparable to the aluminum alloys, especially AZ91HP. From this study, Sonsino and Dieterich concluded that magnesium alloys can be a good alternative to aluminum if the corrosion and creep effect can be avoided. Hasegawa et al. [11] performed low cycle axial fatigue tests on AZ31 extrusion under stress- and strain-controlled conditions. They found that while the hysteresis loops of strain-controlled tests were asymmetric, stress-controlled loading produces symmetric hysteresis. Hasegawa et al. performed strain-controlled tests under completely reversed loading. Stress-controlled tests were performed under completely reversed loading and with a mean stress. The authors found that stress-controlled fatigue life data could be successfully correlated using the Coffin-Manson equation, which was not the case for the strain-controlled test. They introduced a mean stress term to the Coffin-Manson equation. Using their proposed equation and the Smith-Watson-Topper (SWT) model, Hasegawa et al. were able to predict the fatigue life for all tests within ±2.0x bounds. Uematsu et al. [63] reported stress-controlled tests on AZ31B for different extrusion conditions. They showed a sharp transition in the stress-life curve behaviour at lives around 10^5 cycles. A similar sharp transition trend was observed by Ishihara et al. [91] for AZ31B extrusion and rolled sheet in extrusion/rolled and transverse directions, Tokaji et al. [88] for rolled AZ31 and Nan et al. [89] for AZ31 extrusion. Chen et al. [20] studied axial low cycle fatigue behaviour of AM50 extrusion. They found that hysteresis loops of tests that were performed at strain amplitude of 0.65% or lower are symmetric with negative mean stress. However, tests that were performed at higher strain amplitudes were found to produce asymmetric hysteresis with a positive mean stress. Unlike Hasegawa et al. [11], the authors were able to correlate the fatigue life using the standard Coffin-Manson equation. Also, Chen et al. [20] found that AM50 extrusion exhibits dynamic strain aging, appearing as serrated

flow in the hysteresis loops at high strain amplitude. Yang et al. [92] performed very high cycle fatigue tests on AZ31 extrusion and found that the fatigue strength at 10^9 cycles was 88.7±4.1 MPa. Tokaji et al. [88] and Koike et al. [82] found the fatigue limit for AZ31 sheet was 50 and 70 MPa, respectively. Because yielding in compression is less than half that in tension, Yang et al. argued that at low stress levels twins are more likely to be activated during compression reversal than slip during tension reversal. Hence, they proposed that twin bands are the preferable locations for the initiation of fatigue cracks. Yang et al. supported their proposal by microstructural observation of the tested specimens. Begum et al. [19] investigated low cycle axial fatigue properties of AZ31 extrusion and proposed a correlation between plastic strain amplitude and number of cycles. Also, they measured the elastic modulus during loading and unloading parts of each cycle. Begum et al. found that the modulus of elasticity measured from the unloading part is fairly constant as the cycling progresses. However, it was found that the modulus of elasticity measured from the loading part increases with the number of cycles, especially at high strain amplitudes. Begum et al. attributed this to pseudoelasticity. Matsuzuki and Horibe [93] analyzed the fatigue damage process in AZ31 extrusion. They performed tensile and plastic strain controlled tests on annealed and as-received specimens of AZ31. Matsuzuki and Horibe found no significant difference in the mechanical properties or the fatigue behaviour of the two materials except that the fatigue life of as-received specimens is slightly longer than for annealed specimens. They attributed the difference to the fact that the two materials have different dislocation densities. By analyzing the dependency of the hysteresis loops and the mean stress on the plastic strain amplitude, the authors concluded that there is a transition region that separates the type of the plastic deformation mechanism. They suggested that twinning is predominant at high plastic strain amplitude whereas slip is predominant at low plastic strain amplitude. Also, Matsuzuki and Horibe noticed that the

transition region coincides with the knee point in the bi-linear strain-life curve. Ishihara et al. [94] performed fatigue experiments to investigate the effect of load ratio on fatigue life and crack propagation behaviour of AZ31 extrusion. Like Nan et al. [88] and Tokaji et al. [89], Ishihara et al. found that fatigue cracks initiate after 5-10% of total fatigue life. Therefore, they suggested that fatigue life can be approximated by crack propagation life. Also, they found that the effect of mean stress on fatigue strength can be estimated by the Gerber relationship. Later, Ishihara et al. [95] conducted fatigue tests on AZ91 diecast and AZ61 extrusion and found that the initiation lives of these alloys are minimal. Arguing that fatigue life can be approximated by propagation life, they employed fracture mechanics approach and assumed initial crack length as the size of defects or inclusions for diecast and extrusion alloys, respectively. Ishihara et al. found that fatigue life can be correlated with stress intensity factor. Park et al. [21] investigated the effect of anisotropy on the low cycle behaviour of hot-rolled AZ31 plate. They performed low cycle axial fatigue tests for both rolling and normal directions. They found that while completely reversed straining in the rolling direction results in a positive mean stress due to twinning in compression, applying the same load in the normal direction results in a negative mean stress due to twinning in tension. This negative mean stress was seen to cause a beneficial effect on the fatigue life. Later, Park et al. [14] performed stress- and strain-controlled axial tests on hot-rolled AZ31 plate. They reported the same observation as Hasegawa et al. [11] regarding the disappearance of the asymmetric feature of the hysteresis loop for stress-controlled tests. Park et al. [14] suggested the use of energy as a fatigue damage parameter for two reasons. First, they found that energy is a stable parameter. Second, they used it as an alternative to avoid using Coffin-Manson type models that depend on the value of plastic strain amplitude. The authors attributed the latter to the ambiguity in determining the plastic strain amplitude from the asymmetric hysteresis loop generated from

strain-controlled tests. YJ Wu et al. [96] studied the role of twinning and slip in cyclic deformation of AZ31 extrusion. They performed cyclic tension-tension strain-controlled tests in two different directions such that the deformation mechanism is either twinning or slip. Their experiment showed that the hysteresis loop of the slip dominant specimen exhibits low plasticity and high positive mean stress. On the other hand, the hysteresis loop of the twinning dominant specimen exhibits considerable plasticity but very low positive mean stress, although both tests were performed at the same strain amplitude. YJ Wu et al. performed a series of cyclic tests in both directions and found that the twinning dominant direction possessed longer fatigue life compared to the slip dominant directions. Wu et al. [17] studied the effect of texture and extension twins on the low cycle fatigue behaviour of the rolled AZ31 alloy. They performed cyclic axial tests along three directions: rolling, transverse and normal. Wu et al. found that both Coffin-Manson's and Basquin's equations can be successfully used to correlate the LCF lives of the rolled AZ31 alloy for all of the investigated directions. Although both directions show tensile mean stress developments, the authors found that the rolling direction possesses slightly better fatigue resistance than the transverse direction. In contrast, cyclic axial loading along the normal direction was seen to develop compressive mean stress that usually results in a beneficial effect. However, the fatigue resistance in this direction was found to be the least. Wu et al. attributed this to the fact that the lattice orientation, and consequently the deformation mechanisms involved, resulted in brittle behaviour. Although it induces different deformation mechanisms, Wu et al. concluded that the initial loading mode of the cycle (tension or compression) had no significant effect on the low cycle fatigue resistance of the rolled AZ31 alloy. In addition, the authors compared fatigue resistant of several magnesium alloys with structural aluminum alloys, such as AA7XXX types, AA7175 and AA7150, and found that magnesium alloys possess better fatigue resistance, especially at high strain

amplitudes. Zhang et al. [97] studied cyclic behaviour of AZ61A extrusion and performed monotonic and multiaxial tension-torsion cyclic tests. The authors observed that while cyclic shear hysteresis is symmetric, the combined axial-torsional loading produces asymmetric shear hysteresis loops. They attributed this to the twinning-detwinning process that occurs due to the application of axial cyclic load. In addition, Zhang et al. found that nonproportional hardening was insignificant and attributed this observation to the limited number of slip systems and to twin formation. Li et al. [98] examined the effect of strain amplitude on tension-compression fatigue behaviour of AZ61A extrusion. They found that when the strain amplitude is higher than 0.5%, shear cracking and significant twinning were observed. Conversely, tensile cracking and little twinning were observed at strain amplitudes lower than 0.5%. They suggested that fatigue crack initiation is dominated by dislocation slip when the strain amplitude is less than 0.5% and by a twinning-detwinning process when the strain amplitude is greater than 0.5%. Park et al. [99] examined the role of initial $(10\bar{1}2)$ twin in the fatigue behaviour of rolled AZ31 Mg alloy. To do this, they machined cylindrical samples with a large gage length and diameter and then applied pre-tension loading of 2, 5 and 8%. After that, they re-machined these samples to smaller sizes for monotonic compression and fatigue loading. To induce initial $(10\bar{1}2)$ twinning, they machined all samples along the normal direction. This way, tensile loading acts parallel to the c-axis which directly activates twinning mechanism. As far as monotonic compression, it was found that the compressive yield and ultimate strengths vary similarly with respect to the amount of pre-tension strain. They reach their minimum at 2% pre-tension strain case and then increase with increasing pre-tension strain. Cyclic behaviour was also seen to depend on pre-tension strain. While cyclic tension-compression loading along the normal direction induces compressive mean stress, application of exactly the same loading on 5 and 8% pre-tensioned specimens induces positive mean stress. The authors attributed

this to the fact that as pre-tension strain increases, the amount of twins does also. Therefore, the compressive reversal is consumed by the detwinning process which requires low compressive flow stress. On the contrary, tensile flow stress was found to increase with pre-tension strain leading to the development of positive mean stress. Comparing fatigue life with amount of pre-tension strain, Park et al. found that the latter has a negative effect on the former. They argued that this was due to the development of positive mean stress, possibility that twin boundaries affect crack initiation and propagation and the reduction of ductility because of the pre-tension. Yu et al. [100] studied fatigue damage development in pure polycrystalline magnesium under cyclic tension-compression loading. They performed strain controlled tests at 1.0 and 0.12% strain amplitudes. Tests were interrupted at different stages and SEM analysis was conducted. The authors observed around 80% and 50-70% of the separation fatigue life, which is the number of cycles until specimens failed by separation, is spent in initiating microcracks with insignificant crack growth for 1.0 and 0.12% strain amplitudes, respectively. Also, it was found that grain boundary cracking is persistent under all applied strain amplitudes. The authors observed both intergranular and transgranular crack growth modes. They found that transgranular crack growth at 1% strain amplitude is due to cleavage cracking along twin boundary. On the other hand, transgranular crack growth at 0.12% strain amplitude is dominated by slip-induced cleavage cracking on slip planes. Keeping in mind that Yu et al. [46] tested pure polycrystalline magnesium, their observations regarding crack initiation life disagrees with the observations of Tokaji et al. [88] on rolled AZ31, Nan et al. [89] on AZ31 extrusion, Ishihara et al. [94] AZ31 extrusion and Ishihara et al. [95] on AZ91 diecast and AZ61 extrusion. Yu et al. [22] investigated multiaxial behaviour of AZ61A extrusion under strain-controlled axial-torsional loading condition. They defined equivalent strain as the radius of the minimum circle that circumscribes the strain loading path. Using this

definition, Yu et al. found that the highest and the lowest fatigue lives were obtained from in-phase and 90° out-of-phase loading, respectively. Fatigue lives from pure axial and torsional loading were found to fall in between. According to Jiang's [101] cracking definition, the authors examined the cracking behaviour of AZ61A extrusion and concluded that the material exhibits mixed or shear cracking when the equivalent strain is less than or greater than 0.5%, respectively. Yu et al. successfully estimated the multiaxial fatigue life using modified Smith-Watson-Topper, that was proposed by Jiang and Sehitoglu [102], and Fatemi-Socie parameters, especially for the low cycle regime. Lv et al. [23] investigated the influence of specimen orientation on the fatigue properties of AZ31 sheet. The authors performed monotonic tensile and compressive and cyclic axial tests along the rolling and transverse directions. Cyclic tests were performed under stress- and strain-controlled conditions. From monotonic tests, Lv et al. found that the elongation along the transverse direction is higher than that along the rolling direction. This was seen to be associated with obvious necking and shear failure on the specimens that were machined along the transverse and rolling directions, respectively. Lv et al. ascribed this to the fact that prismatic $< a >$ or pyramidal $< a >$ slips could be easily activated on the transverse specimens but not on the ones along the rolling directions. Lv et al. were successfully able to correlate the fatigue lives using Coffin-Manson's and Basquin's equations. In addition, they found that the transverse specimens possess higher fatigue lives than the ones that were machined along the rolling direction. Lv et al. calculated the strain energy density and found that at strain amplitude less than 0.7%, the hysteresis energy of the rolling direction specimens is higher than that of the transverse directions. Jordon et al. [15] studied the effect of twinning, slip and inclusions on the fatigue behaviour of AZ61 extrusions. Monotonic and cyclic tests were performed along the extrusion and transverse directions. Different parameters such as grain orientation, grain size, particle size and cyclic hardening were

incorporated in a Multi-Stage Fatigue (MSF) model. Using this model, the authors were able to predict strain-life results for extrusion and transverse directions. Also, based on this model, it was found that fatigue life determination is more dependent on inclusion size than the anisotropic effects due to texture, yield and hardening. Jordon et al. compared their experimental finding with other lightweight structural alloys such as AM50 Mg casting, A356-T6 Al casting, 7075-T651 Al rolling, AM30 Mg extrusion and AZ31 and AZ31B Mg extrusions, and found that AZ61 magnesium extrusion possess good fatigue resistance compared to other alloys. Uniaxial ratcheting and low cycle fatigue behaviour of hot-rolled AZ91D magnesium under cyclic tension were investigated by Lin et al. [103]. They examined the effects of stress amplitude, mean stress and stress rate on the uniaxial ratcheting response of the material. Lin et al. found that the ratcheting strain increases rapidly with stress amplitude. Similarly, they found that when the mean stress is increased the ratcheting strain and the ratcheting strain rate increase as well. However, it was found that the ratcheting strain and the ratcheting strain rate decease when the stress rate is increased. Finally, the authors found that increasing the stress rate improves the fatigue life. Zhu et al. [71] investigated low cycle behaviour of an ultrafine-grained AZ31 magnesium extrusion that was processed by equal-channel angular pressing. Comparison between the low cycle fatigue behaviour of the conventional extrusion and the ultrafine-grained one revealed two major differences. First, while it is considered as a characteristic of AZ31 extrusion to show asymmetric cyclic behaviour when subjected to tension-compression loading, the hysteresis of the ultrafine grain samples showed no signs of twinning and was symmetric. Second, the ultrafine grained alloy exhibits cyclic softening while the conventional alloy exhibits cyclic hardening. The authors attributed the cyclic softening to the grain coarsening and argued that such coarsening could be related to the equal-channel angular pressing process. The effect of extrusion ratio on the ratcheting behaviour of AZ31B extrusion was

investigated by Zhang et al. [104]. This study showed that grain size decreases and yield strength increases as the extrusion ratio increases. However, the effect of extrusion ratio on the grain size and the yield strength was seen to decrease after an extrusion ratio of 8. Regardless of the extrusion ratio, Zhang et al. found that final ratcheting strain increases as the mean and peak stresses do. Similarly, cyclic softening/hardening behaviour was unaffected by the extrusion ratio. On the other hand, it was found that the extrusion ratio affect the final ratcheting strain variation with the stress amplitude. Zhang et al. experiment shows that the value of ratcheting strain decreases as the extrusion ratio is increased. They attributed this to three changes resulting from the change of extrusion ratio: twinning-detwinning magnitude, yield strength and slope of stress versus plastic strain after yielding and nonlinear elastic effect or pseudoelasticity. Yang et al. [105] investigated monotonic and very high cycle fatigue behaviours of Mg-12Gd-3Y-0.5Zr (GW123k) magnesium extrusion and compared it with AZ31 extrusion. This study was conducted to examine the effect of rare-earth elements on the fatigue performance of magnesium alloys. Microstructural analysis showed that GW123k alloy has finer grain size and abundant fine precipitated particles than AZ31. While it is known that AZ31 extrusion has strong basal texture, pole figure analysis indicated that the orientations of basal planes in GW123k were randomly distributed. However, the intensity of basal plane along extrusion direction was slightly stronger than other directions. Monotonic tension and compression tests of GW123k alloy show no yield asymmetry as compared to AZ31. From fatigue tests, Yang et al. calculated the fatigue limit of GW123k at 10^9 cycles and found it to be 117.5±4.5 MPa. In earlier study, they performed very high cycle fatigue tests on AZ31 extrusion and found its fatigue limit at 10^9 cycles to be 88.7±4.1 MPa [90]. The authors argued that the formation of twins in conventional magnesium alloys such as AZ31 creates localized deformation regions around these twins which make these regions vulnerable to crack initiation.

As a result, GW123k, which was found to deform mainly by slip mechanism, possessed better fatigue resistance than AZ31.

Research has been focused on developing plasticity models capable of predicting the unusual behaviour of magnesium such as twinning and detwinning. Staroselsky and Anand [65] developed a crystal-mechanics-based model for hcp metals such as magnesium. This model takes into account both slipping and twinning deformation mechanisms. The authors were able to predict experimental monotonic stress-strain behaviour of AZ31B extrusion. Lee et al. [106] developed a constitutive model using two-surface plasticity to account for anisotropy in magnesium sheet. The authors implemented this model in ABAQUS and successfully predicted the asymmetric behaviour of AZ31B sheet under uniaxial compression-tension and tension-compression-tension tests with different pre-strain levels. El Kadiri and Oppedal [107] proposed a crystal plasticity model for metals that deform under slip and twin mechanisms. They argued that sigmoidal shape behaviour in monotonic compression is due to dislocation transmutation in the twins. Such process increases the number of dislocations within the twins. Therefore, they explained the rapid increase in the stress due to dislocation-dislocation interaction within the twins and the contribution of the pyramidal slip. Li et al. [108] constructed a plane-stress phenomenological constitutive model capable of producing yield asymmetry and different hardening behaviours due to slip, twinning and detwinning. The authors implemented this model in ABAQUS and they successfully predicted experimental stress-strain responses of AZ31B sheet for uniaxial tension, compression and reversed tension-compression tests. Taking twinning into account, Li et al. compared their model with a polycrystal model and found the former is two orders of magnitude faster than the latter. Hama et al. [109] performed crystal-plasticity finite element analysis to investigate the loading-unloading behaviour of AZ31B sheet. Arguing that pseudoelastic behaviour in magnesium was only explained in terms of twin deforma-

tion; Hama et al. focused on the effect of basal and non-basal slip systems. The authors were able to simulate the inelastic behaviour during loading-unloading process; however, the simulated hysteresis was smaller in magnitude than that from experiment. Hama et al. determined the overall stress during loading by prismatic slip systems. On the other hand, basal slip systems were activated during loading and unloading.

Chapter 3

Material Characterization

This chapter presents the results of the experimental program. Standard testing techniques were employed to characterize the investigated material. Two modes of loading were considered for characterization: axial and torsional. Monotonic and cyclic tests were performed to characterize the material behaviour under the two modes. Then, axial-torsional tests were performed to investigate the multiaxial behaviour of the material under proportional and nonproportional loading conditions. The results for all cyclic tests are used to examine the applicability of different fatigue life models in Chapter 4.

3.1 Material

The investigated material in this research is AZ31B magnesium extrusion. The air-quenched section of AZ31B extrusion was manufactured by Timminco. This section was extruded from a 177.8 mm diameter, 406.4 mm long billet, with an extrusion ratio of 6. The extrusion temperature was between 360 and 382°C, with an extrusion exit speed of 50.8 mm/s.

The geometry and sizes of this section are shown in Fig. 3.1. The chemical composition of the extrusion is listed in Table 3.1. Aluminum is the most important alloying element in Mg-alloys because it provides solid-solution strengthening and facilitates age hardening [110]. It also increases the tensile strength and the hardness. The addition of small amounts of Zn (1 $wt\%$) improves the corrosion resistance of Mg-alloys [111]. Impurities or alloying elements such as iron (Fe), nickel (Ni) and copper (Cu) reduce Mg-alloys corrosion resistance. Manganese (Mn) helps in enhancing the corrosion resistance because it reduces the solubility of Fe in Mg [110].

Table 3.1: Chemical composition for the extruded AZ31B ($wt\%$).

Al	Mn	Zn	Fe	Ni	Cu
3.1	0.54	1.05	0.0035	0.0007	0.0008

This section was selected because it enables three tasks: machining samples at three different orientations, machining tubular specimens and testing AZ31B extrusion in the as-received condition. It should be noted that all of the specimens were machined from the thick portions of the extrusion section. The crystals orientations as well as the definition of the extrusion, transverse and normal directions are illustrated in Fig. 3.2. The microstructure of exactly similar extrusion section was investigated by Beguem et al. [19]. They found that the average grain size varies through the thickness of the 7 mm portion. Begum et al. found that the average grain size at the top surface was about 150 μm while it reached 6 μm at the middle and then increased again to 150 μm at the bottom surface. The microstructures of the thick portion of AZ31B extrusion at different planes are shown in Fig. 3.3. To observe the microstructure the following procedure was followed. First, samples were cut from the location that the specimens were machined from. Then,

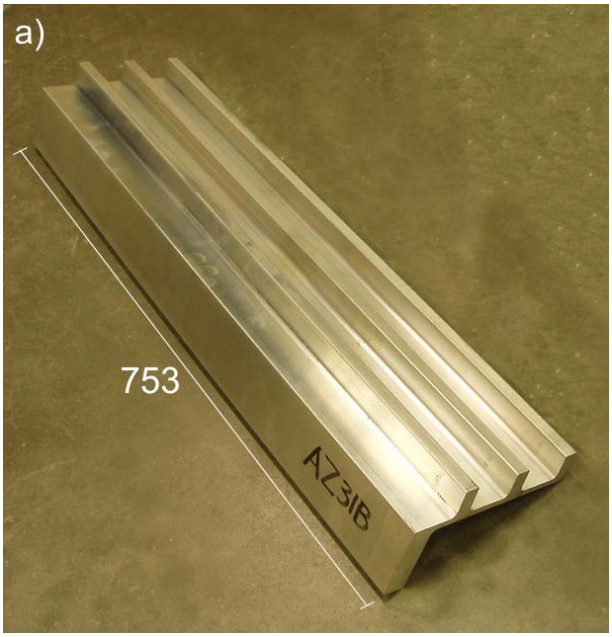

b)

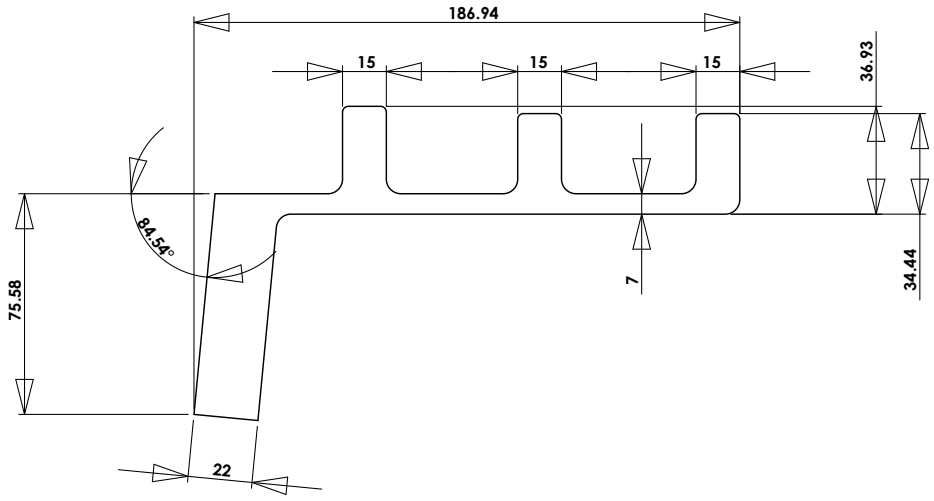

Figure 3.1: AZ31B extrusion. a) Extrusion section. b) Geometry and sizes. Dimensions in mm.

grinding with water was done using 120, 320, 600, 1200, and 4000 grit sand papers. After that, the samples were polished with 3 and 1 μm diamond past, and with cooling and lubricating liquid. Etchant was prepared from 4.2 g of Picric acid, 10 ml of Acetic acid, 70 ml of Ethanol and 10 ml of Distilled Water. The samples were etched for 3-4 seconds and then were dried with hot air. Finally, the sample were observed using optical microscope equipped with digital imaging system. It is seen from this figure that the extrusion section has different microstructural features depending on the orientation. The average grain size of the transverse-longitudinal plane (T-L) in Fig. 3.3a is 58.8 μm. In general, this plane has more uniform grain size distribution than other plans. The transverse-depth plane (T-D) in Fig. 3.3b has a combination of large and fine grains with an average grain size of 17.8 μm. To some extent, the microstructure of the depth-longitudinal plane (D-L) in Fig. 3.3c is similar to that of the (T-D) plane except that the former has a higher density of large grains and has some elongated grains parallel to the longitudinal, i.e., extrusion, direction. Therefore, the average grain size of the (D-L) plane is 34.6 μm, which is almost double that of the (T-D) plane. Taking into account the differences in the extrusion parameters, the average grain size found here is comparable to that reported the literature [70, 105, 112]. It is seen from Fig. 3.3 that some grains are twinned but their density is low compared to untwined grains. Also, this figure shows some second-phase particles that were found to be composed of Mg and Al. These are likely to be $Mg_{17}Al_{12}$ second-phase particles that have been observed in AZ31 extrusions [13, 89], AZ61A extrusions [110], and AZ91HP [113] and AM60B [114] castings.

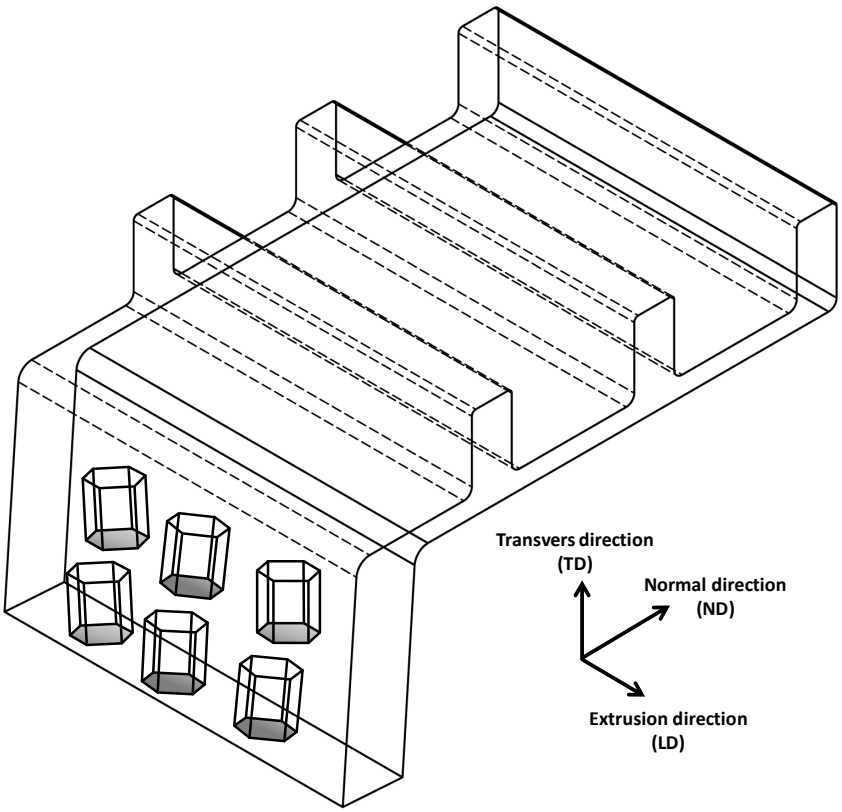

Figure 3.2: A schematic showing crystal orientation within AZ31B extrusion section and the definition of extrusion, transverse and normal directions.

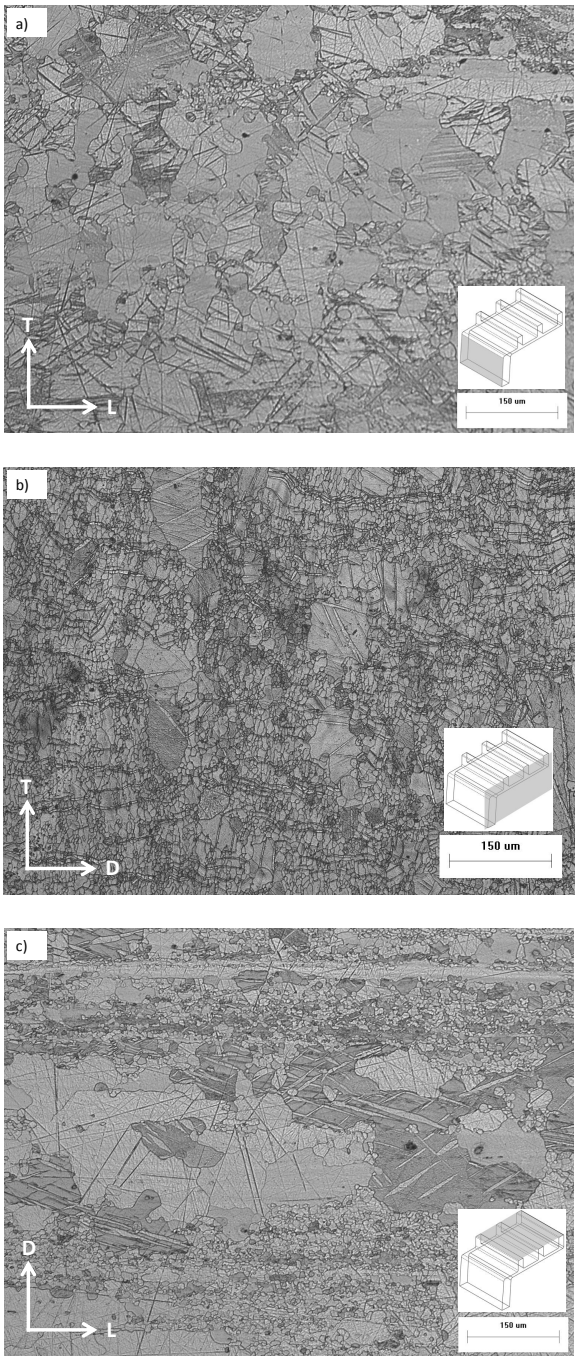

Figure 3.3: Microstructure of AZ31B extrusion. a) T-L plane. b) T-D plane. c) D-L plane.

3.2 Experimental Setup

All tests were performed under standard laboratory conditions. All specimens were uniquely designated such that their exact locations from the extruded section could be identified. To do so, each tooth of the extrusion was assigned a letter as shown in Fig. 3.4. The first letter indicates the name of the alloy. Z stands for AZ31B. The second letter indicates the tooth of the extrusion, either A, B, C or D. This is followed by a number that recognizes the extrusion section's number. A total of four AZ31B extruded sections were used. The last two numbers specify the location of the specimen in a specified tooth in a row-column convention. To machine tubular specimens, the following procedure was used. First, the thick portion of the extrusion section was cut into blocks, and then these blocks were turned into cylinders with a diameter of about 15.3 mm. Second, holes were drilled from both sides in two stages using two drill pits: 1/4" and 19/64". To ensure concentricity, cylindrical inserts that have approximately the same diameters of the two drill bits were inserted in one side of the specimen. Third, two long inserts were placed in the each side of the tubes and then the outer profile was cut. It is worth mentioning that the inner diameter was machined before the outer one to avoid bulging because the tubular specimens have a wall thickness of only 1 mm. Finally, the outer diameter was turned to size through polishing while the inner diameter was turned to size through honing. The outer gage section of all specimens were machined in a single pass and was polished circumferentially using 1200 grit sand paper. The surface finishes of the inner and outer surfaces of the gage section were measured and were found to be within 0.2-0.4 μm. No liquid coolant was used during the machining. All tests were performed on a digitally-controlled Instron servo-hydraulic frame that has a capacity of $\pm$25 kN and $\pm$100 N.m.

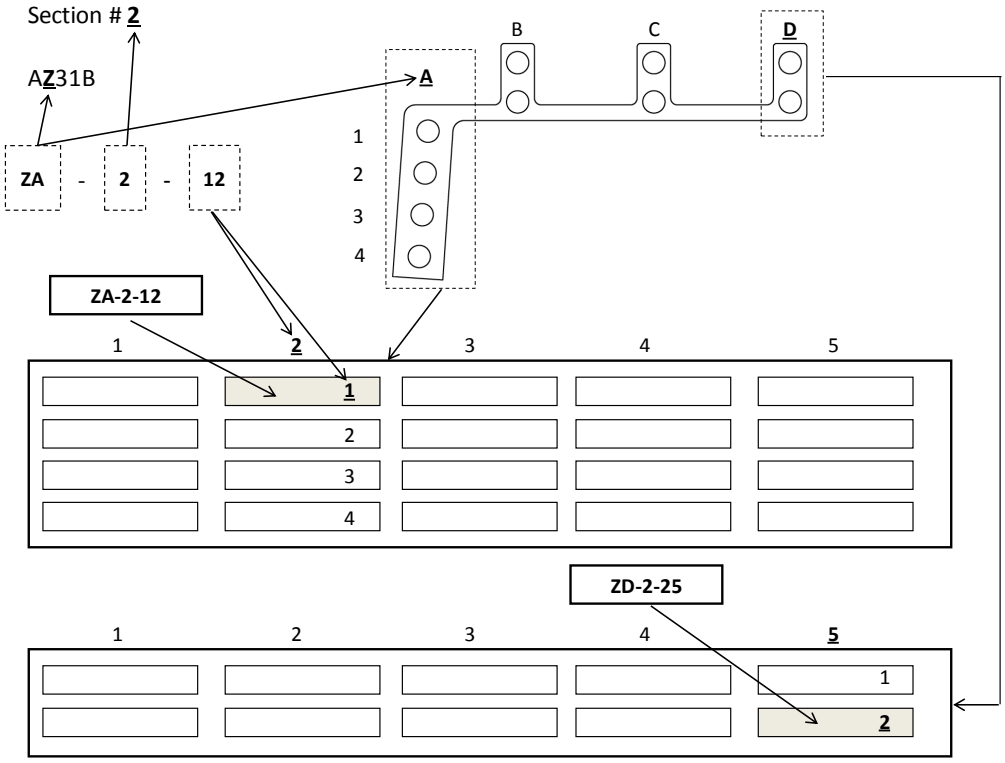

Figure 3.4: A schematic illustrating specimen designation technique.

3.2.1 Monotonic Tests

Two different types of smooth specimens were used in this investigation: flat and tubular. Monotonic tensile tests were performed on flat specimens that were machined in three orientations: extrusion, 45° and transverse directions. Hereafter, these three orientations are referred to as LD, 45° and TD, respectively. To avoid buckling, monotonic compressive tests were performed on sub-sized tubular specimens, and were also tested in the same three orientations as for monotonic tensile tests. Monotonic torsional specimens were only machined in one orientation, the extrusion direction (LD). Monotonic torsion tests were performed on full-sized tubular specimens. All cyclic tests were also performed on full-sized tubular specimens. The geometries and sizes of these specimens are shown in Fig. 3.5. A schematic showing the locations of these specimens on the AZ31B extrusion section is given in Fig. 3.6. In addition, this figure illustrates the orientations of the specimens with respect to the extrusion section. Axial and torsional monotonic tests were performed under displacement and rotation controlled conditions, respectively. An Instron extensometer with a gage length of 12.5 mm and ±5.0 mm displacement was used for monotonic axial tests. Epsilon's biaxial extensometer was used for monotonic torsional tests. This extensometer has a gage length of 20 mm, and ±1.0 mm of axial extension, and ±3.0° of rotation. In the cases when the displacement limit of either extensometer was reached, the following procedure was followed. First, tests were stopped without unloading. After that, the extensometer was removed and reset to the zero position. Then, the extensometer was mounted on the specimen again. Finally, the test was resumed. For monotonic torsion, this procedure was repeated several times until complete failure had occurred.

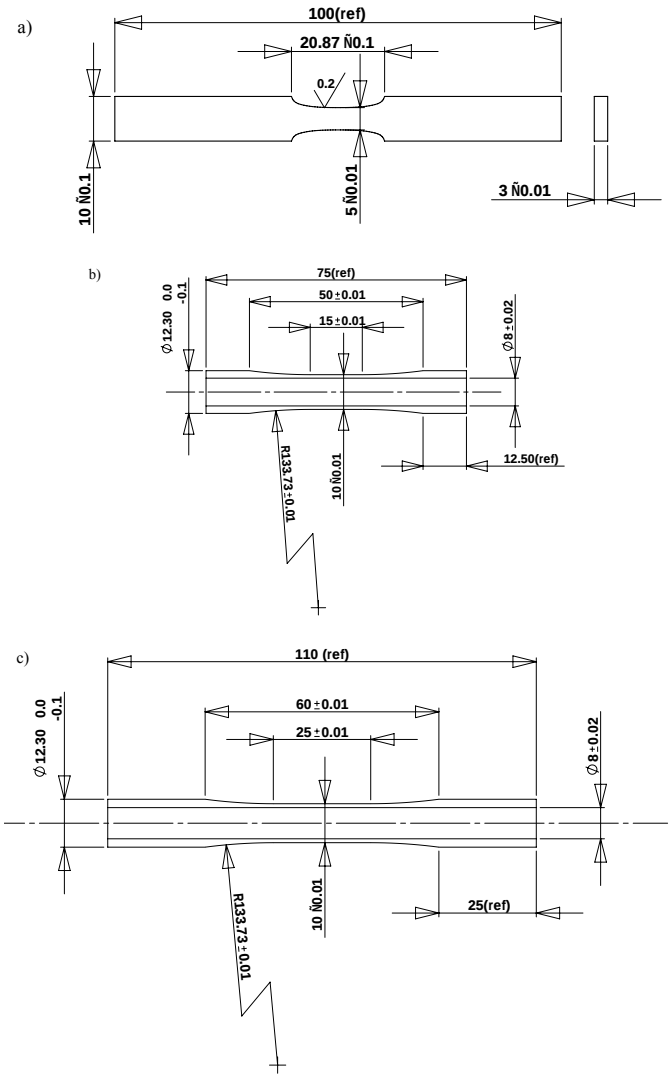

Figure 3.5: Geometries and sizes of machined specimens. a) Monotonic tensile tests. b) Monotonic compressive tests. c) Monotonic torsional and cyclic tests.

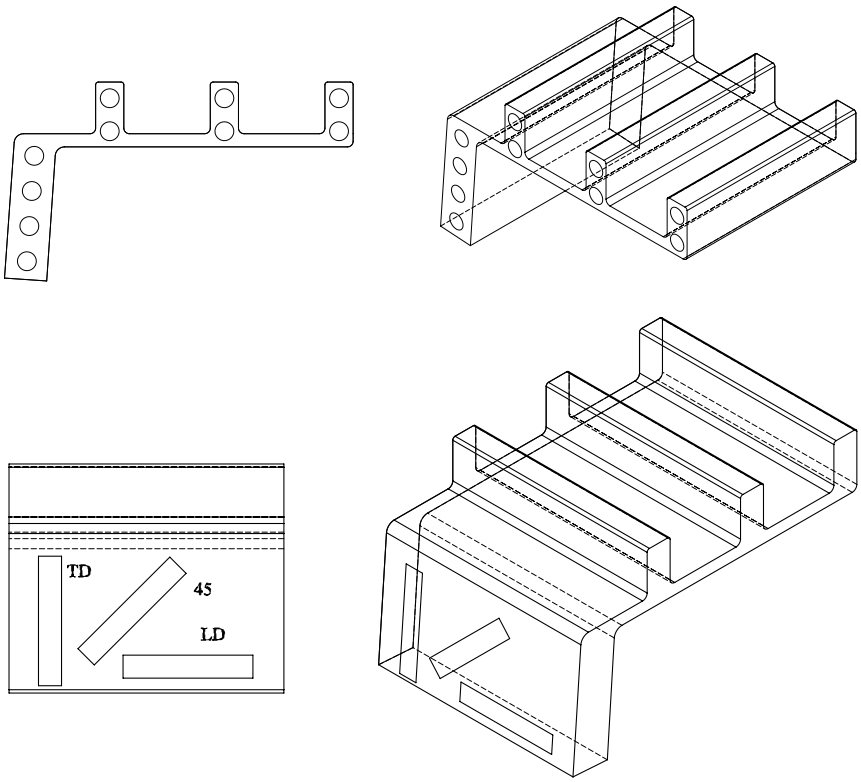

Figure 3.6: Locations of smooth specimens on the extrusion section.

3.2.2 Cyclic Tests

All cyclic tests were performed on full-sized tubular specimens shown in Fig. 3.5c. Instron's extensometer with 10 mm gage and ±1.0 mm limits was used for axial strain measurement. On the other hand, the same extensometer as for monotonic torsion test in Section 3.2.1 was used for torsional and multiaxial cyclic tests. All tests were performed under completely reversed straining. In the cases when the number of cycles exceeded 10^4, tests were stopped and were switched to load controlled mode. Tests that exceeded 10^7 cycles were considered as run-out. To avoid deforming tubular specimens by gripping, two cylindrical steel inserts were inserted at the gripping sides of the specimen. Also, this helps avoiding the possibility of miss-aligning the specimen with respect to the load during the test. A sinusoidal waveform was used in all cyclic tests and frequency ranges of 0.1-1.0 and 5-15 Hz were used for strain- and stress-controlled loading conditions, respectively. All cyclic tests were performed at standard laboratory conditions. To ensure the repeatability of the results, at least two replicates were tested for almost every loading level. Tests were stopped at an average load drop, axial or torsional, of 50%.

3.3 Monotonic Behaviour

3.3.1 Tensile Loading

To investigate the monotonic axial behaviour, three duplicates were tested at each orientation, i.e, extrusion (LD), 45° and transvers (TD) directions. Caution was taken while gripping the specimens between the flat jaw-faces to ensure that the specimens were aligned axially with respect to the loading direction. Monotonic tensile stress-strain curves at LD, 45° and TD are shown in Fig. 3.7. The engineering tensile stress-strain curves show five significant characteristics. First, the moduli for the LD, 45° and TD were found to be 43.7, 43.5 and 40.6 GPa, respectively. Second, the difference in yield strength at 45° and at TD was 18%, whereas, the difference between the LD and TD was 74%. Another notable difference was the hardening behaviour for the three different orientations. For the LD, AZ31B deforms plasticity with very low hardening, and the average monotonic power hardening exponent was as low as 0.0238. However, significant power hardening-like behaviour was observed at 45°, with an average monotonic power hardening exponent of 0.386. This is 16 times the hardening exponent for the LD. With upward-facing concavity, attributed to deformation twinning, the hardening behaviour for the TD was not representative of usual metal behaviour. Thus, it is not reasonable to fit it with a power relation such as the Ramberg-Osgood relation. The average ultimate tensile strengths for the LD and for 45° are within 10%. The maximum value of 246.6 MPa was obtained in the TD. This is 18% higher than the minimum value obtained at 45°. Finally, the ductility of AZ31B extrusion was found to attain maximum and minimum values at 45° and TD, respectively. The directional monotonic tensile properties of AZ31B extrusion are listed in Table 3.2.

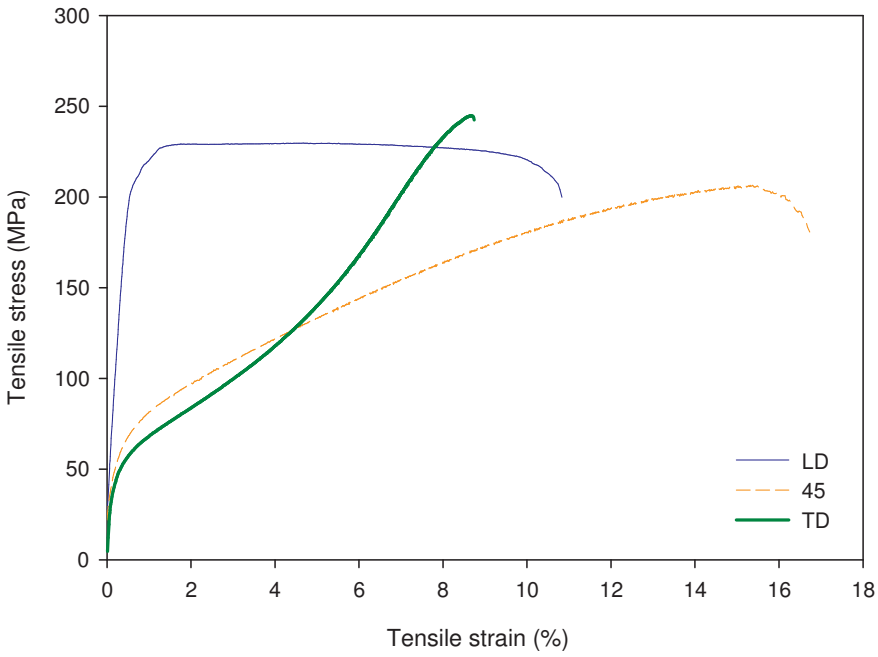

Figure 3.7: Monotonic tensile stress-strain curves at different orientations.

Table 3.2: Average directional monotonic tensile properties for AZ31B extrusion from flat specimens for different orientations.

	E (GPa)	$S_{yt0.2\%}$ (MPa)	S_{ut} (MPa)	$\%EL$	$\%RA$	K (MPa)	n
LD	43.72	213.33	227.45	10.01	20.46	260.01	0.0283
stdev	0.22	3.06	2.36	1.29	2.06	5.00	0.0047
45°	43.50	65.67	208.95	17.51	21.26	497.72	0.3861
stdev	2.36	4.51	5.65	0.8	1.32	13.2	0.0245
TD	40.59	55.67	246.62	9.38	9.28	-	-
stdev	1.528	6.03	6.18	0.55	0.69	-	-

The fractured specimens in Fig. 3.8 show that both the LD and TD tensile specimens failed nearly at the plane of maximum normal stress. However, the 45° specimen failed on the plane of maximum shear stress i.e., at an angle of 45°. Though only one specimen at each orientation is shown here, this observation also applies to other duplicates.

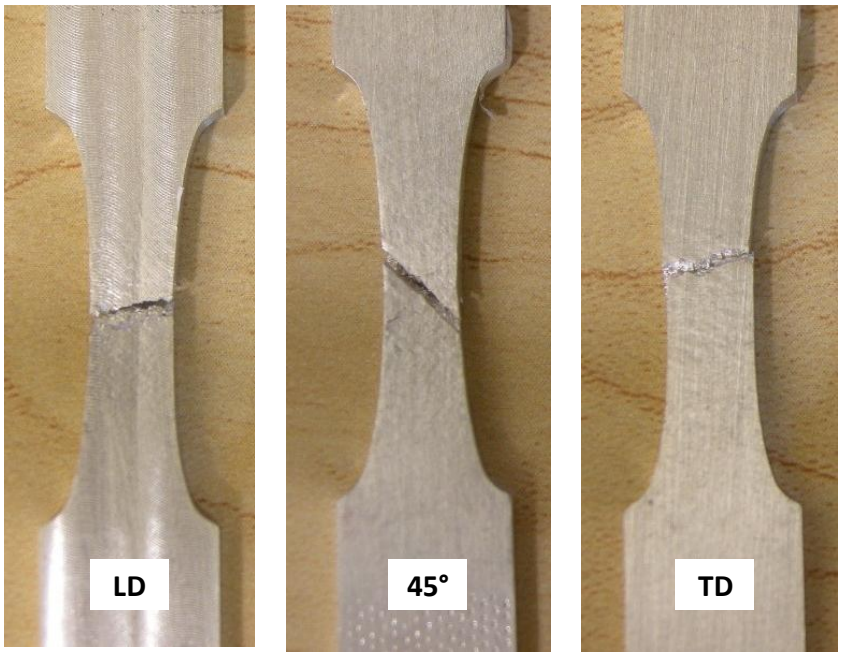

Figure 3.8: Fractured specimens for tensile tests at LD, 45° and TD directions.

The monotonic axial stress-strain curves in Fig. 3.7 show the anisotropic behaviour typical of extruded AZ31B alloy. This behaviour is attributed to the activation of deformation twinning. The extrusion process results in aligning the basal plane with the extrusion direction, i.e., the longitudinal direction, with the c-axis perpendicular to it [12, 61, 62, 81]. Metals with hexagonal crystal structure, such as magnesium, deform plastically using different mechanisms: slipping, twinning and detwinning [17, 61, 62, 65, 81, 84, 107, 115].

These mechanisms can be activated depending on the loading orientation with respect to the basal plane. An extension along the c-axis activates the tension twins. Therefore, the dominant plastic deformation mechanism in a tensile specimen that is machined such that its loading axis is parallel to the extrusion direction is slip. A tensile specimen machined along the transverse direction has its basal plane perpendicular to the loading axis. This results in a direct extension of the c-axis, which activates the tension twins. The concave up shape of the tensile curve in the transverse direction is an indication of the formation of tension twins. The unusual shape of the tensile stress-strain curve at the TD is due to the fact that twinning, detwinning and slip are activated in sequence throughout the test. First, twinning occurs leading to low stress yielding. As the loading continues, the twinning process ends and detwinning starts, resulting in concave upward hardening. Finally, a slip mechanism starts causing rapid increase in the hardening rate. This rapid hardening rate is attributed to the contribution of hard pyramidal slip [107]. Due to the different deformation mechanisms involved, it is seen that not only hardening is affected. The yield strength for the LD is more than three times than that at 45° and TD. This is because in the LD, it is difficult for tensile loading to activate either basal slip or tension twins [62]. Taking into account the extrusion texture, tensile load on specimens machined at 45° can be resolved into two components: tensile, i.e., normal to the c-axis, and shear. Therefore, it can be anticipated that the shear stress component can activate the low critical resolved shear stress (CRSS) slip system such as the basal slip. Consequently, the yield strength for 45° is less than that of LD. It is worth mentioning that the CRSS for basal slip and for extension twin for pure magnesium are in the order of 1.0 and 2.0 MPa, respectively [116]. On the other hand, the CRSS for non-basal slip, such as prismatic and pyramidal, are 40-100 times larger than that for basal slip [62, 116]. Similar differences in the monotonic tensile behaviour were reported by Barnett [61] and Kleiner and Uggowitzer [62], who did

experiments on AZ31 and AZ61 extrusions, respectively. Also, keeping in mind that the transverse direction in this study corresponds to the normal direction of rolled magnesium, Lou et al. [81] and Wu et al. [17] observed the same behaviour reported here but on rolled AZ31B-O and AZ31B, respectively. As far as Poisson's ratio, researchers such as Lou et al. [81], Sun Chul Choi et al. [117] and Somekawa and Mukai [118] used a value of 0.35. Wang et al. [119] used a value of 0.33. For the purposes of this study, the value of Poisson's ratio was found to have an insignificant effect. Therefore, a value of 0.35 was used.

3.3.2 Compressive Loading

Similar to monotonic tensile tests, monotonic compression tests were performed at three orientations: extrusion LD, 45° and TD. One specimen was tested at each orientation. The engineering monotonic compressive stress-strain curves of AZ31B extrusion are shown in Fig. 3.9. Like monotonic tension, the compressive stress-strain curves show five different characteristics. The elastic moduli for the three directions are comparable, with the largest difference of 11% between the value at 45° and TD. The 0.2% offset yield is the lowest at 45° with a value of 94 MPa, while the highest value, 127 MPa, was observed in the TD. In contrast, the ductility in the TD is the lowest, with a fracture strain of -5.3%. Its values at LD and 45° were -12.6% and -16.8%, respectively. The ultimate compressive stress was found to reach the maximum value, 364 MPa, in the LD. The ultimate compressive strengths at 45° and TD were 230 MPa and 316 MPa, respectively. The post yielding behaviour in the LD is sigmoidal with upward concavity. Conversely, the post yielding in the TD seems to behave in a power hardening fashion. At 45° it starts with a linear hardening and ends with a relatively steady hardening. In addition, it is seen from Fig. 3.9 that the material exhibits a serrated flow as observed in the stress-strain curve of 45° direction. The

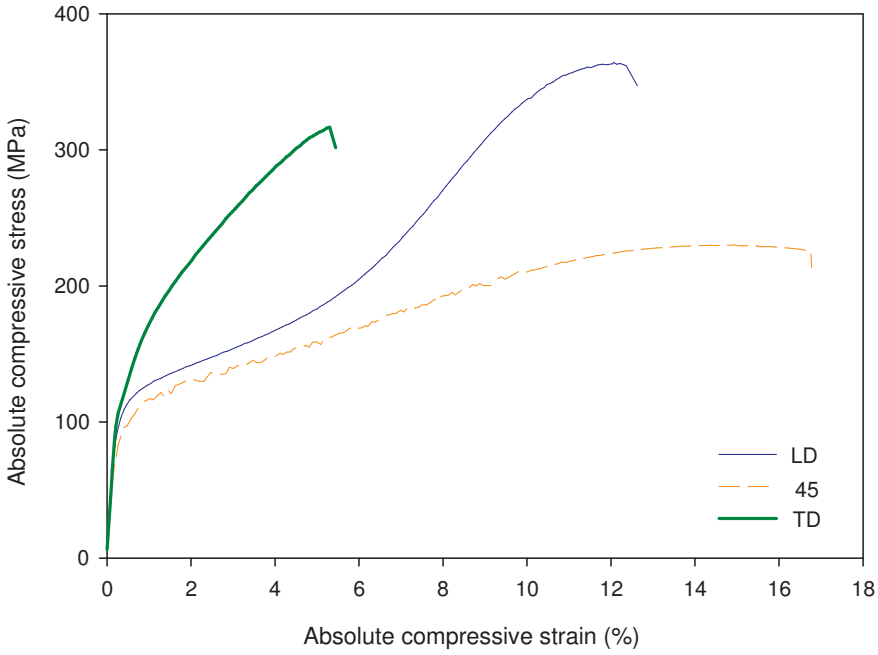

Figure 3.9: Monotonic compressive stress-strain curves for different orientations.

directional monotonic compressive stress-strain properties of AZ31B extrusion are listed in Table 3.3.

Table 3.3: Directional monotonic compressive properties for AZ31B extrusion from sub-sized tubular specimens for different orientations.

	E_c (GPa)	$S_{yc0.2\%}$ (MPa)	S_{uc} (MPa)	e_{cf} (%)
LD	43.9	108	364.1	12.6
45°	41.0	94	230.3	16.8
TD	45.9	127	316.7	5.3

Fractured specimens for the three monotonic compression tests are shown in Fig. 3.10. It appears from this figure that the LD specimen failed at the plane of maximum shear. On the other hand, the 45° specimen failed at an angle of about 18° while the TD specimen failed at an angle of 40° from the plane of loading.

Comparison between the tensile stress-strain curves for the TD and the compressive stress-strain curve for LD reveals obvious similarity in the hardening behaviour. In effect, both tests result in extension of the c-axis and the upward concavity in both curves supports the fact that the operating deformation mechanism in both tests is the same. With the basal plane parallel to the extrusion direction (LD), compressive loading causes extension of the c-axis, which explains the behaviour of the monotonic compressive stress strain curve. Similar to monotonic tensile behaviour in the TD, the rapidly increasing strain hardening rate of the monotonic compressive stress-strain curve in the LD indicates the end of the detwinning process and the start of hard pyramidal slip deformation [107]. As compressive loading along the TD is not likely to activate tension twins, slip is the dominant plastic deformation mechanism. El Kadiri and Oppedal [107] proposed a crystal plasticity model for metals that deform under slip and twin mechanisms. They argued that

sigmoidal shape behaviour in monotonic compression, like the one in the LD in Fig. 3.9, is due to dislocation transmutation in the twins. Such a process increases the number of dislocations within the twins. Therefore, they explained the rapid increase in the stress due to dislocation-dislocation interaction within the twins and the contribution of the pyramidal slip. This disagrees with the notion that the cause of hardening is due to twin-dislocation interactions [115,120]. Though tension twinning is not expected to be active in either case, the monotonic behaviour of the tensile test in the LD and compressive loading in the TD is not comparable. Their ductility, yielding stresses and post-yielding behaviours are different. Wu et al. [17] investigated the effect of texture and twinning deformation on the axial low cycle behaviour of rolled AZ31B. They performed directional monotonic tensile and compressive tests. Taking into account the texture similarity between the extruded and the rolled AZ31B, Wu et al. reported similar differences between monotonic compressive tests in normal and rolling directions. They attributed the observed behaviour in the normal direction, equivalent to the TD here, to the fact that pyramidal slip and contraction twins cause shear instability at room temperature. The effect of texture can also be observed on the value of the 0.2% yield strength. Comparing the tensile and compressive yield strengths in the LD, the effect of twinning deformation can be observed as the yield strength in compression is about 50% of the yield in tension. At 45°, tensile and compressive loads produce different yielding and post-yielding behaviour. Resolving the load into shear and normal components, a tensile load at 45° creates shear and normal tensile loads. On the other hand, a compressive load at 45° creates shear and normal compressive loads. Essentially, the difference in behaviour is related to the resolved normal components. As mentioned previously, compressive loading parallel to the basal plane causes extension along the c-axis, which activates tension twins. This is the case with the monotonic compressive test that was performed in the 45° direction. Conversely, the normal

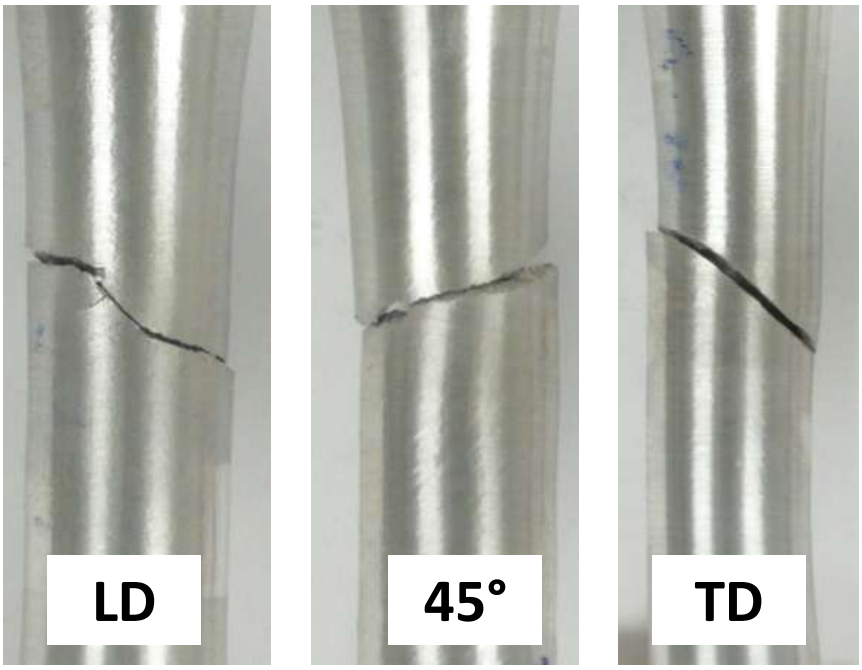

Figure 3.10: Fractured specimens for compressive tests at LD, 45° and TD.

component in the monotonic tensile test machined at 45° direction causes contraction of the c-axis. The monotonic tensile and compressive tests in the TD cause direct extension and contraction along the c-axis, respectively. Comparing the tensile and compressive fracture strains, it is seen from Table 3.2 and 3.3 that the LD and the 45° have relatively similar values. However, the tensile and the compressive fracture strains in the TD are 9.4 and 5.3%, respectively. The low ductility in the compressive test could be related to the activation of pyramidal slip and contraction twins as suggested by Wu et al. [17]. Serrated flow was observed by Chen et al. [20] in the tensile and compressive reversals of the hysteresis loop of AM50 extrusion and they attributed to dynamic-strain-aging phenomenon.

3.3.3 Shear Loading

Two torsion tests were performed on tubular specimen cut along the extrusion direction (LD). Torsion produces a pure shear state of stress in the specimen; therefore, it reveals the behaviour of AZ31B under shear stress alone. The monotonic shear stress-strain curve is shown in Fig. 3.11. For monotonic torsion, the shear modulus was found to be 16.5 GPa. The 0.2% yield and ultimate shear strength were found to be 46 and 162 MPa, respectively. Unlike the monotonic tensile behaviour, extruded AZ31B shows a linear hardening behaviour when loaded monotonically under torsion. As a result, the linear hardening modulus, H, was calculated and is listed in Table 3.4. It should be noted here that additional specimens were tested under monotonic torsional loading, however, they were discarded because of bucking. The monotonic torsional behaviour shows a linear hardening behaviour as illustrated in Fig. 3.11. Ideally, the crystals are oriented such that the basal plane is parallel to the extrusion direction. In this case, shear loading is not

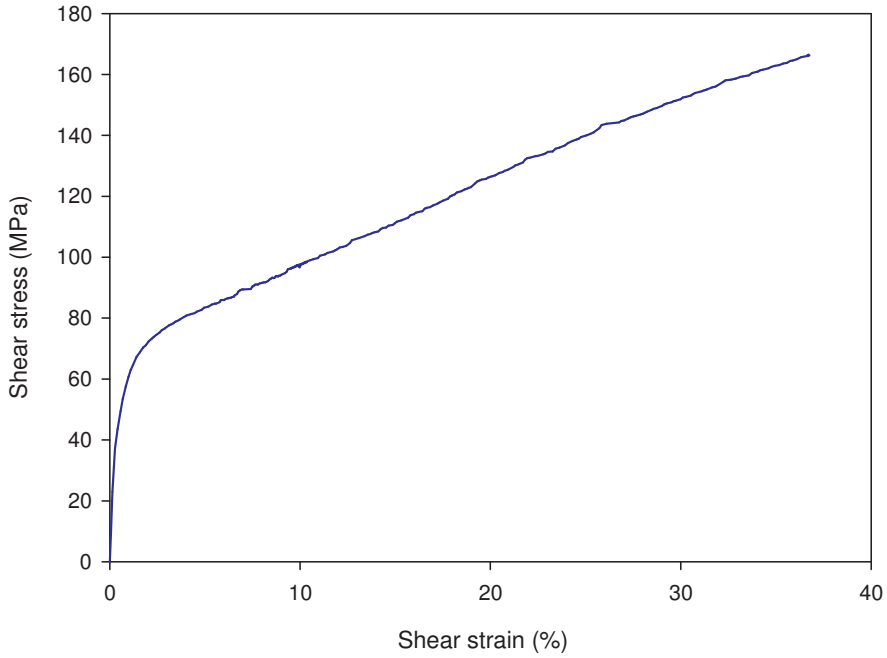

Figure 3.11: Monotonic shear stress-strain curve.

Table 3.4: Average monotonic shear properties for AZ31B extrusion.

	G (GPa)	$\tau_{y0.2\%}$ (MPa)	τ_u (MPa)	H (MPa)
	16.47	46.89	162.3	274.91
stdev	0.188	0.155	5.904	5.6427

expected to cause extension along the c-axis and no twinning deformation is anticipated. However, Lou et al. [81] reported twinning to occur in monotonic simple shear at high shear strains. The shear test performed in [81] is isochoric simple shear, with a test set-up recently devised by Lopes et al. [121], which does not provide a pure shear state. In simple shear tests, equal and opposite normal stresses along the c-axis and perpendicular to the c-axis accompany the shear stress. The normal stress components in simple shear test at lower strains are an order of magnitude less than the shear stress components, but can grow to significant values at higher strains and after yielding [122]. The presence of normal stress in a simple shear test, which can lead to extension along the c-axis, justifies the observation of twins forming in these tests. Zang et al. [97] performed multiaxial experiment on AZ61A extrusions. Similar to Lou et al. [81] they observed mechanical twinning at large shear strain amplitudes. However, they found that the existence of twins has no influence on the symmetry of the shear hysteresis. Zang et al. [97] attributed this to the existence of some grains that are in a favourable orientation for twinning. The cyclic shear behaviour of AZ31B extrusion was also found to be symmetric as discussed in Section 3.5.2.

3.4 Pseudoelasticity

Loading-unloading tension, compression and torsion tests were performed to investigate the pseudoelasticity of AZ31B extrusion as shown in Figs. 3.12-3.14. Beside pseudoelasticity, these figures show that the material exhibits serrated flow when loaded in tension and compression. This phenomenon was only seen in the monotonic compressive stress-strain curve for 45° direction as shown in Fig. 3.9. Two aspects are considered here to evaluate the significance of pseudoelasticity: the pseudoelastic strain which is also known

as the anelastic strain, ε_{an} and the secant modulus, E_s as shown in Fig. 3.15. For shear mode, the anelastic strain and the secant modulus are γ_{an} and G_s, respectively. The stress and the strain at which the unloading-reloading takes place are defined as σ_{LU} and ε_{LU}, respectively. It is seen from Fig. 3.12 that pseudoelasticity is significant at all monotonic tension tests except for the LD. Nevertheless, it is seen that such behaviour exists even at a stress of 150 MPa which is 30% less than the 0.2% offset yield strength.

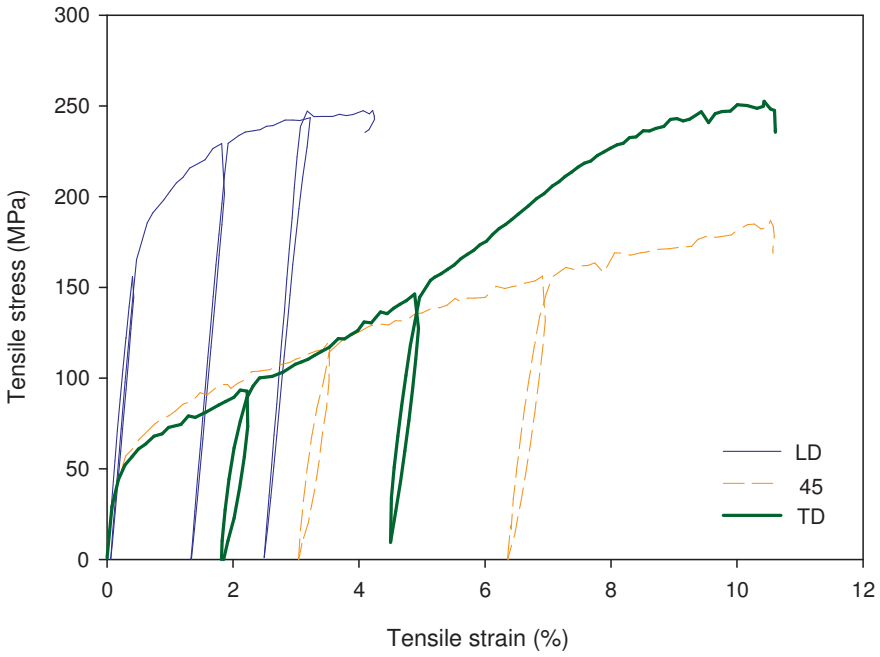

Figure 3.12: Loading-unloading behaviour for monotonic tensile loading at different orientations.

The loading-unloading behaviour of the monotonic compressive loading shown in Fig. 3.13 indicates that pseudoelasticity is significant in both the LD and TD. Fig. 3.14 shows the loading-unloading behaviour of two specimens loaded in monotonic torsion in the LD but at different strain levels. This figure shows that AZ31B extrusion forms significant hysteresis

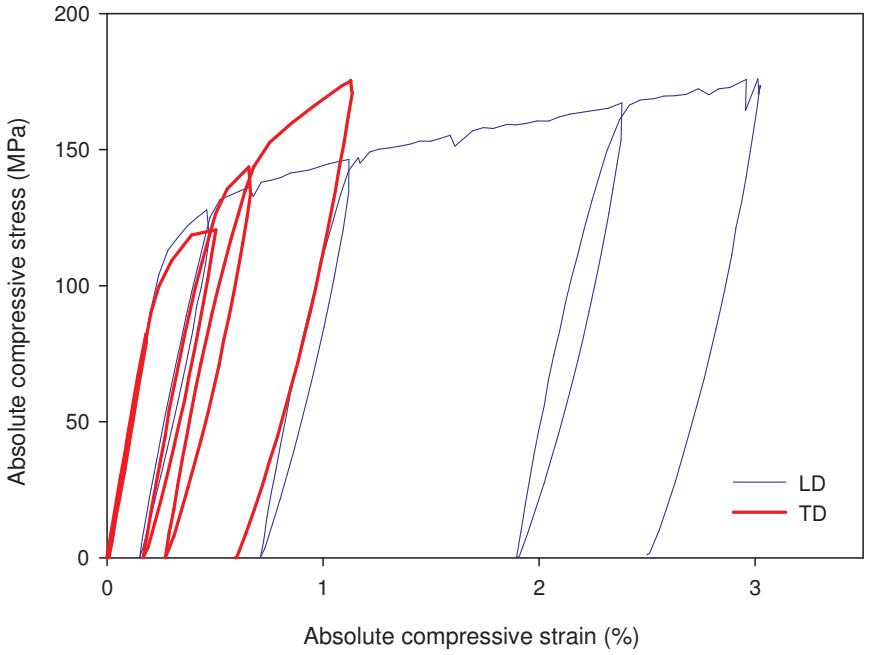

Figure 3.13: Loading-unloading behaviour for monotonic compressive loading at different orientations.

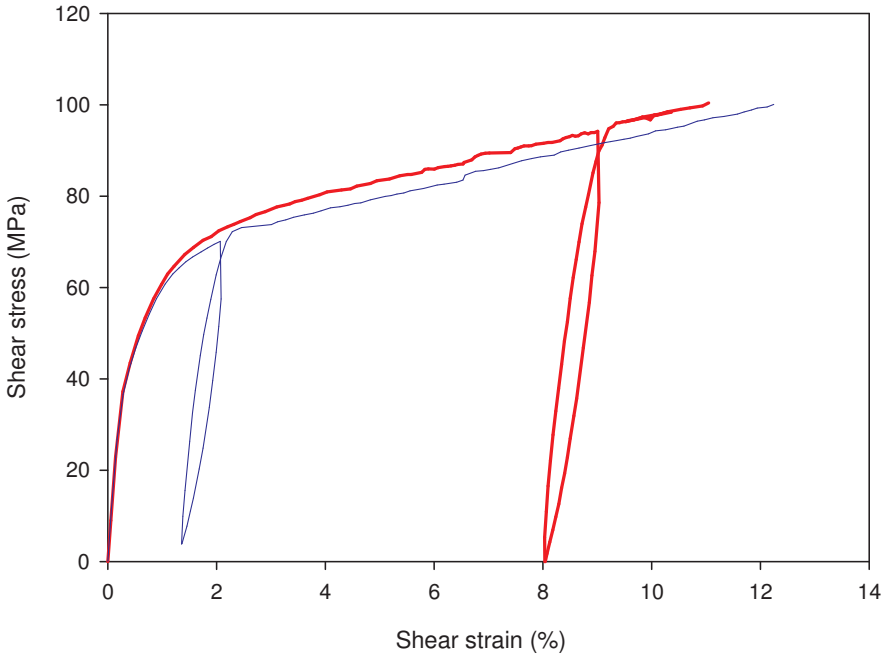

Figure 3.14: Loading-unloading behaviour for monotonic torsional loading.

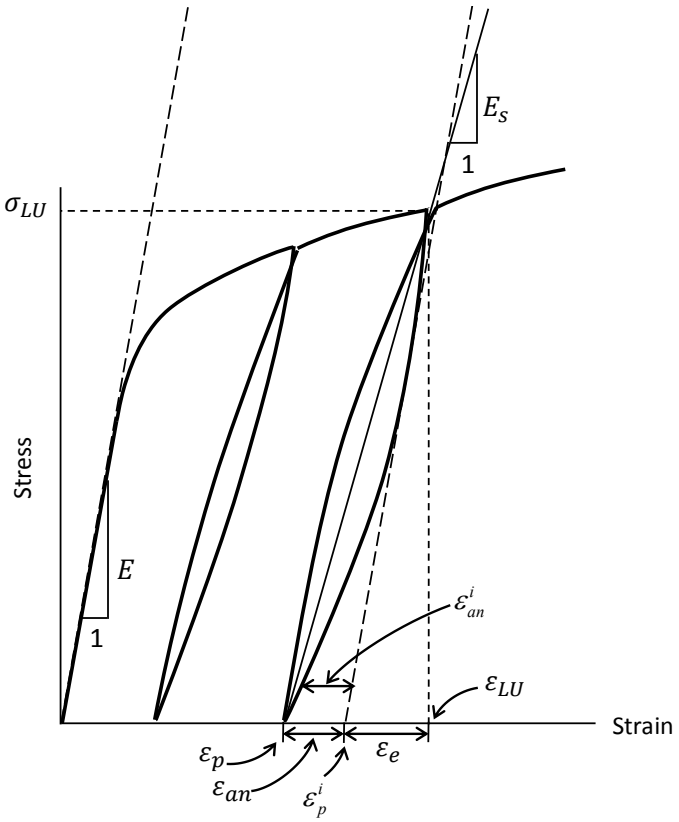

Figure 3.15: A schematic illustrating pseudoelasticity in axial mode. Adopted from Mann G. et al., 2007.

when loaded-unloaded under monotonic torsion. It has been suggested that pseudoelasticity might have an influence on the mechanical design parameters, such as modulus of elasticity, damping coefficient and energy absorption characteristics [83–85]. For magnesium, it has been proposed that pseudoelasticity is related to applied stress and plastic strain [83, 85]. Development of pseudoelastic strain results in a considerable reduction in the value of the elastic modulus [83, 84]. Therefore, axial and torsional moduli listed in Tables 3.2-3.4 were calculated by considering the first few points in the stress-strain curves to avoid the influence of pseudoelasticity on the calculation. In the literature, the origin of pseudoelasticity is attributed to several processes such as reversible movement of dislocation [86], twinning [83–85] or stress induced phase transformations [123]. It is also known that shape memory alloys (SMAs), such as Ni-Ti alloys, show pseudoelasticity [123–127] due to martensitic phase transformation. Zenner and Renner [13] experimentally verified that AZ31 and AZ80 magnesium extrusions and AZ91 and AE42 magnesium die castings exhibit material memory. However, the origin of pseudoelasticity in HCP metals has to be different than that of Ni-Ti alloys, because HCP metals show no phase transformation [84]. Although the loading-unloading tests performed in this study are simple and may not offer enough data to investigate the pseudoelasticity of AZ31B extrusion, they still provide an insight into such behaviour for different orientations and for different modes of loading. The variations of the secant modulus while loading-unloading at different plastic strain levels are shown in Fig. 3.16. The data in this figure were extracted from Figs. 3.12-3.14. It is seen from Fig. 3.16 that the value of the secant modulus during loading-unloading steps decreases in tensile tests that were performed along the LD and compression tests that were performed along the LD and TD. On the other hand, tensile tests along 45° and TD show increasing modulus with TD having a higher rate of increase. The torsion tests show an insignificant change in the secant modulus with plastic strain. Keeping in mind

that no general conclusion can be made from such simple analyses, this figure shows that pseudoelasticity may not always results in a reduction of the secant modulus. In the literature, attempts were made to explain the axial anelastic behaviour in magnesium based on twinning [83–85], fully reversal dislocation-based incipient kink bands [86], or basal and non-basal slip systems [109]. Mann et al. [85] proposed a model that simulates the loading-

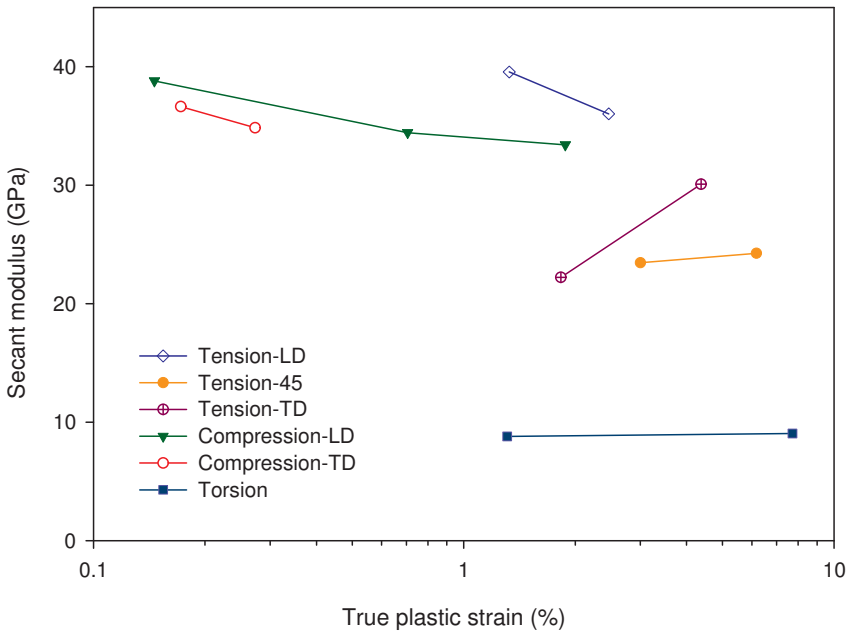

Figure 3.16: Variation of secant modulus with loading-unloading for AZ31B extrusion.

unloading hysteresis in Mg alloys. They observed that anelastic versus true plastic strain curves have a sigmoidal shape; therefore, they suggested a Weibull-type relation between anelastic and true plastic strains. Using this relation, Mann et al. [85] were successfully able to model the loading-unloading hysteresis for Mg-6Zn alloy. Two relations were proposed for anelastic strain calculations: strain- and stress-dependent. The strain-dependent

anelastic strain, ε_{an} can be calculated as

$$\varepsilon_{an} = \varepsilon^*_{an}\Big[1 - \exp\Big\{-\Big(\frac{\varepsilon_p}{\varepsilon_{po}}\Big)^{m_\varepsilon}\Big\}\Big] \tag{3.1}$$

where ε^*_{an} is the maximum value of ε_{an} in the anelastic versus plastic strains curve, ε_{po} is the plastic strain when $\varepsilon_{an}/\varepsilon^*_{an} = 0.63$, and m_ε is the Weibull modulus with respect to the strain. The value of m_ε was determined by trial and error. On the other hand, for a given strain the "*instantaneous*" anelastic strain during unloading, ε^i_{an}, was determined from the applied stress, σ. Hence, the stress-dependent Weibull function is

$$\varepsilon^i_{an} = q\varepsilon_{an}\Big[1 - \exp\Big\{-\Big(1 - \frac{\sigma}{\sigma_{LU}}\Big)^{m_\sigma}\Big\}\Big],\ \varepsilon_p \text{ is constant} \tag{3.2}$$

where σ_{LU} is the stress at which the unloading starts, ε_{an} is given by Eq. 3.1, q is a numerical factor, and m_σ is the Weibull modulus with respect to the stress. Values of q and m_σ are determined by trial and error. The loading-unloading hysteresis can be determined by combining Eqs. 3.1 and 3.2 such that the anelastic strain during unloading, $\varepsilon^i_{an,u}$ is given by

$$\varepsilon^i_{an,u} = \varepsilon_{LU} - \frac{\sigma_{LU} - \sigma}{E} - \varepsilon^i_{an} \tag{3.3}$$

The anelastic strain during reloading, $\varepsilon^i_{an,r}$ is given by

$$\varepsilon^i_{an,r} = \varepsilon^i_{an} + \frac{\sigma}{E} + \varepsilon^1_p - \varepsilon_{an} \tag{3.4}$$

where ε^1_p is the linear elastic unloading strain. From Fig. 3.15, $\varepsilon^1_p = \varepsilon_{LU} - \sigma_{LU}/E = \varepsilon_p + \varepsilon_a$. Hence, Eq. 3.4 can be re-written as

$$\varepsilon^i_{an,r} = \varepsilon^i_{an} + \frac{\sigma}{E} + \varepsilon_p \tag{3.5}$$

To use this model for the present data, a series of unloading-reloading steps have to be performed to generate enough data in the anelastic-plastic strain curve such that the parameters of the Weibull function can be determined. Because only several unloading-reloading steps were performed in this study, anelastic-plastic strain data points were extracted from Figs. 3.12-3.14. Then, these data were compared with the data available in Mann et al. data as shown in Fig. 3.17. Although there are only two points, it can be seen from this figure that the transverse compression data for AZ31B extrusion are comparable to Mg-6Zn data. Mann et al. [85] determined the Weibull function parameters for Mg-6Zn

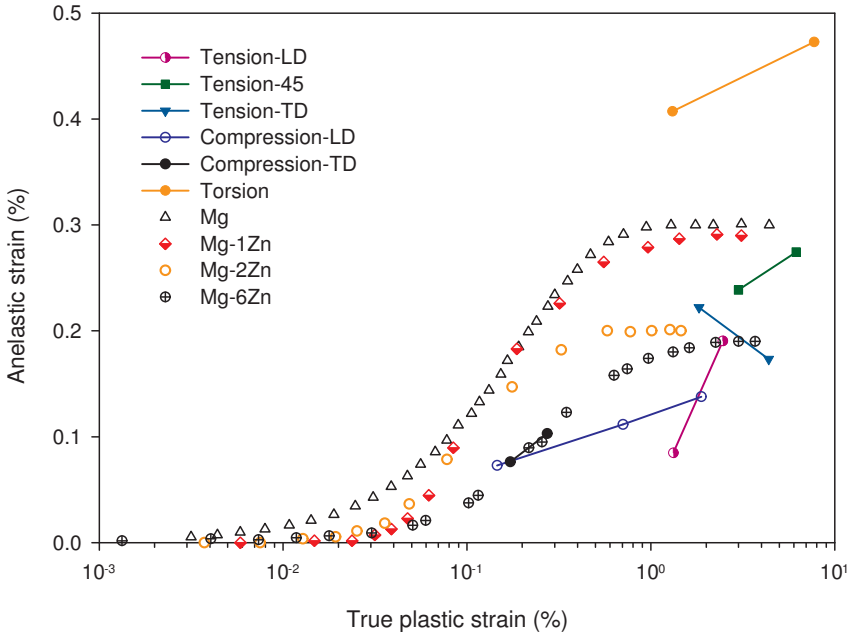

Figure 3.17: Anelastic strain as a function of true plastic strain. Mg and Mg-Zn data are from Mann G. et al., 2007.

as listed in Table 3.5. Using these parameters, the hysteresis loops for compressive loading along the TD, shown in Fig. 3.13, are calculated as shown in Fig. 3.18. It is seen from this figure that the calculated loading-unloading loops are comparable to the experimental ones.

However, the size of the calculated hysteresis is less than the experimental one. It should be kept in mind that the Weibull parameters in Table 3.5 were used as an approximation. The variation of anelastic strain with respect to plastic strain is sigmoidal as shown in Fig. 3.17. Therefore, accurate determination of Weibull parameters requires more detailed experimental data than those in Fig. 3.17. Equations 3.1-3.5 require prior knowledge

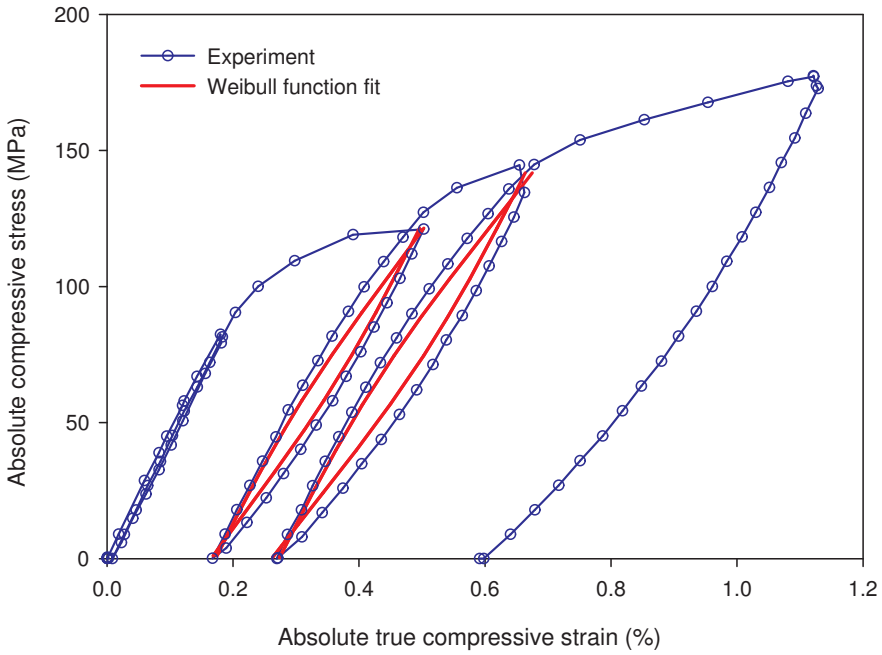

Figure 3.18: Experimental and calculated loading-unloading hysteresis for compressive loading along the transverse direction (TD). Weibull function is proposed by Mann G. et al., 2007.

of σ_{LU}, ε_{LU} and ε_p. While σ_{LU} and ε_{LU} can be determined from the stress-strain curve, determination of ε_p can only be achieved by performing loading-unloading tests. As a result, Mann et al. proposed a simplified relation for Eq. 3.1. Instead of using the plastic strain, ε_p, as an independent variable, they used the linear elastic unloading strain, ε_p^1.

Hence, Eq. 3.1 becomes

$$\varepsilon_{an} = \varepsilon^*_{an}\Big[1 - \exp\Big\{-\Big(\frac{\varepsilon^1_p}{\varepsilon_{po}}\Big)^{m_\varepsilon}\Big\}\Big] \tag{3.6}$$

In that case, the value of ε_{po} in Table 3.5 increases to 0.005. Mann et al. compared the results of both Eqs. 3.1 and 3.6 and found that the difference was indistinguishable. When Eq. 3.6 was used for transverse compression tests of AZ31B, it turned out that some

Table 3.5: Weibull function parameters for Mg-6Zn (Mann G. et al., 2007).

ε^*_{an}	ε_{po}	m_ε	m_σ	q
0.002	0.004	1.0	3	1.5

manipulation in the fitting parameters needed to be done, especially in the value of the parameter q. As mentioned earlier, fitting parameters by trial and error to get the best fit in the anelastic-plastic strain curve requires a significant amount of data. Because a detailed curve for AZ31B is not available, it was not possible to determine these parameters accurately. However, by updating the value of ε_{po} and q to 0.005 and 0.7, respectively, redetermination of the loading-unloading hysteresis was achieved as shown in Fig. 3.19. This figure shows that the two hysteresis loops compare very well with the experimental data except that the second one did not close.

3.5 Cyclic Behaviour

3.5.1 Axial (Tension-Compression) Loading

Sixteen tubular specimens were tested at different axial strain amplitudes. The second and half-life hysteresis loops for different strain amplitudes are shown in Fig. 3.20. This figure

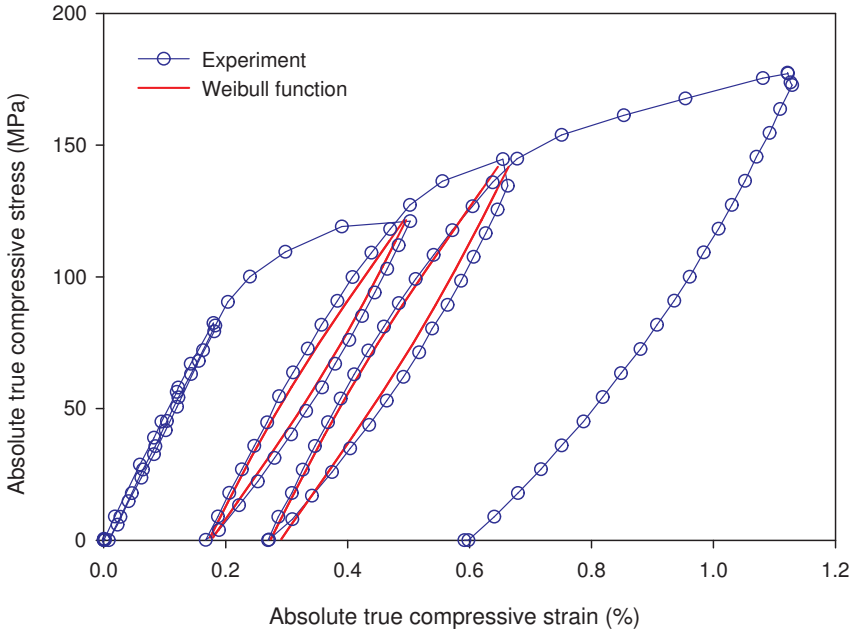

Figure 3.19: Experimental and calculated loading-unloading hysteresis for compressive loading along the transverse direction (TD) using Eq. 3.6.

reveals the distinct features of the cyclic axial behaviour of AZ31B extrusion, especially at strain amplitudes higher than 0.3%. First, by considering the applied strain it is seen that the positive side of the hysteresis has less plasticity than the negative side. In other words, the shape of the hysteresis is not symmetric. Second, the maximum and the minimum stresses are not equal in magnitude although all tests were performed with completely reversed straining. Finally, the part of the cycle from minimum compression to maximum tension i.e., the tension reversal has a distinct point, hereafter referred to as the inflection point, at which the hardening behaviour increases rapidly. Comparing the second and the half-life hysteresis in Fig. 3.20a and b, the following observations can be made. Cyclic hardening is evident as the magnitude of maximum and minimum stresses increases for all tests. However, this increase is more pronounced in tension than in compression. Also, cyclic hardening can be seen as the hysteresis size at a given strain amplitude appears to be smaller at half-life cycle than at the second cycle. In addition, the strain values at zero stress are negative at half-life, but not at the early cycles. The strain-life curve for pure cyclic axial loading for AZ31B extrusion is shown in Fig. 3.21. This figure shows that the material has a distinct knee after 44×10^4 reversals. Variations of axial peak stresses with cycling are presented in Fig. 3.22a. This figure reveals different hardening behaviour for AZ31B extrusion in tension and in compression. While the maximum and minimum peak stresses for 0.2 and 0.3% strain amplitudes are similar, the difference between these peaks becomes more pronounced at higher strain amplitudes. Cyclic hardening is more significant in tension than in compression. Variation of axial stress amplitude and mean stress with cycling are shown in Figs. 3.22b and c, respectively. Similar to the peak stresses, the stress amplitudes and the mean stresses for 0.2 and 0.3% strain amplitudes show minimal change with cycling. On the other hand, for strain amplitudes higher than 0.3% the stress amplitude increases gradually in a nonlinear fashion until failure. The mean stress

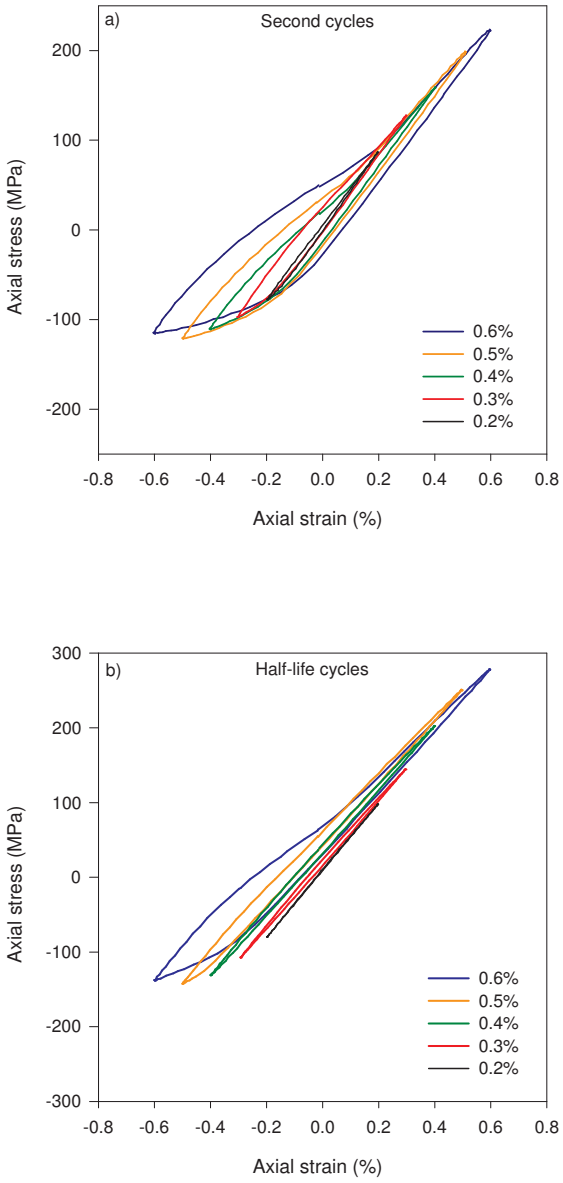

Figure 3.20: Hysteresis loops for cyclic axial tests of AZ31B extrusion. a) Second cycles. b) Half-life cycles.

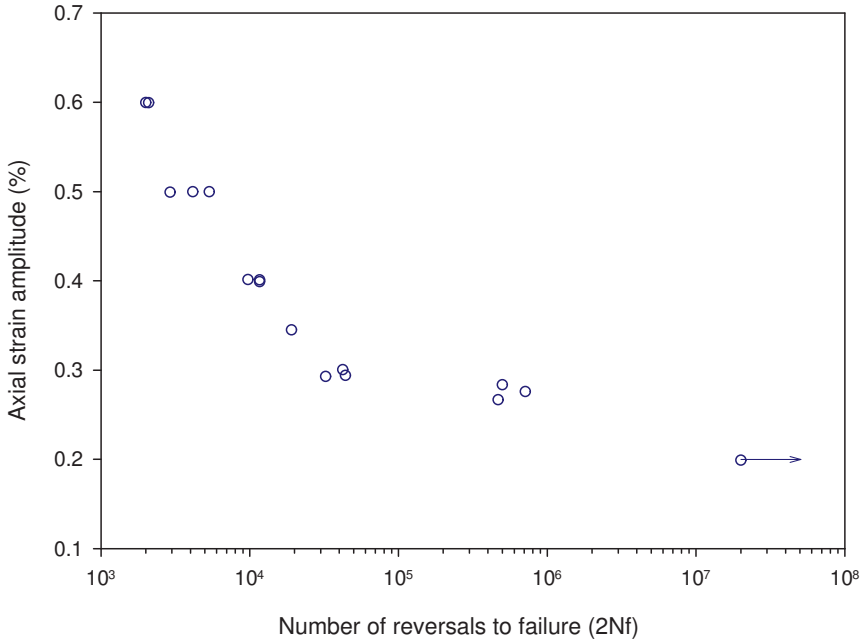

Figure 3.21: Axial strain-life curve for AZ31B extrusion.

starts with a slight decrease until about 35 cycles and then increases sharply until failure. The variation of axial plastic strain amplitude with cycling is shown in Fig. 3.22d. This figure indicates that, as cyclic hardening increases, the capacity to accommodate plastic deformation of AZ31B extrusion decreases. Except for 0.2 and 0.3% strain amplitudes, the plastic strain amplitude for all tests decreases significantly in a nonlinear fashion with cycling until failure. Different strain energy densities that can be calculated from cyclic axial hysteresis behaviour are shown in Fig. 3.23. Calculation of these energies for each cycle reveals the cyclic behaviour of the strain energy density of the material. The evolution of axial plastic strain energy density with cycling is shown in Fig. 3.24a. This figure shows that the evolution of plastic strain energy density is similar to that of plastic strain amplitude in Fig. 3.22d. The evolution of the sum of axial plastic and positive elastic energy densities with cycling is shown in Fig. 3.24b. It should be noted here that the hysteresis energy were calculated until 10^4 cycles because tests that exceeded this number of cycles were switched to load controlled condition. Fig. 3.24 figure shows that the addition of the positive elastic energy to the plastic strain energy results in a more consistent parameter. On the other hand, the sum of the negative elastic energy and the plastic strain energy or the sum of all energies result in unsteady parameters as shown in Figs. 3.24c and d. Although the evolution of the sum of all energies with cycling seems to be comparable to that of the sum of plastic and positive elastic energies, a closer analysis indicates that the latter is steadier than the former. A summary of all cyclic axial test results is given in Table 3.6.

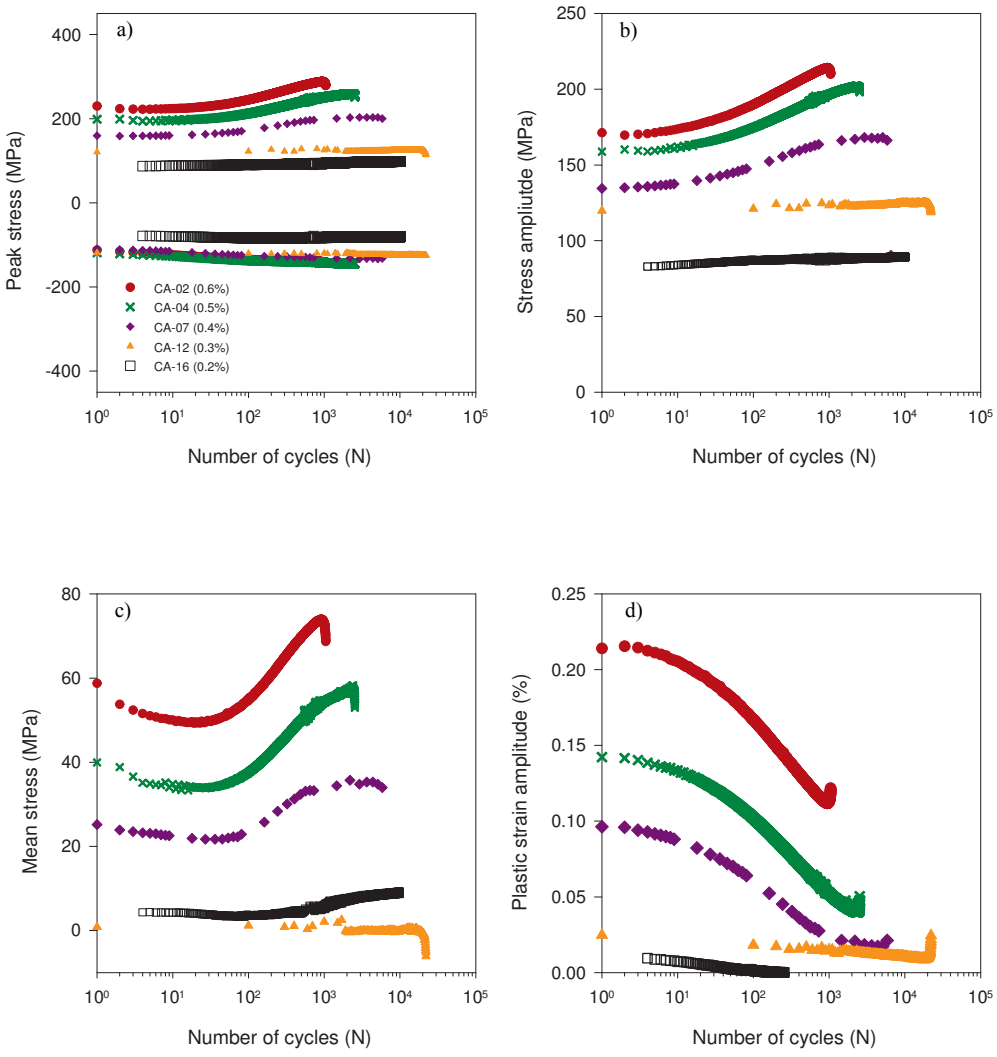

Figure 3.22: Axial stress and strain responses with cycling. a) Peak stress. b) Stress amplitude. c) Mean stress. d) Plastic strain amplitude.

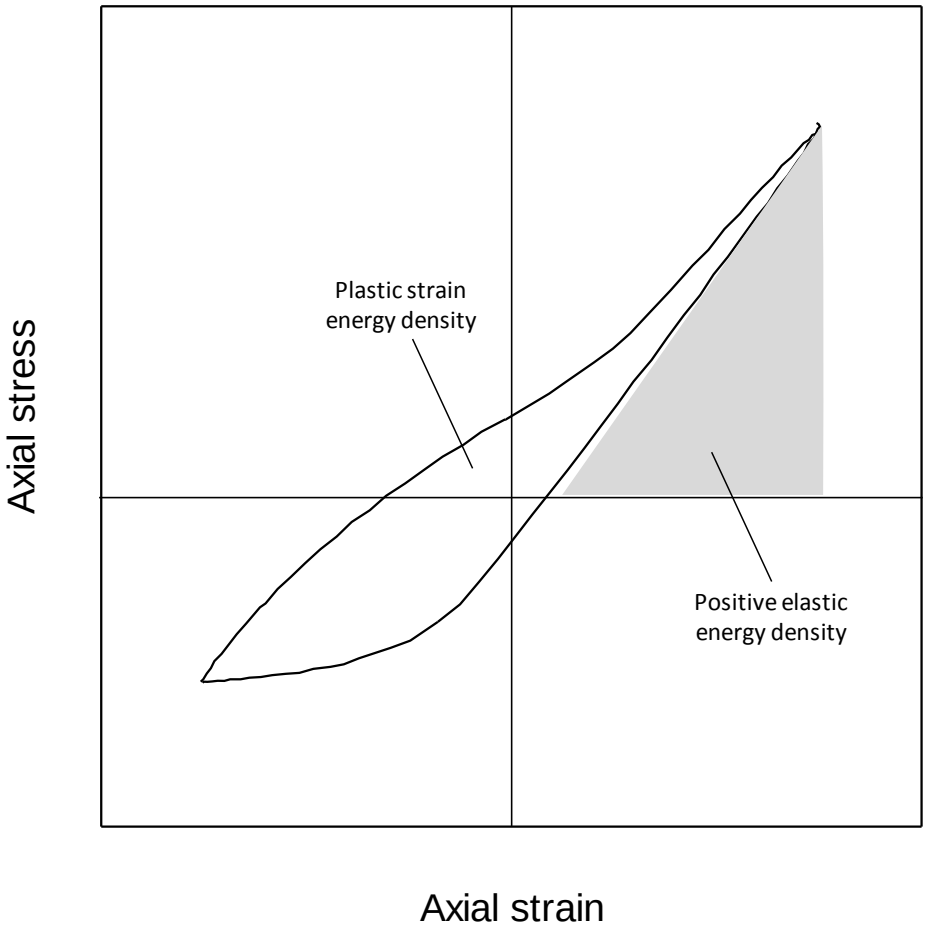

Figure 3.23: Hysteresis energies for cyclic axial loading.

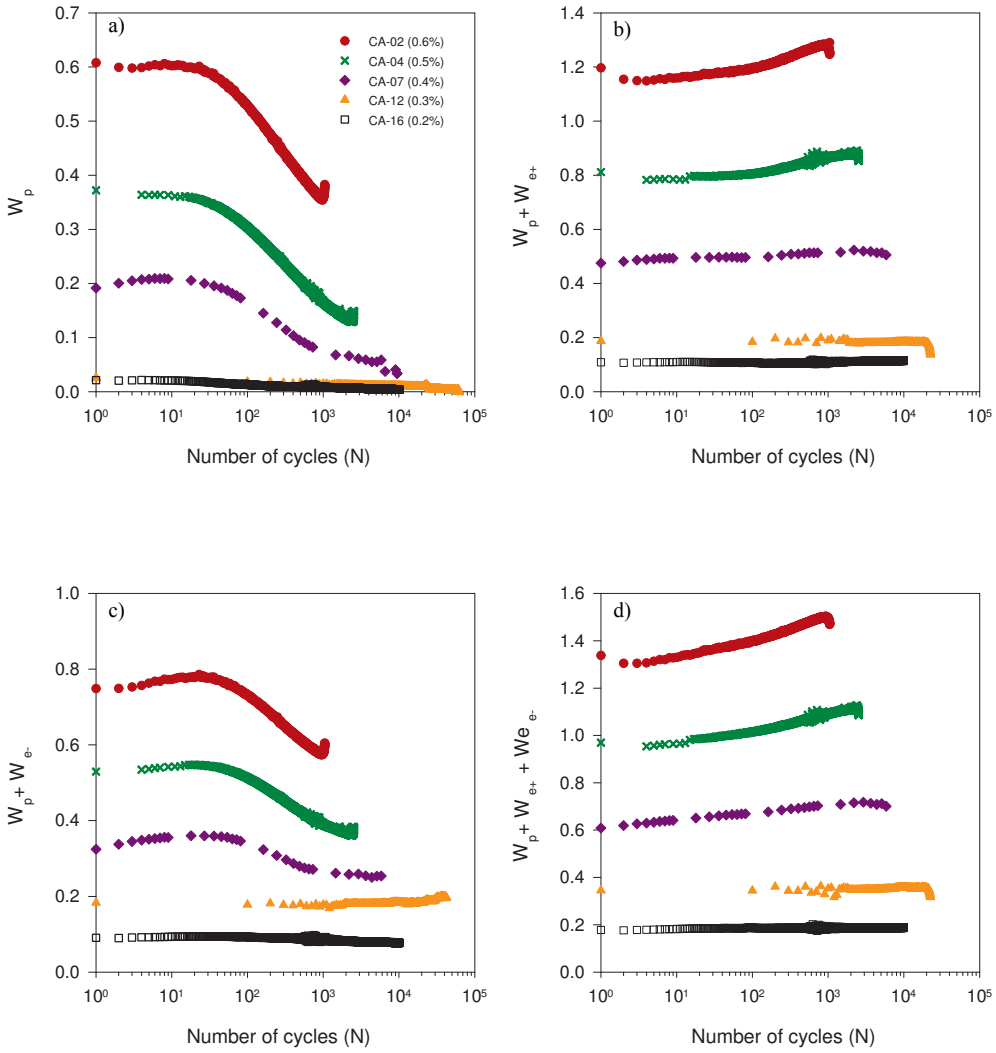

Figure 3.24: Evolution of hysteresis energy densities with cycling for pure axial loading. a) Plastic strain energy. b) Sum of plastic and positive elastic energies. c) Sum of plastic and negative elastic energies. d) Sum of plastic and positive and negative elastic energies. Energy in (MJ/m^3).

Table 3.6: Cyclic axial test summary. N_f is fatigue life at initial σ_a drop and N_f^* is fatigue life at 50% load drop. Stress in (MPa) and energy in (MJ/m^3).

Test ID	Test No.	$\varepsilon_a(\%)$	σ_a	σ_m	W_p	W_{e+}	W_{e-}	N_f	N_f^*
ZA-4-24	CA-01	0.600	214.36	74.10	0.365	0.952	0.225	1,000	1,180
ZC-1-25	CA-02	0.600	208.48	70.07	0.396	0.864	0.213	1,045	1,050
ZB-4-24	CA-03	0.500	193.01	52.94	0.182	0.674	0.219	1,458	NA
ZB-4-26	CA-04	0.500	196.73	54.24	0.164	0.701	0.226	2,069	2,375
ZB-4-13	CA-05	0.500	202.08	62.22	0.126	0.778	0.218	2,675	2,685
ZB-4-23	CA-06	0.400	169.68	39.65	0.054	0.488	0.188	4,860	NA
ZB-4-21	CA-07	0.400	166.98	35.70	0.066	0.457	0.192	5,832	NA
ZB-4-22	CA-08	0.400	168.35	34.38	0.066	0.458	0.200	5,832	6,557
ZA-1-21	CA-09	0.345	144.39	16.39	0.059	0.296	0.187	9,545	NA
ZA-1-22	CA-10	0.290	130.71	25.17	0.007	0.278	0.127	16,200	16,221
ZA-1-23	CA-11	0.300	130.49	12.43	0.022	0.234	0.159	21,100	21,400
ZA-1-12	CA-12	0.294	124.70	0.17	0.010	0.174	0.173	22,000	58,493
ZC-1-23	CA-13	0.267	118.78	13.05	0.014	0.194	0.124	233,911	233,911
ZB-3-25	CA-14	0.283	123.41	7.77	0.019	0.192	0.149	249,313	249,313
ZD-3-12	CA-15	0.276	122.85	21.89	0.012	0.233	0.114	356,293	356,293
ZD-3-13	CA-16	0.199	89.12	8.98	0.004	0.107	0.072	run-out	run-out

Extruded AZ31B has a strong texture, with the majority of the basal planes parallel to the extrusion direction [61, 64, 84]. Only loading that causes extension along the c-axis can activate tension twinning [12, 61, 62, 68, 81]. Therefore, twinning is the dominant plastic deformation mechanism in compression. The reflection of this on the cyclic behaviour can be seen from three characteristics: load asymmetry with high tensile and low compressive stresses, larger plastic strain in compression than in tension, and cyclic hardening that can be observed from the increase of maximum stress and the decrease of plastic strain energy, i.e., the enclosed area of the hysteresis loop. To analyze the cyclic axial behaviour, two representative strain amplitudes, 0.6 and 0.3% are considered next. At 0.6% strain amplitude, the yield for the first tension reversal is 200 MPa, close to the monotonic value. However, during the compression reversal, the orientation of crystals allows extension along the c-axis, which activates tension twins. Yield for the first compression reversal after tension reversal is about -50 MPa, 54% less than the monotonic 0.2% offset yield strength in compression, at both the 0.3% and 0.6% strain amplitudes. However, it is found from Fig. 3.9 that the monotonic compression stress value at which the stress-strain behaviour departs from linearity is around -60 MPa. This is 20% higher than the yield stress in the compressive reversal. Comparing the second and the half-life cycles for 0.6%, it is seen that hardening increases with cycling. Similar behaviour was also observed by Hasegawa et al. [11] and Brown et al. [12] for AZ31 and AZ31B extrusion, respectively. This was not observed for the 0.3% case, because the half-life cycle indicates that the cyclic behaviour became linear. By unloading from compression, two processes are activated in sequence: detwinning and slip. As a result, the tension reversal of high strain amplitude tests in Fig. 3.20a show two distinct behaviours, separated by the inflection point. This is similar to the monotonic tensile and compressive stress-strain curves shown in Figs. 3.7 and 3.9 for TD and LD, respectively. The twinning deformation causes a re-orientation of the lattice to

about 86.6° [12,20,61,62]. In this case, the lattice orientation is in a favourable position to detwin through subsequent tensile loading [12,20,62,81,112]. Considering the part before the inflection point, it is seen from the 0.6% hysteresis that there is no distinctive yielding point. In fact, a closer analysis of the hysteresis shows that the unloading curve is nonlinear until the inflection point. This indicates that the detwinning process starts immediately upon unloading [17]. It has been demonstrated that the twinning process generates local tensile stress that drives the detwinning upon unloading from compression, without the need for applying tensile loading [84, 128]. Wu et al. [128] estimated the twinning and detwinning activation stresses for ZK60A magnesium extrusion and found them to be 15 and 6 MPa, respectively. This may support the fact that the extension twinning is the main cause of pseudoelasticity in magnesium, as discussed in Section 3.4. After the exhaustion of the detwinning process, slip deformation becomes operative in order to accommodate the applied strain, which is seen as a rapid increase in the strain hardening rate after the inflection point [78,129]. Pole figure analysis shows that by the end of the tension reloading reversal, the texture had reversed to its original orientation [12, 17, 81]. However, this process was seen to saturate with cycling and residual twins were observed [12]. Unlink the second cycle, the 0.6% hysteresis at half-life shows a distinct yield point of about -60 MPa during the tension reversal as shown in Fig. 3.20b. This is associated with an increase in the hardening rate after yielding in compression and a decrease in they hysteresis size. The increase in the hardening rate in compression suggests that the capacity of twin formation decreases with cycling. The decrease in the hysteresis size, i.e., plastic strain energy density, and the increase in the stress amplitude, which are discussed next, is a clear indication of cyclic hardening. The cyclic hardening behaviour can be shown by plotting the stress response with the number of cycles as shown in Fig. 3.22. For 0.6% specimens, the hardening evolves in a nonlinear manner until failure. For 0.3% specimens,

the hardening is minimal. Similar behaviour was observed in extruded AZ31B [19,112] and extruded AM30 [130]. As the cyclic axial hardening is more prominent in tension than in compression, the stress amplitude and mean stress are expected to increase with cycling as shown in Figs. 3.22b and c. The development of cyclic hardening can be attributed to the formation of twins. As explained in Section 3.3.2, El Kadiri and Oppedal [107] suggested that dislocation-dislocation interaction within the twins causes the hardening in material that deforms under twinning and slip mechanisms. Conversely, it was also proposed that the cause of hardening is due to twin-dislocation interactions [115, 120]. El Kadiri and Oppedal [107] only considered monotonic compressive loading. Based on their proposal and for the cyclic axial loading considered here, the hardening during the tensile reversal which follows the compressive reversal can be explained. However, the influence of the second part of the cycle, which is compression following tension, on the cyclic hardening may not be explained using the same argument. The final decrease in the maximum stress while the minimum stress is still increasing may be related to damage evolution, which reduces tensile strength without affecting compressive strength. This may, as generally expected, be an indication of tensile reversals being more detrimental than compressive reversals in the nucleation and growth of cracks. Mean stress development for different strain amplitudes is shown in Fig. 3.22c. At 0.6%, the mean stress steadily decreases during the first 50 cycles, and then sharply increases until failure. This kind of behaviour was also observed for the 0.3% specimen, but was less pronounced. Similar trends were reported for AZ31B extrusions [11] and AM30 extrusions [130]. The variation of plastic strain amplitude with number of cycles shown in Fig. 3.22d demonstrates the nonlinear variation of the plastic strain amplitude with respect to the number of cycles. It is obvious that all strain amplitudes have the same behaviour although it is less pronounced at 0.2% and 0.3%. The plastic strain amplitude decreases nonlinearly until it increases

abruptly due to crack formation [112]. This agrees with the observed cyclic hardening as cycling progresses, and softening in tensile reversal near failure due to damage evolution, as discussed earlier. The same behaviour as for AZ31B extrusion was reported by Hasegawa et al. [11] for AZ31B, and Begum et al. [130], for extruded AM30. Different hysteresis energy densities have been examined. The purpose here is to investigate the applicability of strain energy density to be used as a fatigue damage parameter. Energy is a scalar quantity which is also independent of direction. Therefore, there is no ambiguity in adding energies from different modes of loading like axial and shear. The evolution of different hysteresis energy densities in Fig. 3.24 shows that the sum of plastic and positive elastic energy densities is a stable parameter that can be used as a fatigue damage parameter. In addition, it is seen that the plastic strain energy density decreases with cycling. This means that the amount of plasticity decreases with cycling, which is an indication of cyclic hardening. Detailed discussion about the use of strain energy density in fatigue analysis is provided in Chapter 4.

3.5.2 Shear Loading

Twenty one tubular specimens were tested under cyclic shear loading. Hysteresis loops at the second and half-life cycles are shown in Fig. 3.25. It is seen from this figure that the hysteresis from the second and the half-life cycles are symmetric in shape and in load. The strain-life curve for cyclic shear loading is shown in Fig. 3.26. The shear strain-life curve is similar to the axial one in the sense that they both show distinctive knees. However, the knee in the shear mode starts at about 50×10^3 reversals. Shear stress and strain responses with cycling are shown in Fig. 3.27. The variations of peak shear stresses in Fig. 3.27a illustrate the cyclic symmetry of shear loading. Shear stress amplitude variation

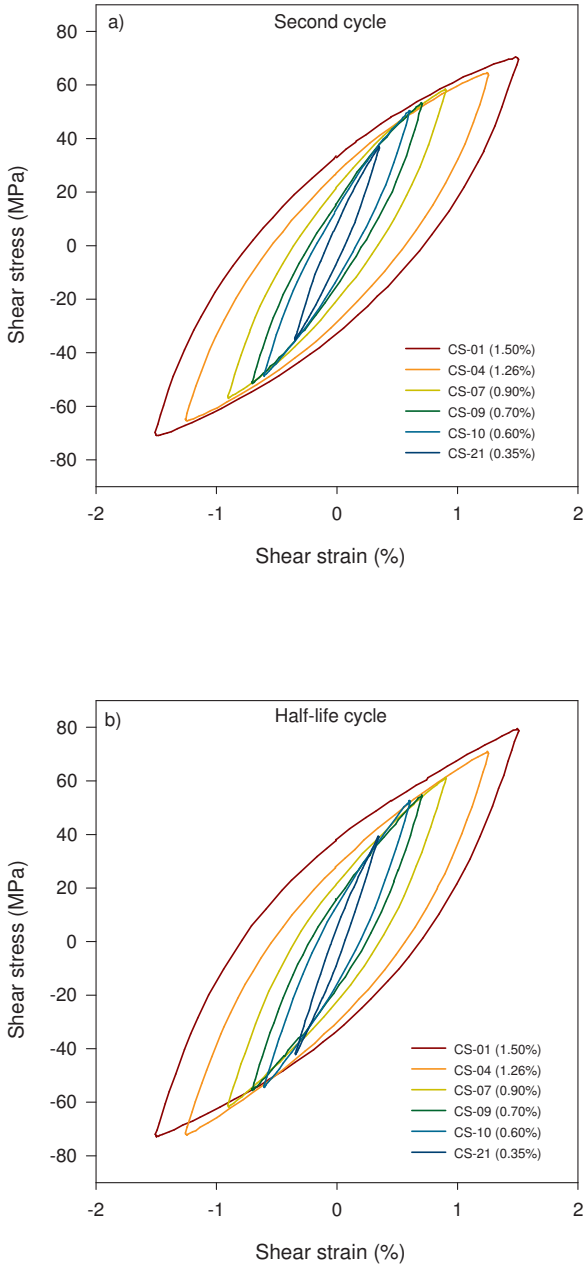

Figure 3.25: Cyclic shear hysteresis for AZ31B extrusion. a) Second cycle. b) Half-life cycle.

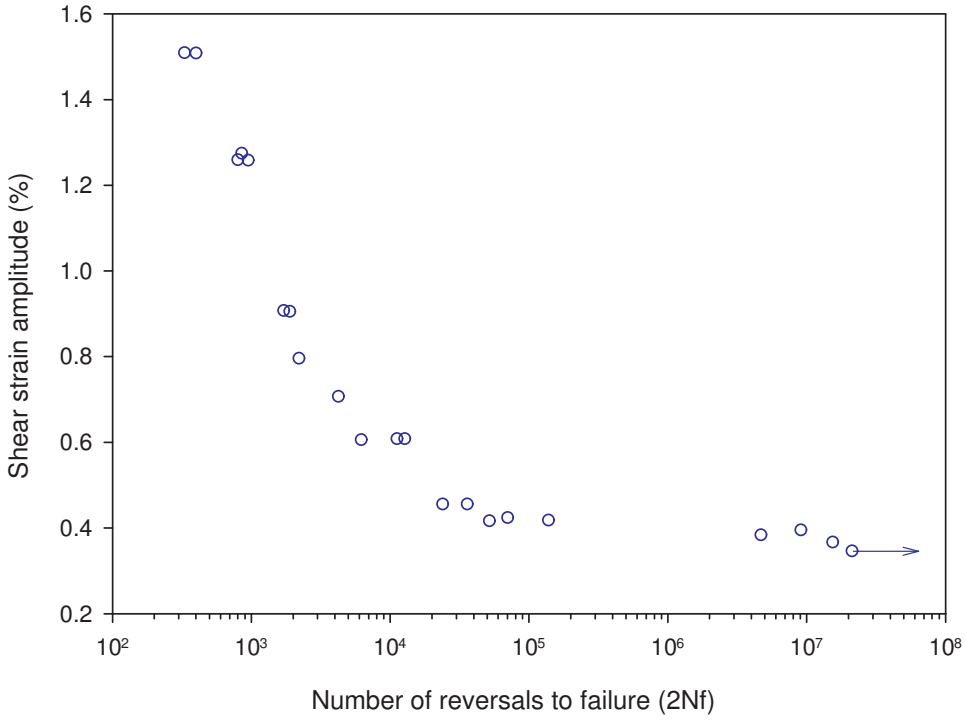

Figure 3.26: Shear strain-life curve of AZ31B extrusion.

with cycling is shown in Fig. 3.27b. This figure shows that, depending on the strain amplitude, two different behaviours can be observed. At shear strain amplitudes of 0.9% or higher, the stress amplitude increases gradually until it reaches a stable value towards the end of the test. At lower shear strain amplitudes, the shear stress amplitude decreases gradually and then continues to increase until the end of the test. However, it is found that these variations are not as significant as in cyclic axial loading. Due to the load symmetry, it is seen from Fig. 3.27c that the mean shear stress is very low, not exceeding ±5.0 MPa. Fig. 3.27d shows the shear plastic strain amplitude variation with cycling. This figure shows that the variation of the plastic strain amplitude for all strain amplitudes is generally minor. Similar to axial loading, the three different energy densities that can be calculated from cyclic shear hysteresis are illustrated in Fig. 3.28. The evolution of plastic strain energy density, sum of plastic and positive elastic energy densities, sum of plastic and negative elastic energy densities, and sum of all energy densities with cycling, are shown in Figs. 3.29a-d, respectively. It is seen from these figures that the evolution of these energy densities are similar. This is not the case in cyclic axial loading. However, because it was found that only the sum of plastic and positive elastic energy densities gave a stable energy parameter in cyclic axial loading, the same parameter is used for cyclic shear loading. Hence, the total strain energy density for shear mode is defined as the sum of the plastic and the positive elastic energy densities. A summary of all cyclic shear tests is given in Table 3.7.

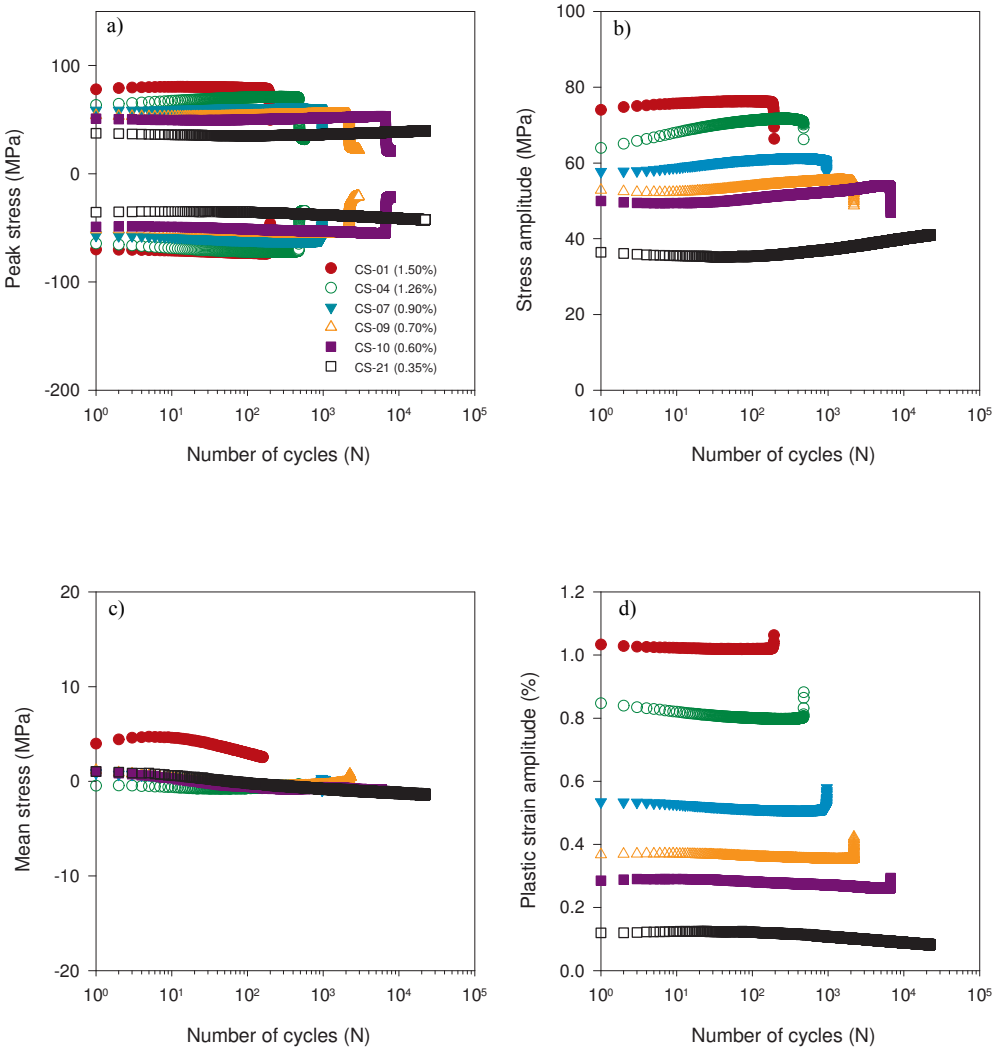

Figure 3.27: Shear stress and strain responses with cycling. a) Peak stress. b) Stress amplitude. c) Mean stress. d) Plastic strain amplitude.

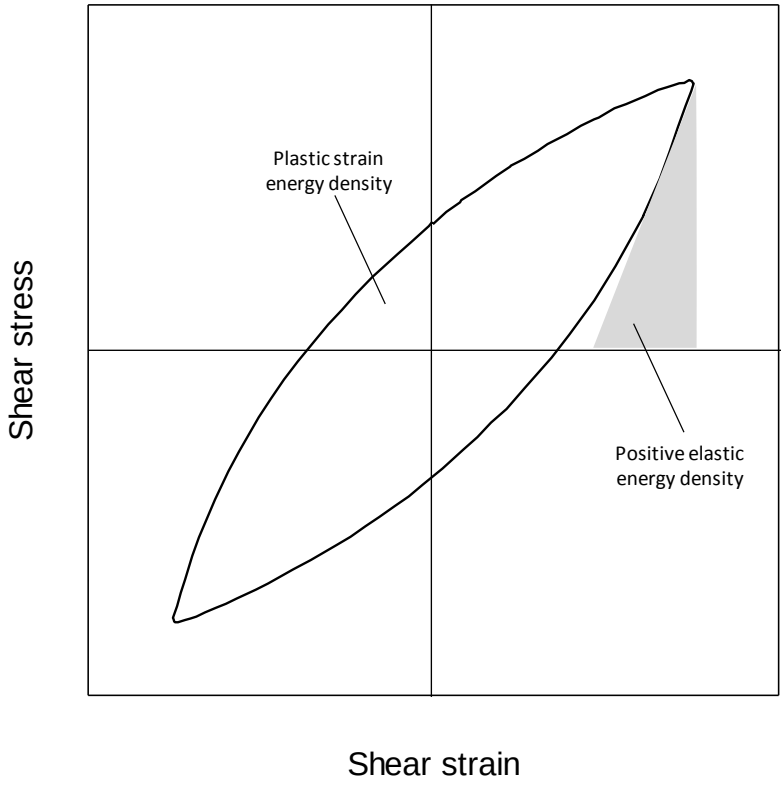

Figure 3.28: Strain energy densities calculated form cyclic shear hysteresis.

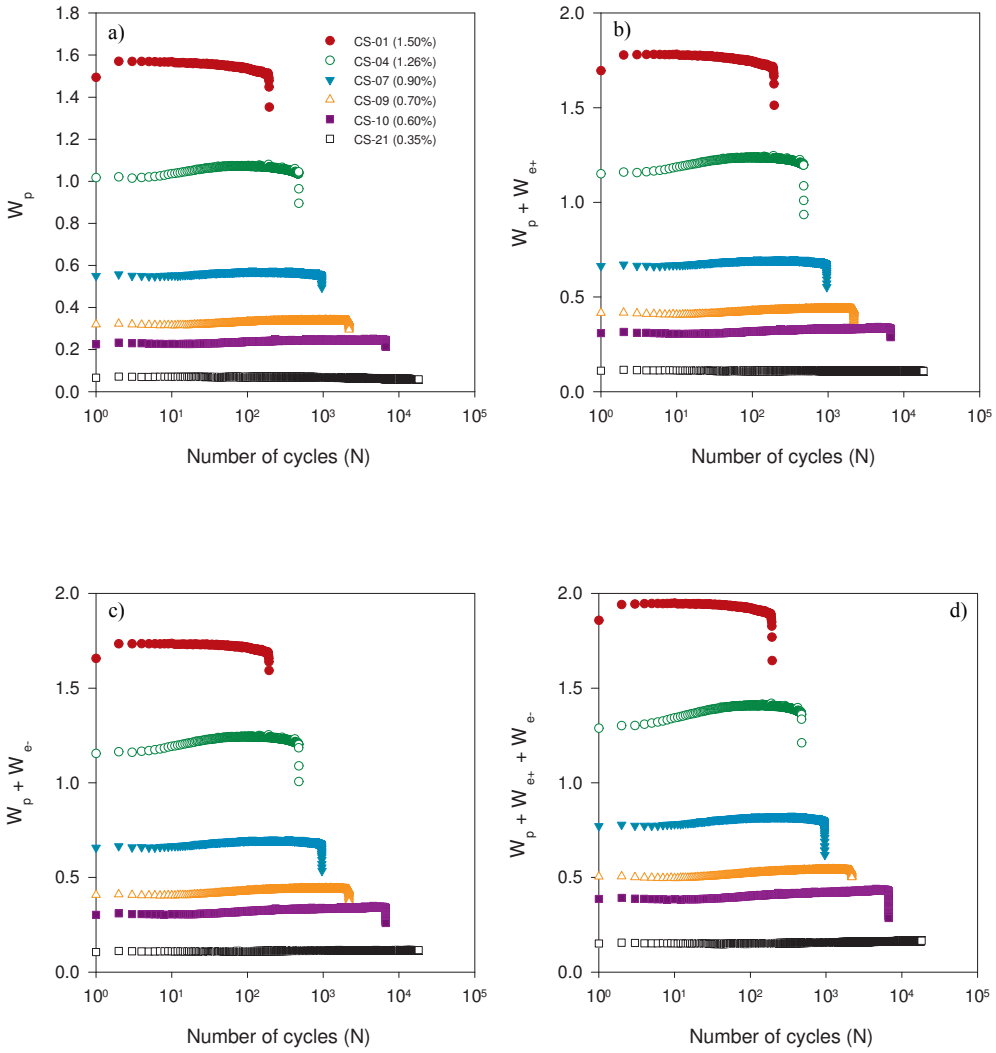

Figure 3.29: Evolution of hysteresis energy densities with cycling for pure shear loading. a) Plastic strain energy. b) Plastic and positive elastic strain energies. c) Plastic and negative elastic strain energies. d) Plastic and positive and negative elastic strain energies. Energy in (MJ/m^3).

Table 3.7: Cyclic shear test summary. N_f is fatigue life at initial τ_a drop and N_f^* is fatigue life at 50% load drop. Stress in (MPa) and energy in (MJ/m^3).

Test ID	Test No.	γ_a (%)	τ_a	τ_m	W_p	W_{e+}	W_{e-}	N_f	N_f^*
ZB-1-21	CS-01	1.51	76.24	3.30	1.542	0.210	0.177	165	222
ZB-1-22	CS-02	1.51	77.94	-0.05	1.564	0.201	0.202	200	216
ZB-1-16	CS-03	1.26	69.48	-0.51	1.077	0.158	0.163	400	433
ZA-4-11	CS-04	1.26	71.69	-0.67	1.065	0.167	0.174	474	501
ZB-1-13	CS-05	1.27	68.71	-0.59	1.092	0.154	0.159	427	482
ZA-4-31	CS-06	0.91	60.01	-0.12	0.565	0.119	0.120	855	947
ZA-4-32	CS-07	0.91	61.52	-0.25	0.566	0.125	0.127	947	1,091
ZB-3-15	CS-08	0.80	55.65	-1.02	0.435	0.099	0.107	1,100	1,611
ZA-4-14	CS-09	0.71	55.24	-0.40	0.334	0.100	0.103	2,119	2,283
ZB-1-26	CS-10	0.61	53.59	-0.89	0.244	0.092	0.098	6,364	6,864
ZB-1-25	CS-11	0.61	53.14	-1.85	0.242	0.087	0.100	5,599	5,949
ZB-1-23	CS-12	0.61	52.64	-1.50	0.238	0.087	0.097	3,093	3,281
ZA-4-21	CS-13	0.46	47.00	-2.74	0.117	0.065	0.082	11,945	12,530
ZA-4-22	CS-14	0.46	46.53	-1.83	0.132	0.066	0.078	17,923	17,214
ZB-1-12	CS-15	0.42	43.78	-1.43	0.112	0.060	0.068	25,912	25,912
ZC-1-15	CS-16	0.42	44.27	-2.46	0.116	0.058	0.072	35,147	35,147
ZC-1-21	CS-17	0.42	45.09	-2.13	0.114	0.061	0.074	69,124	69,124

Continued on next page

Table 3.7 – continued from previous page

Test ID	Test No.	γ_a (%)	τ_a	τ_m	W_p	W_{e+}	W_{e-}	N_f	N_f^*
ZA-4-42	CS-18	0.38	45.60	-2.70	0.074	0.061	0.077	2,342,105	2,342,105
ZD-1-15	CS-19	0.40	43.41	-1.11	0.093	0.059	0.066	4,541,965	4,541,965
ZA-4-44	CS-20	0.37	43.20	-4.89	0.080	0.049	0.077	7,693,873	7,693,873
ZD-1-25	CS-21	0.35	40.75	-1.41	0.059	0.051	0.059	run-out	run-out

The cyclic shear behaviour is obviously symmetric as seen from Fig. 3.20. Cyclic torsional specimens were all machined along the extrusion direction i.e., LD. Generally, this means that the crystals are oriented such that their basal planes are aligned with the extrusion direction, with their c-axis perpendicular to it. Pure shear stress, which produces no normal stress along and/or perpendicular to the c-axis, yields symmetric behaviour. This means that slip is the dominant plastic deformation mechanism. Although twins were observed in cases where large shear strain amplitudes were applied, their effect on the cyclic shear behaviour was insignificant [81, 97]. Also, due to the fact that the basal planes are generally oriented parallel to the extrusion direction, the basal and the prismatic planes come under direct shear loading. Basal slip is the dominant slip system in AZ31B at room temperature with the lowest CRSS among other slip systems [62, 81, 116]. Therefore, basal slip could be the dominant slip system in shear loading. This argument is discussed based on cracking behaviour of shear tests in Section 3.5.4. The variations of peak shear stresses with cycling in Fig. 3.27a show that the maximum and the minimum stresses vary equally. This symmetry in the cyclic hardening is not observed in the axial mode. The variation of shear stress amplitude versus number of cycles in Fig. 3.27b indicates that extruded AZ31B exhibits cyclic hardening, but to a lesser extent compared to cyclic axial loading. Because the hardening is symmetric in shear loading, the mean shear stress variation with number of cycles is expected to be minimal, as shown in Fig. 3.27c. Opposite to the cyclic axial, the second and the half-life cyclic shear hysteresis behaviour show no significant change in the hysteresis loop's shape or size. Therefore, it is anticipated for the plastic strain amplitude to be steady with cycling, which is clearly seen in Fig. 3.27d. Like the axial mode, the different shear energy densities shown in Fig. 3.28 were calculated up to 10^4 cycles. Because of cyclic symmetry in the shear mode the variations of these energies with cycling is not significant as shown in Fig. 3.29.

3.5.3 Multiaxial Loading

Thirty four tubular specimens were tested under multiaxial axial-torsional loading. Axial and torsional loads were combined using three phase angles: proportional with $\varphi = 0°$ and nonproportional with $\varphi = 45°$ and $\varphi = 90°$. Multiaxial stress-strain responses for three selected tests are shown in Fig. 3.30. Additional stress-strain responses for different multiaxial tests are available in Appendix A. Comparing the hysteresis of the axial mode for the three different phase angles it appears that the characteristics of cyclic axial loading are preserved. However, as cyclic hardening increases, half-life hysteresis becomes narrower, indicating lesser plastic deformation. This is also observed in cyclic axial loading. The hysteresis loops of the shear mode seem to be distorted due to the application of axial load; however, the half-life hysteresis loops appear to be relatively symmetric. It is worth mentioning here that the tests shown in Fig. 3.30 were performed at the same axial and shear strain amplitudes. Therefore, these figures reveal the effect of phase angle on the cyclic stress-strain behaviour of the material.

a)

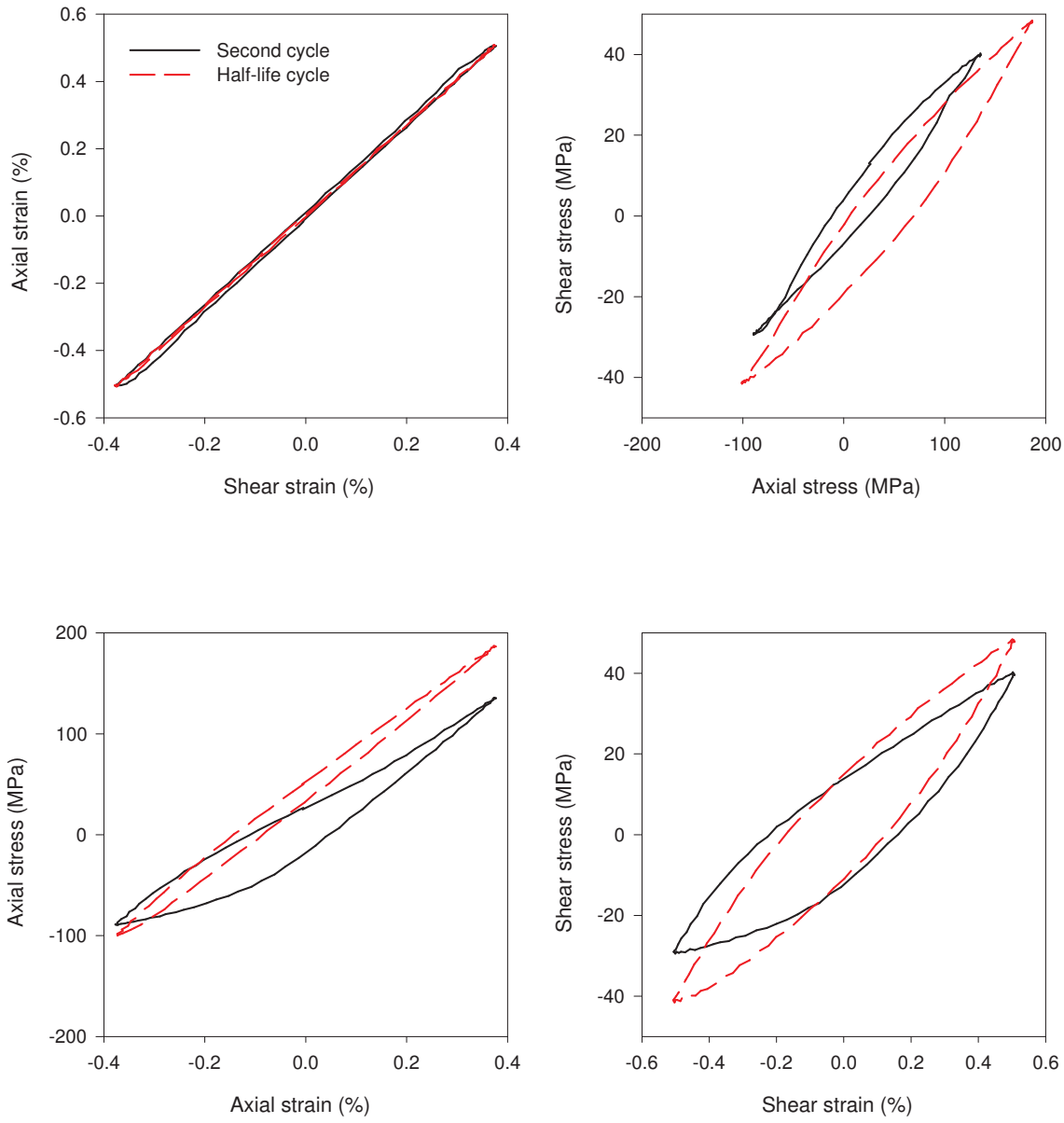
Second cycle
Half-life cycle
Axial strain (%)
Shear strain (%)
Shear stress (MPa)
Axial stress (MPa)
Axial stress (MPa)
Axial strain (%)
Shear stress (MPa)
Shear strain (%)

b)

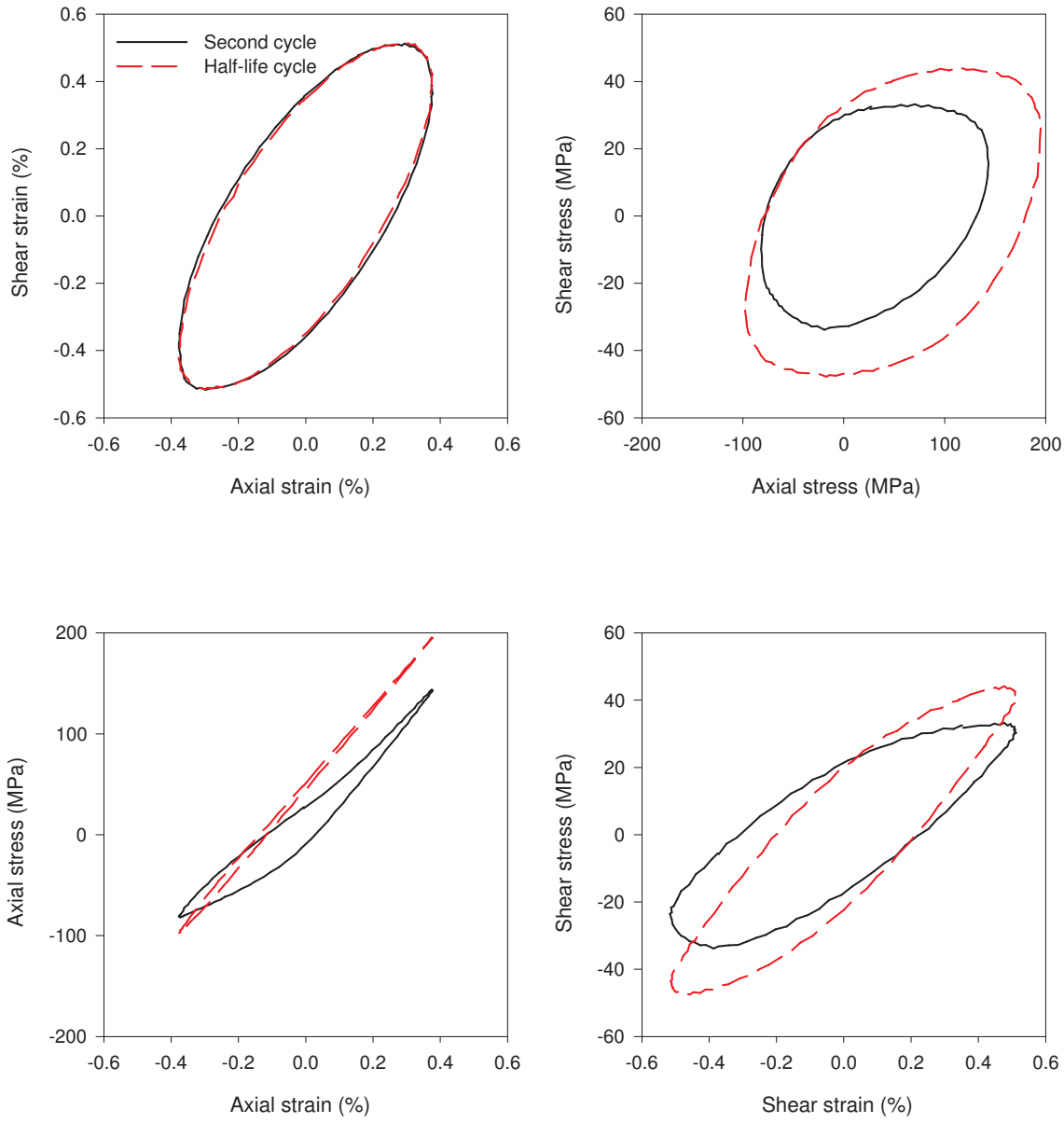
Second cycle
Half-life cycle
Shear strain (%)
Axial strain (%)
Shear stress (MPa)
Axial stress (MPa)
Axial stress (MPa)
Axial strain (%)
Shear stress (MPa)
Shear strain (%)

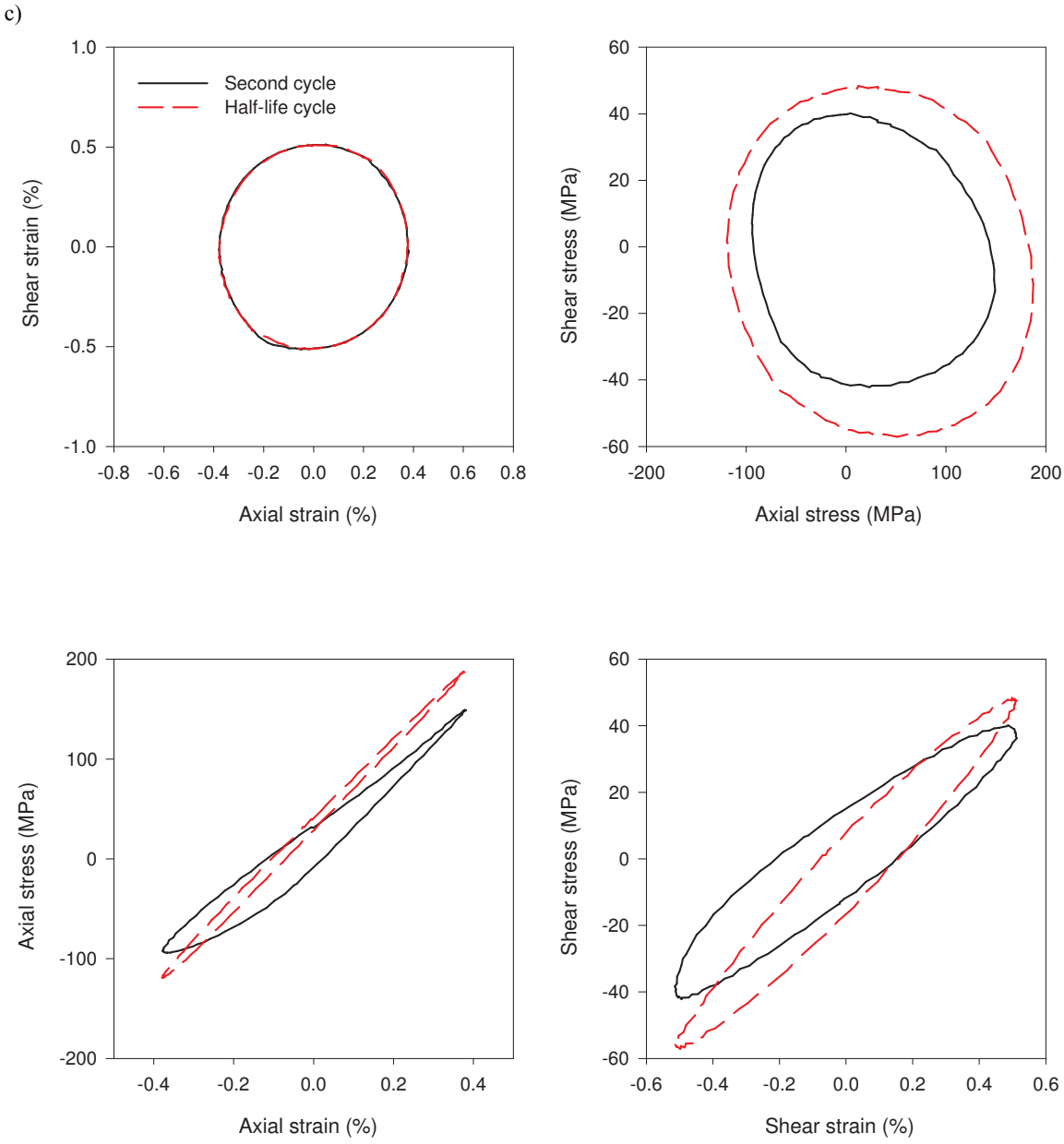

Figure 3.30: Multiaxial stress-strain response, $\varepsilon_a = 0.38\%$ and $\gamma_a = 0.51\%$. a) Proportional: BA-0-9. b) 45° out-of-phase: BA-45-4. c) 90° out-of-phase: BA-90-8.

Fig. 3.31 compares the axial and the shear responses for three multiaxial tests that were performed at different loading conditions. The purpose of this figure is to show the effect of the axial mode, which is mainly responsible for activating twinning-detwinning mechanisms, on the shear mode. Considering the second cycle, it can be seen from Fig. 3.31 that the portions of the shear hysteresis that correspond to twinning i.e., steps 3 to 4 and detwinning i.e., 4 to 5 are different than the other portions. In the proportional test, the half-life hysteresis of the axial mode is showing the same behaviour as for the second cycle. As a result, the effect of twinning and detwinning on shear hysteresis can still be seen. However, this is not the case for 90° out-of-phase loading. To some extent, the half-life axial behaviour is similar to the one for the second cycle. However, the shape of the half-life shear hysteresis became fairly symmetric in shape but with a negative mean stress. The half-life axial behaviour for 45° out-of-phase loading is nearly linear and no signs of twinning or detwinning can be observed from the hysteresis loop. In that case, the shear response at half-life is almost symmetric. In Fig. 3.32, the axial and shear hysteresis from the three multiaxial tests shown in Fig. 3.30 are combined. These tests were performed at same axial and shear strain amplitudes. The only difference here is the phase angle. The purpose of this comparison is to show the effect of the phase angle on the cyclic stress-strain response. At both the second and half-life cycles, the phase angle seems to have no influence on the axial mode. On the other hand, a noticeable difference can be seen on the shear hysteresis.

a)

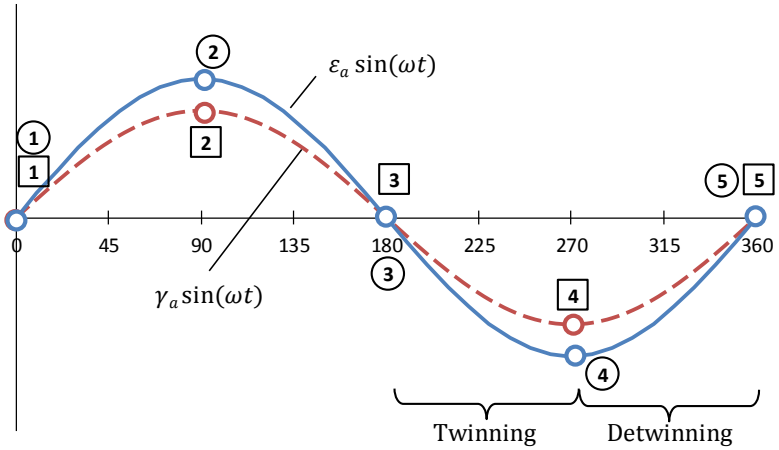
$\varepsilon_a \sin(\omega t)$
$\gamma_a \sin(\omega t)$
0
45
90
135
180
225
270
315
360
Twinning
Detwinning

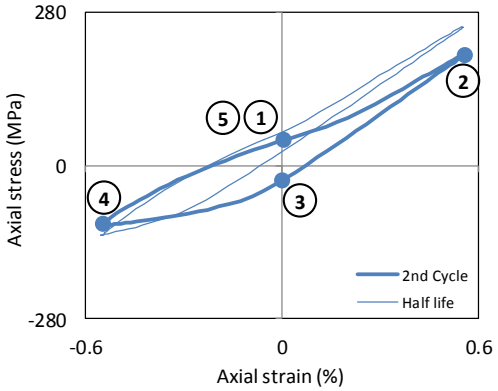
Axial stress (MPa)
280
0
-280
-0.6
0
0.6
Axial strain (%)
2nd Cycle
Half life

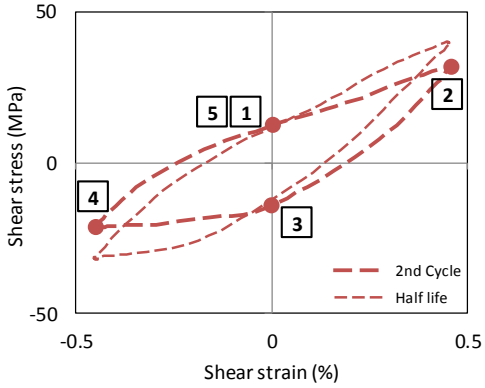
Shear stress (MPa)
50
0
-50
-0.5
0
0.5
Shear strain (%)
2nd Cycle
Half life

b)

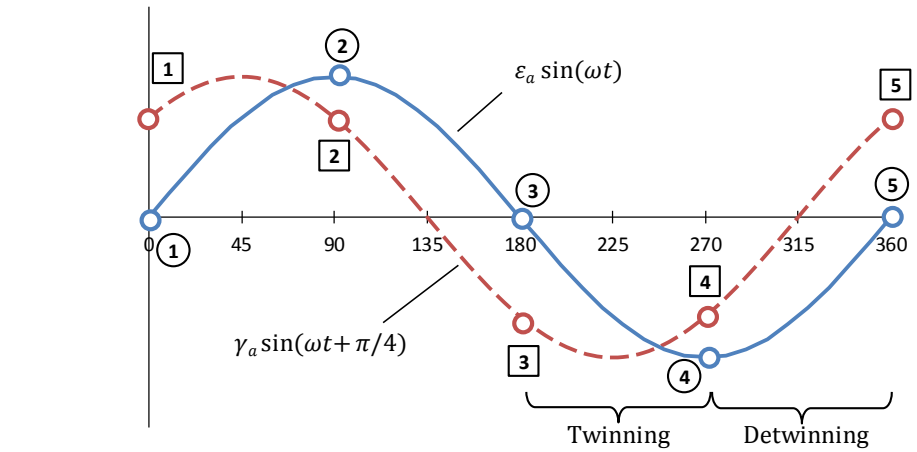
$\varepsilon_a \sin(\omega t)$
$\gamma_a \sin(\omega t + \pi/4)$
0
45
90
135
180
225
270
315
360
Twinning
Detwinning

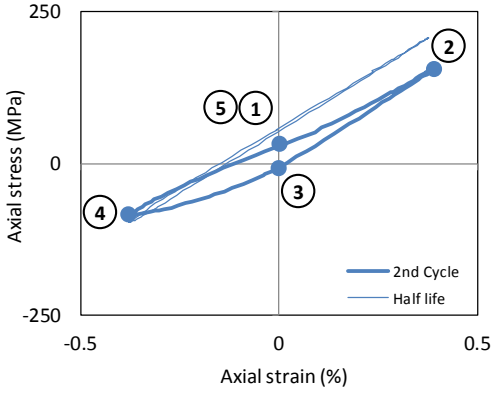
Axial stress (MPa)
Axial strain (%)
2nd Cycle
Half life

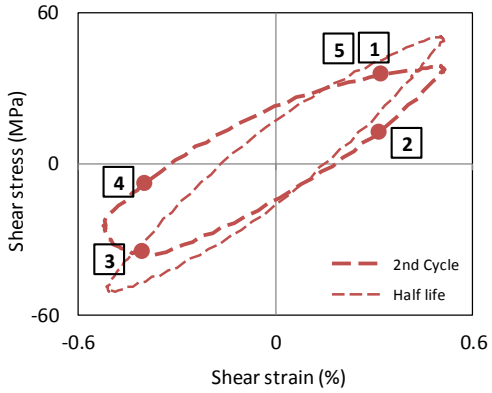
Shear stress (MPa)
Shear strain (%)
2nd Cycle
Half life

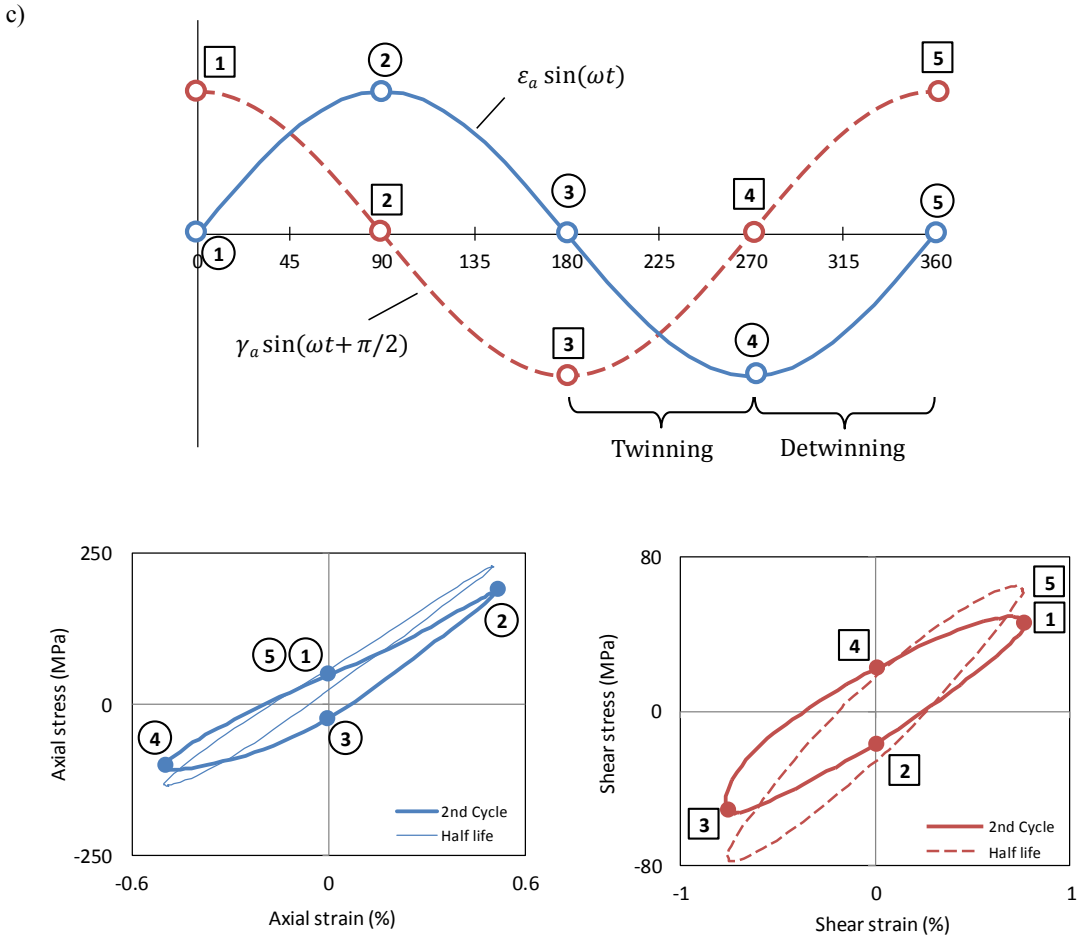

Figure 3.31: Comparison between axial and shear modes. a) Proportional: $\varepsilon_a = 0.55\%$ and $\gamma_a = 0.46\%$. b) 45° out-of-phase: $\varepsilon_a = 0.38\%$ and $\gamma_a = 0.52\%$. c) 90° out-of-phase: $\varepsilon_a = 0.50\%$ and $\gamma_a = 0.76\%$.

To get a detailed view of the multiaxial behaviour of AZ31B extrusion, the stresses and strains for several multiaxial tests are presented in Figs. 3.33 and 3.34. The tests in these figures were performed at axial and shear strain amplitudes of 0.3 and 0.8%, respectively. The purpose of this comparison is to show the effect of phase angle on the stress and strain responses over the number of cycles. The peak stress variation with cycling reveals the

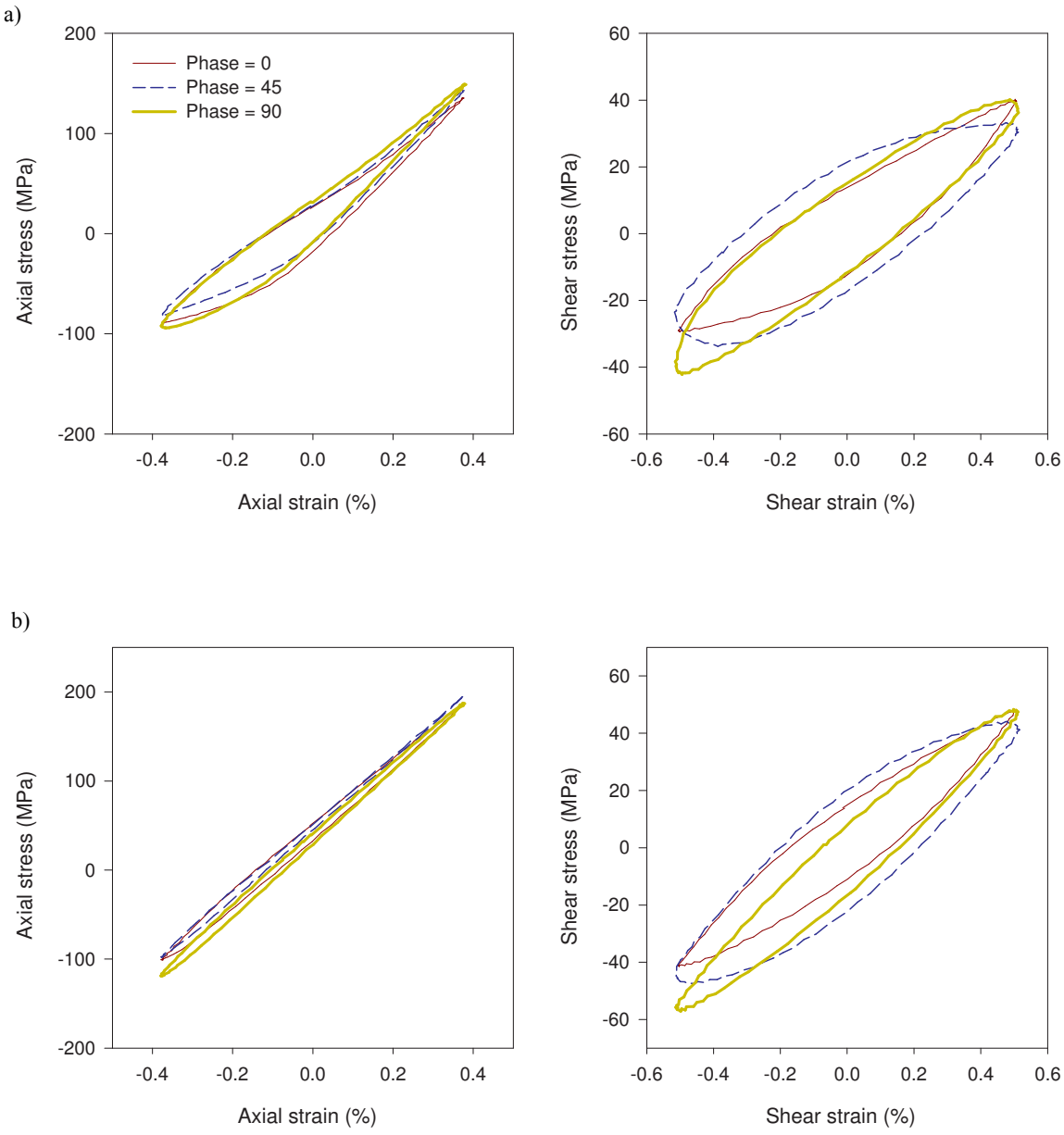

Figure 3.32: Comparisons between axial and shear stress-strain responses from multiaxial tests. Strain amplitudes for multiaxial tests are $\varepsilon_a = 0.38\%$ and $\gamma_a = 0.51\%$. a) Second cycles. b) Half-life cycles.

cyclic hardening behaviour, which is asymmetric in axial mode and symmetric in shear mode as seen from Figs. 3.33a and 3.34a. This observation may not be clearly seen from Figs. 3.33a and 3.34a, however, mean stress variation with cycling, Figs. 3.33c and 3.34c, show that the mean stress development in axial mode is higher than that in shear mode. Considering the variation of axial and shear stress amplitudes with cycling, it is seen that phase angle has an influence on the hardening behaviour of the material. At a given cycle, the stress amplitude increases as the phase angle does. In other words, it can be said that AZ31B extrusion exhibits additional hardening due to nonproportionality. The variation of plastic strain amplitude with cycling is generally opposite to the stress amplitude behaviour. For a given cycle, the plastic strain amplitude decreases as the phase angle increases as seen from Figs. 3.33d and 3.34d. The phase angle effect on fatigue life is illustrated in Fig. 3.35. In this figure, the results for four different sets of tests that were performed under different phase angles but same strain amplitudes are plotted. Data from cyclic axial and torsional tests were also included for comparison. Two methods of representation were considered: von Mises equivalent strain and total energy density. It is worth mentioning here that from plasticity point of view, von Mises equivalent strain may not be applicable for anisotropic material such as Mg-alloys. However, it has been used here as a tool to combine both axial and torsional strains. In general, the two equivalent measures, strain and energy, show the same behaviour. Considering multiaxial tests only, it is seen that phase angle had no significant effect on fatigue life. Comparison between multiaxial and cyclic axial tests at the same equivalent strain or total energy density shows that multiaxiality has no influence on fatigue life. On the contrary, it appears from Fig. 3.35 that cyclic shear loading is more detrimental than cyclic axial and multiaxial loading. The observation regarding the phase angle effect could be explain in terms of total energy density as shown in Fig. 3.36. In this figure, the total energy densities for the same sets of

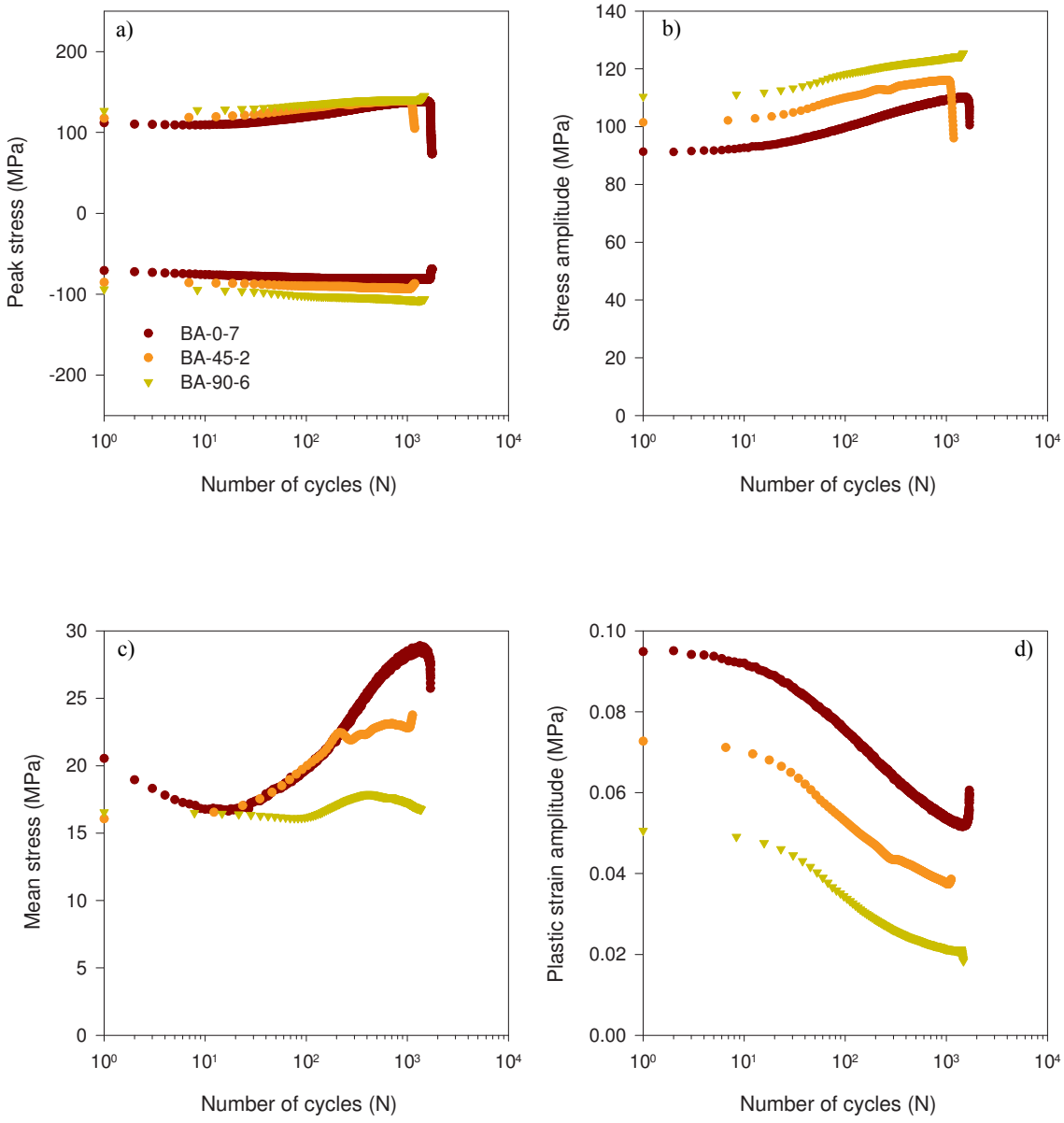

Figure 3.33: Comparison between axial mode responses of three multiaxial tests performed at three phase angles. $\varepsilon_a = 0.3\%$ and $\gamma_a = 0.8\%$. a) Peak stresses. b) Stress amplitude. c) Mean stress. d) Plastic strain amplitude.

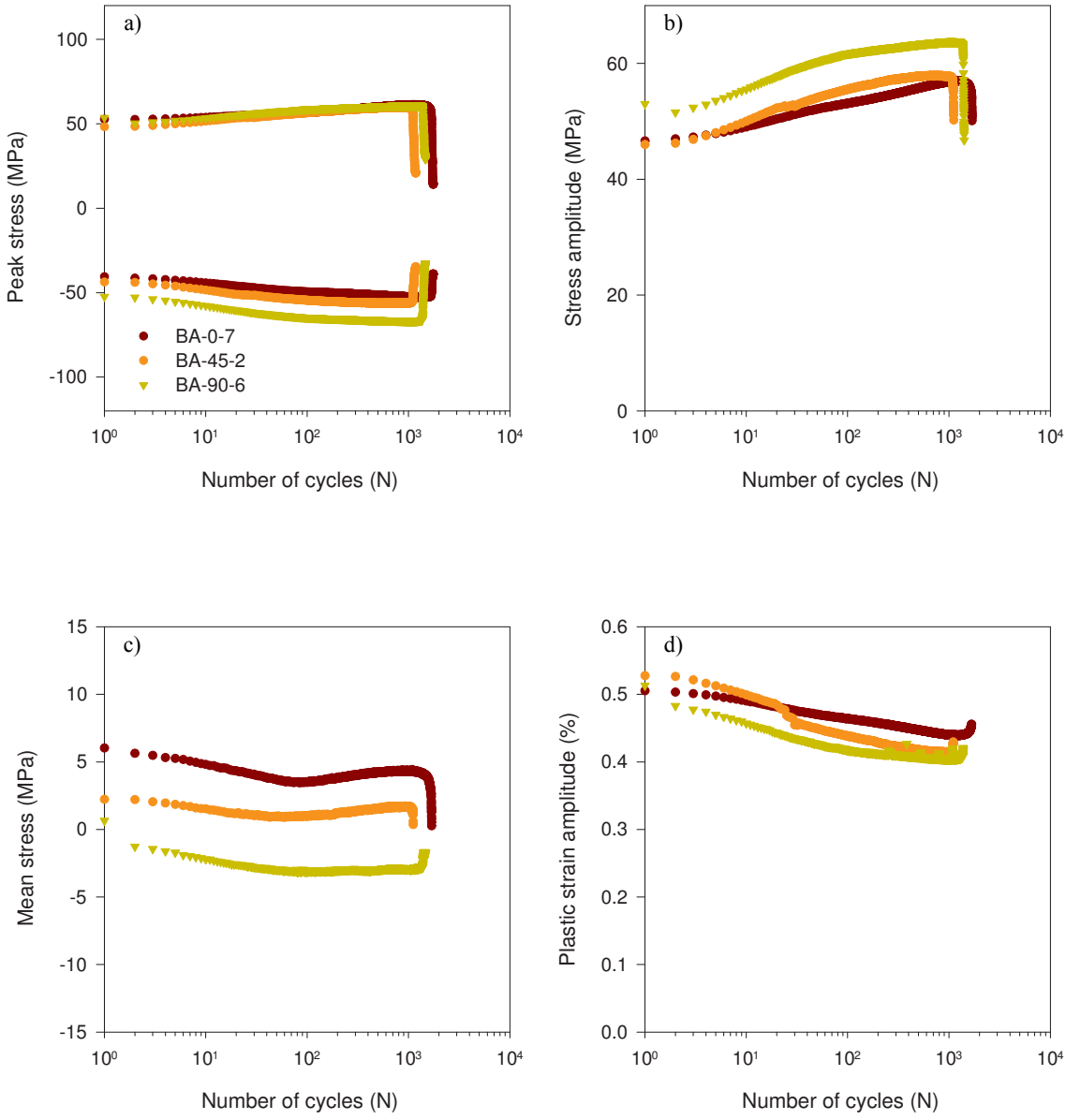

Figure 3.34: Comparison between shear mode responses of three multiaxial tests performed at three phase angles. $\varepsilon_a = 0.3\%$ and $\gamma_a = 0.8\%$. a) Peak stresses. b) Stress amplitude. c) Mean stress. d) Plastic strain amplitude.

tests in Fig. 3.35 are presented. In general, this figure shows that the total energy densities for the tests performed at same axial and shear strain amplitude but different phase angle are fairly comparable. Therefore, their fatigue lives are comparable even though they were tested at different phase angles. Similar to cyclic axial and shear tests, energy density evolutions for selected proportional and nonproportional tests in Figs. 3.37-3.39 show that the sum of plastic and positive elastic energy densities provides a fairly stable parameter. A summary of all multiaxial tests is given in Tables 3.8-3.10.

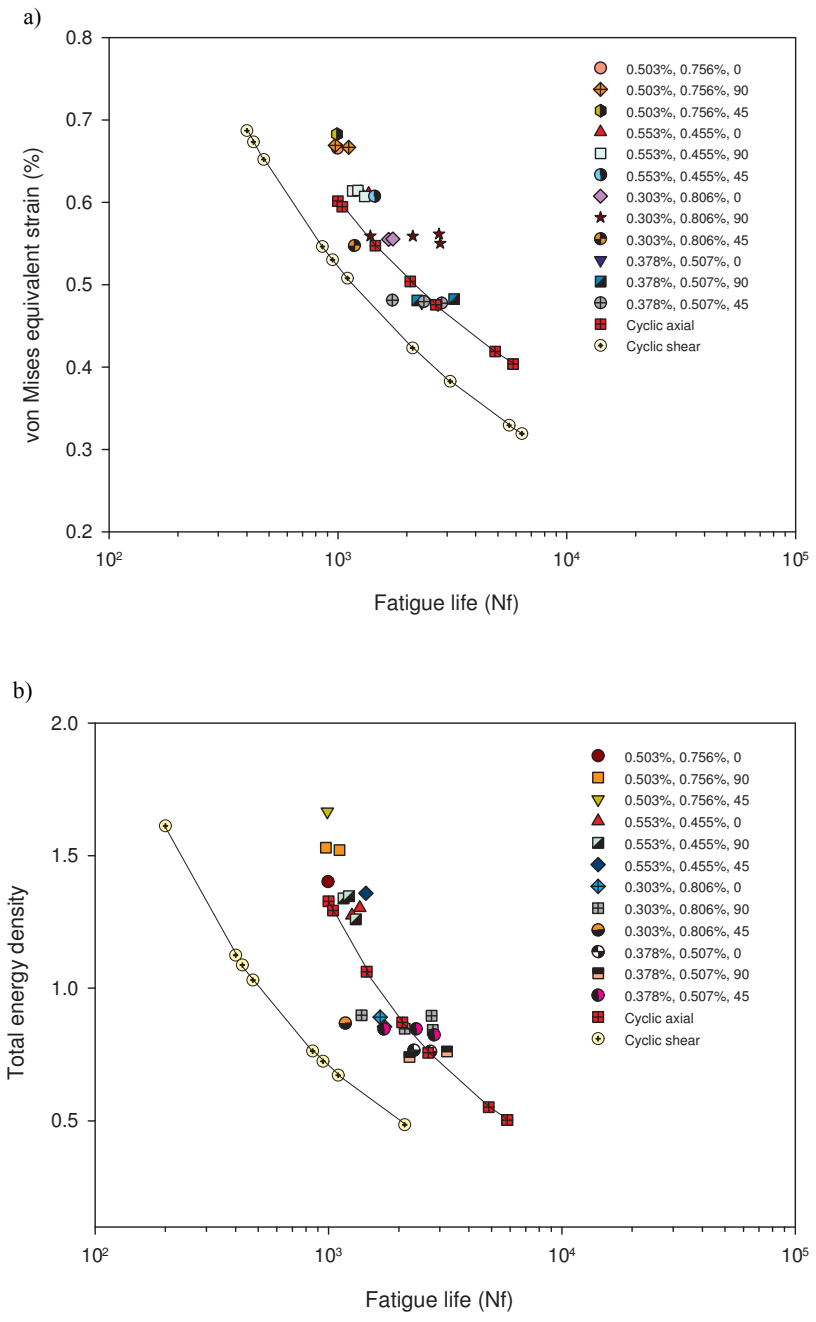

Figure 3.35: Phase angle effect. a) Based on von Mises equivalent strain. b) Based on strain energy density in (MJ/m^3). In legend: ε_a (%), γ_a (%), φ (°).

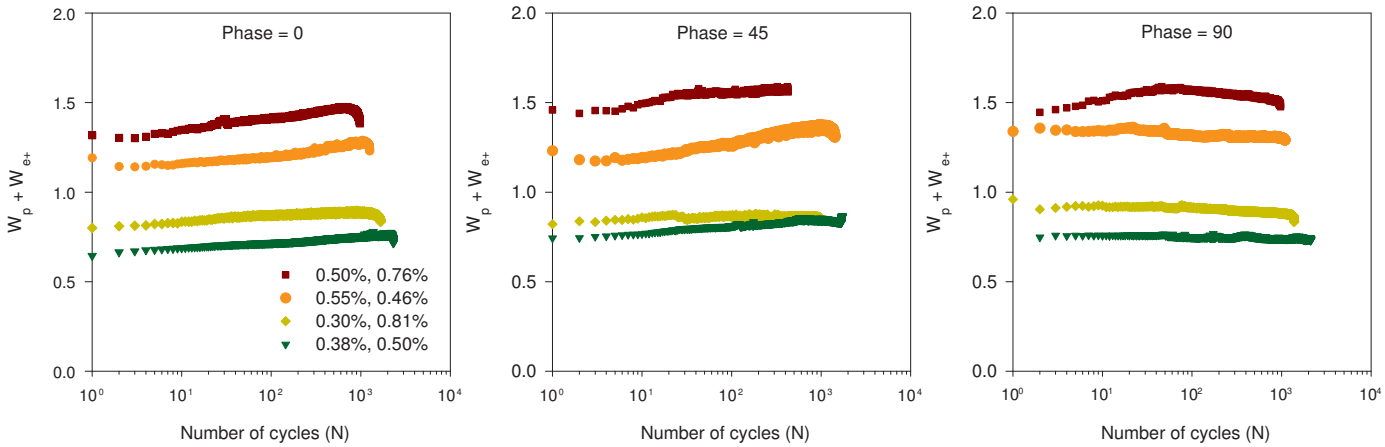

Figure 3.36: Illustration of the insignificance of phase angle effect on multiaxial fatigue life based on strain energy density (MJ/m3). In legend: ε_a (%), γ_a (%).

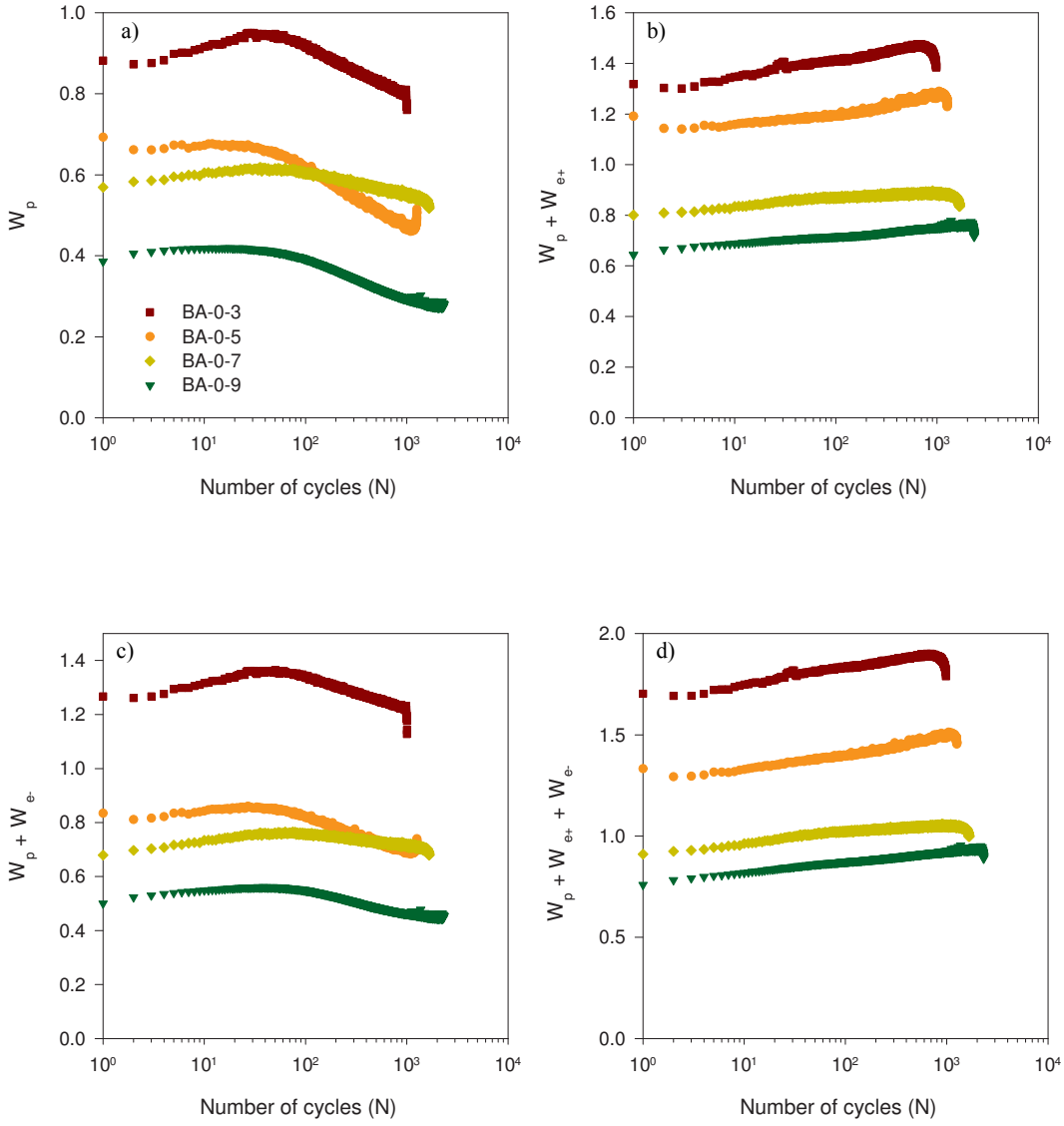

Figure 3.37: Evolution of different energy densities for four proportional tests. a) Plastic strain energy. b) Plastic and positive elastic strain energies. c) Plastic and negative elastic strain energies. d) Plastic and positive and negative elastic strain energies. Energy in (MJ/m^3).

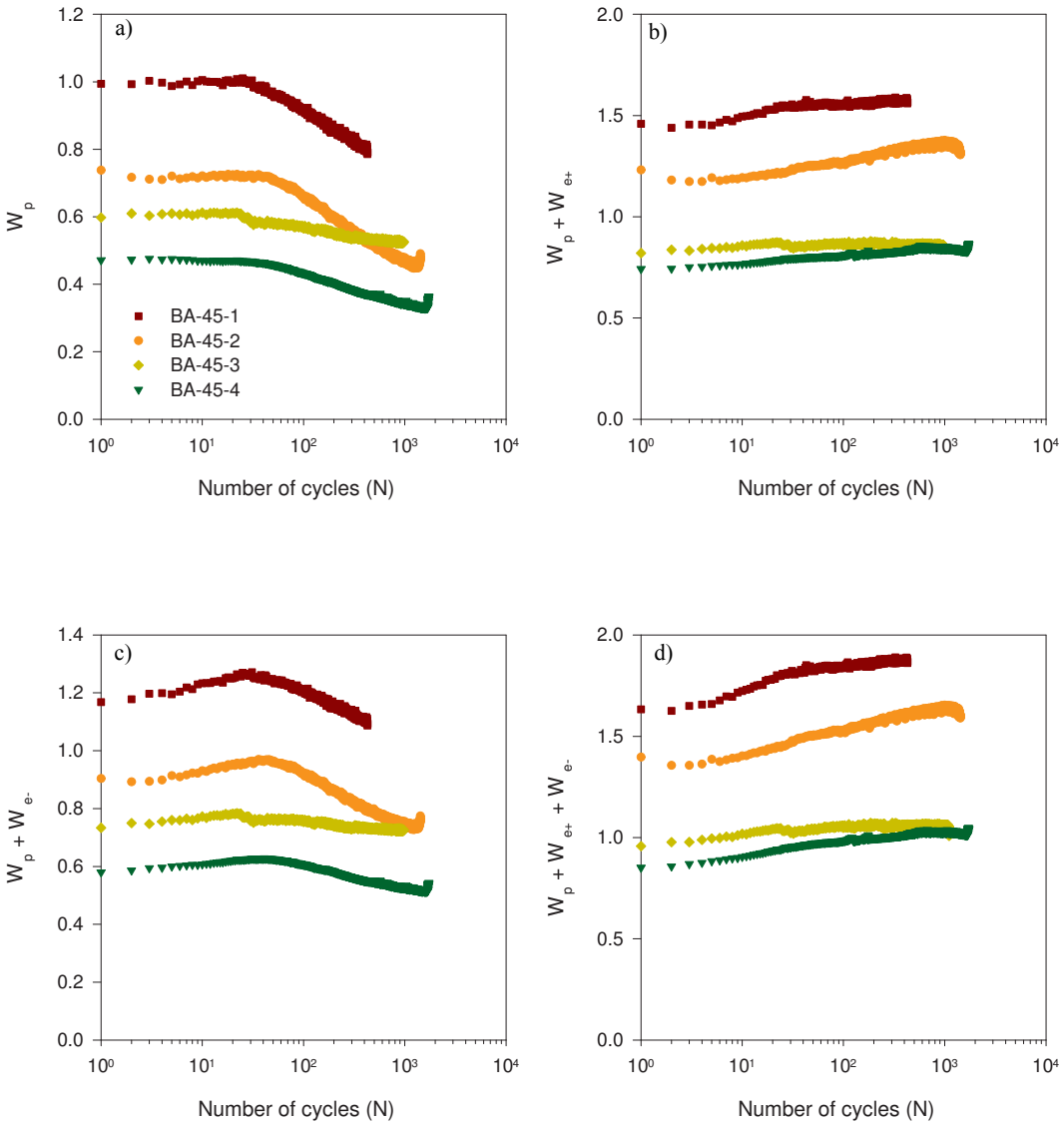

Figure 3.38: Evolution of different energy densities for four 45° out-of-phase tests. a) Plastic strain energy. b) Plastic and positive elastic strain energies. c) Plastic and negative elastic strain energies. d) Plastic and positive and negative elastic strain energies. Energy in (MJ/m^3).

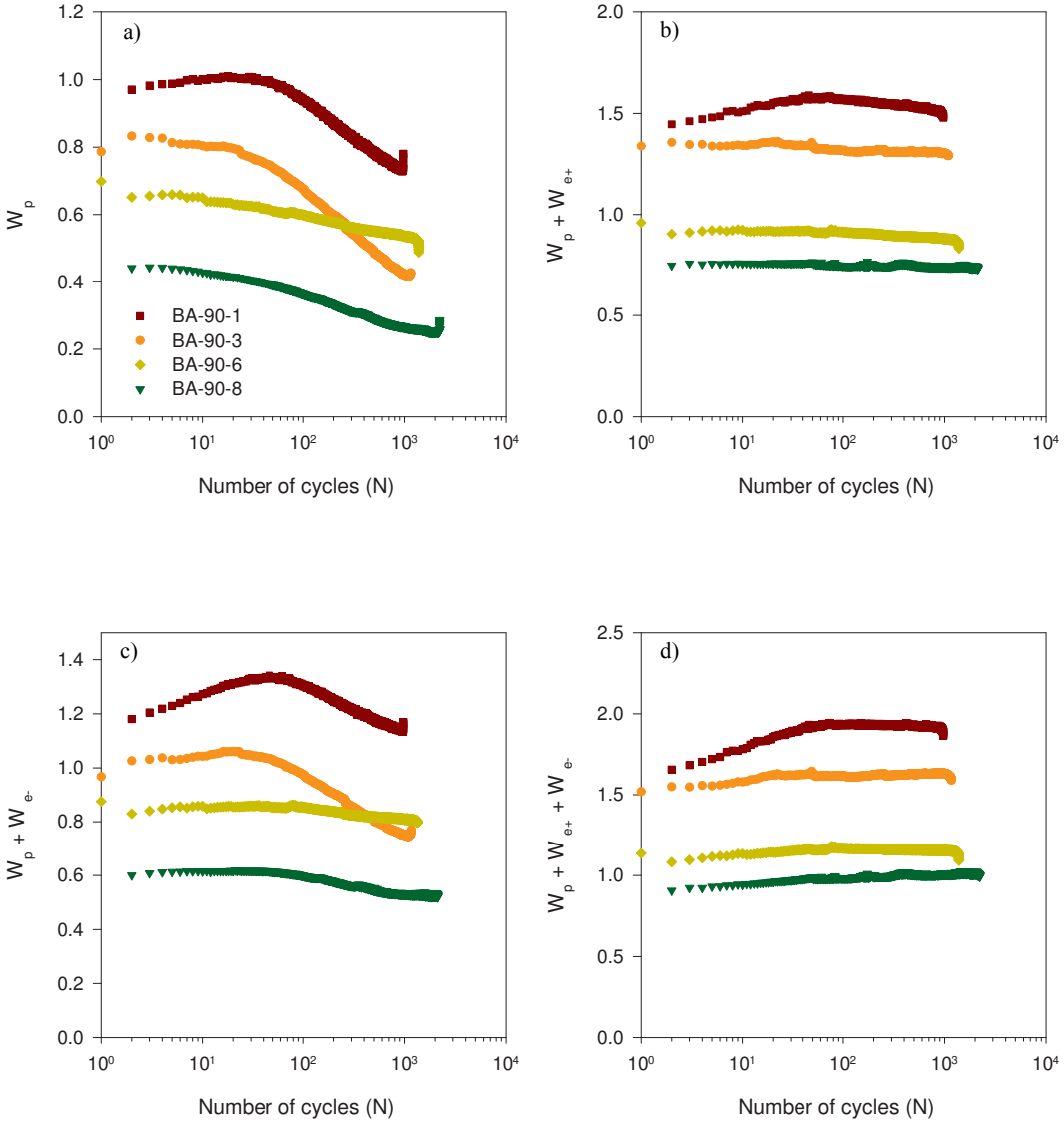

Figure 3.39: Evolution of different energy densities for four 90° out-of-phase tests. a) Plastic strain energy. b) Plastic and positive elastic strain energies. c) Plastic and negative elastic strain energies. d) Plastic and positive and negative elastic strain energies. Energy in (MJ/m^3).

Table 3.8: Multiaxial test summary: stress and strain. Stress in (MPa).

Test ID	Test No.	ε_a (%)	σ_a	σ_m	γ_a (%)	τ_a	τ_m
ZC-4-14	BA-0-1	0.50	165.14	52.95	0.65	45.77	6.31
ZD-4-11	BA-0-2	0.45	160.56	37.24	0.66	49.74	4.97
ZC-4-25	BA-0-3	0.50	159.91	53.73	0.76	52.15	6.08
ZC-4-16	BA-0-4	0.50	166.35	55.62	0.66	46.48	6.56
ZA-4-12	BA-0-5	0.55	189.99	61.81	0.46	36.14	4.15
ZC-4-24	BA-0-6	0.55	187.71	64.41	0.45	37.42	5.90
ZC-4-21	BA-0-7	0.30	108.66	27.86	0.81	56.60	4.37
ZA-4-13	BA-0-8	0.30	111.04	16.81	0.81	58.76	3.32
ZD-4-12	BA-0-9	0.38	144.1	42.87	0.51	44.97	3.42
ZC-4-11	BA-0-10	0.38	146.74	42.61	0.50	44.23	5.22
ZB-3-11	BA-0-11	0.30	121.67	29.32	0.45	42.18	1.85
ZB-3-13	BA-0-12	0.30	121.72	32.80	0.40	35.98	0.82
ZC-3-11	BA-0-13	0.30	123.61	32.12	0.41	41.53	1.54
ZB-3-12	BA-0-14	0.30	121.91	27.44	0.42	41.15	1.74
ZD-1-22	BA-0-15	0.29	122.15	22.87	0.37	39.16	1.66
ZC-3-13	BA-0-16	0.28	116.07	25.17	0.36	37.64	1.04
ZD-1-21	BA-0-17	0.30	125.81	18.82	0.38	39.58	0.94
ZD-1-12	BA-45-1	0.51	184.10	65.10	0.78	65.13	-2.43
ZC-3-26	BA-45-2	0.30	114.91	23.06	0.79	57.75	1.55
ZB-3-26	BA-45-3	0.55	197.53	67.54	0.45	47.63	-2.26
ZB-3-21	BA-45-4	0.38	146.75	48.54	0.52	45.93	-1.85

Continued on next page

Table 3.8 – continued from previous page

Test ID	Test No.	ε_a (%)	σ_a	σ_m	γ_a (%)	τ_a	τ_m
ZB-3-22	BA-45-5	0.38	151.88	54.91	0.51	50.90	-0.16
ZB-3-23	BA-45-6	0.37	152.71	51.42	0.51	50.26	-0.14
ZD-4-22	BA-90-1	0.50	181.80	49.92	0.76	71.13	-6.70
ZD-4-21	BA-90-2	0.50	181.41	47.66	0.76	71.49	-6.22
ZD-4-24	BA-90-3	0.55	200.02	62.50	0.46	51.38	-6.12
ZD-4-26	BA-90-4	0.55	200.14	64.00	0.46	52.30	-6.54
ZD-4-23	BA-90-5	0.55	201.81	57.72	0.44	50.50	-5.30
ZC-1-13	BA-90-6	0.30	123.01	17.68	0.81	63.56	-2.88
ZD-4-16	BA-90-7	0.30	121.29	18.23	0.81	65.24	-3.48
ZC-4-23	BA-90-8	0.38	153.41	34.14	0.51	52.75	-4.40
ZD-4-13	BA-90-9	0.31	123.83	18.04	0.82	66.56	-2.68
ZC-3-16	BA-90-10	0.3	122.93	9.25	0.80	67.79	-1.99
ZC-4-26	BA-90-11	0.38	155.73	35.53	0.51	52.74	-4.09

Table 3.9: Multiaxial test summary: energy density in (MJ/m^3). W_A is axial energy and W_T is torsional energy.

Test No.	W_{Ap}	W_{Ae+}	W_{Ae-}	W_{Tp}	W_{Te+}	W_{Te-}
BA-0-1	0.319	0.544	0.144	0.339	0.087	0.05
BA-0-2	0.219	0.447	0.174	0.341	0.096	0.064
BA-0-3	0.325	0.522	0.129	0.446	0.109	0.068

Continued on next page

Table 3.9 – continued from previous page

Test No.	W_{Ap}	W_{Ae+}	W_{Ae-}	W_{Tp}	W_{Te+}	W_{Te-}
BA-0-4	0.306	0.563	0.140	0.34	0.090	0.051
BA-0-5	0.344	0.725	0.188	0.154	0.052	0.033
BA-0-6	0.354	0.727	0.174	0.162	0.060	0.032
BA-0-7	0.080	0.213	0.075	0.478	0.119	0.088
BA-0-8	0.079	0.187	0.102	0.466	0.124	0.099
BA-0-9	0.110	0.400	0.117	0.181	0.075	0.055
BA-0-10	0.091	0.410	0.124	0.183	0.079	0.049
BA-0-11	0.063	0.261	0.098	0.121	0.062	0.052
BA-0-12	0.065	0.273	0.090	0.095	0.043	0.040
BA-0-13	0.052	0.277	0.096	0.106	0.060	0.051
BA-0-14	0.064	0.255	0.102	0.102	0.059	0.050
BA-0-15	0.036	0.240	0.113	0.078	0.053	0.045
BA-0-16	0.044	0.228	0.095	0.078	0.048	0.043
BA-0-17	0.048	0.239	0.131	0.074	0.053	0.048
BA-45-1	0.119	0.710	0.162	0.710	0.126	0.147
BA-45-2	0.001	0.218	0.096	0.537	0.113	0.101
BA-45-3	0.237	0.804	0.193	0.251	0.066	0.080
BA-45-4	0.044	0.436	0.110	0.304	0.062	0.073
BA-45-5	0.039	0.489	0.108	0.236	0.083	0.084
BA-45-6	0.041	0.477	0.117	0.226	0.081	0.082
BA-90-1	0.264	0.614	0.199	0.518	0.133	0.195
BA-90-2	0.291	0.600	0.205	0.493	0.137	0.194

Continued on next page

Table 3.9 – continued from previous page

Test No.	W_{Ap}	W_{Ae+}	W_{Ae-}	W_{Tp}	W_{Te+}	W_{Te-}
BA-90-3	0.324	0.788	0.216	0.161	0.066	0.106
BA-90-4	0.312	0.798	0.212	0.170	0.067	0.111
BA-90-5	0.274	0.770	0.237	0.150	0.066	0.100
BA-90-6	0.068	0.226	0.127	0.486	0.118	0.142
BA-90-7	0.035	0.223	0.121	0.467	0.123	0.152
BA-90-8	0.082	0.402	0.163	0.181	0.075	0.105
BA-90-9	0.057	0.230	0.128	0.478	0.131	0.154
BA-90-10	0.056	0.200	0.148	0.449	0.139	0.156
BA-90-11	0.093	0.418	0.165	0.174	0.076	0.104

Table 3.10: Multiaxial test summary: fatigue life. N_f is fatigue life at initial σ_a and/or τ_a drop and N_f^* is fatigue life at 50% load drop.

Test No.	N_f	N_f^*
BA-0-1	674	675
BA-0-2	925	1,144
BA-0-3	994	1,121
BA-0-4	1,012	1,114
BA-0-5	1,260	1,261
BA-0-6	1,362	14,449
BA-0-7	1,665	1,759

Continued on next page

Table 3.10 – continued from previous page

Test No.	N_f	N_f^*
BA-0-8	1,736	1,848
BA-0-9	2,322	3,060
BA-0-10	2,738	3,187
BA-0-11	3,375	4,001
BA-0-12	3,870	4,398
BA-0-13	4,427	7,088
BA-0-14	4,974	5,654
BA-0-15	8,215	10,714
BA-0-16	8,650	10,555
BA-0-17	10,495	14,874
BA-45-1	989	991
BA-45-2	1,181	1,181
BA-45-3	1,445	1,445
BA-45-4	1,730	1,995
BA-45-5	2,375	2,567
BA-45-6	2,839	3,061
BA-90-1	974	974
BA-90-2	1,115	1,133
BA-90-3	1,159	1,175
BA-90-4	1,222	1,240
BA-90-5	1,307	1,307
BA-90-6	1,386	1,474

Continued on next page

Table 3.10 – continued from previous page

Test No.	N_f	N_f^*
BA-90-7	2,123	2,248
BA-90-8	2,220	2,244
BA-90-9	2,765	2,837
BA-90-10	2,800	2,874
BA-90-11	3,215	3,340

During proportional loading, axial and torsional modes are in-phase. The hysteresis loop for the axial mode shown in Fig. 3.30a indicates that the behaviours of cyclic axial and multiaxial proportional loading are similar. In fact, the axial mode hysteresis in Fig. 3.30a shows the characteristic features of cyclic axial loading shown in Fig. 3.20, such as twinning and detwinning mechanisms. On the contrary, the shear hysteresis loop for the second cycle in Fig. 3.30a is different from that of cyclic torsional loading shown in Fig. 3.25. Figure. 3.30a suggests that the torsional mode behaviour is influenced by the twinning-detwinning processes associated with the axial mode. To provide a better understanding, a comparison between the cyclic behaviour for the axial and the torsional modes during multiaxial tests is illustrated in Fig. 3.31. It should be noted that these tests were performed at different strain amplitudes than those shown in Fig. 3.30. Figure 3.31a compares the axial and the shear modes for proportional test. Because the two loads are in-phase, the hysteresis loops for both the axial and the torsional modes start at the same point. After point 3, the compressive loading starts and the twinning process starts as well. Because twinning causes re-orientation of the lattice, it is expected that such re-orientation would influence the torsional mode behaviour as seen from the shear mode hysteresis in Fig. 3.31a. After point 4, the twinned lattices are in a favorable position to detwin by subsequent tensile

load. Also, it is seen that the detwinning continues after point 5, as the inflection point appears after point 1. This means that the detwinning will continue until the beginning of the next cycle. Comparison between the twinning and detwinning portions on the shear hysteresis in Fig. 3.31a and the other parts of the hysteresis loop suggests that these deformation mechanisms have an effect on the shear behaviour. In general, it can be said that if the axial behaviour shows twinning-detwinning characteristics then the shape of shear hysteresis becomes asymmetric. The proportional test in Fig. 3.30a supports this observation from another perspective. By analyzing the axial mode in Fig. 3.30a, it can be seen that the hysteresis of half-life cycle is significantly different than that of the second cycle. The twinning-detwinning deformation at half-life is not as pronounced as in the second cycle. Consequently, shear hysteresis of the half-life is different than that of the second cycle; while the former is fairly symmetric the latter is not. Figures. 3.30b and c show the cyclic behaviour of 45° and 90° out-of-phase loading tests. Similar observation as for the proportional test is observed in the out-of-phase tests. The axial mode hysteresis of the second cycle is similar to that of cyclic axial loading. However, the axial mode hysteresis became nearly linear at half-life. The shear hysteresis at second cycle is not symmetric in shape; however, it became symmetric at half-life. The same observation can be seen from Figs. 3.31b and b where twinning-detwinning portions on the shear hysteresis became similar to the opposite portions of the hysteresis curve at half-life. Of course, this is associated with less pronounced twinning-detwinning deformation on the half-life hysteresis of the axial mode. Ninety degrees out-of-phase loading causes the principal strain axes to rotate during cyclic loading. In some materials, this rotation results in additional hardening development which is different than that observed during uniaxial or multiaxial proportional cyclic loading [60]. To examine the hardening behaviour of AZ31B extrusion when subjected to multiaxial loading, the variation of axial and shear stress amplitudes

with cycling for different multiaxial tests, performed at the same strain amplitude but different phase angles, are shown in Figs. 3.33b and 3.34b. It is clear that the stress response from the 90° out-of-phase test is highest among the multiaxial tests. The 45° out-of-phase is next and finally the proportional test. Therefore, it can be said that AZ31B extrusion exhibits additional hardening due to nonproportionality.

The phase angle effect on fatigue life is illustrated in Fig. 3.35. In this figure, data from cyclic axial, torsional and multiaxial tests are included. It is worthwhile to note that the fatigue life in the multiaxial tests in Fig. 3.35 did not exceed 3×10^3 cycles. Therefore, observations made here cannot be generalized to cases with higher fatigue lives. While it is known [60, 131, 132] that the additional hardening that is caused by nonproportionality generally results in a detrimental effect on the fatigue life, the mechanical behaviour of magnesium during nonproportional loading is different. The additional hardening associated with the application of nonproportional loading is caused by dislocation-dislocation interaction; they are forced to move along all possible slip planes [133]. However, Fig. 3.35 shows that phase angle has no significant influence on the fatigue life. The limited number of slip systems in magnesium might be the reason behind this observation [97]. Also, the fact that the total energy densities for the tests that were performed at same axial and shear strain amplitudes but different phase angles are the same could explain the insignificant effect of phase angle on fatigue life.

3.5.4 Fatigue Cracking Behaviour

As mentioned previously, fatigue tests were stopped at an average of 50% force or torque drop. However, in the cases when fatigue cracks propagated along the longitudinal, i.e., axial, direction of the specimens, this criterion led to very long cracks. In fact, it was found

that all specimens that were tested under cyclic torsional loading develop longitudinal cracks. Therefore, by stopping cyclic torsional tests at 50% torque drop, specimens were found to have cracks with lengths in the order of 10-30 mm. On the other hand, all cyclic axial tests end with complete separation of the specimens. By applying the same failure criterion, multiaxial tests were found to show mixed cracking behaviour. To determine the fatigue life, axial and/or shear stress amplitudes were plotted versus the number of cycles as shown in Figs. 3.22b, 3.27b, 3.33b and 3.34b. It was found that all tests show similar behaviour before final failure. Regardless of the hardening behaviour, such plot always show a very sharp drop in the amplitude near the end of the test. Usually, this drop is followed by either a complete rupture of the specimen or a 50% load drop. Because the sharp drop in the stress amplitude forms nearly a vertical line, it was possible to identify the corresponding number of cycles at the beginning of this line. Using this procedure, the fatigue lives of all cyclic tests were determined. In addition, fatigue lives at 50% load drop are also reported as listed in Tables 3.6, 3.7 and 3.10. After that, a microscopic study was conducted as follows. First, crack initiation and propagation sites were identified. Then, crack measurement was performed using an optical microscope equipped with length measuring scale. In addition, SEM images from the fracture surfaces of selected specimens were taken using secondary electron detector of the scanning electron microscope. It should be noted that the fracture surfaces of the specimens were protected and saved in a sealed and dry cabinet to avoid any source of contamination before the SEM analysis. Figure 3.40 shows SEM images that illustrate the crack initiation and propagation sites on a fatigue test specimen. In most cases, semi-elliptical cracks were observed; therefore, the major, $2c$, and the minor, a, radii were measured. Two angles were measured: crack surface angle, α, and crack depth angle, ξ. These measurements are illustrated in Fig. 3.41. To measure the crack surface angle, the crack initiation and propagation sites were first identified. Then,

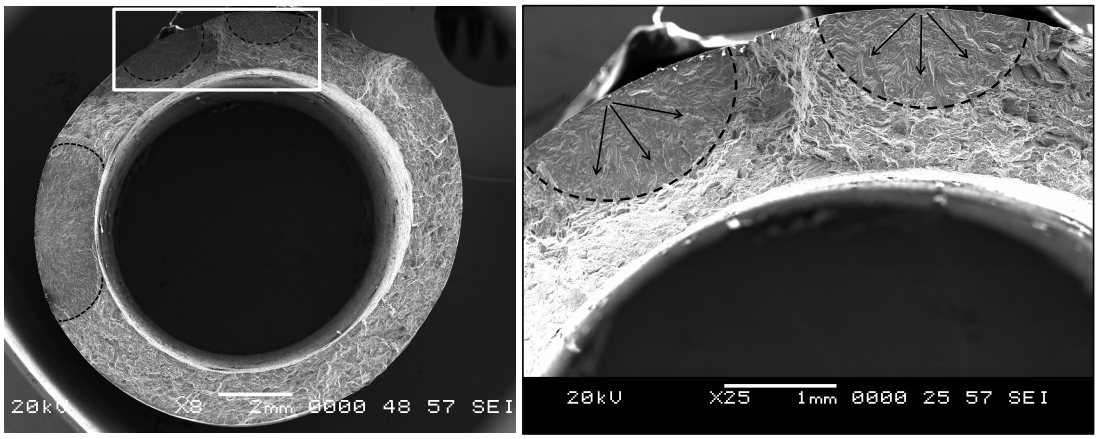

Figure 3.40: Scanning electron microscopy (SEM) images showing crack initiation and propagation sites. The specimen shown was tested under cyclic axial loading with a strain amplitude of 0.3%.

the projected crack height, h, and crack width, w, were measured as shown in Fig. 3.41. Finally, the crack surface angle was calculated as the inverse tangent of the ratio of the height to the width. A summary of these measurements is given in Table 3.11. The average radii were found to be $2c = 2.02 \pm 1.4$ mm and $a = 0.68 \pm 0.3$ mm. It is seen from this table that all cracks have $2c$ larger than a. Based on the definition of cracking behaviour that was discussed earlier in Section 2.2.2 and from Fig. 2.9 it is understood that AZ31B extrusions show Case A type cracking behaviour. It should be noted here that some specimens developed multiple cracks, however, only the largest crack was reported. The thickness of the specimen, t_w, was 1 mm. Also, all of the measurements in this table are based on 50% load drop.

Three fracture specimens that were tested under cyclic axial loading are shown in Fig. 3.42. The arrows in this figure indicate the location of crack initiation sites. It is seen from this figure that the orientations of the cracks are normal to the loading axis as listed

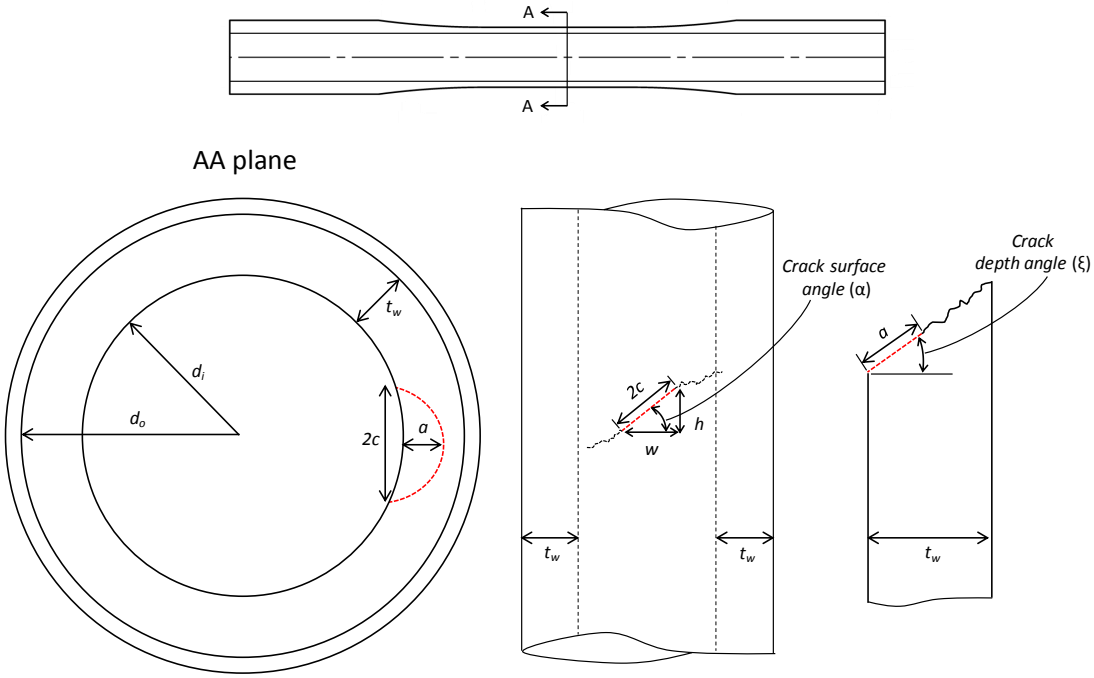

Figure 3.41: Schematics illustrating crack size and crack orientation measurements.

in Table 3.11. SEM images of the fracture surface of a specimen that was tested at 0.3% axial strain amplitude is shown in Fig. 3.43. From the low magnification image, three crack initiation and propagation sites are indicated. The shape of two of these cracks are clearly semi-elliptical. Striations and secondary cracks are observed from the high magnification image shown in Fig. 3.43b.

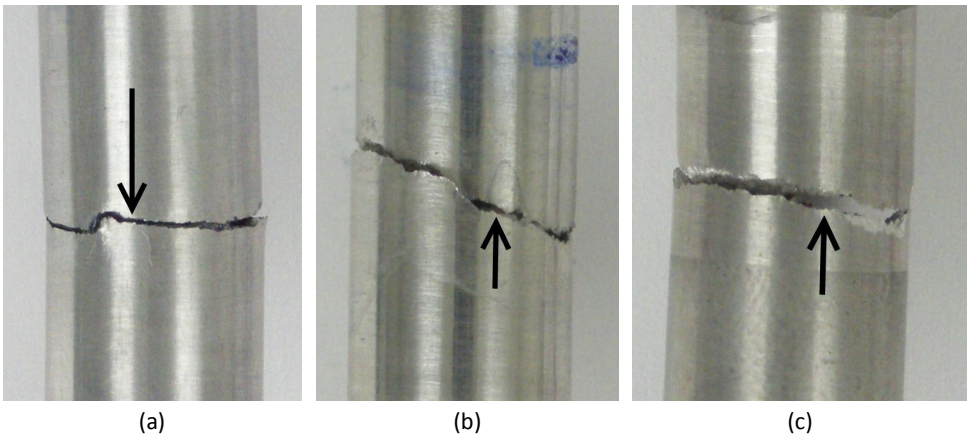

Figure 3.42: Fractured specimens from cyclic axial tests. a) $\varepsilon_a = 0.4\%$. b) $\varepsilon_a = 0.5\%$. c) $\varepsilon_a = 0.6\%$.

Table 3.11: Crack size and orientation of cyclic tests. ξ: crack depth angle, α: crack surface angle, CL: crack initiation location, OS: outer surface and IS: inner surface.

Test No.	ε_a (%)	γ_a (%)	$2c$ (mm)	a (mm)	ξ (°)	α (°)	CL
CA-02	0.600	0.000	3.61	0.33	0	0.00	OS
CA-03	0.500	0.000	1.10	t_w	0	0.00	OS
CA-07	0.400	0.000	1.39	0.77	0	0.00	IS
CA-08	0.400	0.000	1.28	0.58	0	0.00	IS

Continued on next page

Table 3.11 – continued from previous page

Test No.	ε_a (%)	γ_a (%)	$2c$ (mm)	a (mm)	$\xi(^\circ)$	α ($^\circ$)	CL
CA-12	0.267	0.000	1.25	t_w	0	0.00	IS
CS-07	0.000	0.900	1.07	0.47	0	90.00	IS
CS-11	0.000	0.600	1.10	0.40	0	90.00	IS
CS-13	0.000	0.450	1.50	0.26	0	90.00	IS
CS-15	0.000	0.424	1.96	0.42	0	90.00	IS
CS-19	0.000	0.400	1.02	t_w	0	50.20	IS
CS-20	0.000	0.384	1.66	t_w	0	37.80	IS
BA-0-1	0.500	0.649	1.71	NA	0	21.55	IS
BA-0-4	0.500	0.649	6.20	t_w	0	25.16	IS
BA-0-5	0.550	0.450	1.29	NA	0	47.80	IS
BA-0-6	0.550	0.440	1.42	t_w	0	29.63	OS
BA-0-7	0.300	0.800	1.95	NA	0	90.00	IS
BA-0-8	0.300	0.800	1.15	0.33	0	90.00	IS
BA-0-9	0.375	0.500	2.53	NA	inclined	42.11	IS
BA-0-10	0.375	0.500	0.98	t_w	0	32.61	IS
BA-0-11	0.300	0.454	1.65	NA	inclined	40.87	IS
BA-0-12	0.300	0.400	0.79	0.43	0	32.63	IS
BA-0-13	0.300	0.400	1.16	t_w	0	25.84	IS
BA-0-14	0.300	0.418	1.50	t_w	0	24.45	IS
BA-0-15	0.285	0.384	0.88	0.88	0	32.97	IS
BA-0-16	0.275	0.375	0.77	NA	0	36.60	IS
BA-45-1	0.500	0.750	2.71	0.46	0	31.10	IS

Continued on next page

Table 3.11 – continued from previous page

Test No.	ε_a (%)	γ_a (%)	$2c$ (mm)	a (mm)	$\xi(^\circ)$	α ($^\circ$)	CL
BA-45-2	0.300	0.800	1.63	0.31	0	90.00	IS
BA-45-3	0.550	0.450	0.77	0.81	inclined	28.80	IS
BA-45-5	0.375	0.500	3.00	t_w	0	36.46	IS
BA-45-6	0.375	0.500	0.68	t_w	0	21.67	IS
BA-90-1	0.500	0.750	4.92	0.29	0	4.57	OS
BA-90-2	0.500	0.750	3.77	t_w	0	46.60	IS
BA-90-3	0.550	0.450	1.83	t_w	0	21.98	IS
BA-90-5	0.550	0.450	4.42	0.39	0	6.40	OS
BA-90-6	0.300	0.800	1.28	0.45	0	90.00	IS
BA-90-7	0.300	0.800	2.04	0.41	0	90.00	IS
BA-90-8	0.375	0.500	4.90	0.29	0	36.10	IS
BA-90-9	0.300	0.800	1.50	NA	NA	90.00	IS
BA-90-10	0.300	0.800	1.66	0.62	inclined	32.2	IS
BA-90-11	0.375	0.500	2.04	0.73	0	10.14	IS

Monotonic and cyclic torsional specimens failed along the longitudinal direction, i.e., parallel to the basal plane. Metallographic analysis of the AZ31B extrusion in Fig. 3.3c shows that the extrusion process causes internal defects to align and some grains to elongate along the extrusion direction. This makes the longitudinal direction weaker than the transverse direction. The fact that the basal slip system requires the least shear stress could explain the shear cracking behaviour in AZ31B extrusions. Figure 3.44 shows a cracked specimen that was tested at 0.9% shear strain amplitude. The arrow indicates the location where

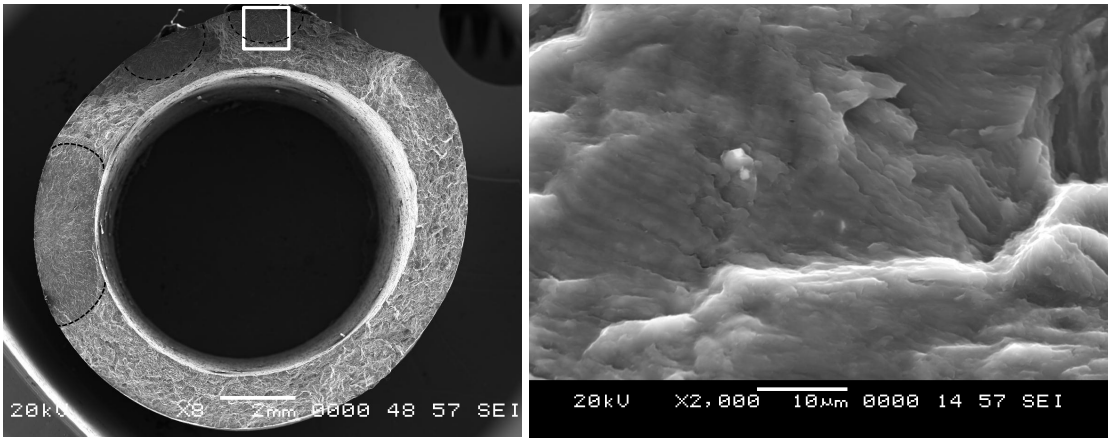

Figure 3.43: Fractured surface of axial specimen tested at $\varepsilon_a = 0.3\%$. a) Low magnification. b) High magnification at the location indicated by the white box.

the crack initiated. This figure shows a long longitudinal crack that has a length of more than 20 mm. An SEM image for a specimen that was tested at 0.45% shear strain amplitude is shown in Fig. 3.45; part of the crack propagation area is indicated by the dashed line. Because crack faces are scraping during the test it is expected that the crack surface will be featureless as shown in Fig. 3.45. Three fractured specimens that were tested under different multiaxial loading conditions are shown in Fig. 3.46. The arrows indicate the locations where fatigue cracks initiated. SEM images for two specimens that were tested under proportional and 45° out-of-phase multiaxial loading are shown in Figs. 3.47 and 3.48, respectively. These images indicate the crack initiation and propagation sites for each test. The cracks shown in these figures initiated from the outer surface and have semi-elliptical shape.

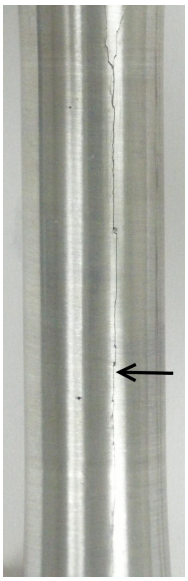

Figure 3.44: Fracture specimen from cyclic shear test. $\gamma_a = 0.9\%$

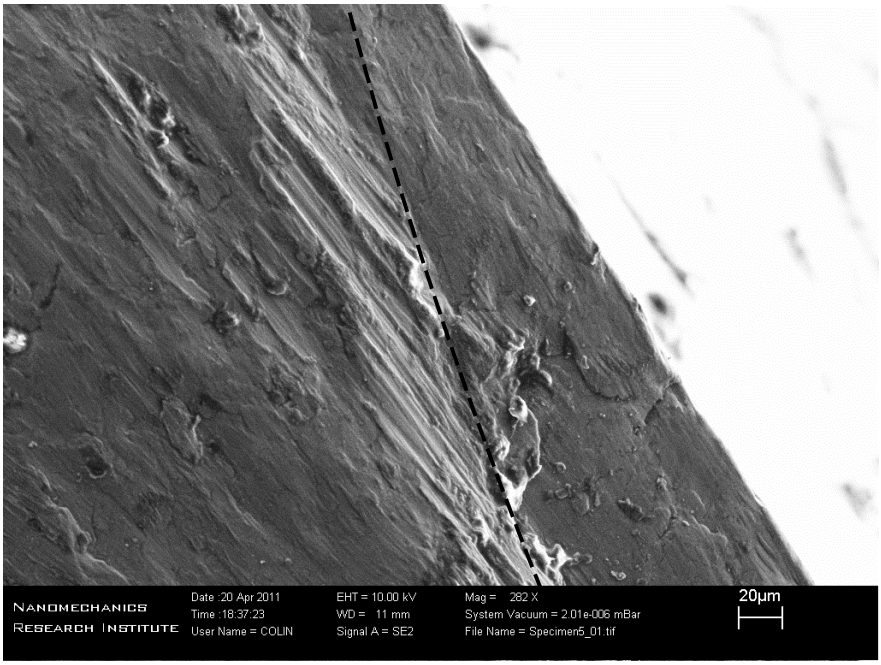

Figure 3.45: Fracture surface of shear specimen. $\gamma_a = 0.45\%$.

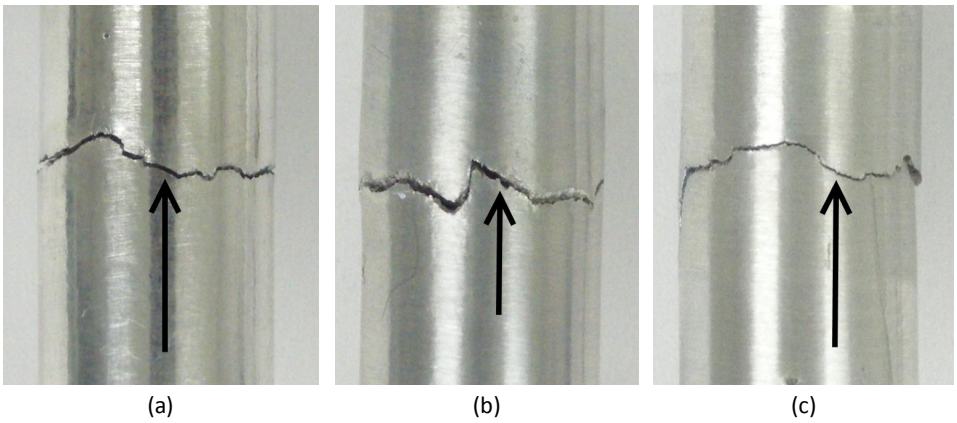

Figure 3.46: Fractured multiaxial test specimens. All tests were performed at $\varepsilon_a \approx 0.55\%$ and $\gamma_a \approx 0.55\%$.

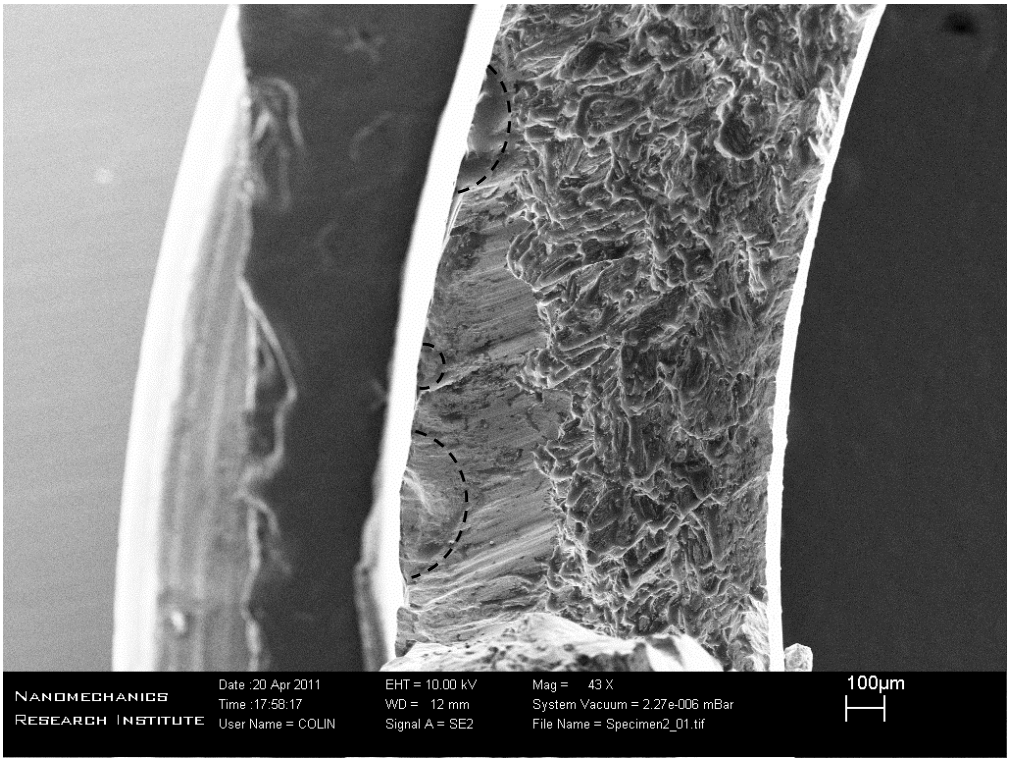

Figure 3.47: Fractured surface for multiaxial in-phase test. $\varepsilon_a = 0.375\%$ and $\gamma_a = 0.515\%$.

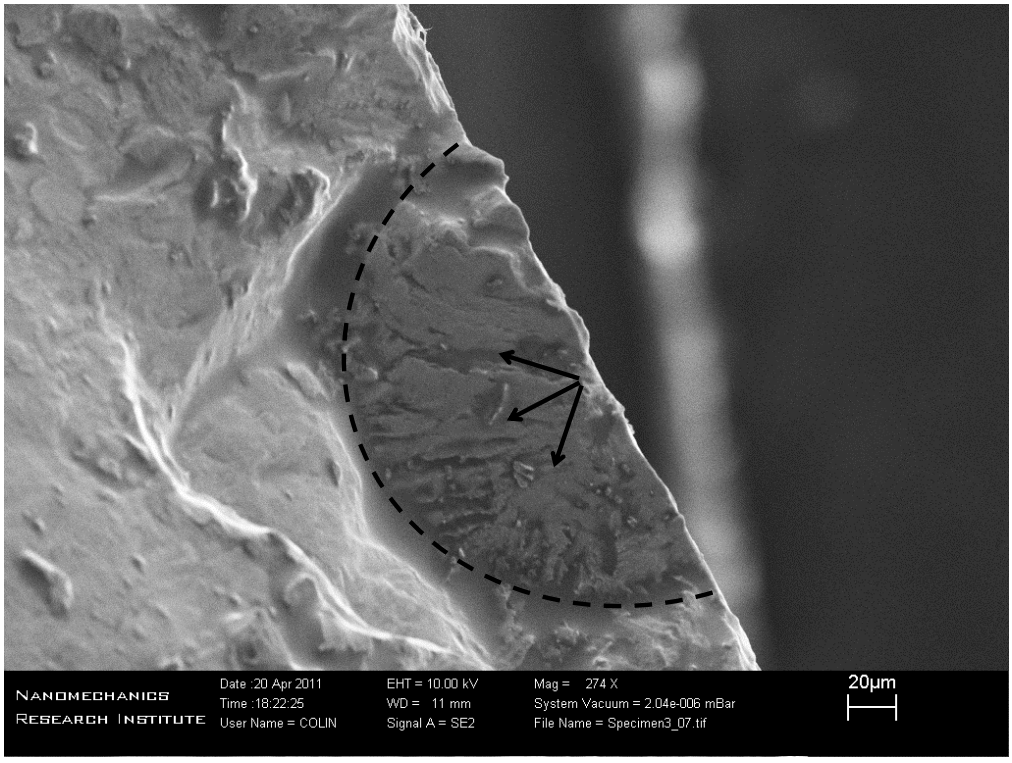

Figure 3.48: Fractured surface for multiaxial 45° out-of-phase test. $\varepsilon_a = 0.375\%$ and $\gamma_a = 0.515\%$.

3.6 Summary

Experimental analyses on the monotonic and cyclic behaviours of AZ31B extrusion were presented and discussed. Directional monotonic tensile and compressive tests showed that the material exhibits pronounced yield anisotropy due to the activation of $(10\bar{1}2)$ extension twinning. Sigmoidal post-yielding behaviour was observed in monotonic tensile and compressive tests at TD and LD, respectively. This behaviour was explained in terms of twinning, detwinning and slip deformation mechanisms. On the other hand, the stress-strain curve for monotonic torsional loading showed a linear hardening behaviour. Pseudoelasticity was observed in all monotonic tests. It was found that Weibul-type relation between the anelastic strain and true plastic strain could be used to predict the anelastic strain and simulate the loading-unlading hysteresis. Similar observations as for monotonic tensile and compressive tests were seen in cyclic axial test. Twinning deformation was activated in the compressive reversal which resulted in low yielding and low rate of hardening. Then, detwinning deformation starts at early stages of the tensile reversal. Once the detwinning was exhausted, an inflection point was observed in the hysteresis curve which was followed with a rapid rate of hardening. The yield asymmetry and the sigmoidal behaviour in the axial hysteresis loop are expected to have implications on whether or not Ramberg-Osgood equation can be used to model the axial hysteresis curve. Also, the significant positive mean stress that was mainly developed due to the yield asymmetry suggest an adoption of fatigue damage models that are capable of including such effect. Cyclic hardening was observed, especially at LCF regime. This hardening was associated with a significant decrease in the plastic strain energy. It was also found that the axial strain-life curve has a knee at 44×10^3 reversals and a pronounced plateau at the HCF regime. Such behaviour in the strain-life curve is expected to limit the applicability of

Coffin-Manson equation. The sum of the plastic and positive elastic axial energy density was fairly constant which suggests that energy-based fatigue damage could be used for fatigue life prediction. Unlike the axial loading, the cyclic shear behaviour of AZ31B was symmetric and no pronounced cyclic hardening was observed. However, the shear strain-life had a knee at 50×10^3 reversals. Similar to the cyclic axial loading, the variation of the sum of plastic and positive elastic shear strain energy densities was fairly constant. Multiaxial cyclic axial-torsional tests were performed at three different phase angles: 0, 45 and 90°. Based on the obtained results, four observations can be made. First, the axial mode showed the same characteristics as seen in cyclic axial tests. On the other hand, the shear hysteresis behaviour was seen to be influenced by the application of axial loading when twinning deformation was observed, especially in the early cycles. Second, comparison between stress amplitude variation with cycling of in-phase and out-of-phase specimens tested at same strain amplitudes shows that the latter have higher stress than the former. Therefore, it can be said that the material exhibits additional hardening due to nonproportionalily. This was evident from the variation of stress amplitude with cycling for multiaxial tests performed at the same strain amplitudes but different phase angle. Third, the phase angle had no pronounced effect on fatigue. Fourth, the sum of plastic and positive elastic axial and shear strain energy densities was fairly constant. Finally, fatigue cracking behaviour was examined on selected specimens. It was found that cyclic axial specimens failed on the plane of maximum normal stress/strain while cyclic shear specimens failed on the plane of maximum shear stress/strain. On the other hand, the failure planes of multiaxial specimens did not coincide with either the plane of maximum normal or shear stress/strain. In general, fatigue cracks started from the surface and had semi-elliptical shape. In addition, this analysis suggests that AZ31B extrusion show Case A cracking behaviour.

Chapter 4

Fatigue Modeling

This chapter consists of three sections. The first section discusses the cyclic stress-strain curves for axial and shear loading. The monotonic and the cyclic stress-strain curves are compared and the hardening due to the application of cyclic loading is revealed. Cyclic parameters for the Ramberg-Osgood equation are obtained and the applicability of this relation to model the cyclic hysteresis loop is investigated. The second section focuses on fatigue life modeling using both strain- and energy-based analyses. Necessary parameters and/or coefficients related to the fatigue life equations, such as the well-known Coffin-Manson, are obtained from strain- and energy-life curves. The third section discussed multiaxial fatigue life prediction methods. Two critical plane models that are strain-based, Smith-Watson-Topper (SWT) and Fatemi-Socie (FS), are considered. These two models were assessed based on their predictions of both fatigue life and cracking plane. The Jahed-Varvani (JV) energy model is used for the energy-based approach. Finally, a generalized energy-based model for fatigue life prediction is discussed.

4.1 Cyclic Stress-Strain Curves

4.1.1 Axial loading

Using the data from the half-life hysteresis curves, the cyclic stress-strain curve for cyclic axial loading was obtained and is shown in Fig. 4.1. The corresponding monotonic tensile and compressive stress-strain curves are also included in this figure for comparison. Because of cyclic asymmetry, the maximum and absolute minimum stresses are not coincident with the amplitude of stress. Figure 4.1 shows that the stress amplitude curve compared very well with the tensile monotonic stress-strain curve. This is not the case for the minimum stress curve and the compressive monotonic stress-strain curve. Hysteresis

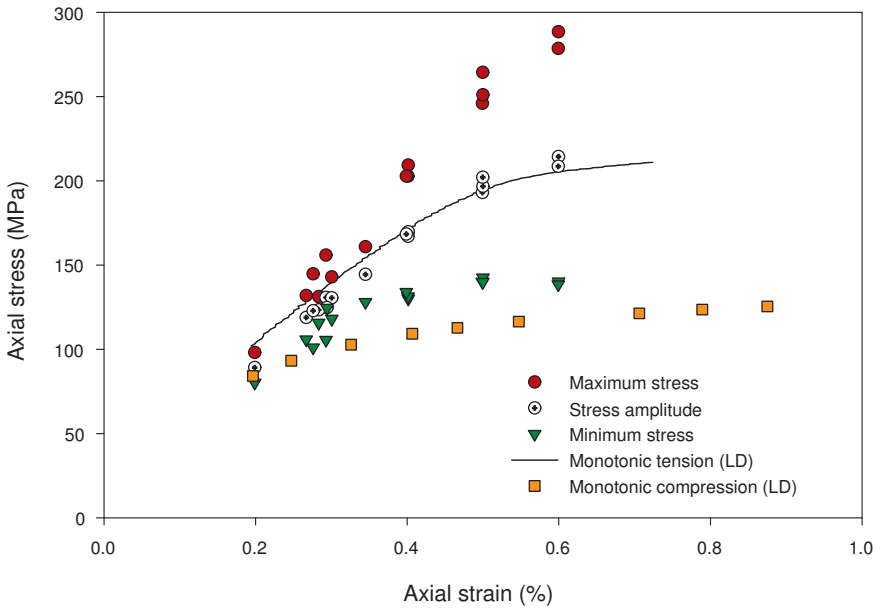

Figure 4.1: Cyclic axial stress-strain curve for AZ31B extrusion.

loops for different axial strain amplitudes are plotted in Fig. 4.2 to investigate the Mas-

ing behaviour for cyclic axial loading. This figure shows that AZ31B extrusion does not exhibit Masing behaviour when subjected to cyclic axial loading. This means that the Ramberg-Osgood relation and the hysteresis doubling principle cannot be used to model the hysteresis loops for axial loading. Nevertheless, in order to further verify this conclusion, Ramberg-Osgood's parameters were calculated using maximum and minimum stresses as well as stress amplitude as listed in Table 4.1. Using these parameters the hysteresis loop for 0.6% axial strain amplitude was modeled and compared to the experimental curve as shown in Fig. 4.3. Again, this figure shows that the Ramberg-Osgood equation cannot model the stress and the shape asymmetries in cyclic axial behaviour of AZ31B extrusion.

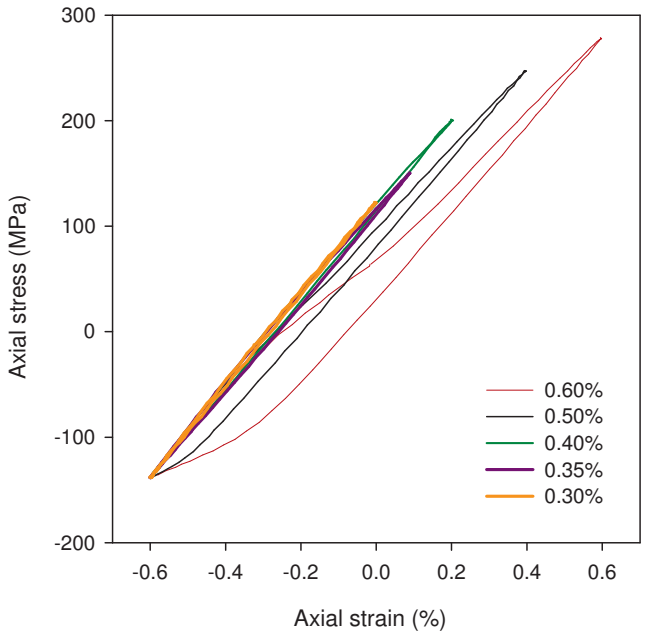

Figure 4.2: Investigation of Masing behaviour in cyclic axial loading.

Table 4.1: Cyclic parameters of Ramberg-Osgood relation for axial loading.

	K (MPa)	n
Using maximum stress	60,274	1.037
Using stress amplitude	9,608	0.738
Using minimum stress	623	0.285

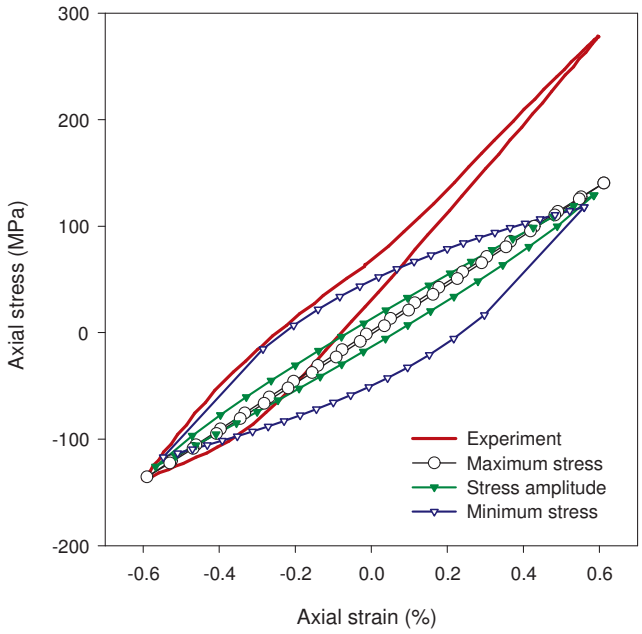

Figure 4.3: Modeling hysteresis loop for 0.6% axial strain amplitude using Ramberg-Osgood's parameters listed in Table 4.1.

Remarks

In the following, a curve fitting based modeling for cyclic axial hysteresis is presented. The purpose of this model is to provide a mathematical-based representation of the cyclic axial hysteresis. While cyclic plasticity can be used to model hysteresis loops for general loading conditions such as multiaxial, the proposed model is mainly based on curve fitting. The compressive and tensile reversals of the axial hysteresis curve have distinct behaviours due to the difference in the deformation mechanisms involved. By performing appropriate stress and strain translations, the two reversals for 0.6% axial strain amplitude hysteresis can be plotted as shown in Fig. 4.4. It is clearly seen from this figure that the compressive reversal has a power-like hardening. On the other hand, the tensile reversal has a sigmoid-type hardening. As a result, Ramberg-Osgood-Type fitting can be employed on the compressive reversal. The stress, σ_{cr}, and strain, ε_{cr}, for the compressive reversal in Fig. 4.4 are related to the maximum stress and strain as

$$\varepsilon_{cr} = \varepsilon_{max} - \varepsilon \tag{4.1}$$

$$\sigma_{cr} = \sigma_{max} - \sigma \tag{4.2}$$

The Ramberg-Osgood equation for the compressive reversal is defined as

$$\varepsilon_{cr} = \frac{\sigma_{cr}}{E_{hy}} + \left(\frac{\sigma_{cr}}{K_{hy}}\right)^{1/n_{hy}} \tag{4.3}$$

where E_{hy}, K_{hy} and n_{hy} are the modulus of elasticity, the cyclic strength coefficient and the cyclic strain hardening exponent calculated from the compressive reversal, respectively. By fitting Eq. 4.3 with the compressive reversal curve in Fig. 4.4, for the second cycle as well as for the half-life cycle, the parameters for the second and half-life cycles were found

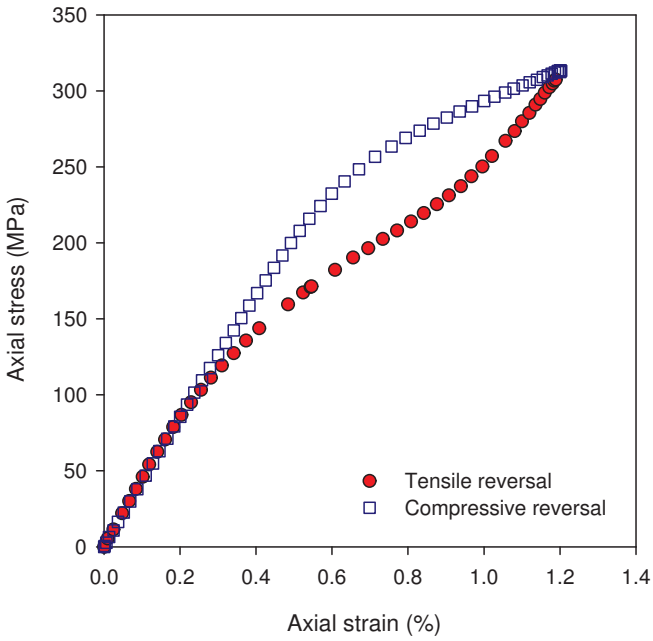

Figure 4.4: Tensile and compressive reversals of the second cycle for 0.6% strain amplitude.

as listed in Table 4.2. Two additional fittings were also performed for 0.4 and 0.26% strain amplitudes and their corresponding parameters are also listed in Table 4.2. Substitution of Eqs. 4.1 and 4.2 into Eq. 4.3 gives

$$\varepsilon = \varepsilon_{max} - \left(\frac{\sigma_{max} - \sigma}{E_{hy}}\right) - \left(\frac{\sigma_{max} - \sigma}{K_{hy}}\right)^{1/n_{hy}} \tag{4.4}$$

Because this formation is done for strain-controlled cyclic axial test, the maximum strain term in Eq. 4.4 can be replaced with the applied strain amplitude. Therefore, Eq. 4.4 can be rewritten as

$$\varepsilon = \varepsilon_{a} - \left(\frac{\sigma_{max} - \sigma}{E_{hy}}\right) - \left(\frac{\sigma_{max} - \sigma}{K_{hy}}\right)^{1/n_{hy}} \tag{4.5}$$

It was demonstrated in Section 3.4 that Weibull function could be used to correlate the sigmoidal relation between the anelastic and true plastic strains. However, it was found here that the Weibull function used in section 3.4 does not provide the best fit for the sigmoidal curve of the tensile reversal. As a result, a different sigmoid function was used. Defining the strain, ε_{tr}, and stress, σ_{tr}, for the tensile reversal as

$$\varepsilon_{tr} = \varepsilon - \varepsilon_{min} \tag{4.6}$$

$$\sigma_{tr} = \sigma - \sigma_{min} \tag{4.7}$$

The sigmoid function that was used to relate the strain to the stress is expressed as

$$\varepsilon_{tr} = \frac{\varepsilon^*_{tr}}{1 + \left(\frac{\sigma_{tr}}{\sigma^*_{tr}}\right)^{m^*}} \tag{4.8}$$

where ε^*_{tr},σ^*_{tr} and m^* are fitting constants. To fit Eq. 4.8, the stress, σ_{tr} was considered as the independents variable. The fitting parameters for Eq. 4.8 are listed in Table 4.3 for

the second and half-life cycles. Substitution of Eqs. 4.6 and 4.7 into Eq. 4.8 gives

Table 4.2: Parameters for Eq. 4.3.

ε_a (%)	Cycle	E_{hy}(GPa)	K_{hy}(MPa)	n_{yh}
0.60	Second	41.56	596.85	0.121
	Half-life	41.56	622.21	0.059
0.40	Second	43.12	466.87	0.08
	Half-life	43.12	362.70	0.009
0.26	Second	44.57	426.70	0.086
	Half-life	44.57	252.03	0.00072

$$\varepsilon = \varepsilon_{min} + \frac{\varepsilon^*_{tr}}{1 + \left(\frac{\sigma - \sigma_{min}}{\sigma^*_{tr}}\right)^{m^*}}, \text{ for } \sigma > \sigma_{min} \tag{4.9}$$

Again, because this formation is done for strain-controlled test, Eq. 4.9 can be rewritten in terms of the applied strain amplitude as

$$\varepsilon = \frac{\varepsilon^*_{tr}}{1 + \left(\frac{\sigma - \sigma_{min}}{\sigma^*_{tr}}\right)^{m^*}} - \varepsilon_a, \text{ for } \sigma > \sigma_{min} \tag{4.10}$$

Using Eqs. 4.5 and 4.10 the compressive and tensile reversals for 0.6, 0.4 and 0.26% strain amplitudes were evaluated as shown in Figs. 4.5-4.7. It is seen from these figures that the Ramberg-Osgood- and the sigmoid-type fittings for the compressive and tensile reversal are in good agreement with the experimental results. However, it is seen from Fig. 4.5a that the yield stress and the inflection point predicted by the sigmoid function do not match those in the experimental curve. It is worth mentioning that the fitting constants for the half-life hysteresis at 0.4 and 0.26% may not be unique. The hysteresis loops for these amplitudes are fairly linear. Therefore, it is expected that there are threshold values for the fitting constants after which Eqs. 4.5 and 4.10 start to predict linear hardening. Fig. 3.20 shows that the hardening behaviour of the axial hysteresis depends on the applied strain as well

as the cycle's number, i.e., second or half-life cycle. This can be seen from Tables 4.2 and 4.3 as the values of all fitting constants, except for E_{hy}, change with respect to both the strain amplitude and the cycle's number. If these constants were to be functions of the applied strain amplitude, then, five equations, one for each constant, are needed to model the hysteresis at second cycle. Similar number of equations is required to model the hysteresis at half-life. Further analysis is required to investigate the dependency of each constant on the strain amplitude and the cycle's number.

Table 4.3: Parameters for Eq. 4.8.

ε_a (%)	Cycle	ε^*_{tr}	σ^*_{hy}(MPa)	m^*
0.60	Second	0.0280	358.7	-1.860
	Half-life	0.0388	801.6	-1.310
0.40	Second	0.0213	407.2	-1.361
	Half-life	0.2290	7130.0	-1.091
0.26	Second	0.0371	1103.0	-1.108
	Half-life	40.81	1273×10^3	-1.042

4.1.2 Shear loading

The cyclic stress-strain curve for shear loading is shown in Fig. 4.8. Because the cyclic shear behaviour is symmetric, it is seen from this figure that the maximum and the absolute minimum stresses as well as the stress amplitude curves are all coincident. Therefore, it is reasonable to fit the cyclic shear stress-strain curve with the Ramberg-Osgood relation as shown in Fig. 4.8. The cyclic shear hardening coefficient, $K_s^{'}$, and the cyclic shear hardening exponent, $n_s^{'}$, were found to be 226.9 MPa and 0.2442, respectively. Also, the monotonic shear stress-strain curve is compared to the cyclic shear stress-strain curve in Fig. 4.9. This comparison shows that the difference between the two curves is small. Yet,

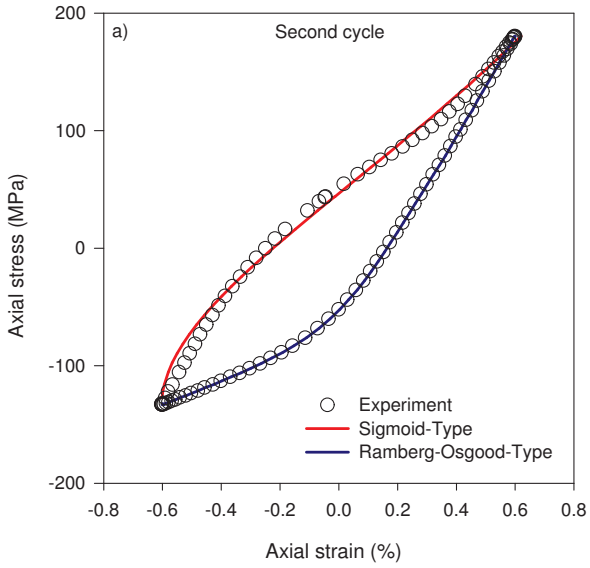

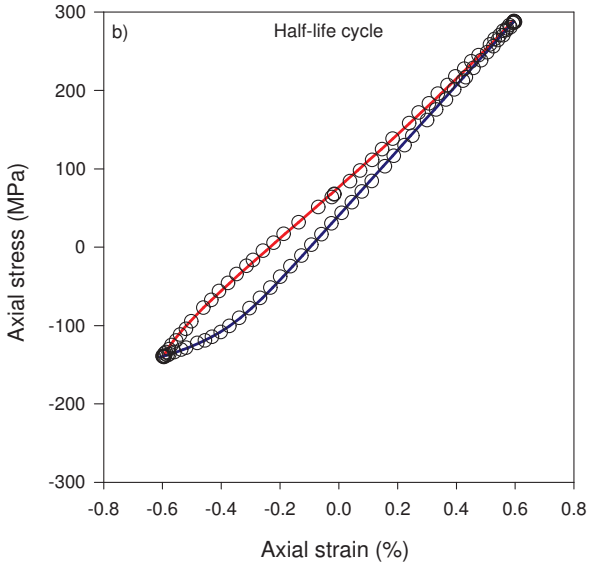

Figure 4.5: Modeling 0.6% strain amplitude axial hysteresis using Ramberg-Osgood- and sigmoid-types equations. a) Second cycle. b) Half-life cycle.

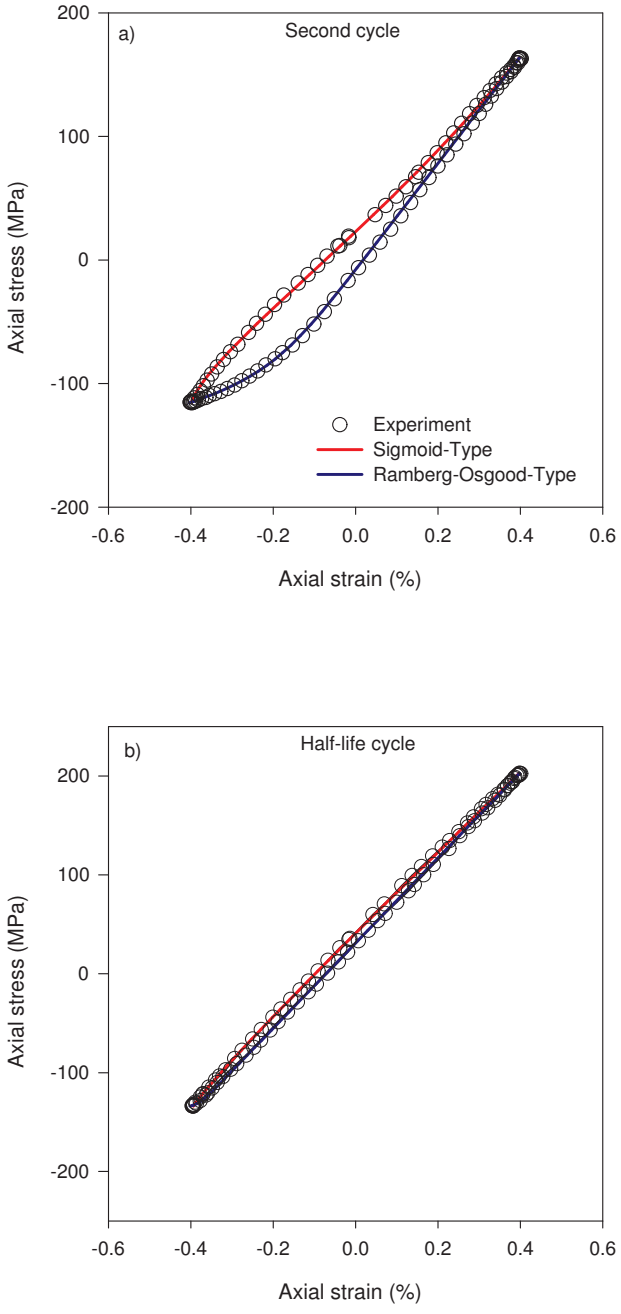

Figure 4.6: Modeling 0.4% strain amplitude axial hysteresis using Ramberg-Osgood- and sigmoid-types equations. a) Second cycle and b) Half-life cycle.

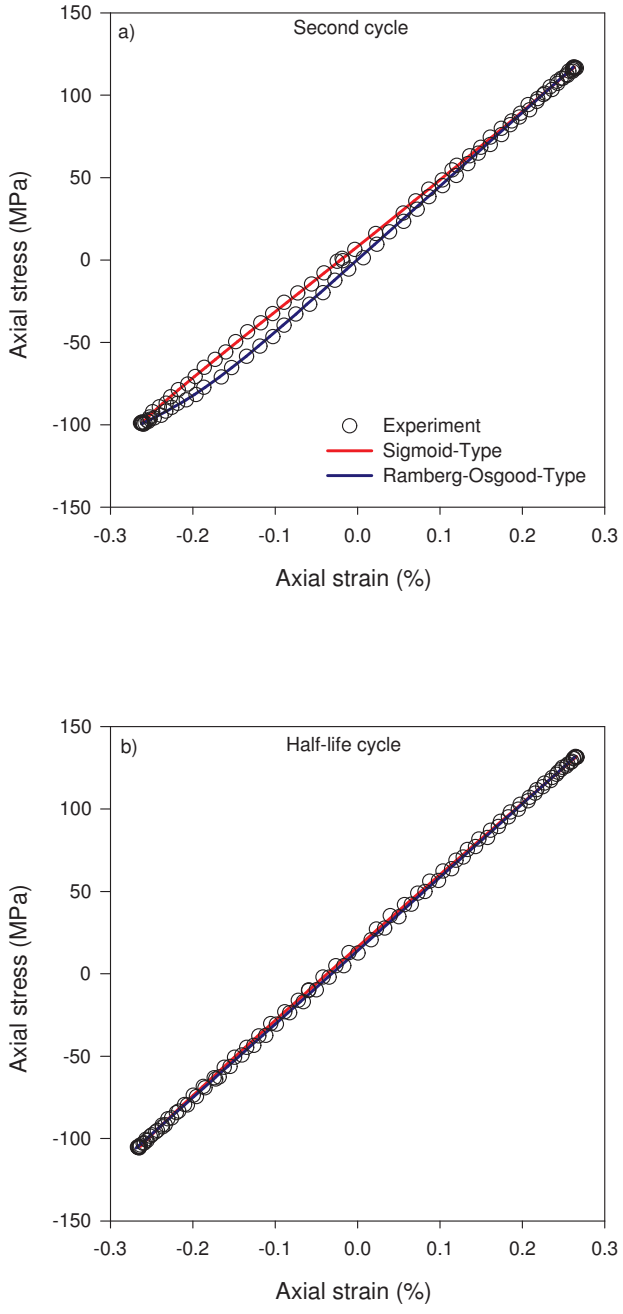

Figure 4.7: Modeling 0.26% strain amplitude axial hysteresis using Ramberg-Osgood- and sigmoid-types equations. a) Second cycle and b) Half-life cycle.

as the stress from the cyclic curve is higher than that from the monotonic one, it can be said that AZ31B extrusion cyclically hardens due to the application of cyclic shear loading. The hardening increases with the shear strain, reaching a maximum difference of 10% at a shear strain of 1.7%. The Masing behaviour of AZ31B extrusion is illustrated in Fig. 4.9a. This

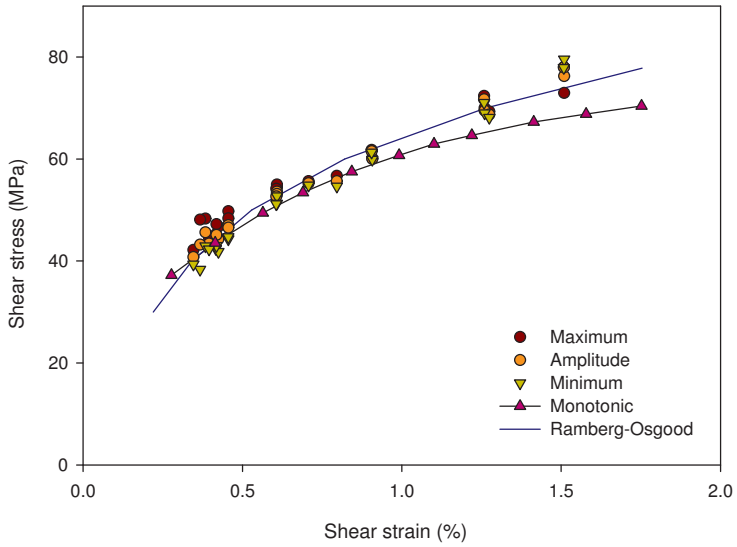

Figure 4.8: Cyclic stress-strain curve for pure shear loading.

figure shows that the Masing hypothesis is not perfectly obeyed, especially at low strain amplitudes. As mentioned earlier, the cyclic Ramberg-Osgood's parameters were evaluated from the cyclic shear stress-strain curve. Figure 4.9b compares the Ramberg-Osgood's predictions with the experimental hysteresis for three different shear strain amplitudes. This figure shows that the cyclic behaviour in shear loading can be predicted using the cyclic Ramberg-Osgood's relation with reasonable accuracy. Two parameters can be used to assess the accuracy of Ramberg-Osgood prediction: stress and plastic strain energy density. Predictions of these parameters using Ramberg-Osgood are compared with experimental values in Table 4.4. It is seen from this table that the predicted maximum and minimum

stresses compared very well with the experimental results. On the other hand, the difference between the predicted and the experimental plastic strain energy densities varies from 19 to 39%. The Ramberg-Osgood equation overestimates the plastic strain energy, which can be clearly seen from Fig. 4.9b. Although AZ31B extrusion does not perfectly obey the Masing

Table 4.4: Stress response and plastic strain energy densities for three different shear strain amplitudes. Comparison between experimental and Ramberg-Osgood's predictions. W_p in (MJ/m^3) and τ in (MPa).

		Ramberg-Osgood	Experiment	Difference (%)
1.50%	W_p	1.84	1.54	19.18
	τ_{max}	74.21	79.54	6.70
	τ_{min}	-74.25	-72.95	1.78
0.80%	W_p	0.61	0.43	39.35
	τ_{max}	59.52	54.63	8.95
	τ_{min}	-59.73	-56.67	5.39
0.36%	W_p	0.10	0.08	23.47
	τ_{max}	41.79	38.31	9.08
	τ_{min}	-41.78	-48.09	13.11

hypothesis, predictions using Ramberg-Osgood are close to the experimental results. As a result, the shear response of AZ31B extrusion can be predicted using its cyclic stress-strain curve and a simple deformation plasticity rule as described by Jahed and Dubey [134]. The same method can be used to find strain energy densities [135].

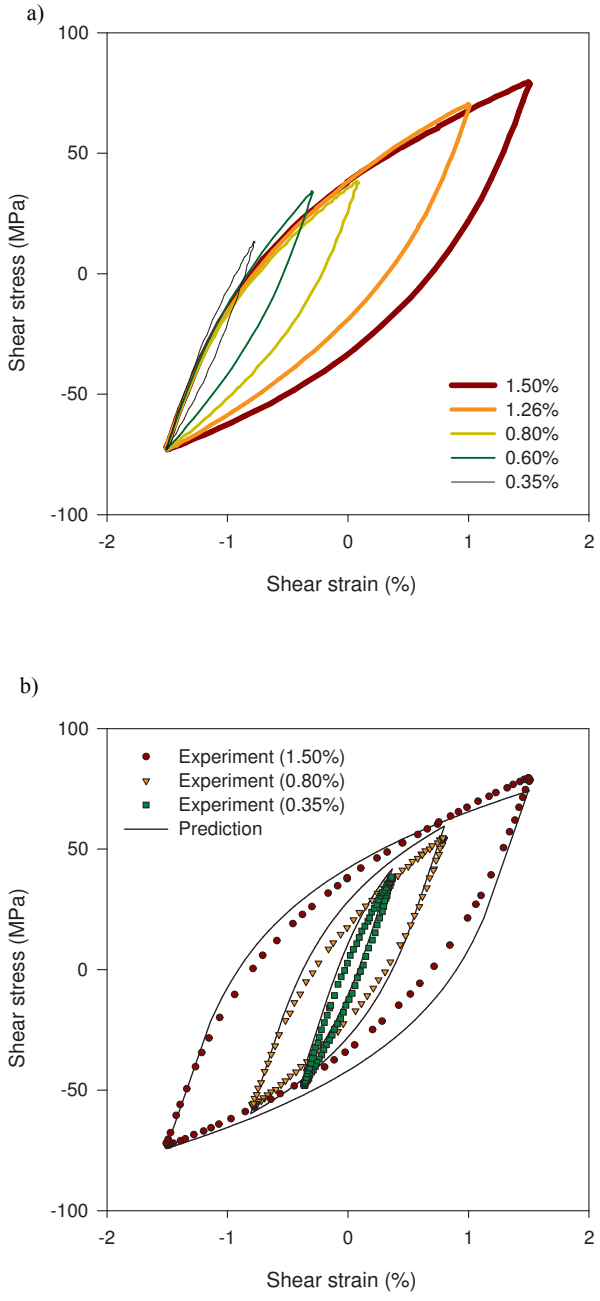

Figure 4.9: Cyclic shear behaviour. a) Masing behaviour. b) Prediction of cyclic shear hysteresis using cyclic Ramberg-Osgood relation.

4.2 Fatigue Life Equations

4.2.1 Standard Coffin-Manson Equations for Strain-Based Approach

The axial strain-life curve shown in Fig. 3.21 suggests that AZ31B extrusion has a fatigue limit at about 0.2% strain. Fittings of axial elastic and plastic parts of the Coffin-Manson's equation are shown in Fig. 4.10. From this figure, the axial strain-life equation was found to be

$$\varepsilon_a = \frac{495.82}{43.72 \times 10^3}\left(2N_f\right)^{-0.115} + 1.589\left(2N_f\right)^{-0.939} \tag{4.11}$$

The Coffin-Manson and the experimental axial strain-life curves are compared in Fig. 4.10c. This comparison shows that the Coffin-Manson equation cannot model a strain-life curve with a sharp knee and a pronounced plateau. Instead, only the LCF data can be fitted with the Coffin-Manson equation. The shear strain-life curve in Fig. 3.26 suggests that AZ31B extrusion has a fatigue limit at about 0.35% shear strain. Analogous to cyclic axial loading, fittings of the shear elastic and plastic parts of Coffin-Manson's equation are shown in Fig. 4.11. The corresponding shear-life equation was found to be

$$\gamma_a = \frac{102.7}{15.52 \times 10^3}\left(2N_f\right)^{-0.0656} + 0.114\left(2N_f\right)^{-0.405} \tag{4.12}$$

The predicted and experimental shear strain-life curves are compared in Fig. 4.11c. Similar to the axial case, Coffin-Manson's relation is incapable of modeling the whole strain-life curve, especially at HCF.

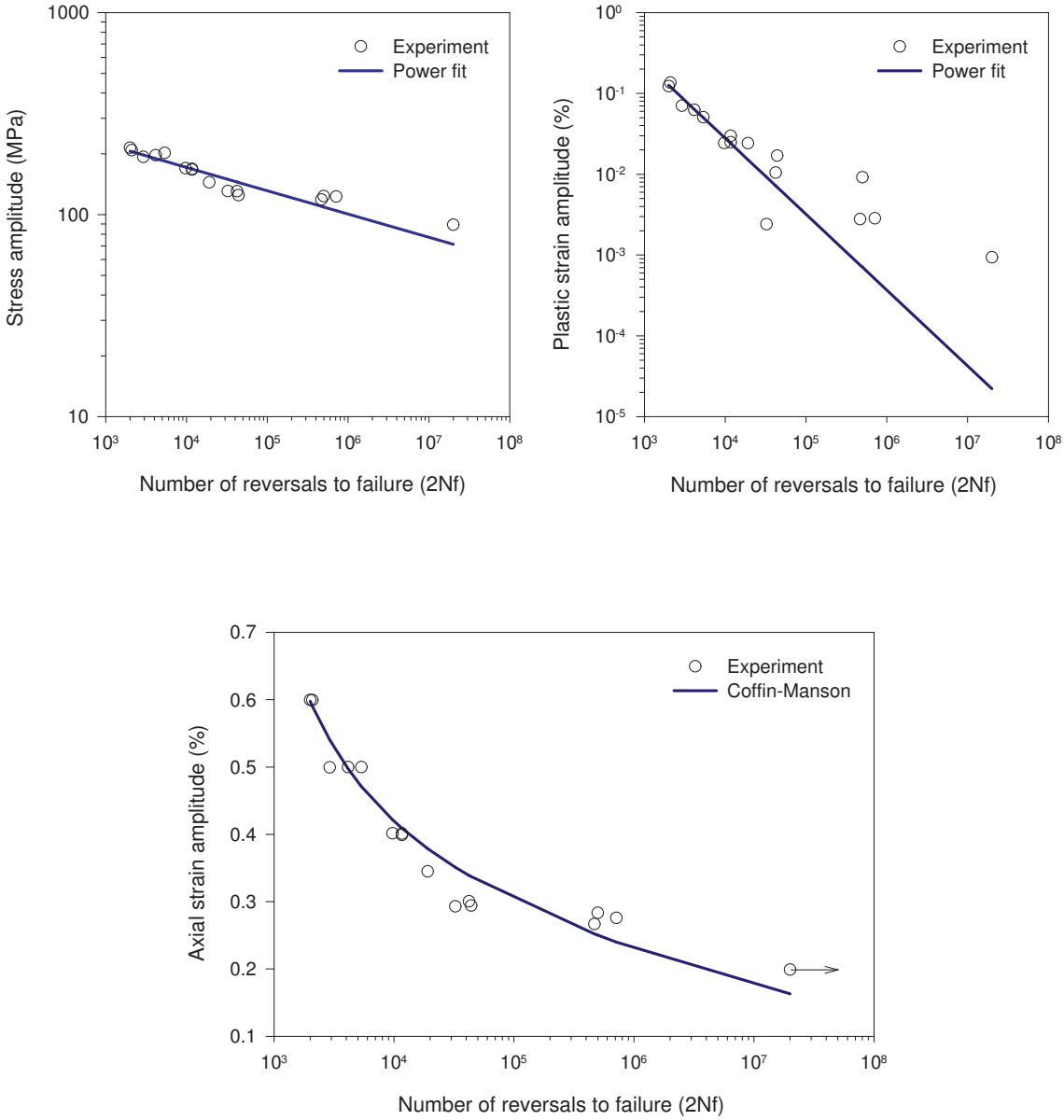

Figure 4.10: Coffin-Manson fitting for cyclic axial loading, Eq. 4.11.

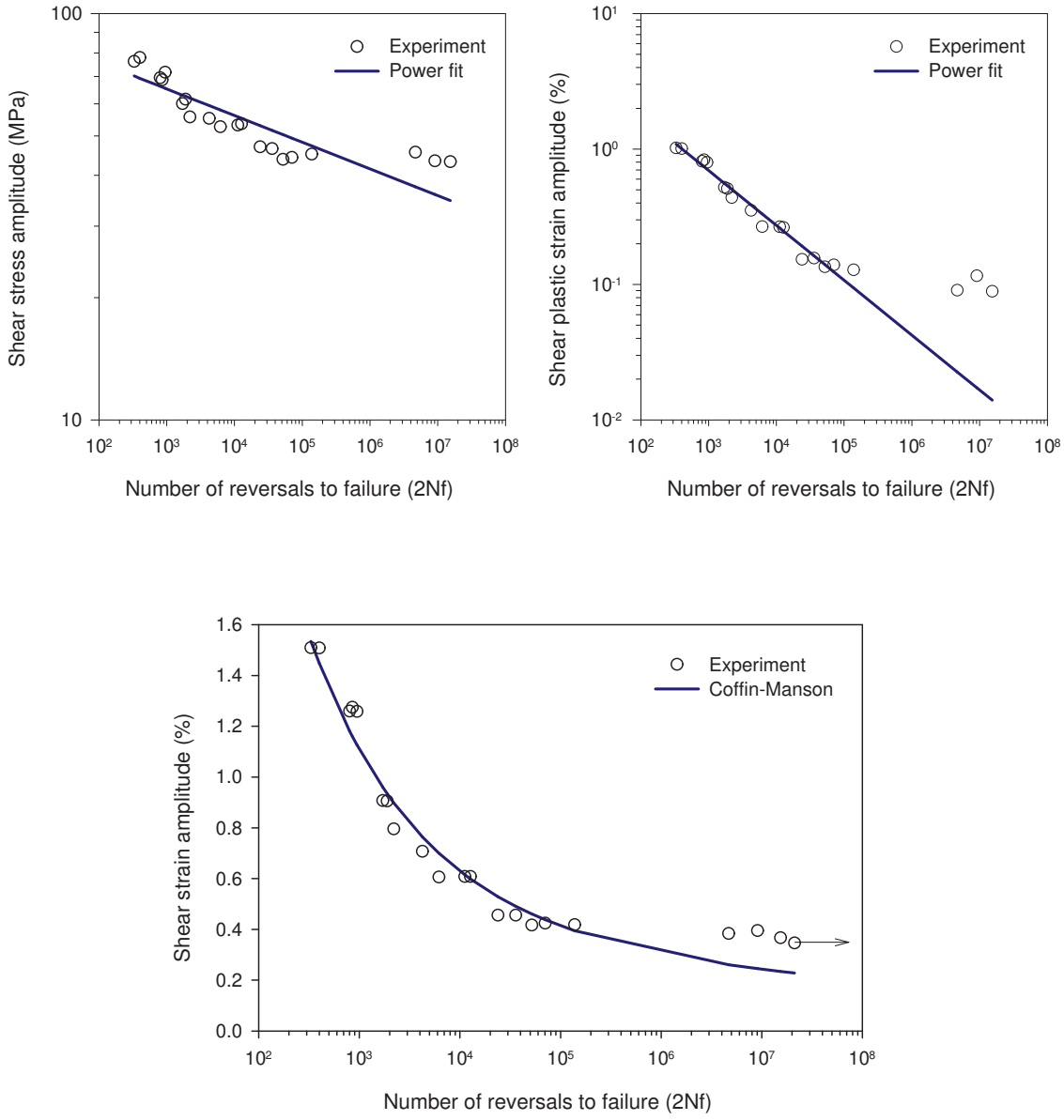

Figure 4.11: Coffin-Manson fitting for cyclic shear loading, Eq. 4.12.

4.2.2 Standard Coffin-Manson-Type Equations for Energy-Based Approach

Coffin-Manson-Type equations, Eqs. 2.58 and 2.59, can be used to model axial and shear energy-life curves. Modeling for the axial energy-life curve is shown in Fig. 4.12 and the corresponding axial energy-life equation was found to be

$$\Delta W_A = 12.18\big(N_f\big)^{-0.377} + 971.1\big(N_f\big)^{-1.139} \tag{4.13}$$

The comparison between the experimental and predicted energy-life curve is shown in Fig. 4.12c. Again, the same issue as for axial strain-life is seen. The axial energy-life curve has a knee and the bilinearity of the fatigue life curve causes difficulties in fitting the data with a Coffin-Manson-Type equation. The same procedure was followed for shear loading. Figure 4.13 shows the modeling of the shear energy-life curve. The corresponding shear energy-life equation was found to be

$$\Delta W_T = 0.564\big(N_f\big)^{-0.212} + 30.85\big(N_f\big)^{-0.571} \tag{4.14}$$

This equation is compared with the experimental energy-life curve in Fig. 4.13c. The shear energy-life curve is similar to the strain-life curve as both curves have knees and show bilinear behaviour.

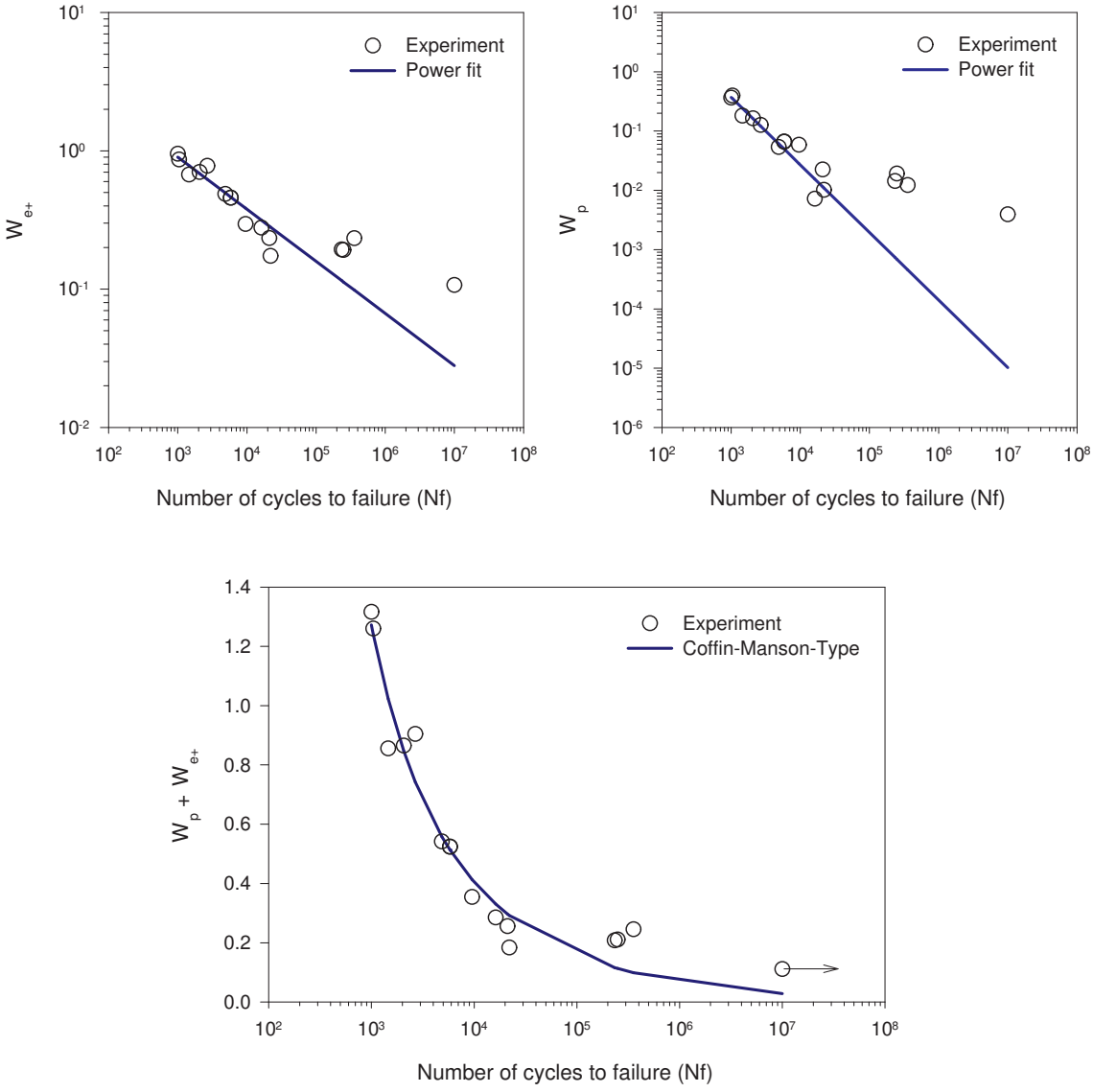

Figure 4.12: Axial energy-life curve modeling using Eq. 4.13. Energy in (MJ/m^3).

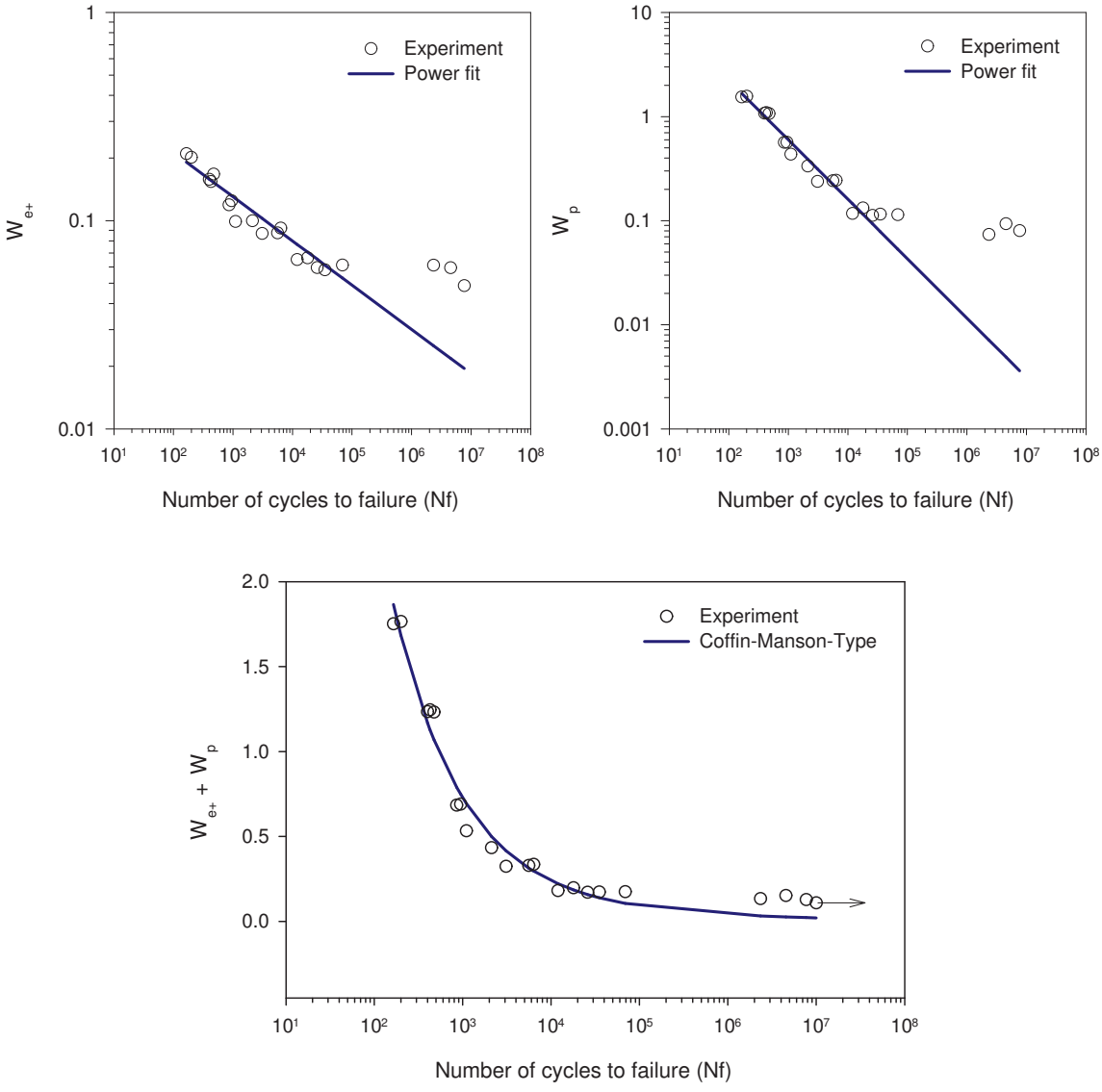

Figure 4.13: Shear energy-life curve modeling using Eq. 4.14. Energy in (MJ/m^3).

4.2.3 Coffin-Manson-Type Equations for LCF

It is clear from the previous section that Coffin-Manson type equations cannot be used to model the whole fatigue life curve of AZ31B extrusion. The bilinearity of the strain-life curve has been observed by many researchers for AZ31, AZ31B and AZ61 extrusions, and AZ91 diecasting [89, 91, 93, 95, 112]. In fact, this bilinearity is not special to magnesium alloys. The knee in fatigue life curve has been observed in many alloys such as TiNi shape memory alloys at 8×10^4 reversals [136], normalized 1045 steel at 10^6 reversals [137] and annealed 316LN stainless strain at 2×10^6 cycles [138]. These studies suggest that only the data before the knee should be fitted with Coffin-Manson equation. After the knee, the relation between the applied strain and fatigue life is critical. In average, 6% change in the strain amplitude results in approximately 40 and 50% change in the fatigue life for axial and shear loading, respectively. Because only two run-outs tests are available for axial and shear loading, it is hard to identify the strain levels below which the life can be assumed as infinite. Therefore, addition testing is required to obtain safe fatigue limits for each loading mode.

4.2.3.1 Strain-Based

Fittings for the LCF data for the axial and shear strain-life curves using Coffin-Manson's equations are shown in Figs. 4.14 and 4.15, respectively. The corresponding Coffin-Manson equations for axial and shear loading were found to be

$$\varepsilon_a = \frac{723.5}{43.72\times10^3}\left(2N_f\right)^{-0.159} + 0.252\left(2N_f\right)^{-0.718}, \text{ for } 2N_f \le 44\times10^3 \tag{4.15}$$

$$\gamma_a = \frac{142.82}{15.54\times10^3}\left(2N_f\right)^{-0.11} + 0.131\left(2N_f\right)^{-0.427}, \text{ for } 2N_f \le 50\times10^3 \tag{4.16}$$

It is seen by comparing Fig. 4.14 with 4.10, and Fig. 4.15 with 4.11, that a better fitting for the LCF is achieved by considering the LCF data only.

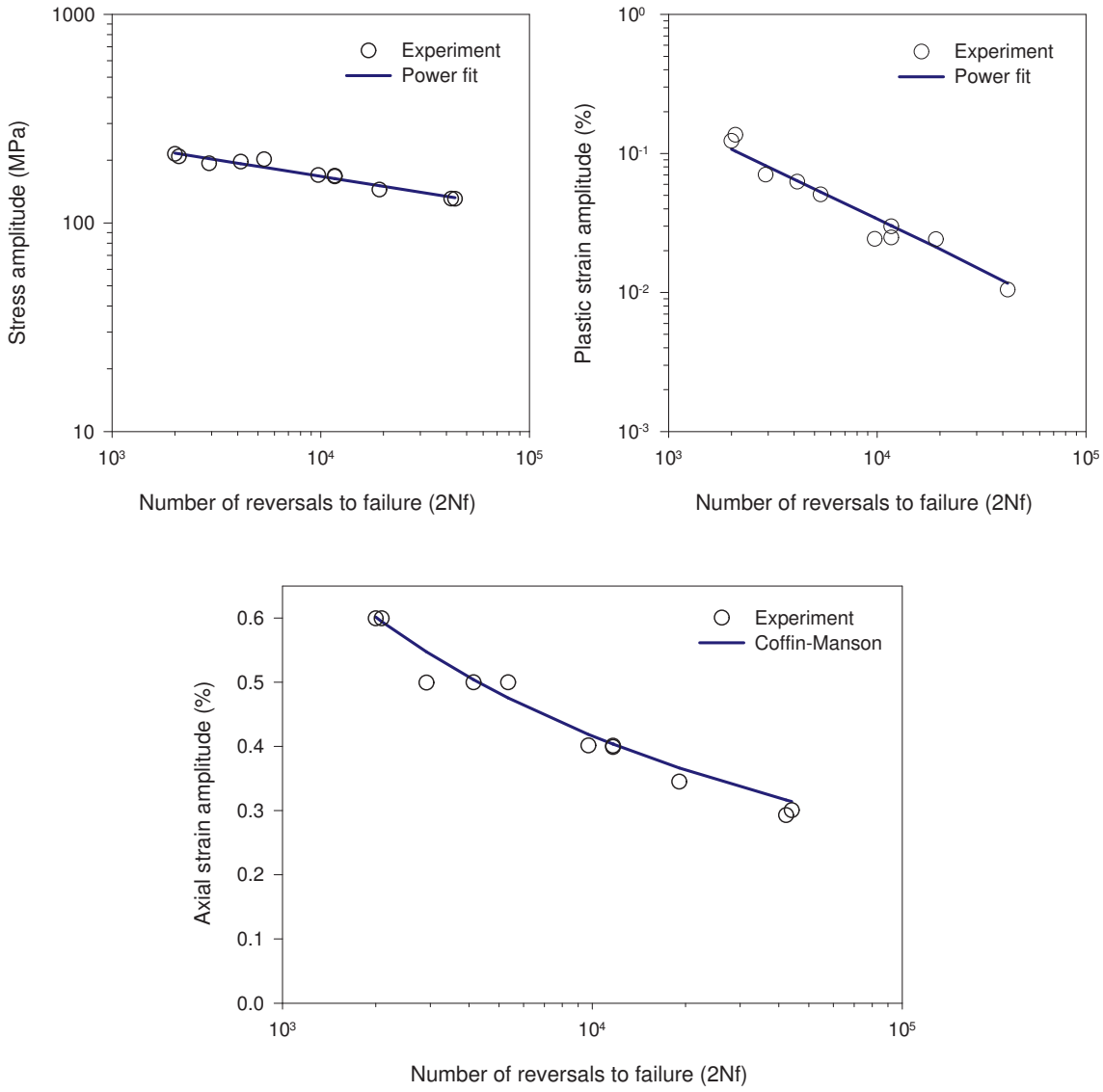

Figure 4.14: Coffin-Manson fitting for LCF data of axial strain-life curve, Eq. 4.15.

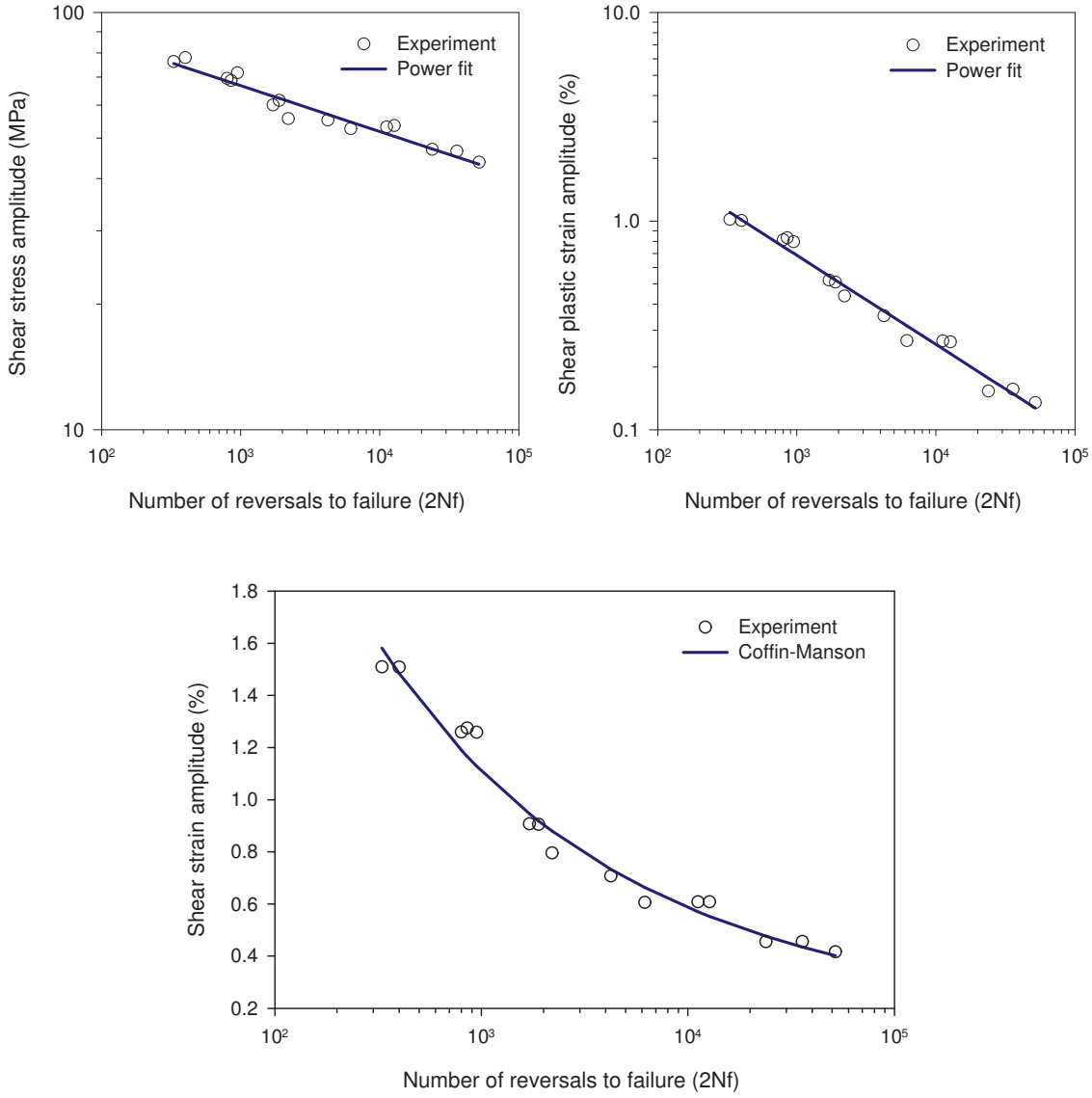

Figure 4.15: Coffin-Manson fitting for LCF data of shear strain-life curve, Eq. 4.16.

4.2.3.2 Energy-Based

By following exactly the same procedure as for the strain-based approach, energy-life equations for axial and shear loading were obtained for the LCF regime. The axial and shear energy-life curves for LCF data are shown in Figs. 4.16 and 4.17, respectively. The corresponding Coffin-Manson-Type equations for axial and shear energy-life were found to be

$$\Delta W_A = 20.29\big(N_f\big)^{-0.44} + 510.74\big(N_f\big)^{-1.052}, \text{ for } N_f \leq 22 \times 10^3 \tag{4.17}$$

$$\Delta W_T = 0.67\big(N_f\big)^{-0.242} + 27.72\big(N_f\big)^{-0.56}, \text{ for } N_f \leq 25 \times 10^3 \tag{4.18}$$

Similar to the strain-based situation, it is seen from Figs. 4.16 and 4.17 that by considering only the LCF data, fitting of the experimental LCF data in the energy-life curves was improved compared to that shown in Figs. 4.12 and 4.13.

4.3 Multiaxial Fatigue Life Prediction

Cyclic axial and shear as well as combined axial-torsional cyclic behaviours were discussed in Chapter 3. From a mechanistic view point, mean stress was found to be significant in cyclic axial behaviour of AZ31B extrusion, and this was related to stress symmetry and cyclic hardening. Therefore, damage parameters that incorporate the maximum normal stress term are preferable because it can include cyclic hardening and mean stress effects. It was found that phase angle has no effect on fatigue life, hence, an explicit term that account for phase angle effect in the damage parameter is not needed. Fatigue life modeling for uniaxial loading, i.e., for cyclic axial and shear loadings, was investigated in the previous section. It was found that strain- and energy-life curves for AZ31B extrusion have knees and pronounced plateaus in the HCF regime. Therefore, fatigue life curves were fitted using the

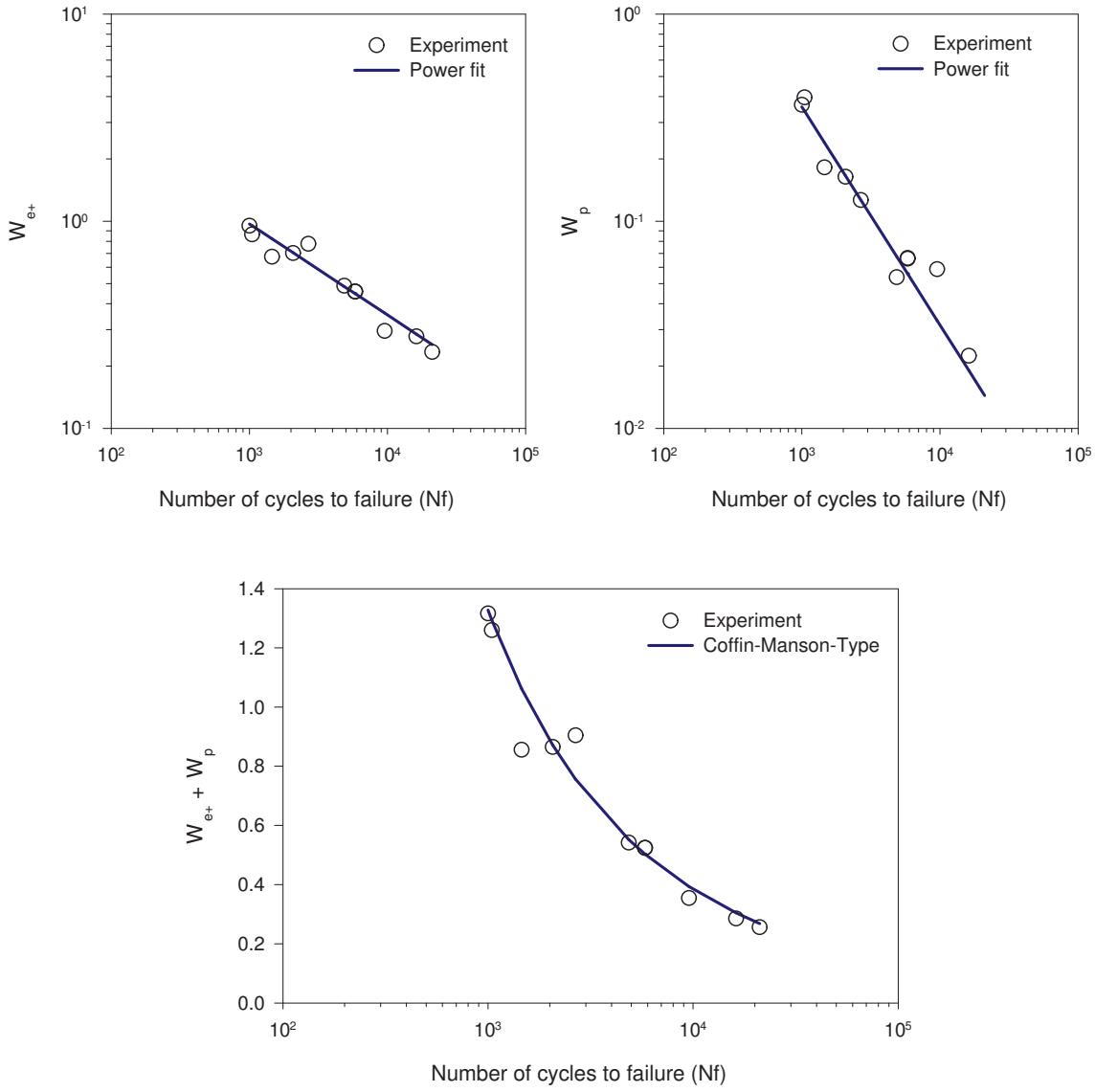

Figure 4.16: Coffin-Manson-Type fitting for LCF data of axial energy-life curve Eq. 4.17. Energy in (MJ/m^3).

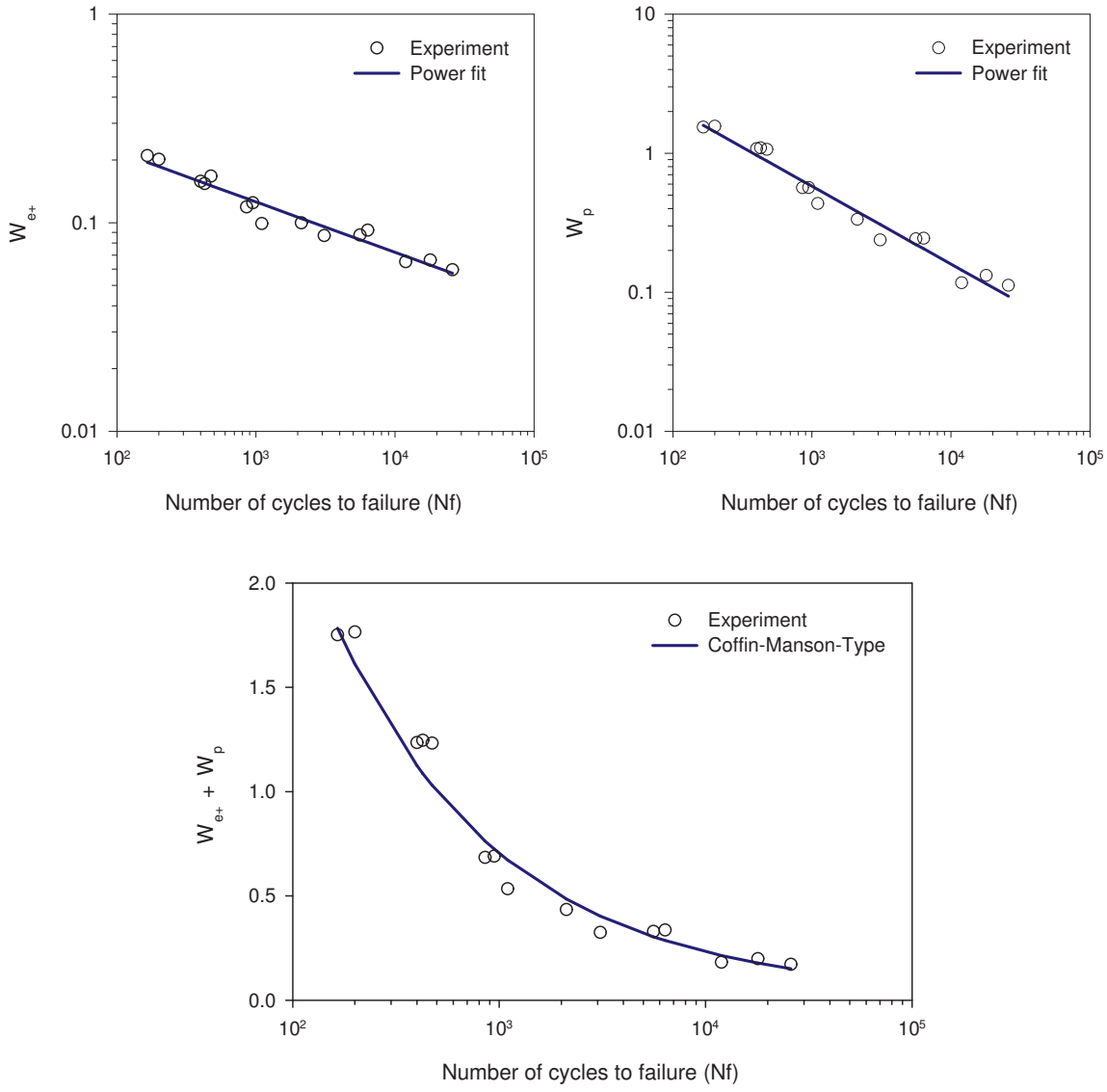

Figure 4.17: Coffin-Manson-Type fitting for LCF data of shear energy-life curve Eq. 4.18. Energy in (MJ/m^3).

LCF data only. Smith-Watson-Topper (SWT) [48, 59] and Fatemi-Socie (FS) [60] models have been widely used to analyze multiaxial loading, for various materials and automotive components [139–144]. Both models are based on strain, can include mean stress effect, and can be used for proportional and nonproportional multiaxial loading conditions. The critical planes for SWT and FS are the plane of maximum normal and shear strains, respectively. Normal and shear stress ranges calculated on the SWT and FS critical planes are shown in Fig. 4.18. On the other hand, normal and shear strain ranges calculated on the same planes are shown in Fig. 4.19. It is clear from these figures that normal and shear strains are better than normal and shear stresses for combining the fatigue data from different loading conditions in a single curve. The highly anisotropic and directional behaviour of wrought Mg alloys suggests that methods which are orientation-independent may be potential candidates for fatigue modeling. Also, when fatigue behaviour for axial loading is compared to torsion loading, a common concept such as equivalent strain, stress, or energy needs to be adopted. An equivalent measure for stress and/or strain requires the adoption of an anisotropic yield function, an associative or non-associative flow rule, and a hardening rule for the evolution of the yield surface. The more commonly used Mises equivalent stress and strain, though a good first approximation, are only valid for isotropic material behaviour and cannot be used for nonproportional multiaxial loading [35, 56]. Hence, strain energy density, which does not have the aforementioned limitations, seems to be a promising measure of damage induced by cyclic axial, cyclic shear or a combination of both modes. Strain energy density, which is an invariant quantity independent of the choice of direction, can be considered as a damage parameter for correlating the fatigue results. To be practical, a fatigue damage parameter must be fairly constant over the entire fatigue life. From the cyclic test results, it was found that the addition of the plastic strain and the positive elastic energy density gives a stable parameter for both uniaxial

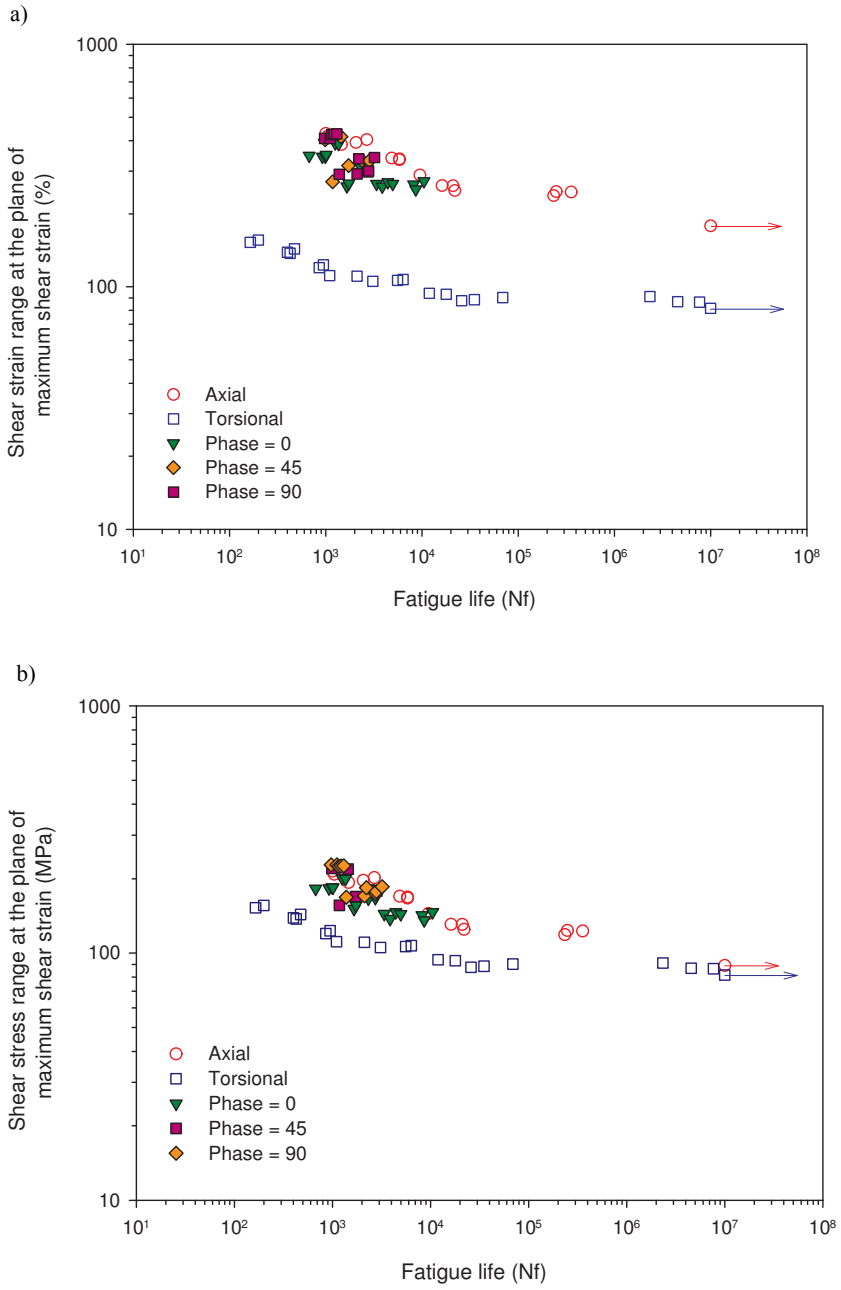

Figure 4.18: Normal and shear stresses. a) At plane of maximum normal strain. b) At plane of maximum shear strain.

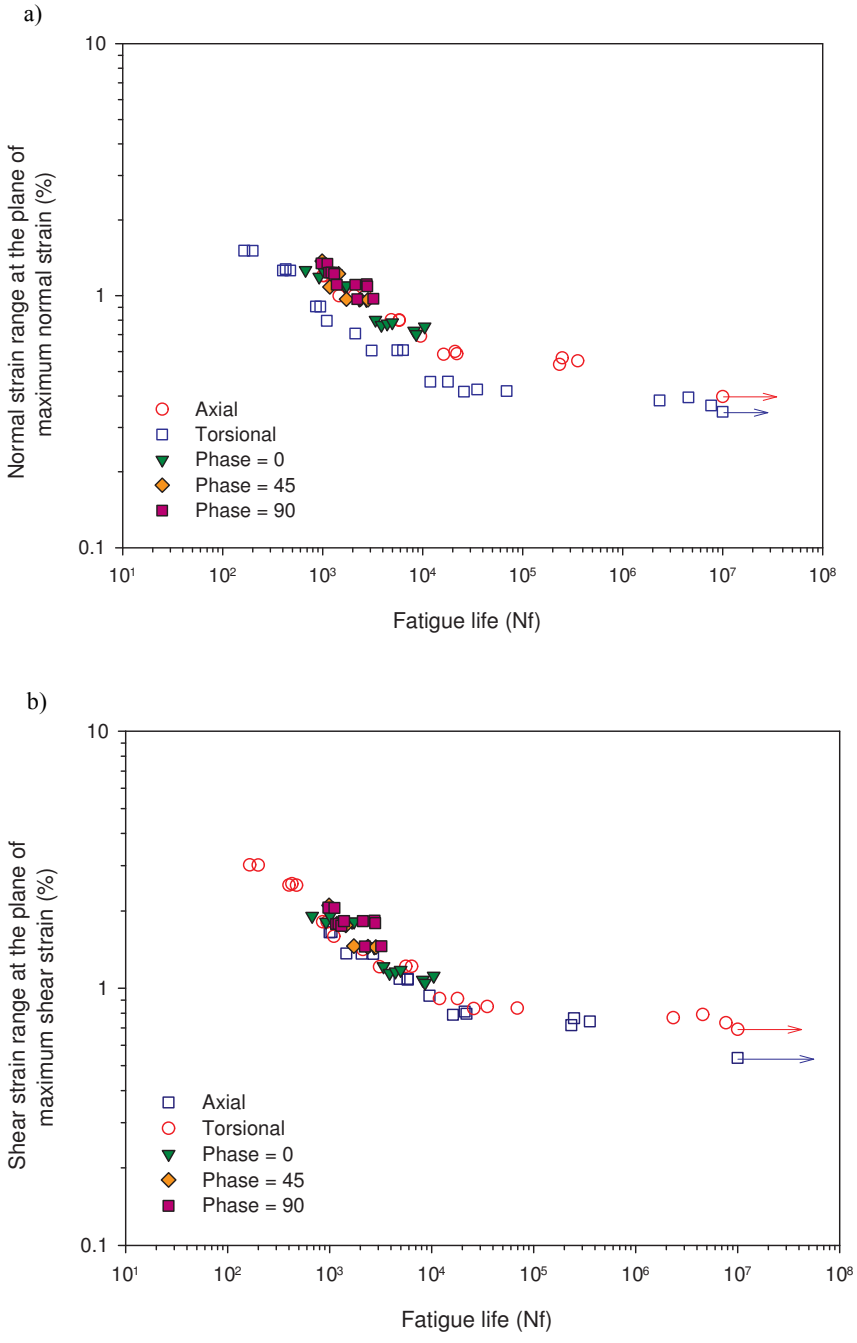

Figure 4.19: Normal and shear strain response. a) At plane of maximum normal strain. b) At plane of maximum shear strain.

and multiaxial cyclic tests. More importantly, the addition of the positive elastic energy density is considered as a method to account for mean stress effects. The Jahed-Varvani (JV) [55] energy-based model, that considers the sum of plastic and positive elastic strain energy densities as a measure of fatigue damage, was also used for fatigue life predictions. As for SWT and FS, the JV model includes a mean stress effect and can be used for both proportional and nonproportional loading conditions.

4.3.1 Critical Plane Approach

4.3.1.1 Smith-Watson-Topper (SWT)

Correlation between SWT parameter and fatigue life as well as fatigue life prediction are shown in Fig. 4.20. The predictions in this figure were obtained using Eq. 2.63. The necessary parameters for the fatigue life were obtained from Eqs. 4.11 and 4.15 for the predictions in Fig. 4.20b and c, respectively. In Fig. 4.20c, the predictions are shown for lives before the knee because the fatigue life equation was only fitted with the data before the knee. Run-out tests, i.e., tests that were stopped at 10^7 cycles without failure, are marked with arrows. In the cases when the model predicted very long life, exceeding 10^8 cycles, the corresponding data points were shifted to the maximum limit in the figure, 10^8 cycles. It is seen that the SWT parameter consolidates all the fatigue data, except data for shear loading, into a single band. This can be seen from the fatigue life prediction as the fatigue lives of all shear tests were overestimated. On the other hand, cyclic axial and multiaxial data mostly fall within the ± 2.0 scatter bounds of life. It is also seen from Fig. 4.20c that an improvement in the fatigue life prediction was achieved, compared to Fig. 4.20b, by using the Coffin-Manson equation that was fitted with the LCF data.

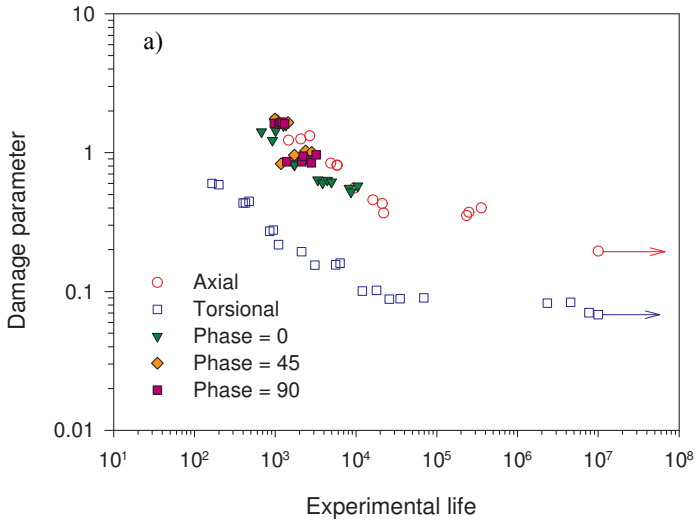
a)
Damage parameter
Experimental life
Axial
Torsional
Phase = 0
Phase = 45
Phase = 90

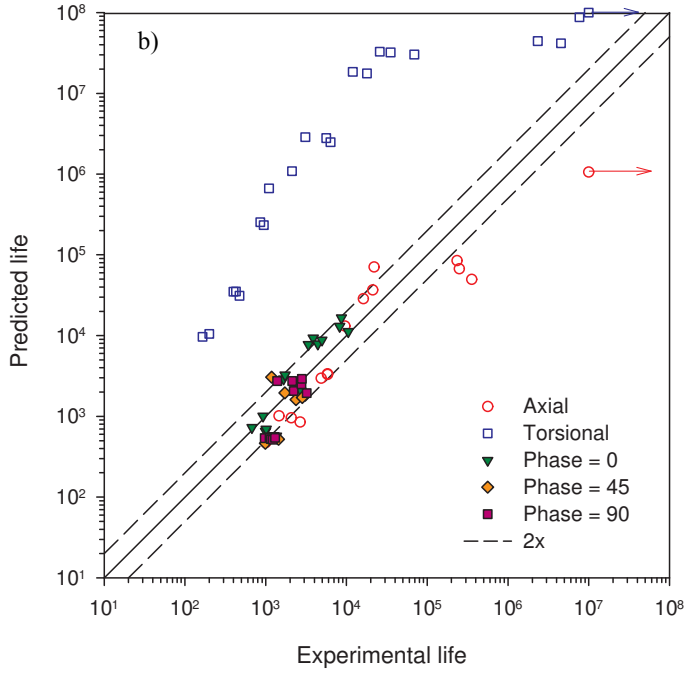
b)
Predicted life
Experimental life
Axial
Torsional
Phase = 0
Phase = 45
Phase = 90
2x

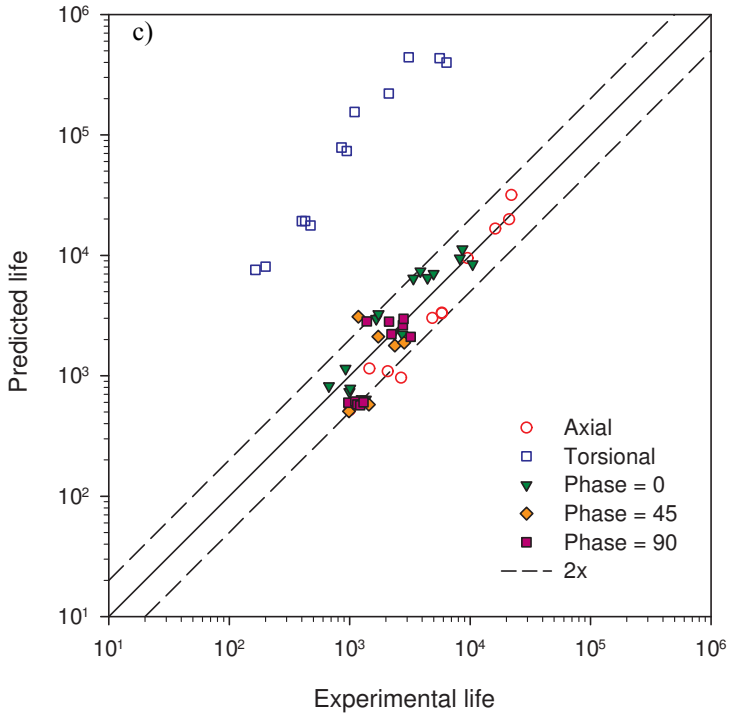

Figure 4.20: Standard Smith-Watson-Topper fatigue life model. a) Damage parameter-fatigue life correlation. b) Fatigue life prediction using standard Coffin-Manson equation. c) Fatigue life prediction using Coffin-Manson equation fitted with data before the knee.

As explained in Section 2.2.1, the maximum stress in Eq. 2.46 is assumed to be equivalent to the stress amplitude. This is correct if the hysteresis loop is symmetric, i.e., magnitudes of maximum and minimum stresses are approximately the same. This is not the case with AZ31B extrusion because the maximum axial stress is higher than the stress amplitude. Consequently, this approach was modified by fitting the maximum axial stress to an equation similar to Basqine's and then using it in the fatigue life equation. Although not shown here, however, a comparison between the original and the modified SWT parameter showed no significant difference or improvement in the predicted fatigue life. In an attempt to improve the prediction of shear lives, the original SWT parameter was rewritten into

a shear form. This was done by replacing the normal stress and strain with their shear counterparts and assuming that the critical plane is the plane of maximum shear strain. Hence, the shear form of SWT becomes

$$\frac{\Delta\gamma_{max}}{2}\tau = \frac{\tau_f^{'2}}{G}(2N_f)^{2b_s} + \tau_f^{'}\gamma_f^{'}(2N_f)^{c_s+b_s} \tag{4.19}$$

Plots of this damage parameter versus fatigue life and fatigue life predictions for this shear form of the SWT parameter are shown in Fig. 4.21. Figure 4.21a shows that the shear form of SWT is better than the standard from in terms of consolidating the fatigue data in a single band. It is also seen that the predictions for shear tests were improved significantly. However, most of the predictions for cyclic axial and multiaxial tests are underestimated. Figure 4.21c shows the predictions based the Coffin-Manson equation that was fitted with the data before the knee. It is seen from this figure that the predictions of shear lives was improved, compared to Fig. 4.21b, as most of the predictions fall between ±2x scatter bands. From safety point of view, the shear form of SWT is better than the standard form because it does not overestimate the life for any loading condition. Yu et al. [22] performed multiaxial test on AZ61A extrusion and used a different modified SWT parameter [101] for fatigue life predictions. The modified SWT parameter that Yu et al. used had both axial and shears terms. Using this modified parameter, Yu et al. were successfully able to predicted fatigue data within ±2x bounds for different multiaxial loading paths, especially for lives under 10^5 cycles. It is worth mentioning that the modified SWT parameter that Yu et al. used requires a function that should reflect the cracking behaviour of the material [102]. This function can be obtained by inspection. Yu et al. were able to obtain a suitable function based on the plastic strain energy density. However, it was found here that their function cannot correlate the cracking behaviour of AZ31B extrusion.

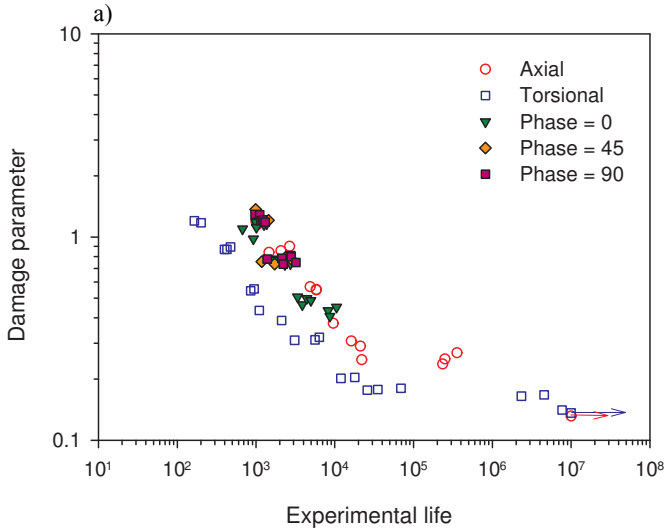
a)
Damage parameter
Experimental life
Axial
Torsional
Phase = 0
Phase = 45
Phase = 90

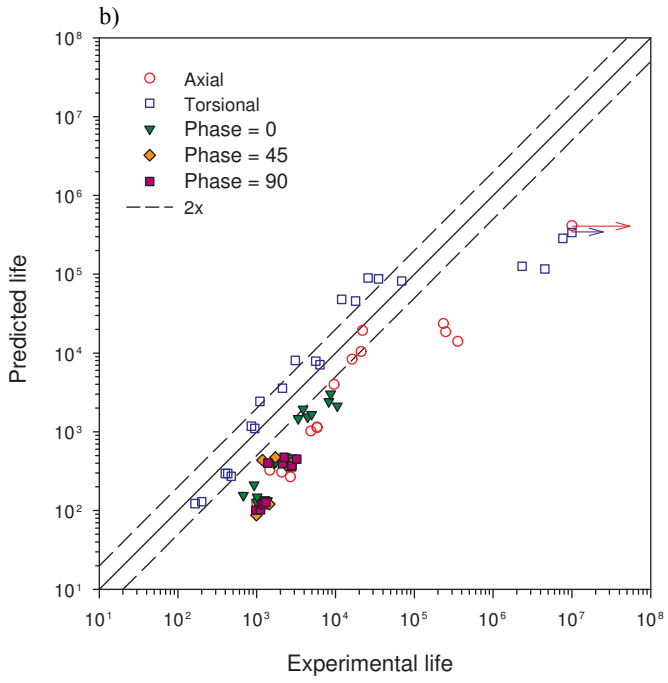
b)
Predicted life
Experimental life
Axial
Torsional
Phase = 0
Phase = 45
Phase = 90
2x

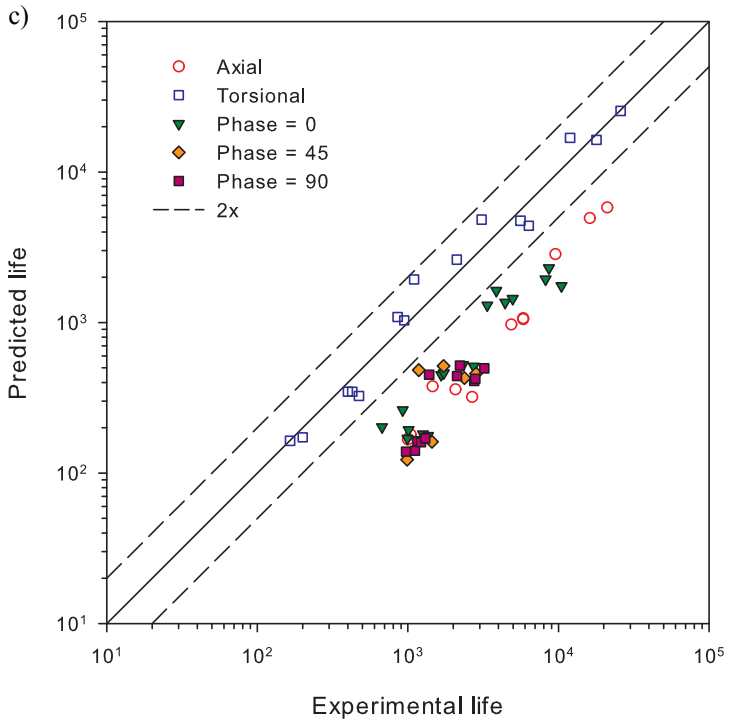

Figure 4.21: Shear Smith-Watson-Topper fatigue life model. a) Damage parameter-fatigue life correlation. b) Fatigue life prediction using standard Coffin-Manson equation. c) Fatigue life prediction using Coffin-Manson equation fitted with data before the knee.

4.3.1.2 Fatemi-Socie (FS)

Fatigue damage correlations with fatigue life and fatigue life predictions of the standard FS model are presented in Fig. 4.22. The FS constant, k, was calculated and was found to be equal to 0.3. This constant helps to combine the baseline data, i.e., cyclic axial and shear, into a single curve as seen in Fig. 4.22a. Also, it is seen from Fig. 4.22a that the FS parameter consolidated all data into a single band. The same procedure as for SWT was followed with FS regarding run-out tests and predictions that exceed 10^8 cycles.

a)

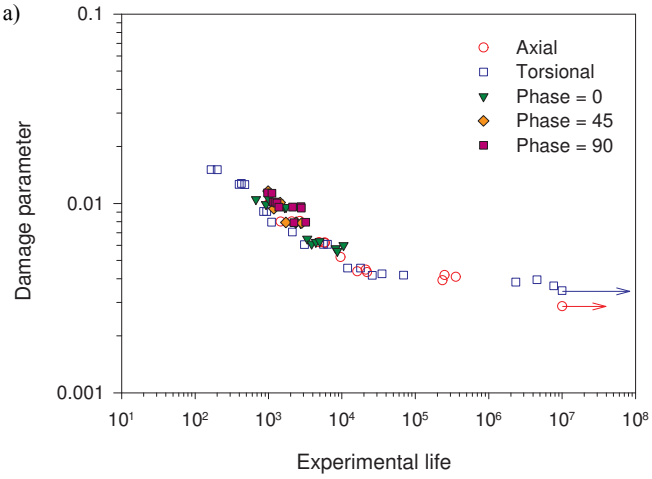
0.1
0.01
0.001
Damage parameter
Axial
Torsional
Phase = 0
Phase = 45
Phase = 90
10^1 10^2 10^3 10^4 10^5 10^6 10^7 10^8
Experimental life

b)

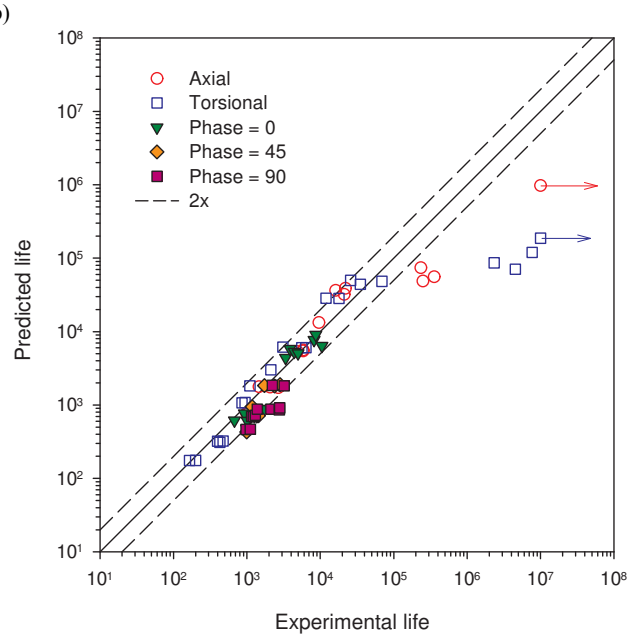
10^8 10^7 10^6 10^5 10^4 10^3 10^2 10^1
Predicted life
Axial
Torsional
Phase = 0
Phase = 45
Phase = 90
2x
10^1 10^2 10^3 10^4 10^5 10^6 10^7 10^8
Experimental life

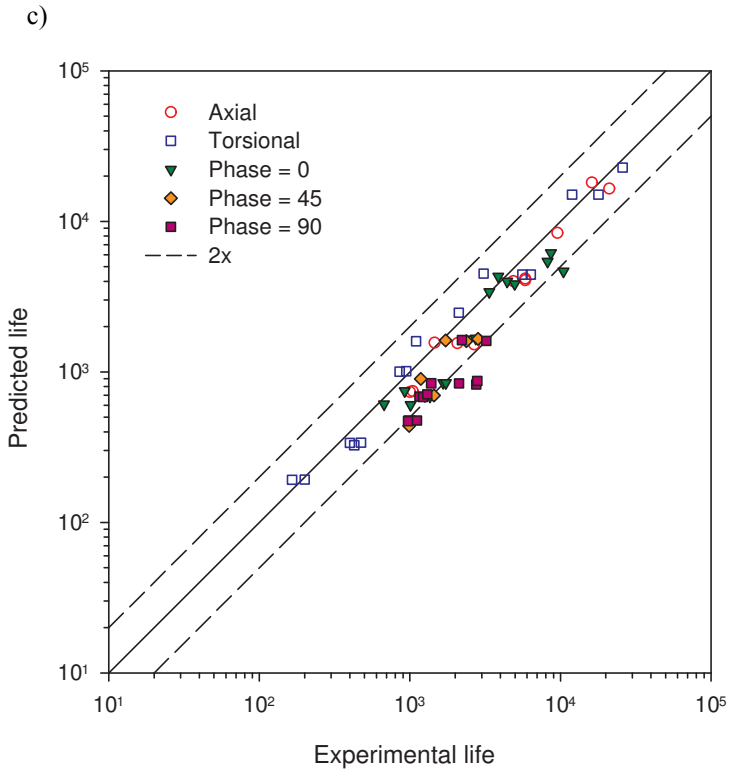

Figure 4.22: Fatemi-Socie fatigue life model. a) Damage parameter-fatigue life correlation. b) Fatigue life prediction using standard Coffin-Manson equation. c) Fatigue life prediction using Coffin-Manson equation fitted with data before the knee.

Figure 4.22b and c show the predictions of the FS used with the fatigue life parameters in Eqs. 4.12 and 4.16, respectively. From Fig. 4.22b, it can be seen that the predictions for low cycle fatigue data mostly fall between the ±2x bounds. However, high cycle fatigue lives were underestimated. There could be two reasons contributing to the error associated with the high cycle fatigue live predictions. First, although the FS model correlates all fatigue data in a single band, high cycle fatigue lives are not uniquely correlated with the damage parameter. Second, the Coffin-Manson equation underestimates the fatigue life in high cycle regime as shown Fig. 4.11. On the other hand, using the Coffin-Manson equation

that was fitted with LCF data, i.e., data before the knee, the predictions for cyclic axial and shear lives were improved as shown Fig. 4.22c. As explained in Section 2.2.2.3, the FS parameter can be used with either shear, Eq. 2.64, or axial, Eq. 2.65, forms of the Coffin-Manson equation. In Fig. 4.23, the FS parameter was used but with cyclic axial properties, i.e., using the axial properties in Eq. 4.11. This figure shows that the predictions for multiaxial tests are fairly similar to those in Fig. 4.22. However, the prediction for axial and shear tests between 10^4-10^5 cycles were degraded, while the predictions for axial tests between 10^5-10^6 cycles were improved. The predictions for high cycle fatigue lives in Fig. 4.23 are slightly better than those in Fig. 4.22. Yu et al. [22] coupled the FS model with Jiang's [101] general criterion to predict multiaxial fatigue life for AZ61A extrusions. Yu et al. were able to predict fatigue life for different multiaxial loading paths within ± 2.0 bounds, but only for lives less than 10^4 cycles. It should be noted that the axial and shear strain-life data in Yu et al. [22] showed no pronounced plateau as observed in the present case for AZ31B extrusion.

4.3.1.3 Fatigue crack prediction

Critical plane models calculate fatigue damage at specific planes. As a result, these planes can be considered as the most likely planes for crack initiation. Comparison between observed crack surface angle, α, and the predictions based on plane of maximum normal and shear strains are provided in Table 4.5. It is seen from this table that predictions of plane of failure based on maximum normal strain plane are in agreement with the observed plane of failure for cyclic axial specimens which is not the case for cyclic shear specimens. The predictions for multiaxial specimens are mostly underestimated, however, some predictions are within a reasonable agreement with the experimental observations. On the other hand, it is seen from this table that predictions of plane of failure based

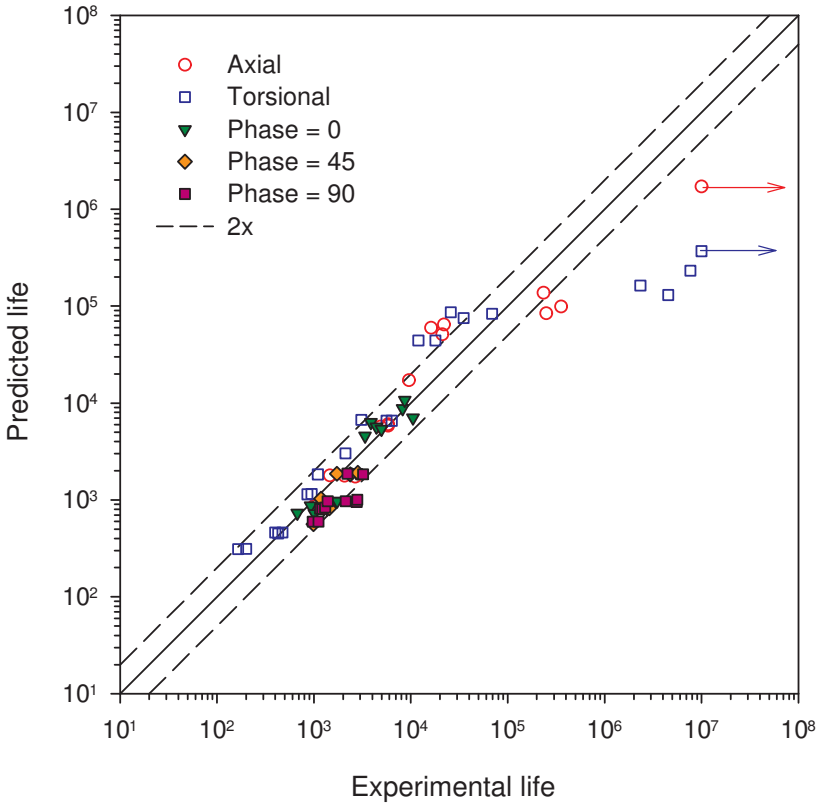

Figure 4.23: Fatemi-Socie fatigue life model with standard Coffin-Manson equation and cyclic axial properties.

on maximum shear strain plane are in agreement with the observed plane of failure for cyclic shear specimens only. The predictions for cyclic axial and multiaxial specimens are mostly overestimated. The comparisons between observed and predicted plane of failure in Table 4.5 are show in Fig. 4.24.

Table 4.5: Comparison between observed crack angle and the planes of maximum normal and shear strains.

Test No.	Observed plane (°)	SWT plane (°)	FS plane (°)
CA-02	0.00	0	45
CA-03	0.00	0	45
CA-07	0.00	0	45
CA-08	0.00	0	45
CA-11	0.00	0	45
CS-02	90.00	45	90
CS-07	90.00	45	90
CS-13	90.00	45	90
CS-15	90.00	45	90
CS-19	50.20	45	90
CS-20	37.80	45	90
BA-0-1	21.55	22	67
BA-0-4	25.16	22	67
BA-0-5	47.80	15	60
BA-0-6	29.63	15	60
BA-0-7	90.00	31	76
BA-0-8	90.00	31	76

Continued on next page

Table 4.5 – continued from previous page

Test No.	Observed plane, α (°)	$\Delta\varepsilon_1$ plane (°)	$\Delta\gamma_{max}$ plane (°)
BA-0-9	42.11	22	67
BA-0-10	32.61	22	67
BA-0-11	40.87	24	69
BA-0-12	32.63	22	67
BA-0-13	25.84	22	67
BA-0-14	24.45	23	68
BA-0-15	32.97	22	67
BA-0-16	36.60	22	67
BA-45-1	31.10	24	69
BA-45-2	90.00	31	76
BA-45-3	28.80	15	60
BA-45-5	36.46	22	67
BA-45-6	21.67	23	68
BA-90-1	4.57	24	69
BA-90-2	46.60	24	69
BA-90-3	21.98	16	61
BA-90-4	22.35	16	61
BA-90-5	6.40	15	60
BA-90-6	90.00	32	77
BA-90-7	90.00	32	77
BA-90-8	36.10	22	67
BA-90-9	90.00	32	77

Continued on next page

Table 4.5 – continued from previous page

Test No.	Observed plane, α (°)	$\Delta\varepsilon_1$ plane (°)	$\Delta\gamma_{max}$ plane (°)
BA-90-10	32.20	31	76
BA-90-11	10.14	22	67

Because experimental crack angle was measured for selected specimens, the SWT and the FS models can be assessed by pre-defining the critical plane. Therefore, instead of searching for the critical plane the observed crack angles in Table 4.5 were considered as the critical planes and the corresponding fatigue lives were calculated as shown in Fig. 4.25. It is seen from this figure that although SWT provides better predictions than FS, however, most fatigue lives were overestimated. Jiang et al. [145] evaluated several critical plane multiaxial fatigue life models including the Fatemi-Socie. They found that while fatigue lives can be well predicted, the predictions of the cracking planes were less accurate.

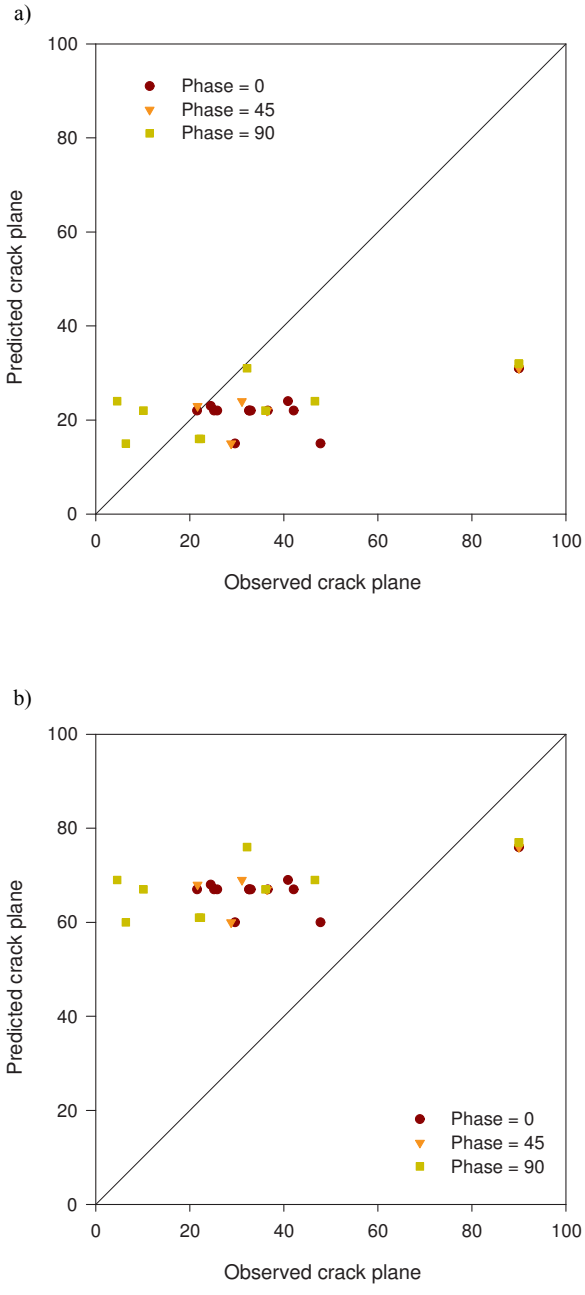

Figure 4.24: Comparison between observed and predicated crack plane angles. a) $\Delta\varepsilon_1$ plane. b) $\Delta\gamma_{max}$ plane.

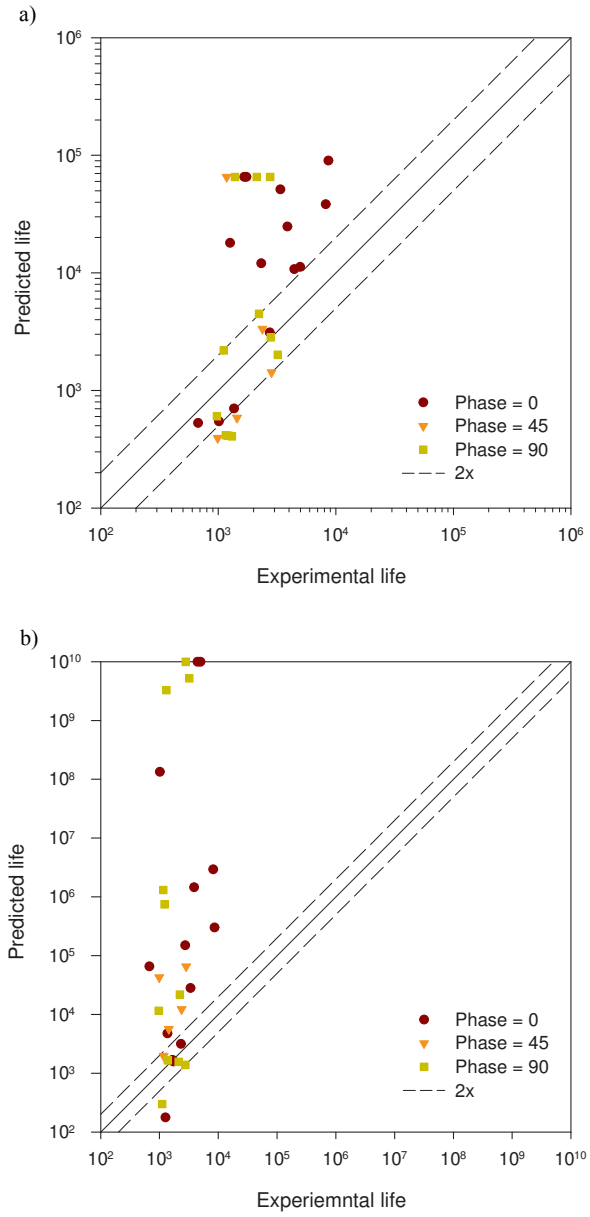

Figure 4.25: Calculation of multiaxial fatigue life by pre-defining critical plane using observed cracking plane. a) SWT. b) FS.

4.3.2 Energy Approach

4.3.2.1 Jahed-Varvani (JV)

Fatigue damage correlations with fatigue life and fatigue life predictions using the JV energy model are presented in Fig. 4.26. Figure 4.26 shows that the JV parameter correlates the fatigue life into a single band. Using the standard Coffin-Manson-Type equation, Eqs. 4.13 and 4.14, it is seen from Fig. 4.26b that while the HCF lives are underestimated, the LCF predictions mostly fall between the ±2x bounds. The underestimation of HCF lives is expected as the modeling of energy-life curves using the standard Coffin-Manson-Type equations, Figs. 4.12 and 4.13, underestimates fatigue lives after the knee. On the other hand, Fig. 4.26c shows the prediction using the Coffin-Manson-Type equations that were fitted with data before the knee. It is seen from this figure that the predictions for axial lives were improved compared to those in Fig. 4.26b.

a)

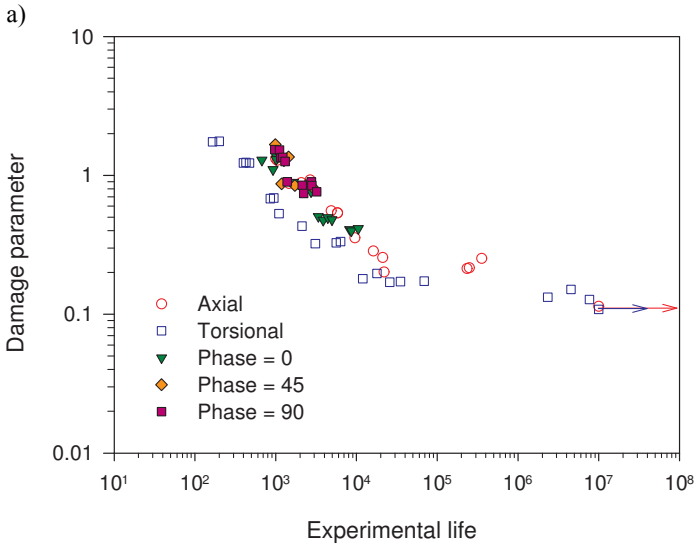
Damage parameter
Experimental life
Axial
Torsional
Phase = 0
Phase = 45
Phase = 90

b)

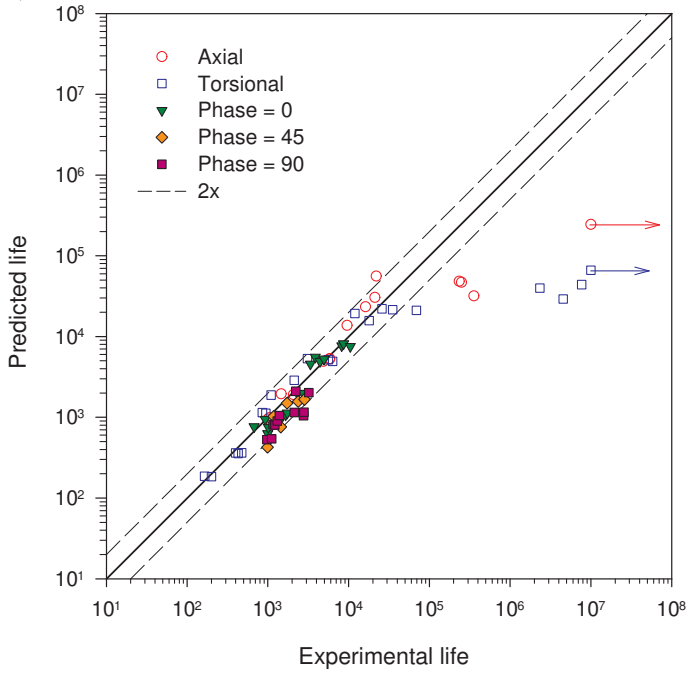
Predicted life
Experimental life
Axial
Torsional
Phase = 0
Phase = 45
Phase = 90
2x

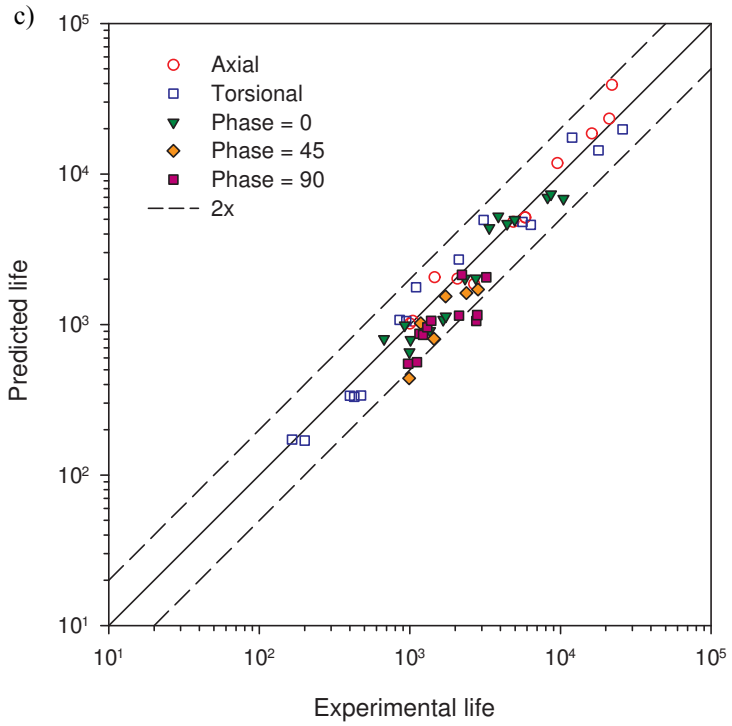

Figure 4.26: Jahed-Varvani fatigue life model. a) Damage parameter-fatigue life correlation. b) Fatigue life prediction using standard Coffin-Manson-Type equation. c) Fatigue life prediction using Coffin-Manson-Type equation fitted with data before the knee.

4.3.2.2 Generalized Energy Model

It has been shown from previous section that total energy density can successfully be used for fatigue life prediction under different loading conditions. Because energy is a scaler quantity, combining axial and torsional effect for multiaxial loading is simple regardless of the observed anisotropy in Mg-alloys. It was found that a simple relationship between the total energy density and fatigue life can be used to correlate and predict fatigue life data

for several Mg wrought alloys. This relation is given by

$$\Delta W_t N_f^m = \bar{C} \tag{4.20}$$

Using all cyclic data from this study, the constants in Eq. 4.20 were found to be $m = 0.64$ and $\bar{C} = 95$ MJ/m^3. Correlation between the total energy density and fatigue life data from this study and from the literature [14, 97, 146] is shown in Fig. 4.26. It is clearly seen from Fig. 4.26a that the total energy density can successfully correlate fatigue life data for AZ31 sheet and extrusion, AZ61A extrusion as well as the investigated AZ31B extrusion. Furthermore, using Eq. 4.20 the fatigue lives for all data were mostly predicted within $\pm$2x scatter bounds as shown in Fig. 4.26b. It is worth mentioning that the fatigue tests in Fig. 4.26 were performed at different loading conditions and loading paths.

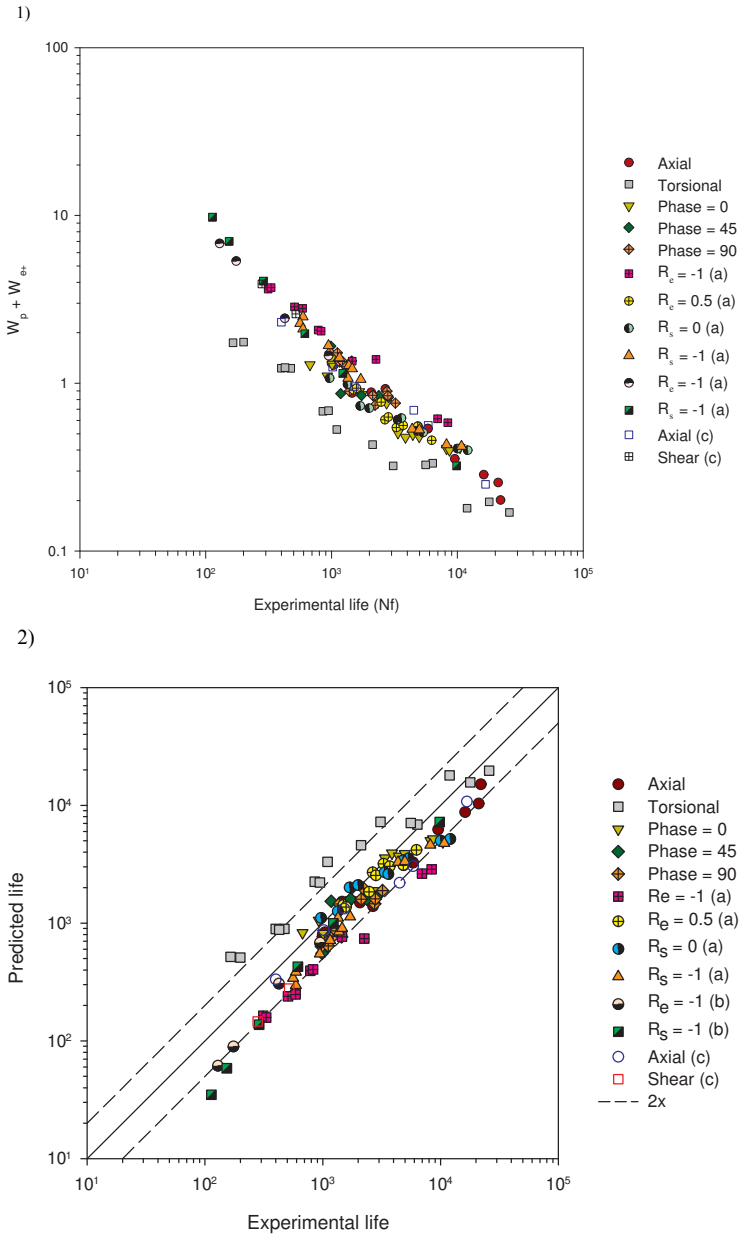

Figure 4.27: Generalized energy model . 1) Damage parameter-fatigue life correlation. 2) Fatigue life prediction. (a) Ref: Hyuk P. et al., 2010. (b) Ref: Shiozawa K. et al., 2011. (c) Ref: Zhang J. et al., 2011. R_e is the strain R-ratio and R_s is the stress R-ratio. Energy in (MJ/m^3).

4.4 Summary

Cyclic stress-strain responses for cyclic axial and shear loading were analyzed. It was found that the cyclic axial behaviour does not obey the Masing hypothesis and the cyclic Ramberg-Osgood relation cannot be used to model axial hysteresis. Rather, it was demonstrated that the axial hysteresis can be modeled by fitting the compressive and tensile reversal independently. Ramberg-Osgood- and sigmoid-type functions were successfully used to model the compressive and the tensile reversals, respectively. The cyclic shear behaviour fairly obeys the Masing hypothesis and the cyclic Ramberg-Osgood relation can be used to model shear hysteresis. Axial and shear strain-life curves suggest that AZ31B extrusion has fatigue limits at about 0.2 and 0.35% axial and shear strain amplitudes, respectively. Because of the bilinearity in strain- and energy-life curves for axial and shear loading, standard Coffin-Manson-Type equations cannot be used to model the entire life curve. Instead, Coffin-Manson-Type equations were fitted using the data before the knee. Fatigue lives for axial and multiaxial loading were predicted within $\pm$2x scatter bounds in the LCF regime using the standard SWT model. On the other hand, shear lives were predicted within $\pm$2x bounds using the shear form of SWT model. Fatigue lives for all loading conditions were predicted within $\pm$2x scatter bounds in the LCF regime using the FS and JV models. It was shown that the SWT and the FS critical planes were not in agreement with the experimental observations. Total energy density was found to correlate fatigue life data for several Mg wrought alloys. It was also found that a simple and general relation between total energy density and fatigue life can be obtained and used to predict the fatigue life for several Mg wrought alloys and under different loading conditions.

Chapter 5

Conclusions and Future Work

5.1 Summary and Conclusions

This study was conducted to characterize and to model the multiaxial fatigue of AZ31B extrusion. Two modes of loading were considered: axial and torsional. Flat and tubular specimens were machined from the extrusion sections and were tested under monotonic and cyclic loading conditions. Monotonic tensile and compressive tests were performed at three different orientations while monotonic shear and cyclic tests were performed along the extrusion direction. Fatigue life modeling and fatigue life predictions methods have been presented and discussed. A detailed summary for the major findings of this study are presented in the following.

1. Metallography

   Three orthogonal planes of the extrusion section were analyzed metallogrpahically. The average grain sizes of the transverse-longitudinal (T-L), the transverse-depth (T-D) and the depth-longitudinal (D-L) planes are 58.8, 17.8 and 34.6 μm. Second phase

particles and twin bands were observed on all planes. While grain sizes appeared to be uniform in the (T-L) plane, significant variation in grain size was observed in the (T-D) and (D-L) planes. This variation was more pronounced in the (D-L) plane.

2. Monotonic tensile behaviour

   Three orientations with respect to the extrusion direction were considered: longitudinal, LD, which is parallel to the extrusion direction, 45° and transverse direction, TD. Due to strong texture, i.e., the basal plane parallel to the extrusion direction with the c-axis perpendicular to it resulting from the extrusion process, it was found that the tensile behaviour was orientation dependent. The maximum and minimum yield strengths were obtained in LD and TD, respectively. Post-yielding behaviour was also dependent on the orientation. The LD had a very low power hardening exponent while the 45° direction had significant hardening, with power-like behaviour. The post-yielding behaviour in the TD was sigmoidal due to twinning-detwinning deformation. The maximum and minimum ultimate tensile strengths were obtained at TD and 45°, respectively. The highest and lowest values of $\%EL$ and $\%RA$ were obtained at 45° and TD, respectively.

3. Monotonic compressive behaviour

   Similar to tensile loading, three orientations with respect to the extrusion direction were considered for monotonic compressive loading: LD, 45° and TD. The monotonic compressive behaviour was also found to be orientation dependent. The maximum and minimum absolute yield strengths were obtained in the TD and 45° directions, respectively. Post-yielding behaviour in the LD was sigmoidal due to twinning-detwinning deformation, while the 45° direction had a mixed linear-power-like behaviour. The post-yielding behaviour in the TD showed rapid hardening with

the lowest compressive fracture strain. The maximum absolute compressive strain was obtained at 45°. The maximum and minimum absolute ultimate compressive strengths were obtained at LD and 45°, respectively.

4. Monotonic pure shear behaviour

   Monotonic shear tests were only performed on specimens that were machined along the extrusion direction. The post-yielding behaviour was linear and could be modeled using linear hardening modulus.

5. Pseudoelasticity

   By performing loading-unloading tests in different orientations, pseudoelasticity was observed for monotonic tensile, compressive and shear loading conditions. Based on a limited analysis and as suggested in the literature, it was found that a Weibull-type relation between anelastic strain and true plastic strain could be used to predict the anelastic strain and to simulate loading-unloading hysteresis behaviour.

6. Cyclic axial behaviour

   Cyclic hysteresis loops were asymmetric due to twinning in compression and slip in tension. An inflection point that separated the end of detwinning and the start of slip was observed, especially at high strain amplitudes. A low hardening rate was observed in compression during the loading reversal due to twinning especially at early cycles. Sigmoidal-type behaviour was observed during the unloading reversal. Cyclic hardening was observed with the rate of hardening more pronounced in tension than in compression, especially at high strain amplitudes. This resulted in a positive mean stress development. Stress amplitude, mean stress and plastic strain amplitude were found to vary with cycling. Comparison between the hysteresis loop from the

second and the half-life cycles showed that the plastic strain amplitude and the plastic strain energy density decreased with cycling due to cyclic hardening. The strain and energy-life curves had a knee at 44×10^3 reversals. During cycling, the sum of plastic and positive elastic axial strain energy densities was fairly constant.

7. Cyclic shear behaviour

   Unlike axial loading, the cyclic shear hysteresis loops were symmetric and no pronounced cyclic hardening was observed during the tests. Therefore, stress and plastic strain amplitude had little variation with cycling. Strain- and energy-life curves had a knee at 50×10^3 reversals. During cycling, the sum of plastic and positive elastic shear strain energy densities was fairly constant.

8. Multiaxial axial-torsion behaviour

   In all multiaxial tests, the axial mode showed the same characteristics seen in cyclic axial tests. However, the shear hysteresis was seen to be influenced by the application of axial loading when twinning deformation was observed, especially in the early cycles. Three observations concerning phase angle can be made. First, the phase angle had an effect on the shear hysteresis only. Second, the phase angle had an influence on the hardening behaviour such that additional hardening was observed due to nonproportionality. Third, the phase angle had no pronounced effect on the fatigue life. During cycling, the sum of plastic and positive elastic axial and shear strain energy densities was fairly constant.

9. Fatigue cracking behaviour

   Microscopic observations of fatigue cracks showed that cyclic axial specimens failed at the plane of maximum normal stress/strain while cyclic shear specimens failed at

the plane of maximum shear stress/strain. The failure planes in multiaxial specimens did not coincide with either the plane of maximum normal or shear stress/strain. In general, fatigue cracks started from the surface and had a semi-elliptical shape. All cyclic tests were stopped at 50% load drop. Based on this criterion the average crack radii $2c$ and a were found to be 2.02 ± 1.4 and 0.68 ± 0.30 mm, respectively. It was also found that AZ31B extrusion show Case A cracking behaviour. In some tests, multiple fatigue cracks were observed. From the SEM analyses, striations and secondary cracks were observed.

10. Cyclic Stress-Strain Response

    Cyclic axial behaviour does not obey the Masing hypothesis and the cyclic Ramberg-Osgood relation cannot be used to model axial hysteresis. Rather, for axial hysteresis to be modeled, the tensile and compressive reversals should be modeled independently. It was found that the hardening behaviour of the compressive reversal is of a power-type. Therefore, it was successfully modeled using Ramberg-Osgood-Type equation. On the other hand, the tensile reversal was model using a sigmoid-type function. Predictions from these functions were comparable with the experimental results for three different axial strain amplitudes. Cyclic shear behaviour fairly obeys the Masing hypothesis and the cyclic Ramberg-Osgood relation can be used to model shear.

11. Fatigue life modeling

    Although only two run-out tests were performed for cyclic axial and shear loading, strain-life curves for these loading modes suggest that AZ31B extrusion has fatigue limits at 0.2 and 0.35% axial and shear strain amplitudes, respectively. Because of the bilinearity in the strain- and energy-life curves for axial and shear loading,

standard Coffin-Manson-Type equations could not be used to model the entire life curves. Instead, they were successfully modeled in the LCF regime. Because of the pronounced plateau, the modeling of the HCF regime became critical. A small change in the strain amplitude resulted in a very large change in the fatigue life. Because of the limited data, the HCF regime could not be modeled properly.

12. Multiaxial fatigue life predictions

    Three fatigue damage parameters were considered: Smith-Watson-Topper, Fatemi-Socie and Jahed-Varvani. The first two parameters are based on strain and are evaluated on specific critical planes. The third parameter is based on energy densities calculated from hysteresis loops. Because strain- and energy-life curves had knees and pronounced plateaus, Coffin-Manson-type equations were fitted twice: using the entire data in the life curve and using the LCF data before the knee. From these fitting, it was found that better modeling of the fatigue life can be achieved by fitting Coffin-Manson-type equation with the LCF data. Similar to the life curves, all of fatigue damage parameters had pronounced plateaus that start at the same lives at which the axial and the shear fatigue-life curves had knees. This means that nearly all tests in the plateau region have approximately the same damage value although they failed at significantly different lives which this is not reasonable. As a result, the fatigue damage parameters were only assessed based on their prediction in the LCF regime. Fatigue lives for axial and multiaxial loading were predicted within $\pm$2x scatter bounds in the LCF regime using the standard SWT model. Shear lives were predicted within $\pm$2x bounds using the shear form of SWT model. Fatigue lives for all loading conditions were predicted within $\pm$2x scatter bounds in the LCF regime using the FS and JV models. Based on the obtained result, it was found that the FS and the JV models make the best predictions for multiaxial fatigue life in the LCF

regime. Total energy density was found to correlate fatigue life data for several Mg wrought alloys. It was also found that a simple and general relation between total energy density and fatigue life can be obtained and used to predict the fatigue life for several Mg wrought alloys and under different loading conditions.

5.2 Future works

This study provided fundamental knowledge about the multiaxial monotonic and cyclic behaviour of AZ31B magnesium extrusion. There are many important aspects that could be considered as the next step in this research. These aspects were not covered in this investigation due to time and resource limitations. A list of recommended future work is summarized in the following:

1. Because automotive structural components are usually subject to variable amplitude loading, it is important to investigate the cyclic behaviour of AZ31B extrusion when subjected to uniaxial and/or multiaxial variable amplitude loading. The effect of the different deformation mechanisms involved such as twinning and detwinning on the cyclic behaviour of AZ31B extrusion when subjected to variable amplitude loading needs to be addressed.

2. In order to be able to model fatigue life near the fatigue limit, an independent high cycle fatigue testing program is needed because of the pronounced plateau in the HCF regime.

3. An anisotropic equivalent measure of stress and/or strain would be useful for fatigue analysis. A suitable anisotropic yield function could be used to calculate equivalent

stress and/or strain form the multiaxial loading state. If this yield function can consolidate both uniaxial and multiaxial fatigue data in a single curve, then a simple uniaxial fatigue model could be used to predict the fatigue life for multiaxial state. This could simplify the fatigue design process for notched components.

4. Anisotropic cyclic plasticity model capable of simulating the uniaxial and the multiaxial cyclic behaviour of AZ31B extrusion is very important, especially for analyzing complex geometry. As complex geometries can only be analyzed using FEA, it would be useful to have an anisotropic cyclic plasticity model that can be implemented in current FEA packages such as ANSYS or ABAQUS, through their User Material Subroutine. Although ANSYS and ABAQUS already have anisotropic plasticity models like the Generalized Hill Potential Theory, these models cannot be used for cyclic loading.

5. Notched specimen testing is useful because it provides a way to verify multiaxial fatigue prediction methods on a component level. A simple cylindrical geometry with a filet could be enough to generate a complex multiaxial state of stress/strains. A strain rosette can be used to measure the strain state. However, the state of stress can only be determined though suitable analytical techniques, which have many limitations, or numerically. Once the states of stress and strain are determined, they can be incorporated into a suitable fatigue life model and then the fatigue life can be predicted.

6. In situ neutron diffraction technique has been a useful method to investigate deformation twinning and detwinning during cyclic loading for many magnesium alloys. However, only axial loading conditions were considered so far. Although the cyclic behaviour in shear loading appears to be typical, In situ neutron diffraction analysis

of cyclic shear loading can provide experimental evidence of the deformation mechanisms involved. The pseudoelasticity in shear loading could also be explained using this technique.

7. Further analysis need to be done on critical plane models such as Smith-Watson-Topper or Fatemi-Socie to improve their predictability of crack plane angle.

8. Further experimental analysis need to be conducted to verify the phase angle effect on fatigue life for wider range of strain amplitudes, especially at HCF.

9. Serrated flow was observed at different orientation in the monotonic tensile and compressive stress-strain curve. However, such behaviour was not investigated. Studying such phenomenon might provide a better understanding of the plastic deformation mechanisms and fatigue damage process in Mg-alloys.

APPENDICES

Appendix A

Hysteresis Loops for Multiaxial Tests

Test No.	ε_a (%)	γ_a (%)	φ (°)
BA-0-1	0.502	0.654	0.0
$2c$ (mm)	a (mm)	α (°)	N_f
1.705	NA	21.55	674

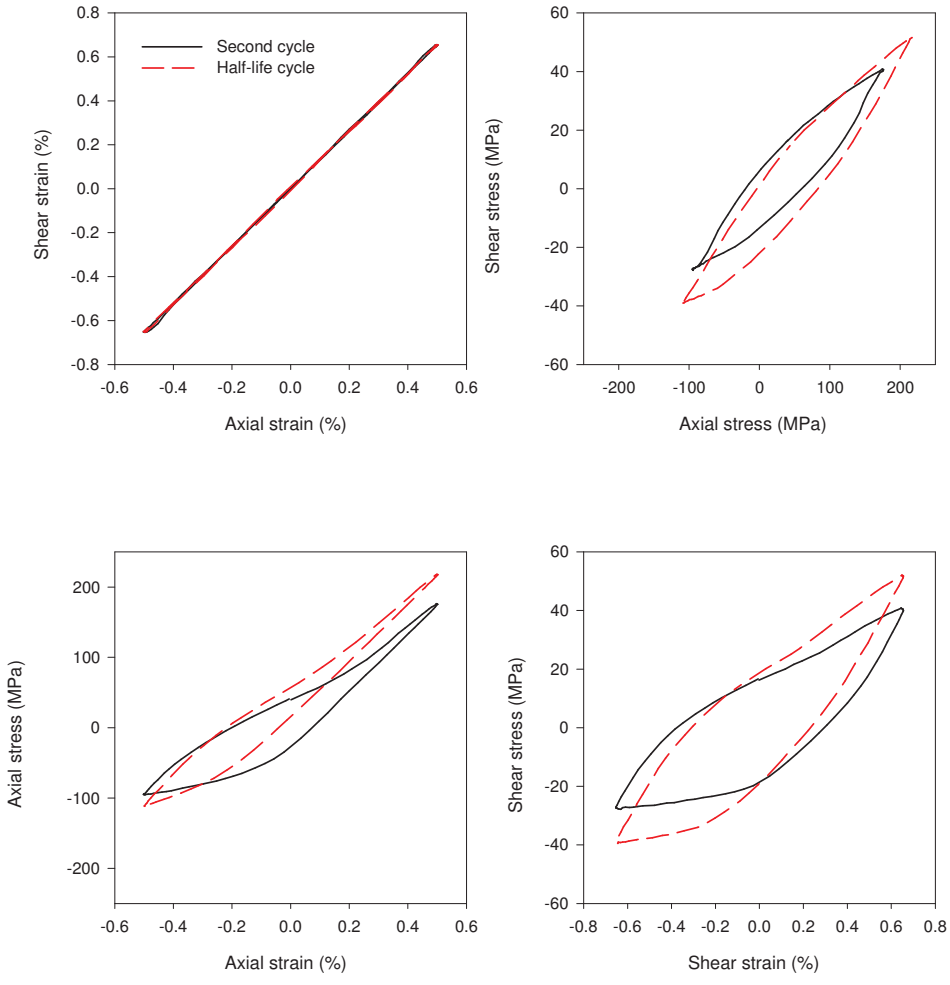

Test No.	ε_a (%)	γ_a (%)	φ (°)
BA-0-2	0.453	0.656	0.0
$2c$ (mm)	a (mm)	α (°)	N_f
NA	NA	NA	925

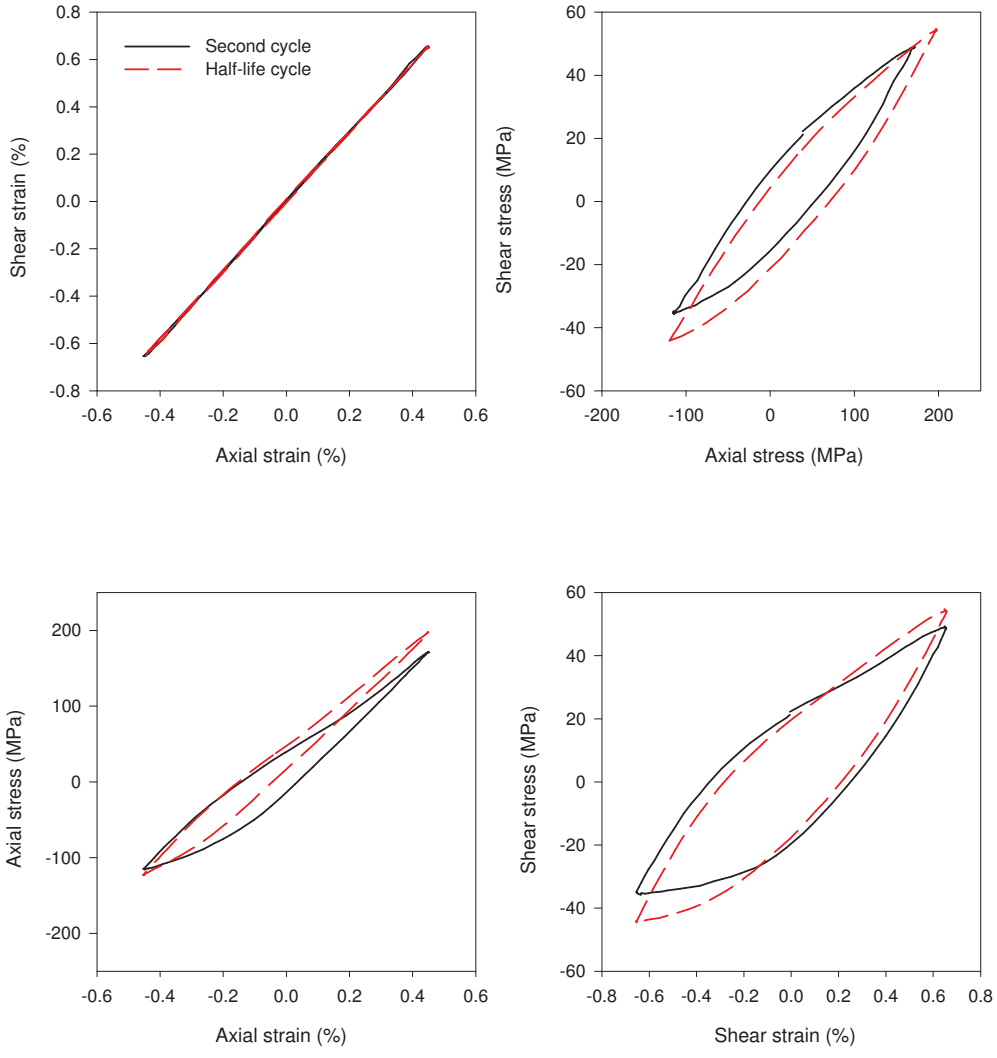

Test No.	ε_a (%)	γ_a (%)	φ (°)
BA-0-3	0.503	0.756	0.0
$2c$ (mm)	a (mm)	α (°)	N_f
NA	NA	Na	994

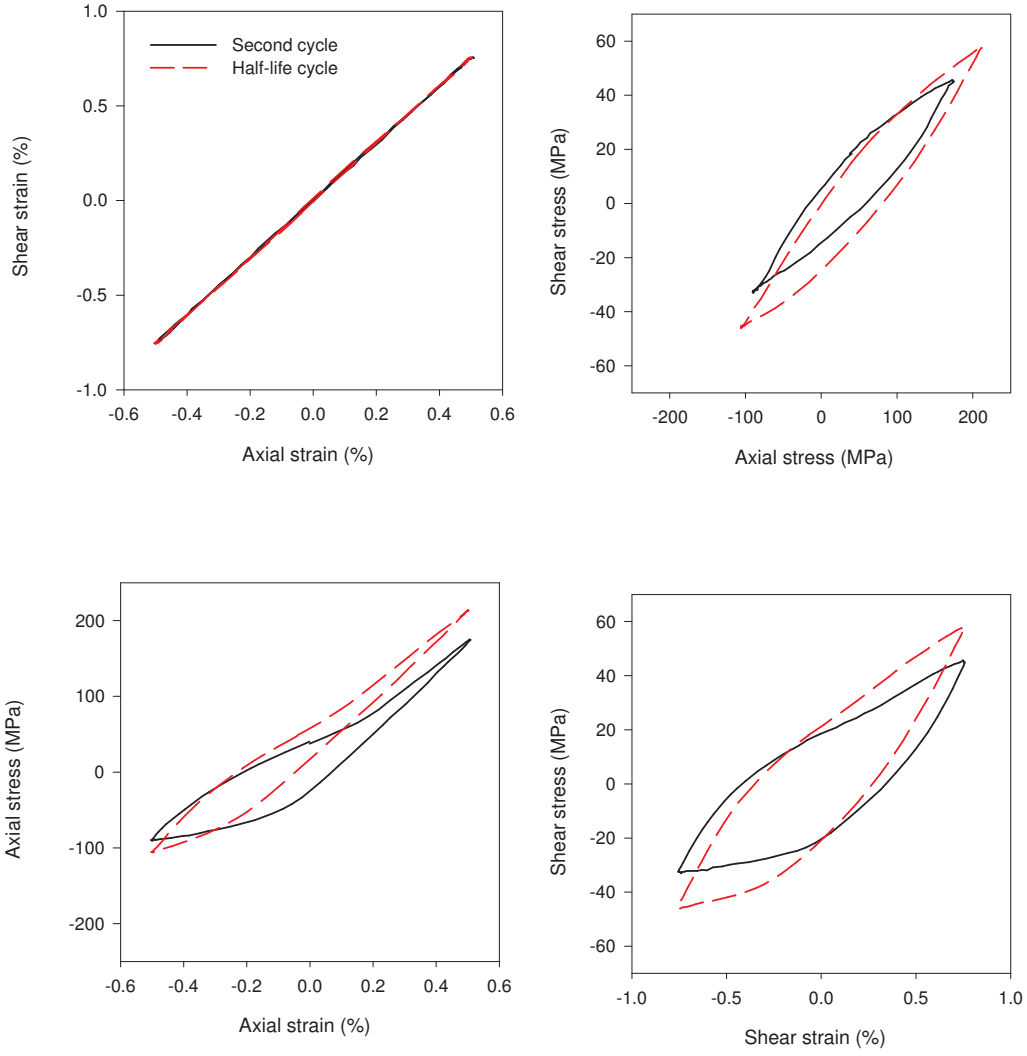

Test No.	ε_a (%)	γ_a (%)	φ (°)
BA-0-4	0.502	0.656	0.0
$2c$ (mm)	a (mm)	α (°)	N_f
6.2	t_w	25.16	1,012

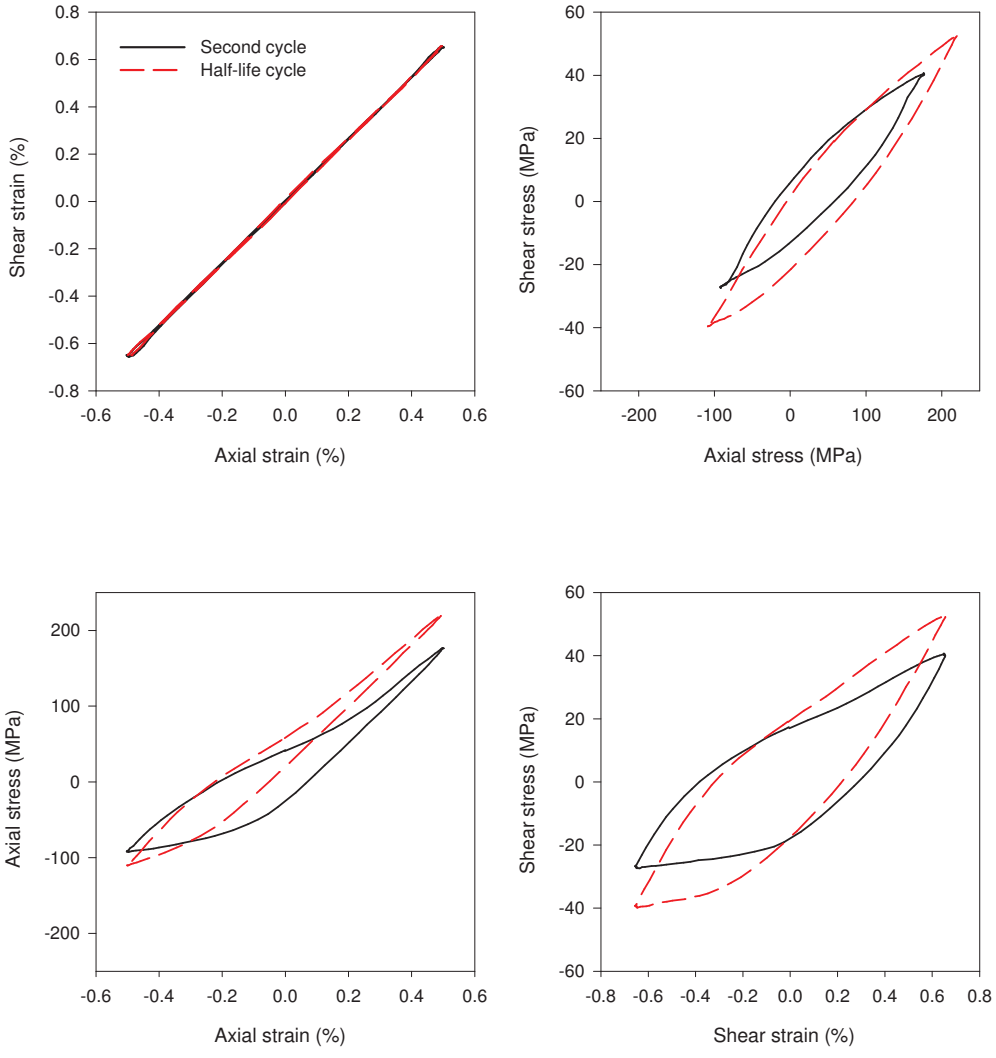

Test No.	ε_a (%)	γ_a (%)	φ (°)
BA-0-5	0.553	0.455	0.0
$2c$ (mm)	a (mm)	α (°)	N_f
1.29	NA	47.8	1,260

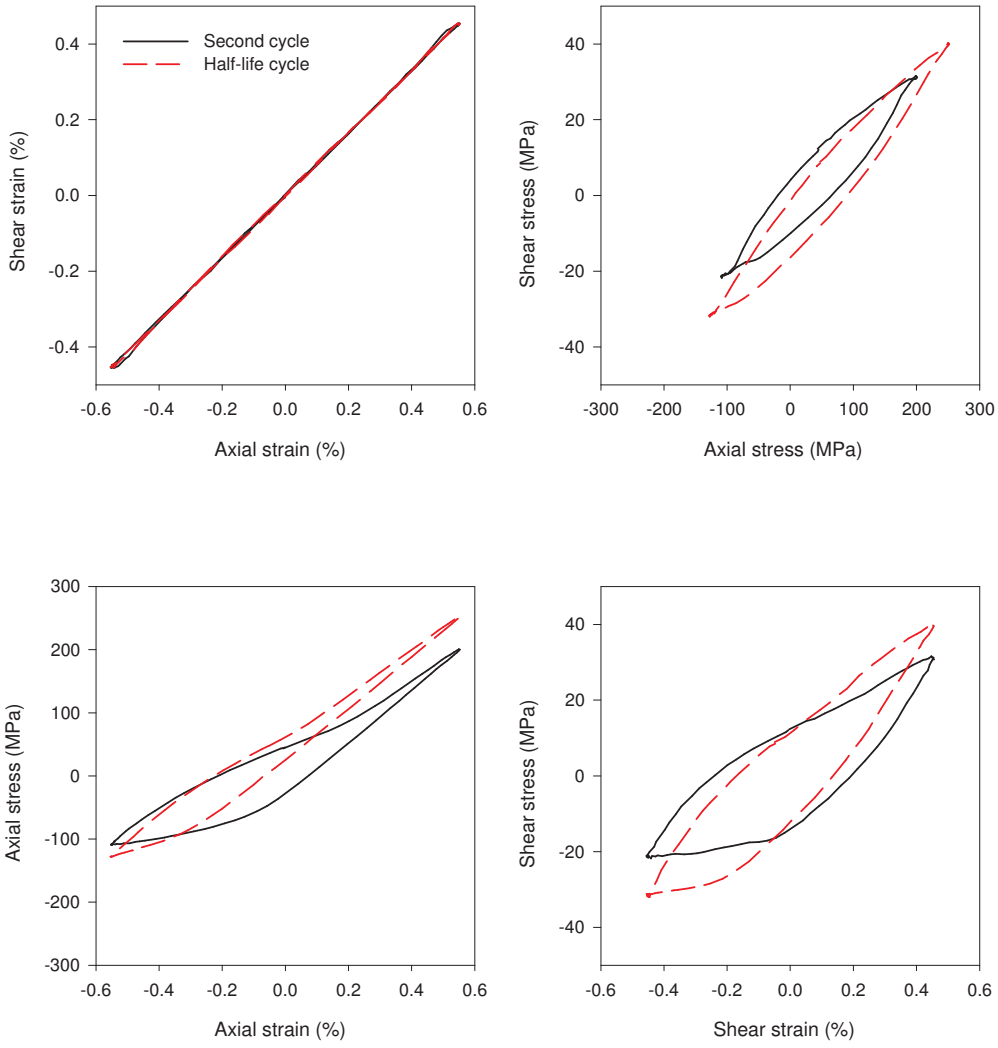

Test No.	ε_a (%)	γ_a (%)	φ (°)
BA-0-6	0.551	0.454	0.0
$2c$ (mm)	a (mm)	α (°)	N_f
1.415	t_w	29.63	1,362

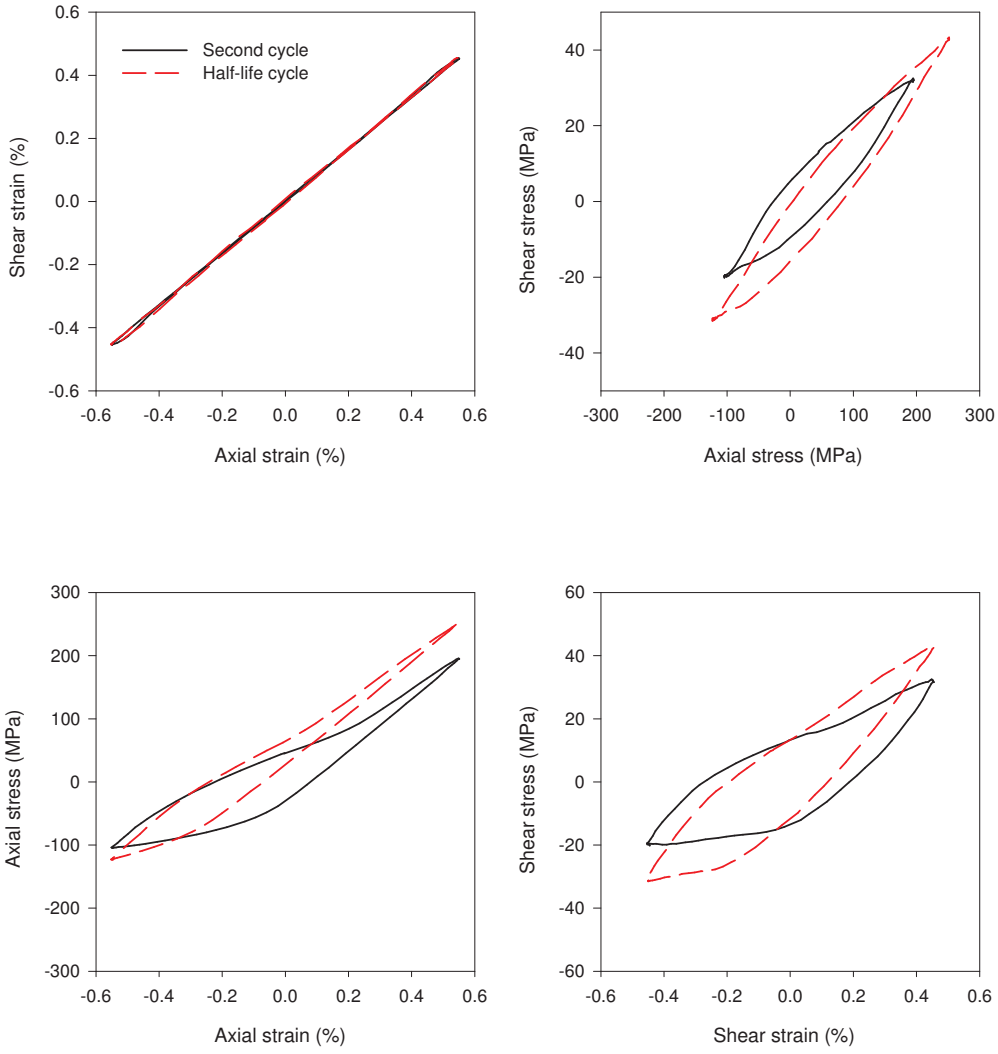

Test No.	ε_a (%)	γ_a (%)	φ (°)
BA-0-7	0.303	0.806	0.0
$2c$ (mm)	a (mm)	α (°)	N_f
1.945	NA	90	1,665

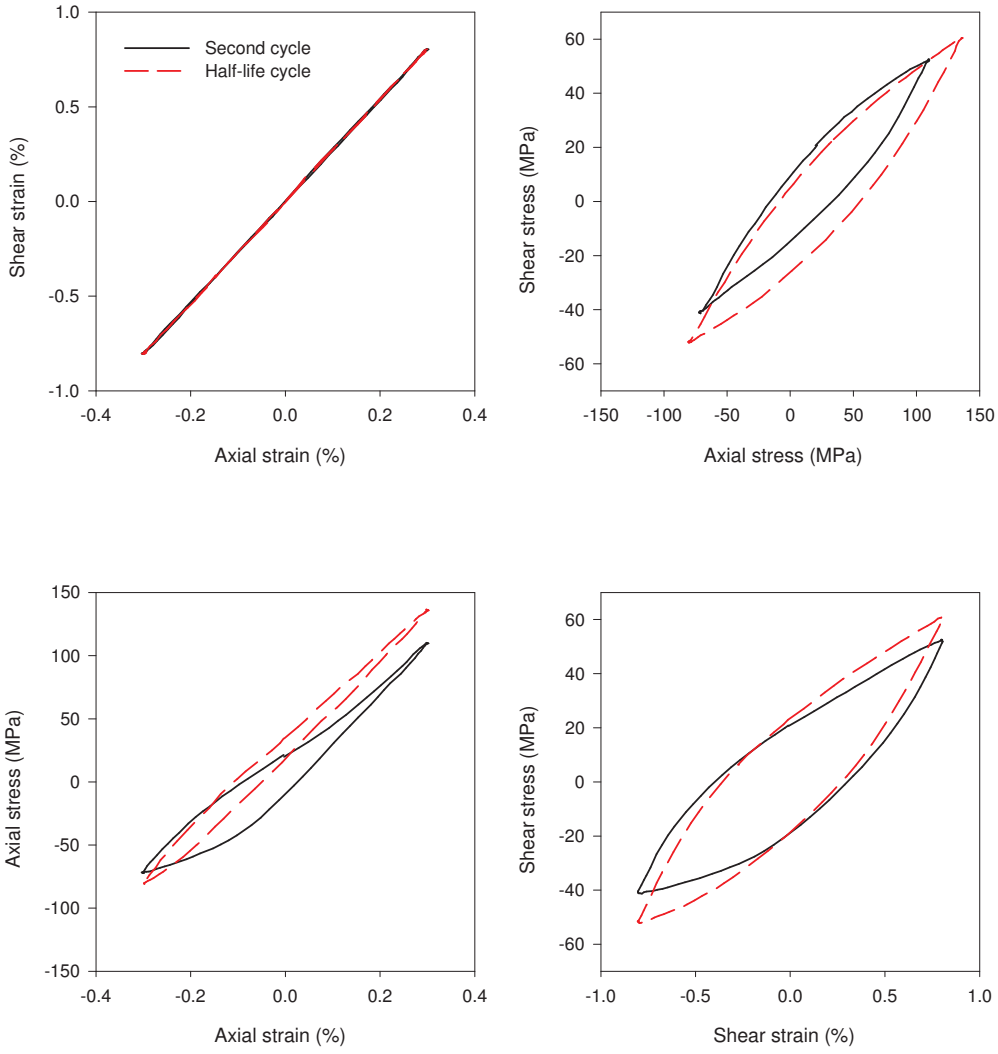

Test No.	ε_a (%)	γ_a (%)	φ (°)
BA-0-8	0.303	0.807	0.0
$2c$ (mm)	a (mm)	α (°)	N_f
1.15	0.33	90	1,736

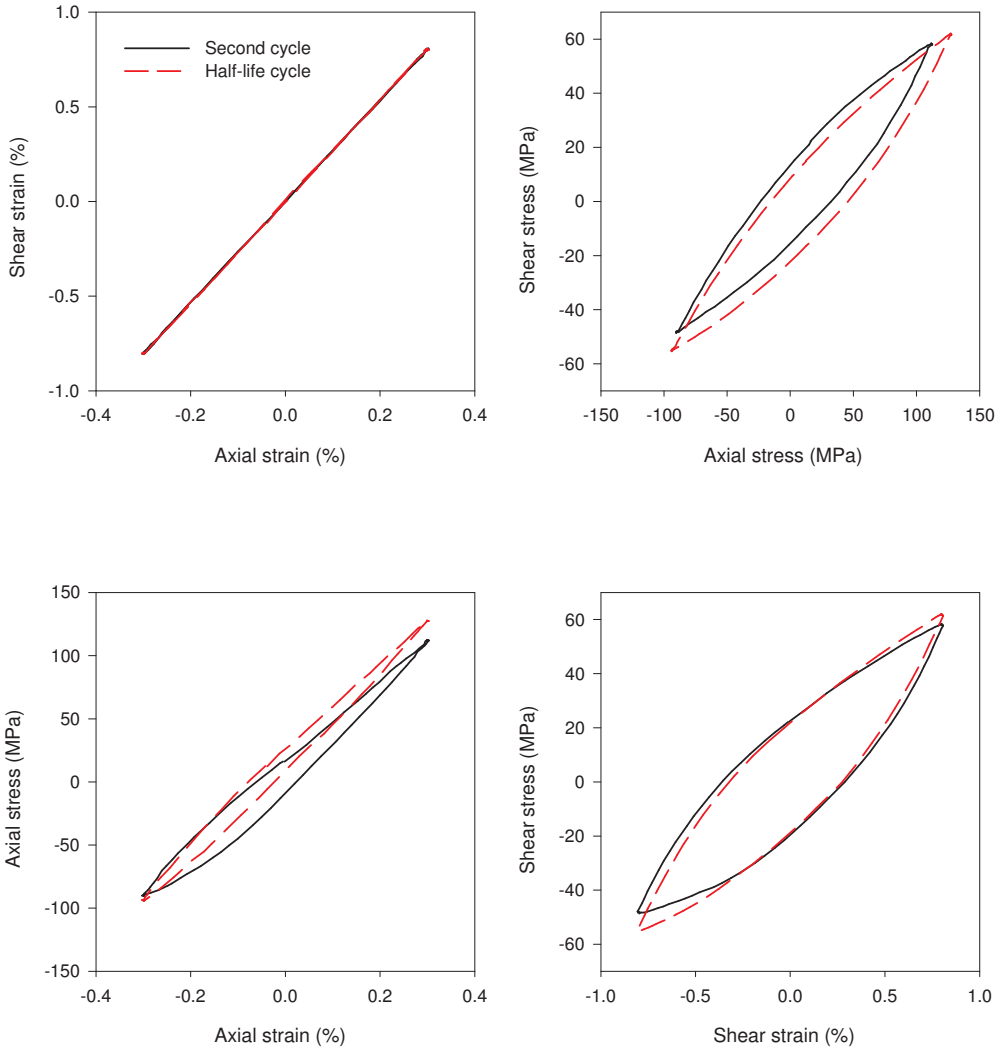

Test No.	ε_a (%)	γ_a (%)	φ (°)
BA-0-9	0.378	0.507	0.0
$2c$ (mm)	a (mm)	α (°)	N_f
2.53	NA	42.11	2,322

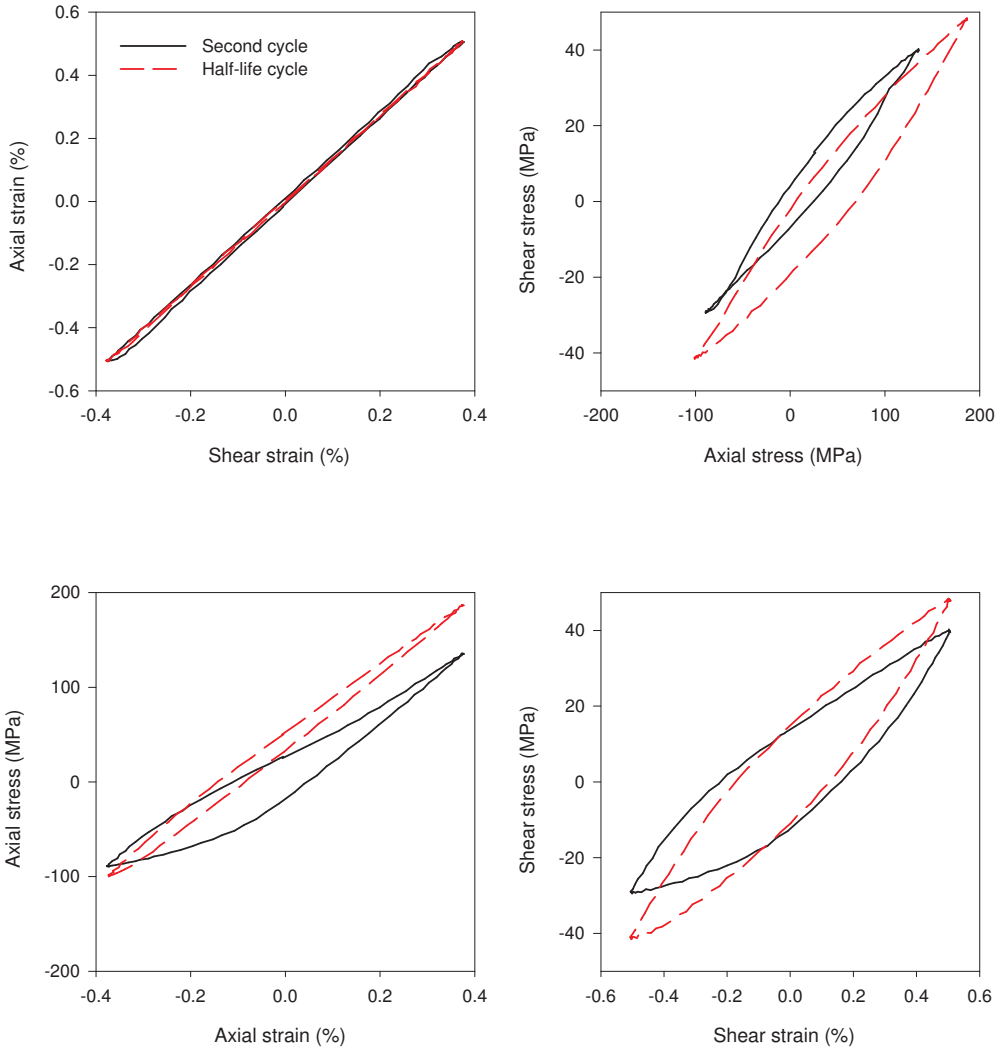

Test No.	ε_a (%)	γ_a (%)	φ (°)
BA-0-10	0.377	0.504	0.0
$2c$ (mm)	a (mm)	α (°)	N_f
0.98	t_w	32.61	2,738

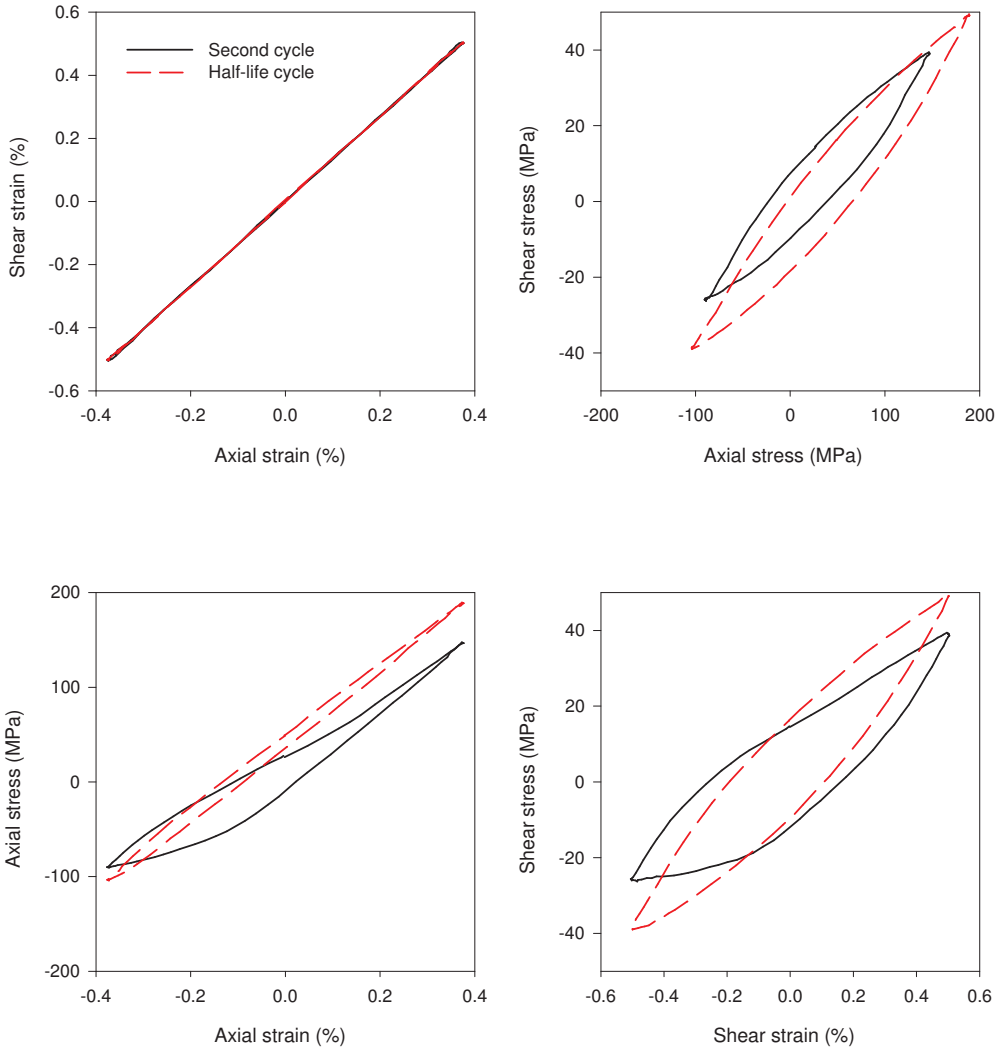

Test No.	ε_a (%)	γ_a (%)	φ (°)
BA-0-11	0.303	0.448	0.0
$2c$ (mm)	a (mm)	α (°)	N_f
1.65	NA	40.87	3,375

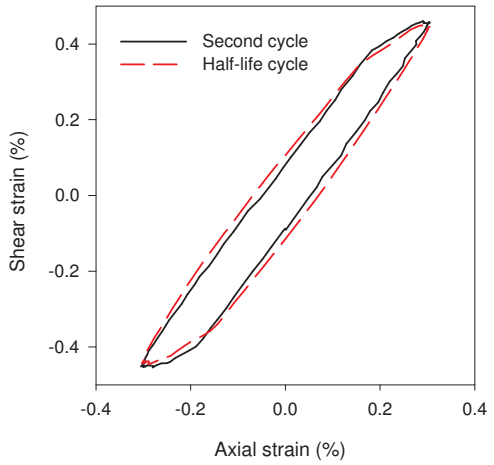

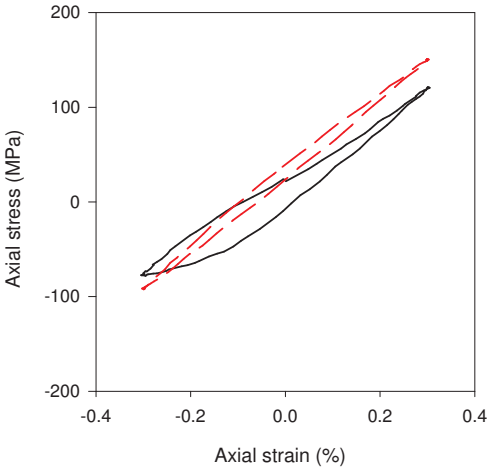

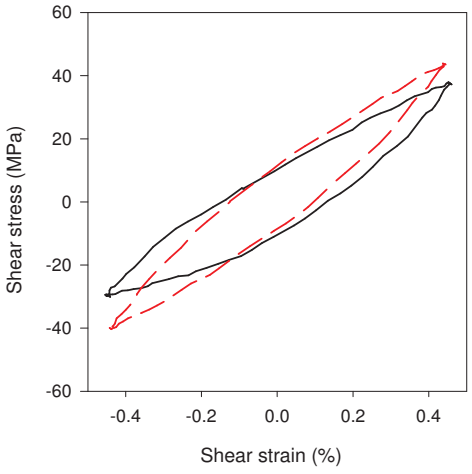

Test No.	ε_a (%)	γ_a (%)	φ (°)
BA-0-12	0.302	0.398	0.0
$2c$ (mm)	a (mm)	α (°)	N_f
0.785	0.425	32.63	3,870

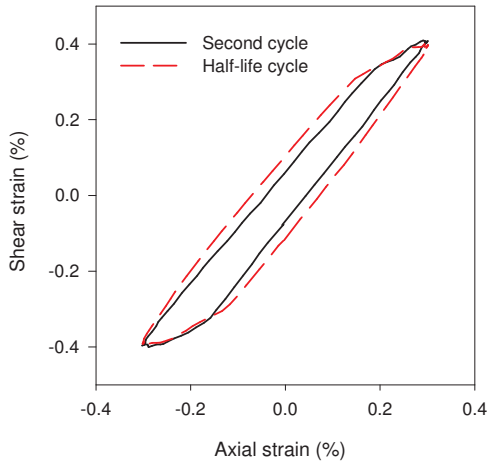

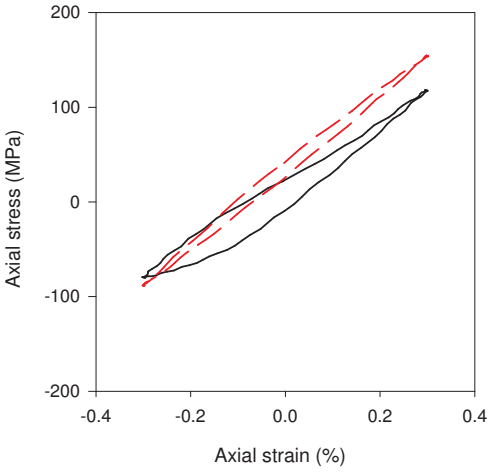

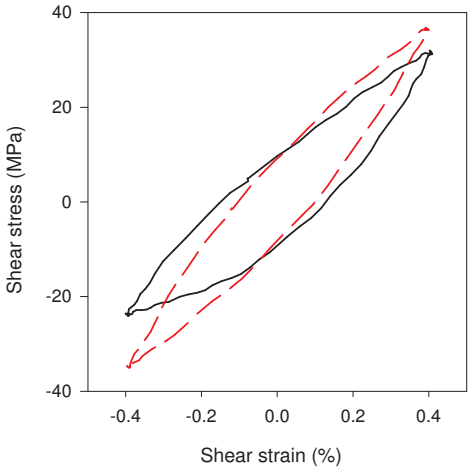

Test No.	ε_a (%)	γ_a (%)	φ (°)
BA-0-13	0.303	0.408	0.0
$2c$ (mm)	a (mm)	α (°)	N_f
1.1625	t_w	25.84	4,427

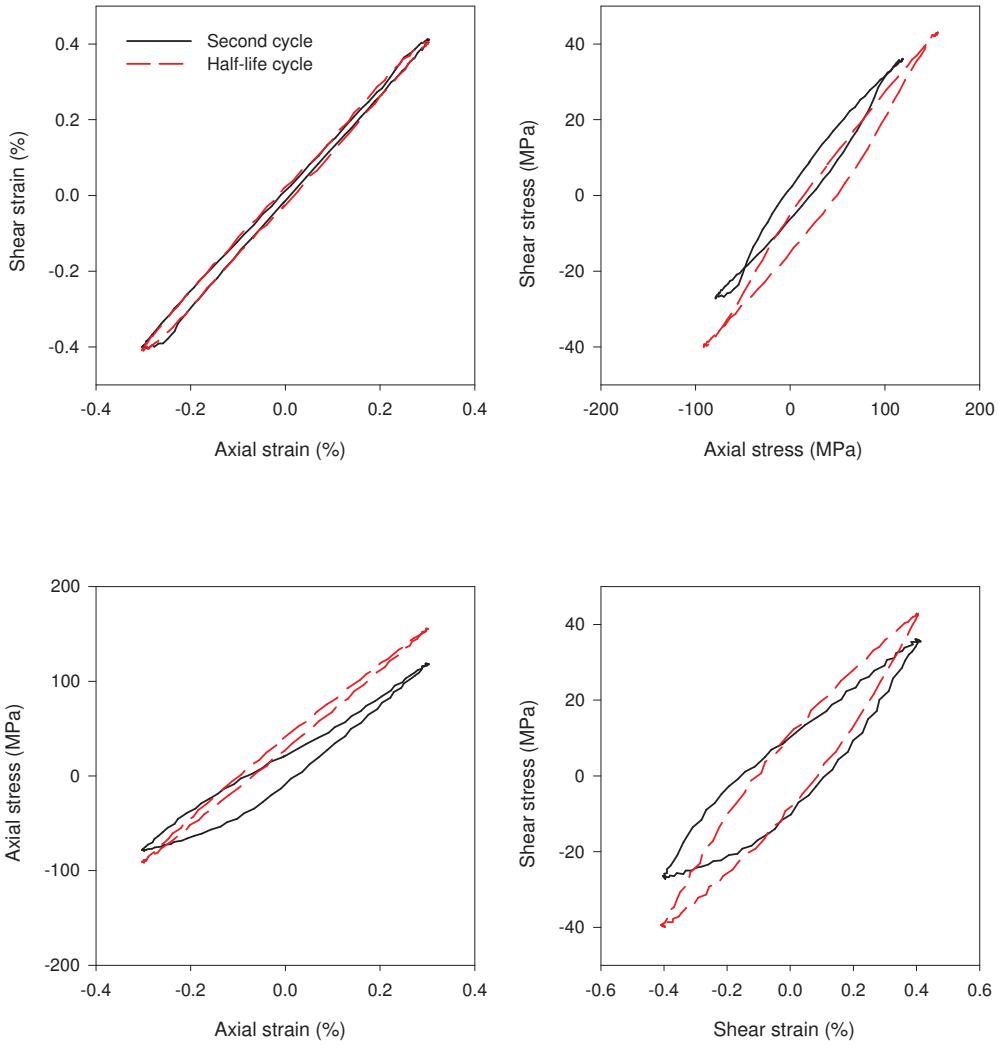

Test No.	ε_a (%)	γ_a (%)	φ (°)
BA-0-14	0.303	0.420	0.0
$2c$ (mm)	a (mm)	α (°)	N_f
1.5	t_w	24.45	4,974

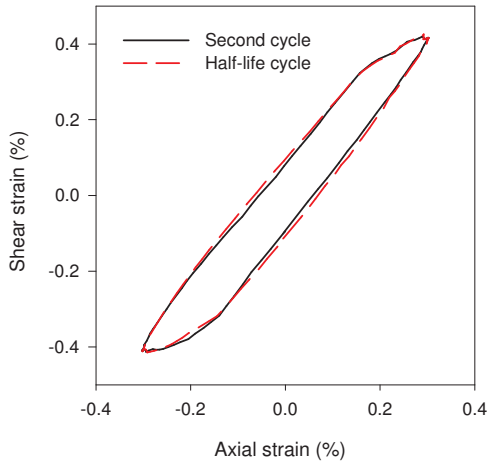

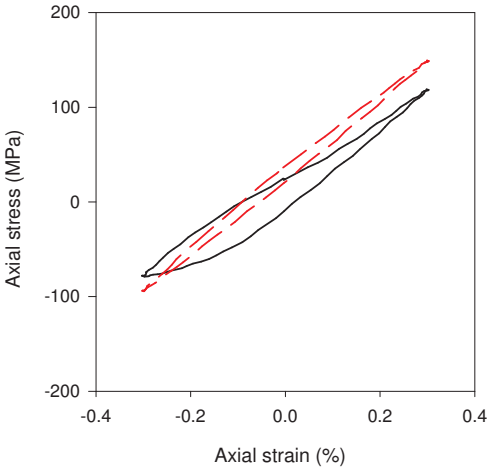

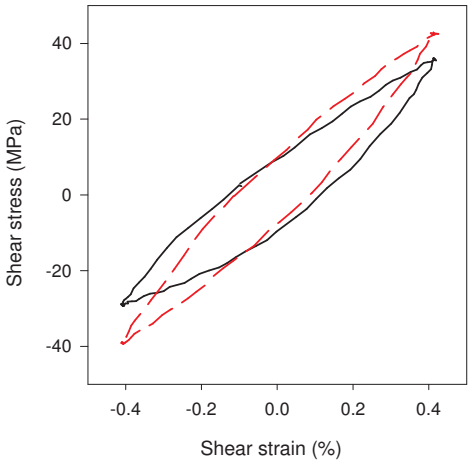

Test No.	ε_a (%)	γ_a (%)	φ (°)
BA-0-15	0.288	0.372	0.0
$2c$ (mm)	a (mm)	α (°)	N_f
0.88	0.88	32.97	8,215

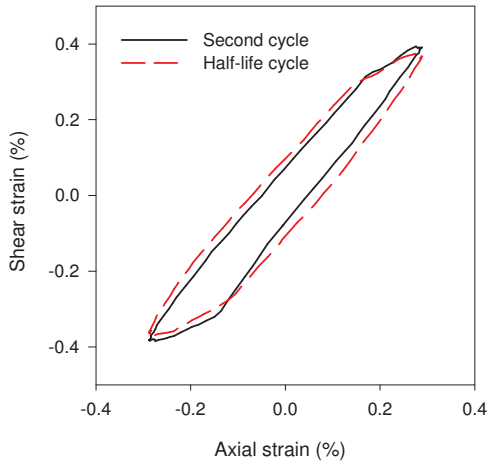

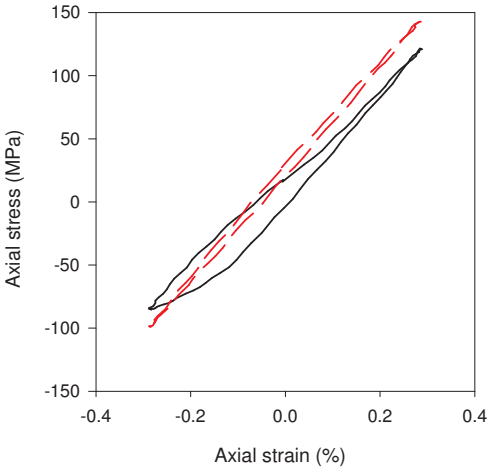

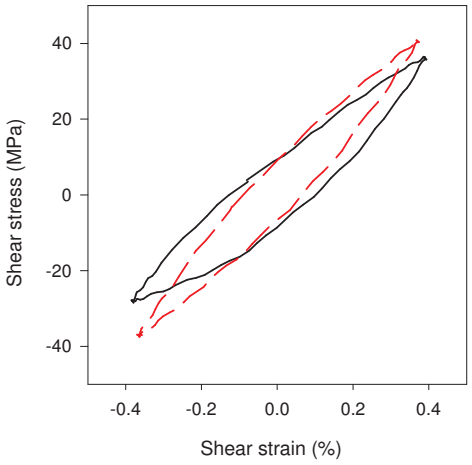

Test No.	ε_a (%)	γ_a (%)	φ (°)
BA-0-16	0.281	0.360	0.0
$2c$ (mm)	a (mm)	α (°)	N_f
0.77	NA	36.6	8,650

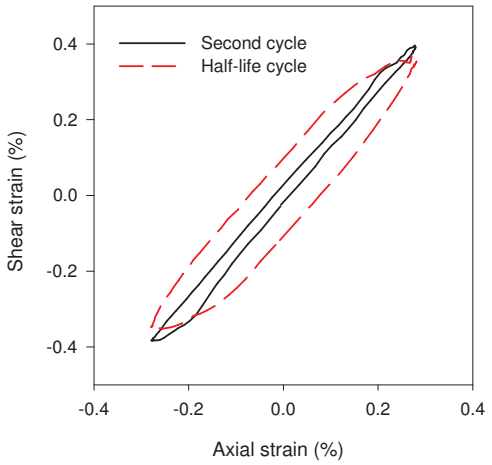

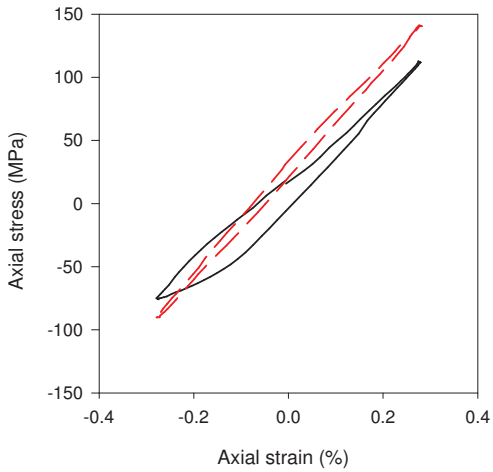

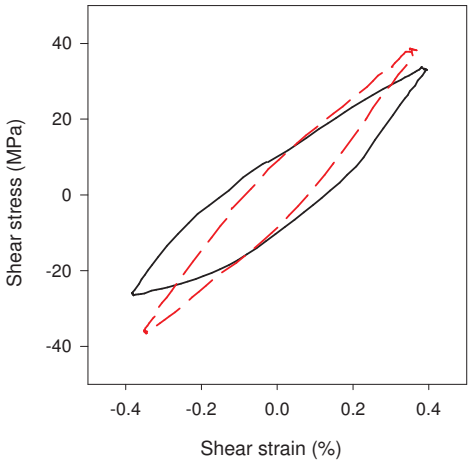

Test No.	ε_a (%)	γ_a (%)	φ (°)
BA-0-17	0.304	0.377	0.0
$2c$ (mm)	a (mm)	α (°)	N_f
NA	NA	NA	10,495

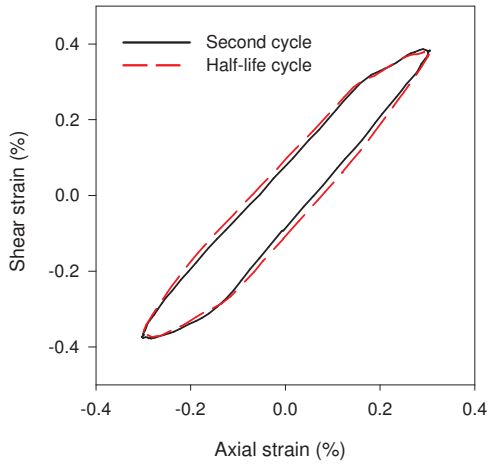

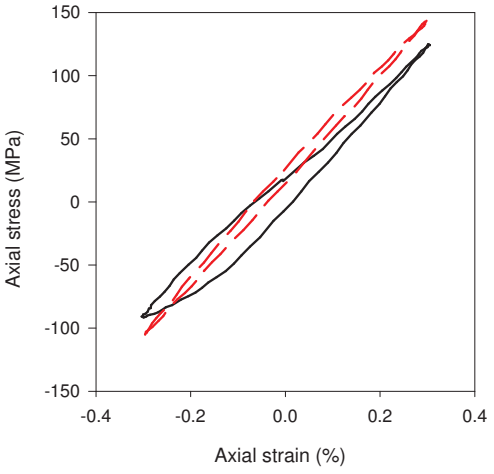

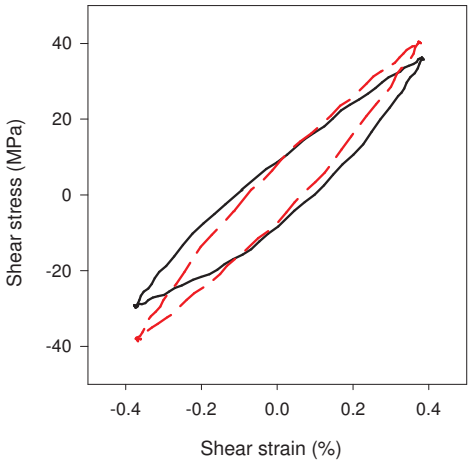

Test No.	ε_a (%)	γ_a (%)	φ (°)
BA-45-1	0.515	0.777	45.0
$2c$ (mm)	a (mm)	α (°)	N_f
2.71	0.455	31.1	989

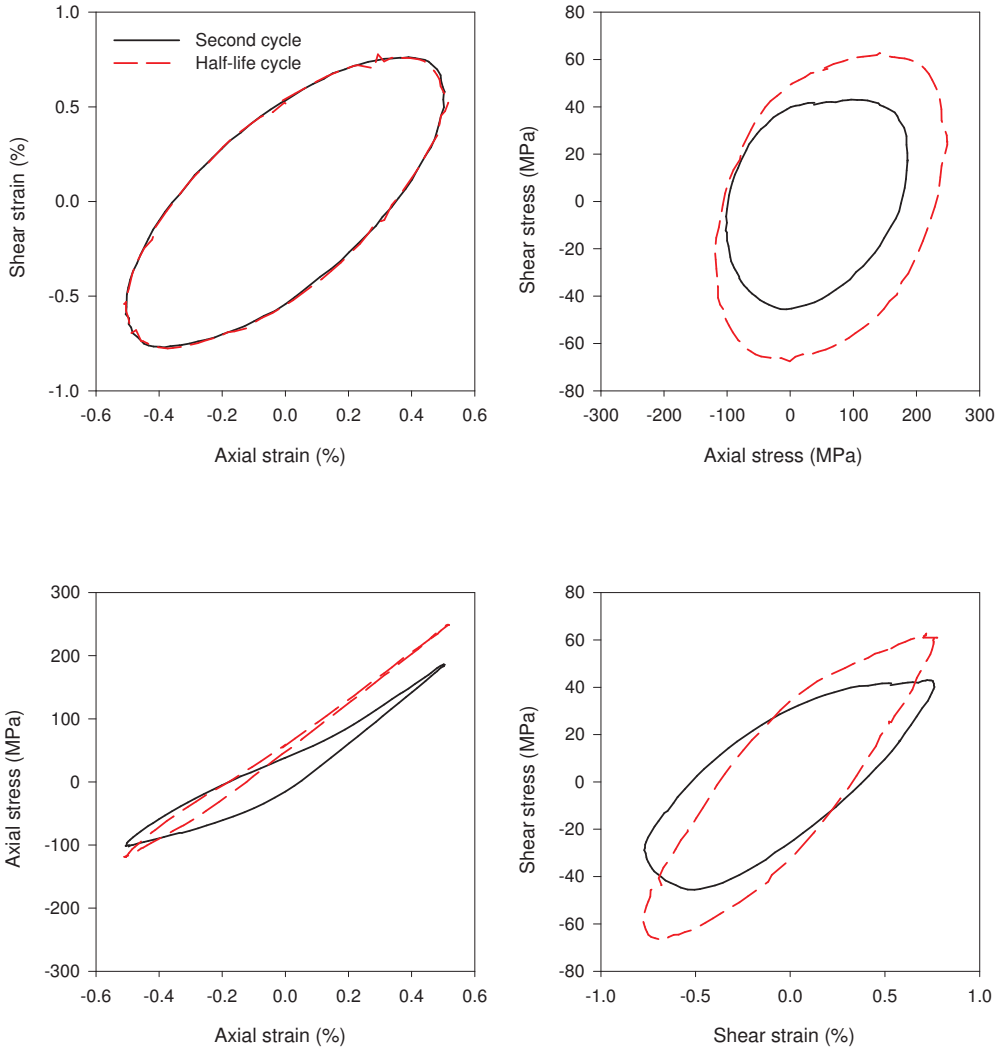

Test No.	ε_a (%)	γ_a (%)	φ (°)
BA-45-2	0.303	0.789	45.0
$2c$ (mm)	a (mm)	α (°)	N_f
1.625	0.31	90	1,181

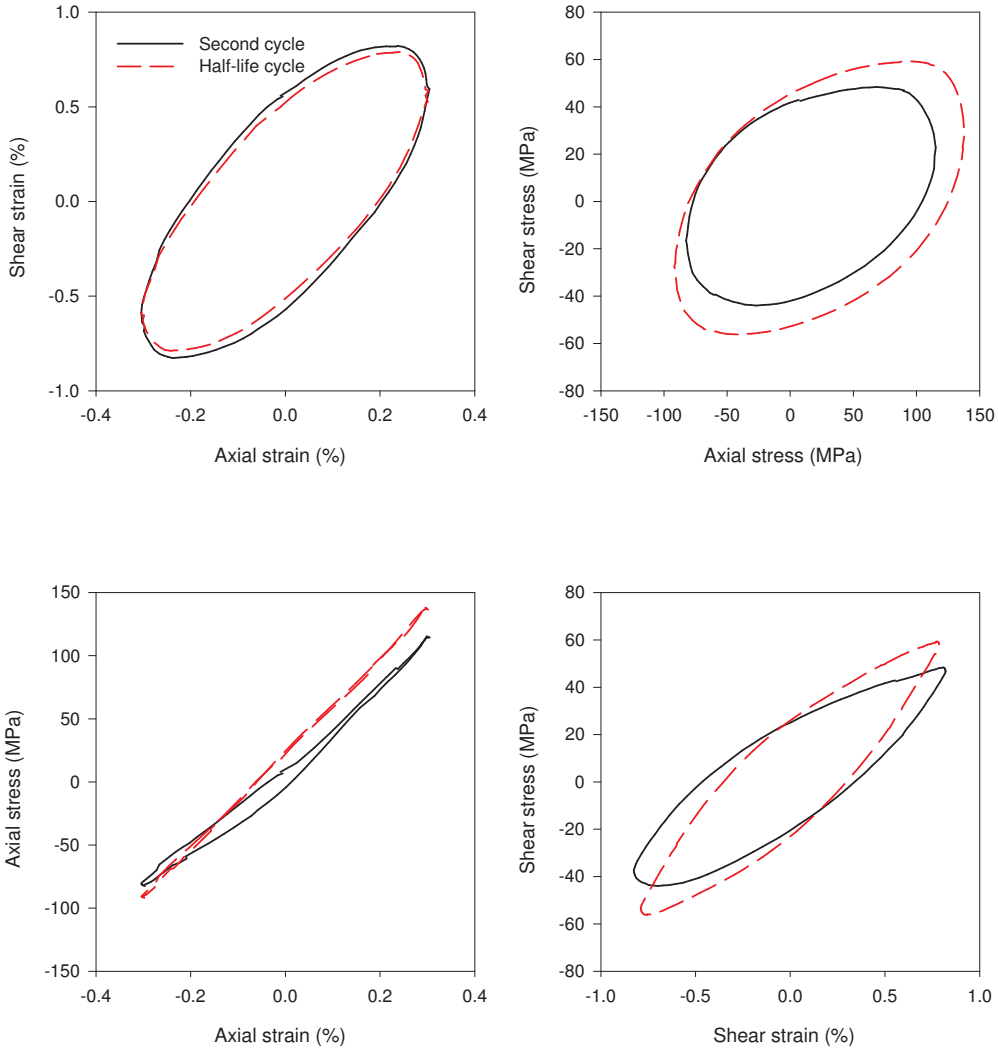

Test No.	ε_a (%)	γ_a (%)	φ (°)
BA-45-3	0.549	0.449	45.0
$2c$ (mm)	a (mm)	α (°)	N_f
0.77	0.805	28.8	1,445

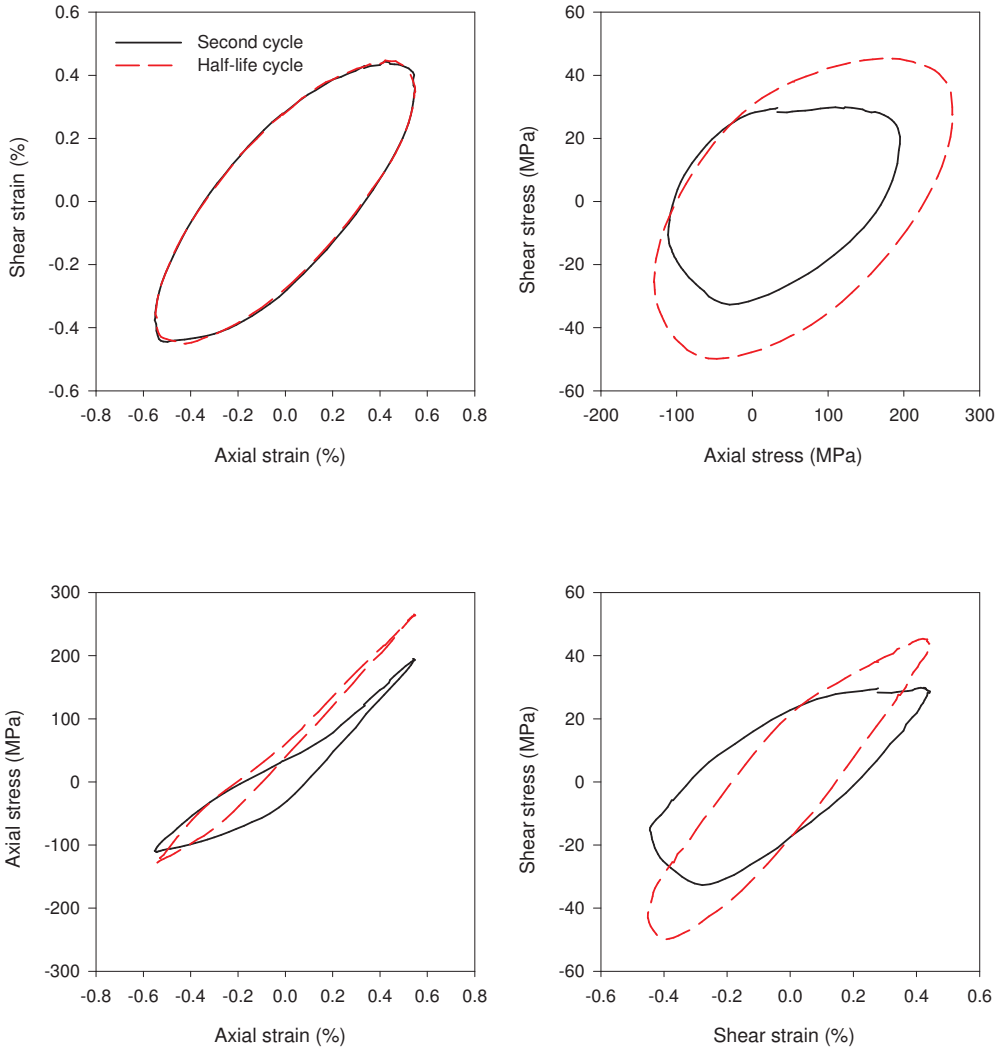

Test No.	ε_a (%)	γ_a (%)	φ (°)
BA-45-4	0.378	0.516	45.0
$2c$ (mm)	a (mm)	α (°)	N_f
NA	NA	NA	1,730

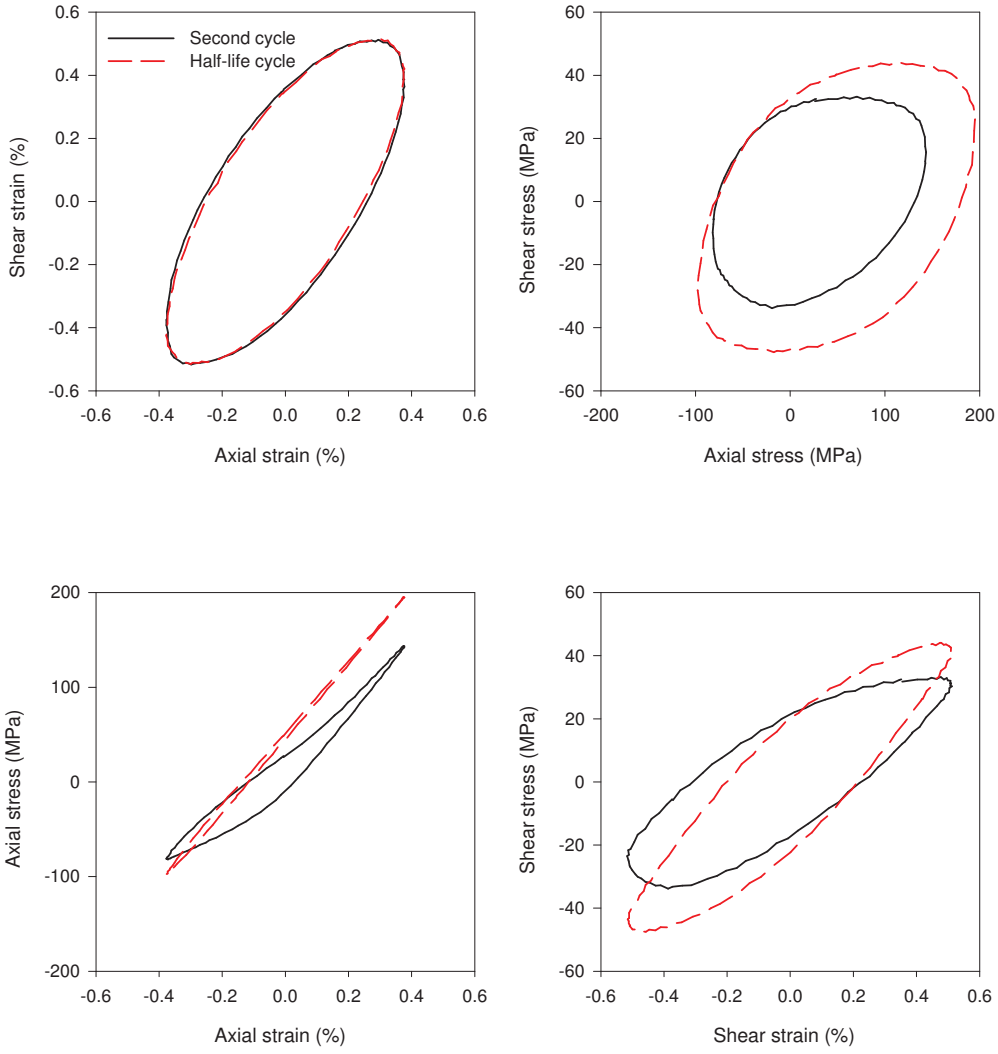

Test No.	ε_a (%)	γ_a (%)	φ (°)
BA-45-5	0.377	0.513	45.0
$2c$ (mm)	a (mm)	α (°)	N_f
3	t_w	36.46	2,375

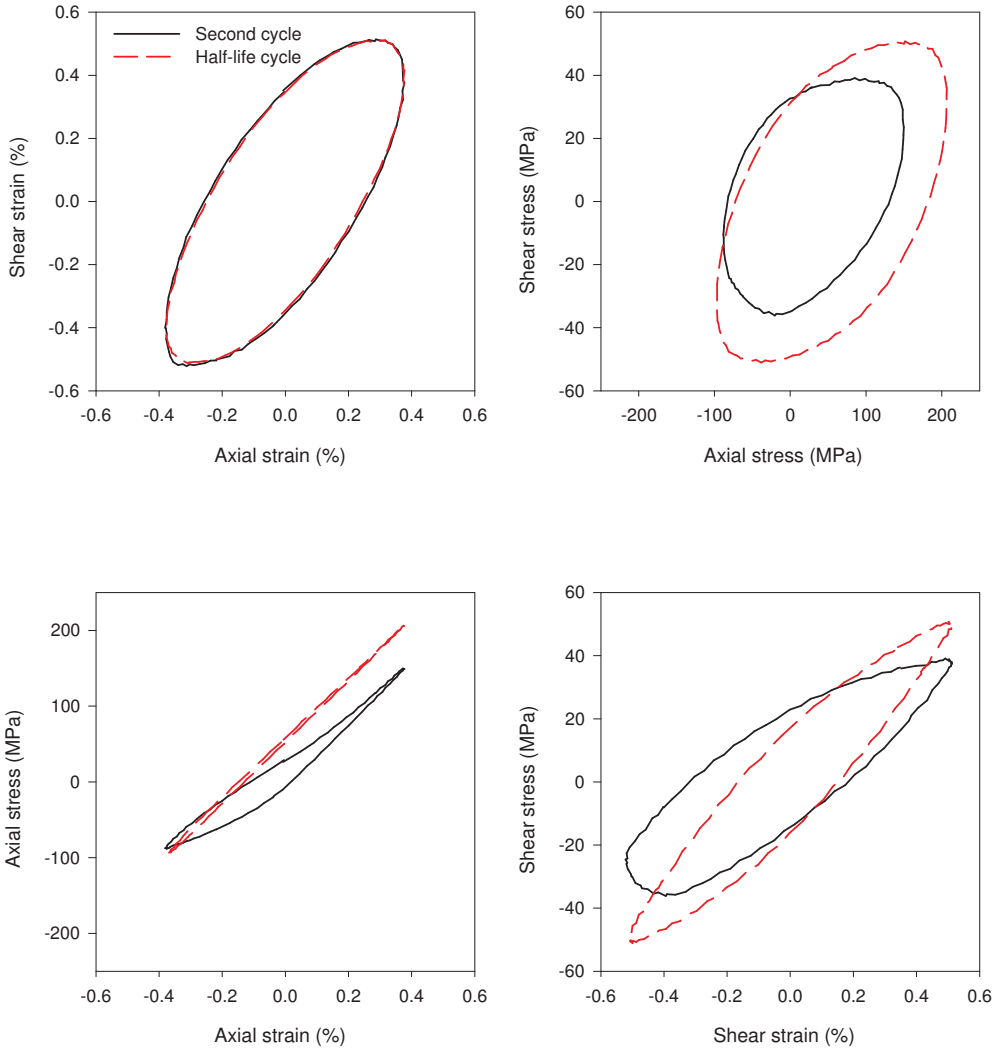

Test No.	ε_a (%)	γ_a (%)	φ (°)
BA-45-6	0.374	0.514	45.0
$2c$ (mm)	a (mm)	α (°)	N_f
0.68	t_w	21.67	2,839

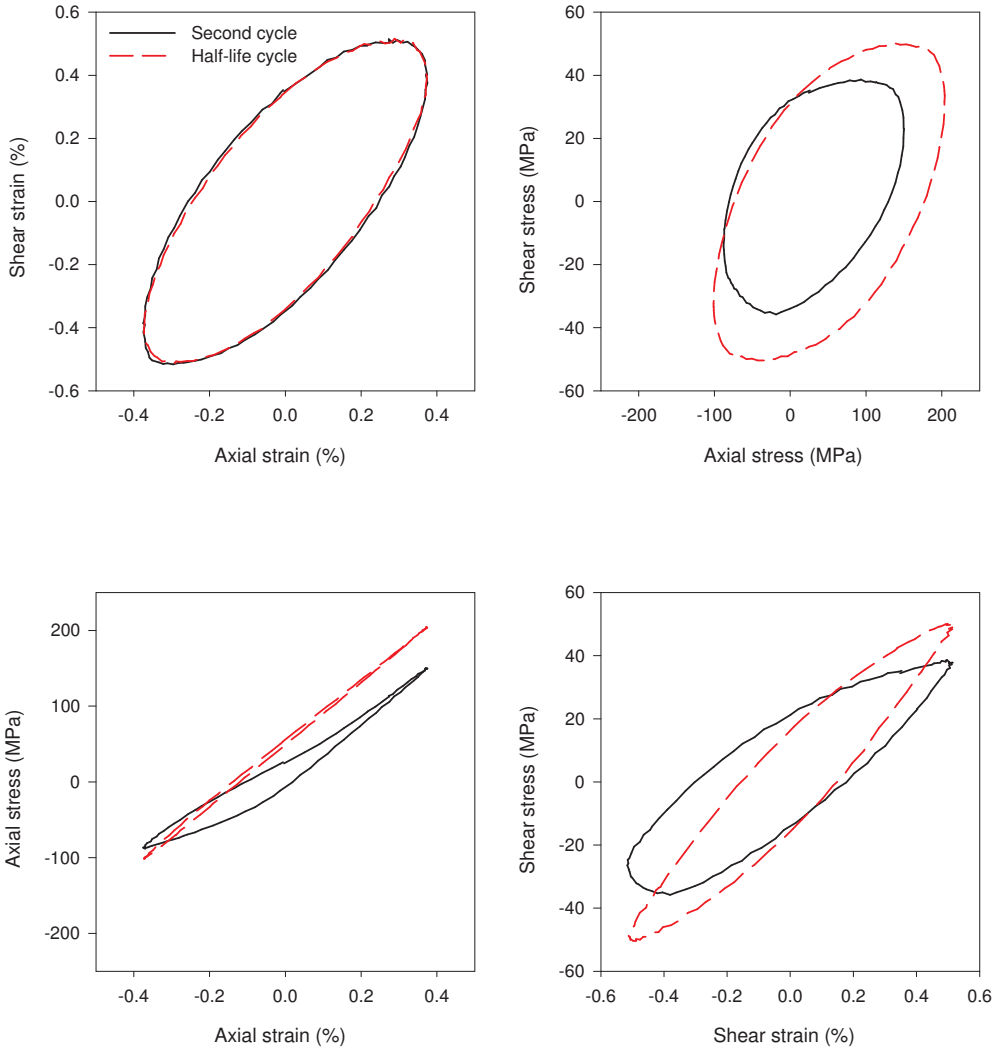

Test No.	ε_a (%)	γ_a (%)	φ (°)
BA-90-1	0.505	0.761	90.0
$2c$ (mm)	a (mm)	α (°)	N_f
4.915	0.29	4.57	974

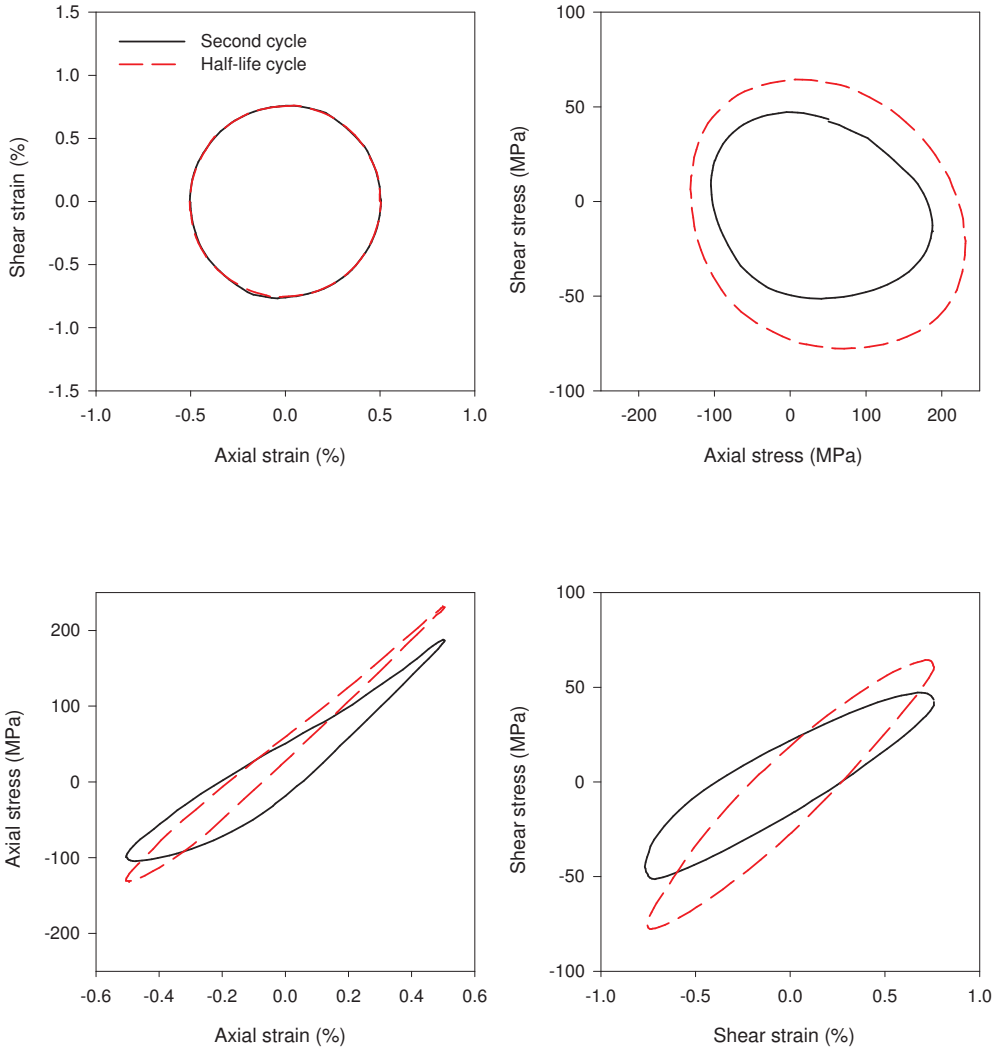

Test No.	ε_a (%)	γ_a (%)	φ (°)
BA-90-2	0.502	0.761	90.0
$2c$ (mm)	a (mm)	α (°)	N_f
3.77	t_w	46.6	1,115

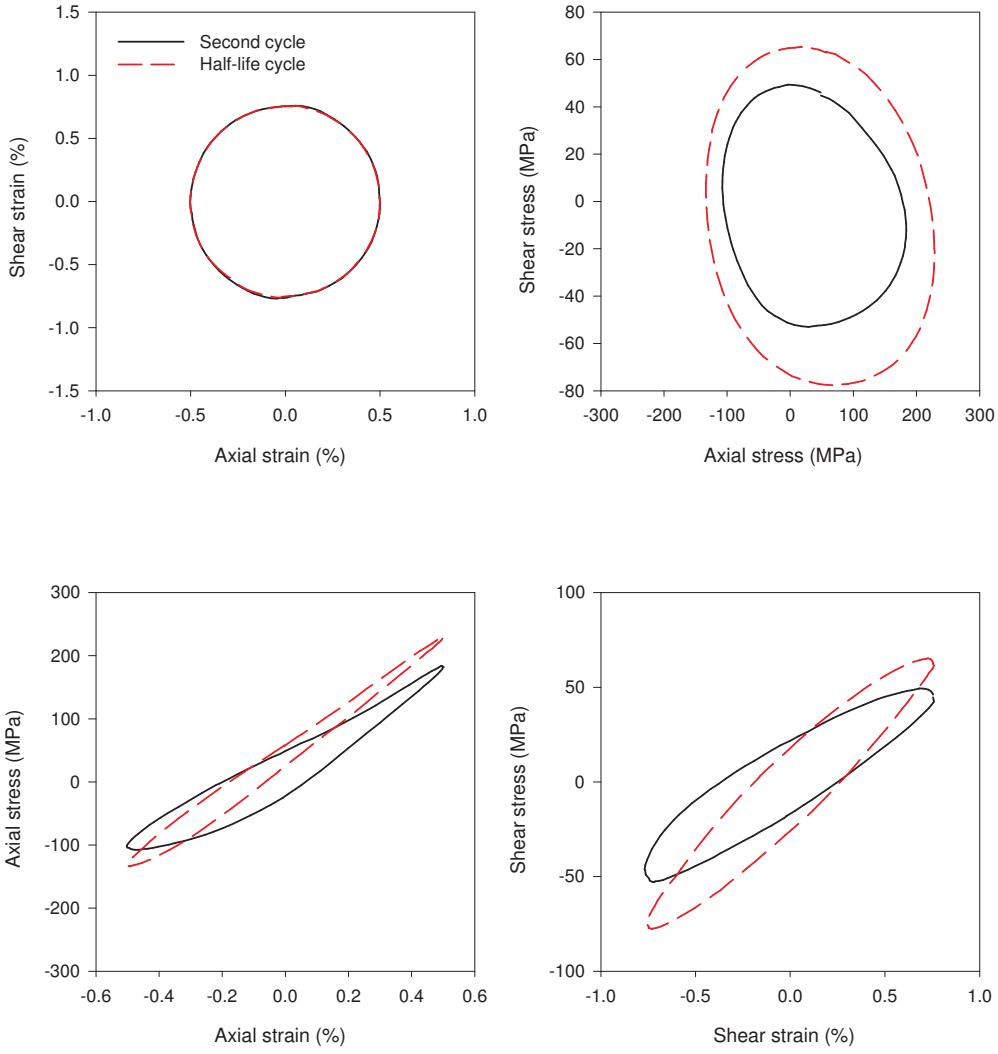

Test No.	ε_a (%)	γ_a (%)	φ (°)
BA-90-3	0.553	0.461	90.0
$2c$ (mm)	a (mm)	α (°)	N_f
1.83	t_w	21.98	1,159

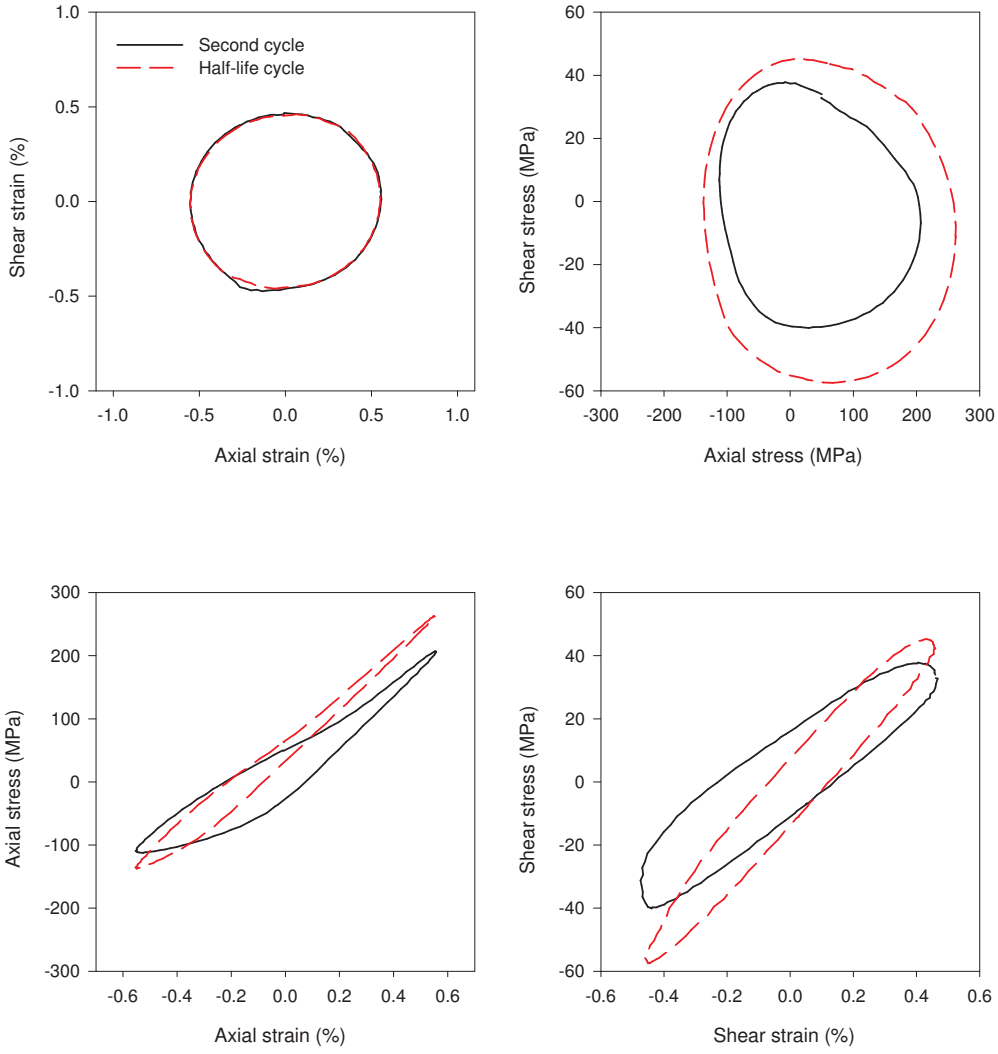

Test No.	ε_a (%)	γ_a (%)	φ (°)
BA-90-4	0.554	0.460	90.0
$2c$ (mm)	a (mm)	α (°)	N_f
NA	NA	NA	1,222

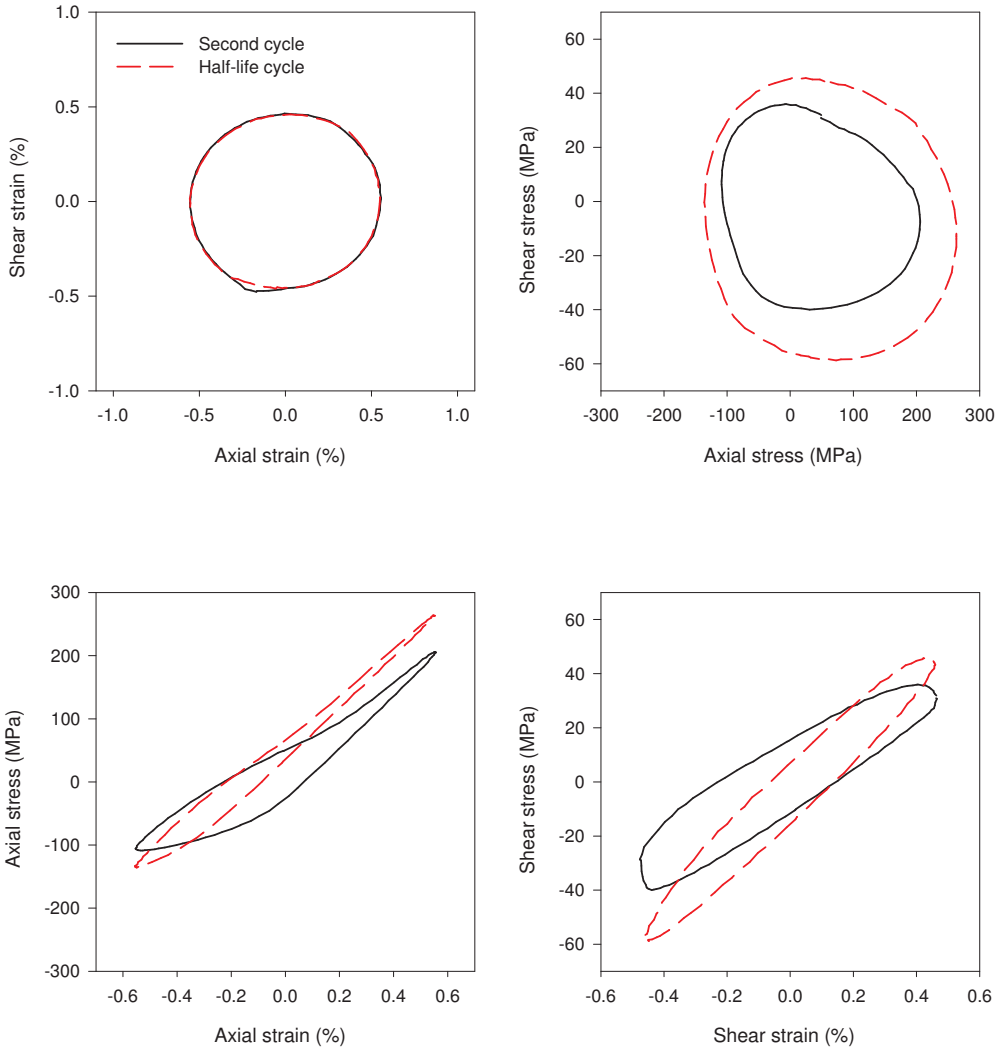

Test No.	ε_a (%)	γ_a (%)	φ (°)
BA-90-5	0.551	0.439	90.0
$2c$ (mm)	a (mm)	α (°)	N_f
4.415	0.385	6.4	1,307

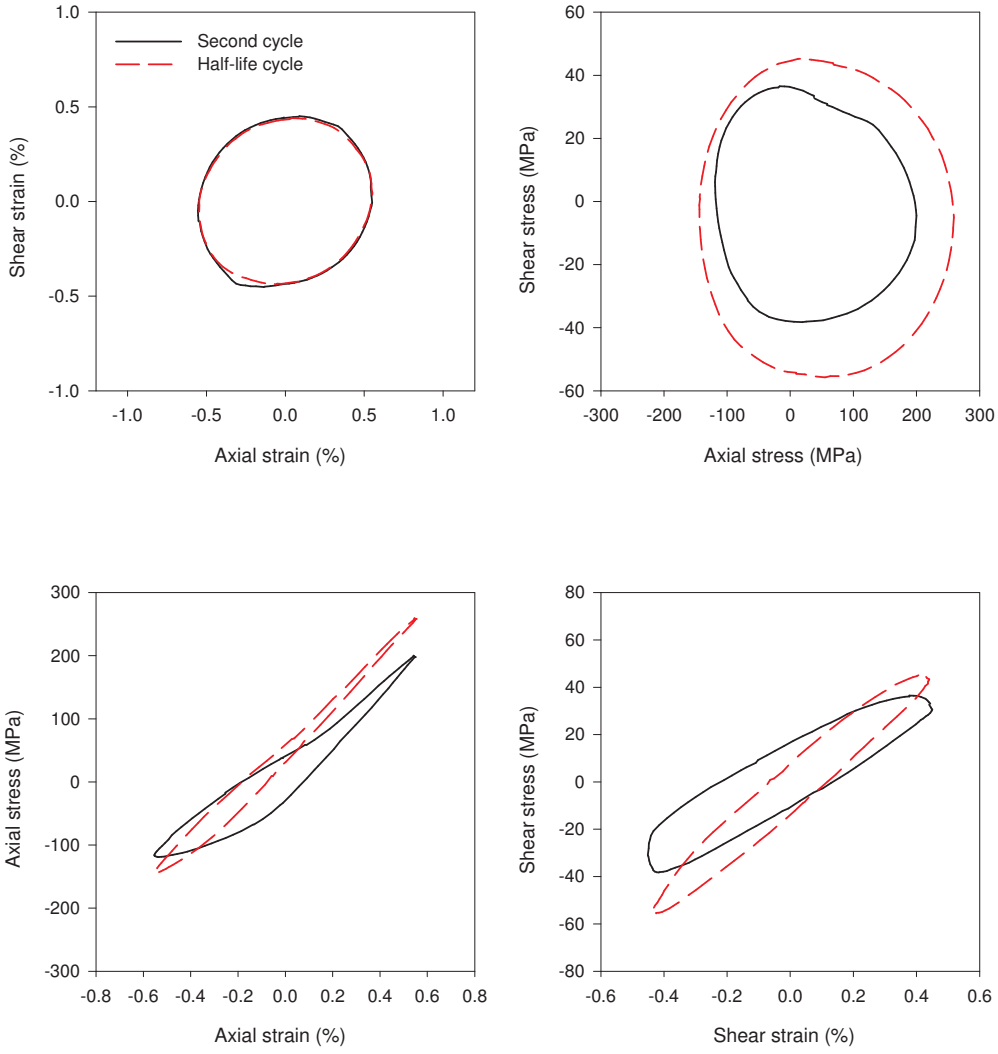

Test No.	ε_a (%)	γ_a (%)	φ (°)
BA-90-6	0.303	0.814	90.0
$2c$ (mm)	a (mm)	α (°)	N_f
1.28	0.445	90	1,386

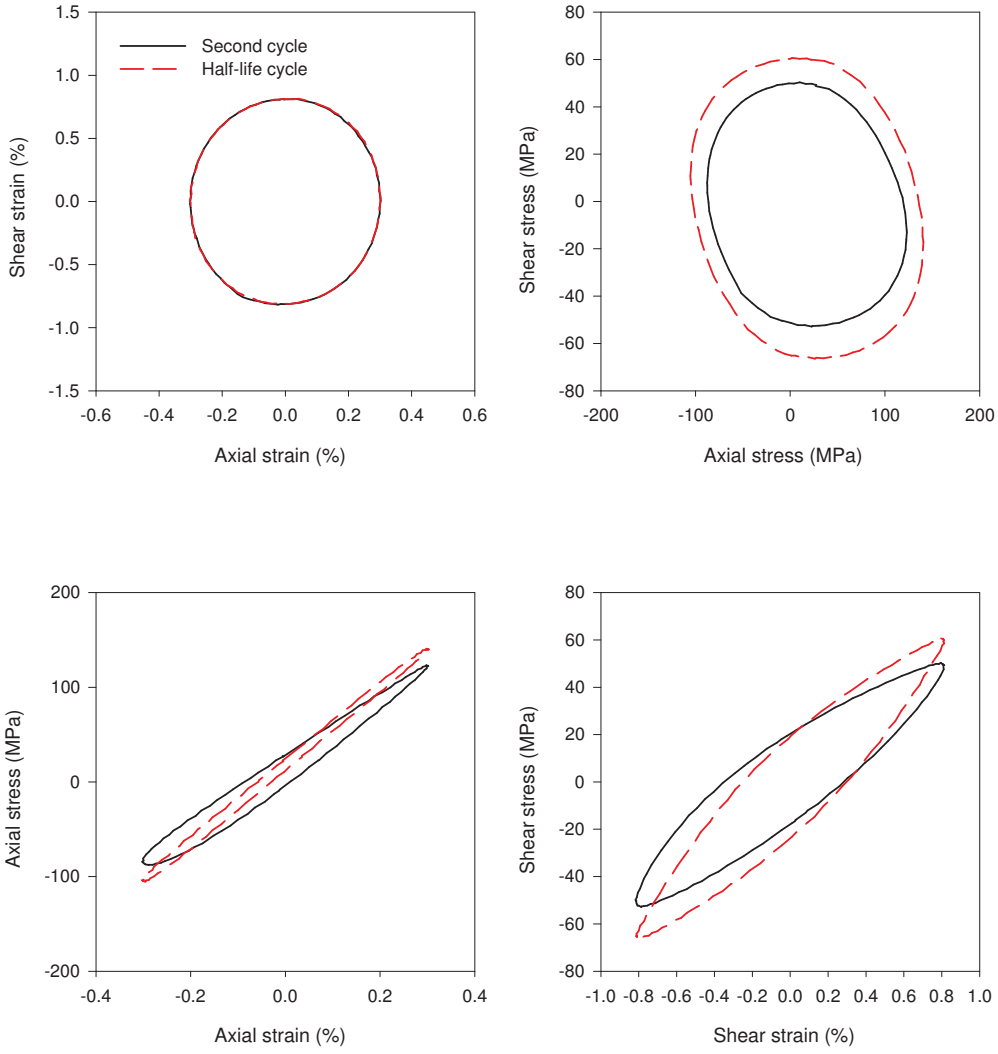

Test No.	ε_a (%)	γ_a (%)	φ (°)
BA-90-7	0.303	0.814	90.0
$2c$ (mm)	a (mm)	α (°)	N_f
2.035	0.41	90	2,123

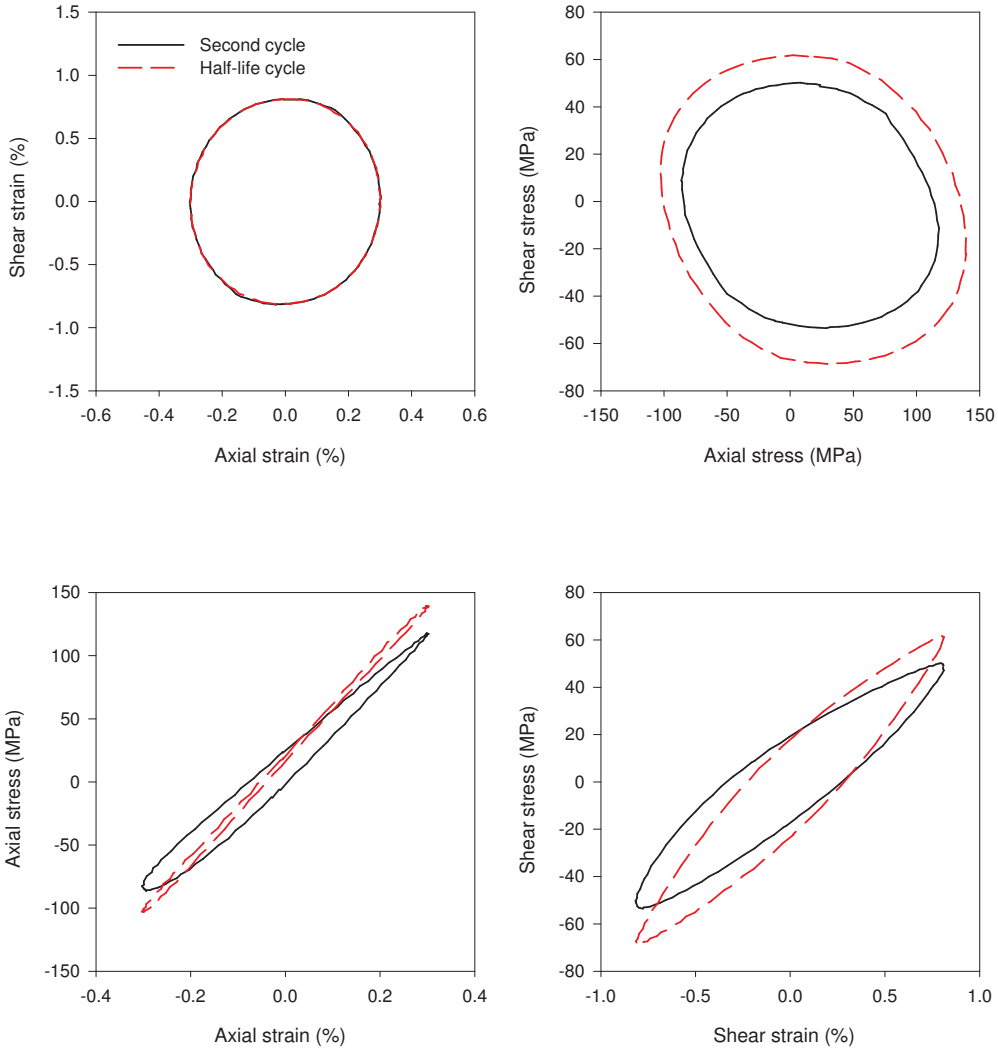

Test No.	ε_a (%)	γ_a (%)	φ (°)
BA-90-8	0.379	0.513	90.0
$2c$ (mm)	a (mm)	α (°)	N_f
4.9	0.29	36.1	2,220

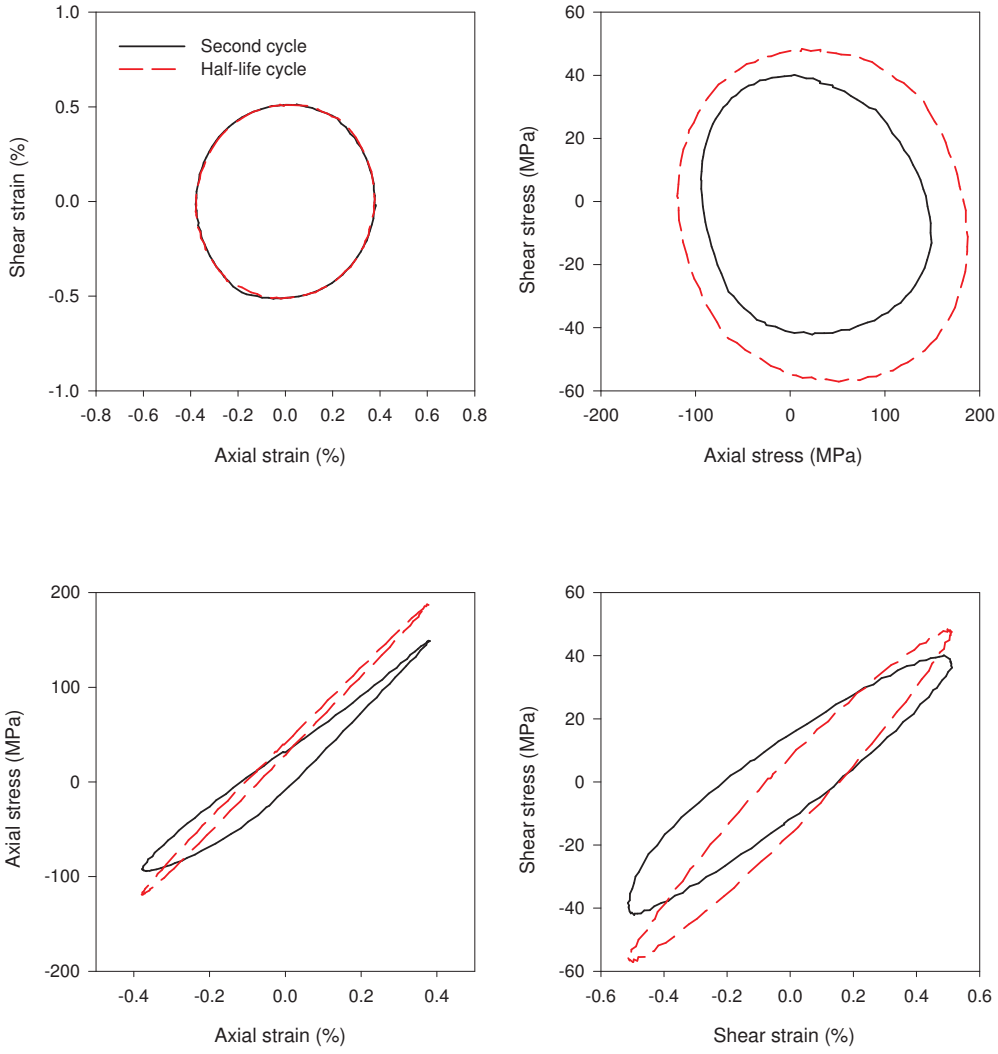

Test No.	ε_a (%)	γ_a (%)	φ (°)
BA-90-9	0.305	0.816	90.0
$2c$ (mm)	a (mm)	α (°)	N_f
1.5	NA	90	2,765

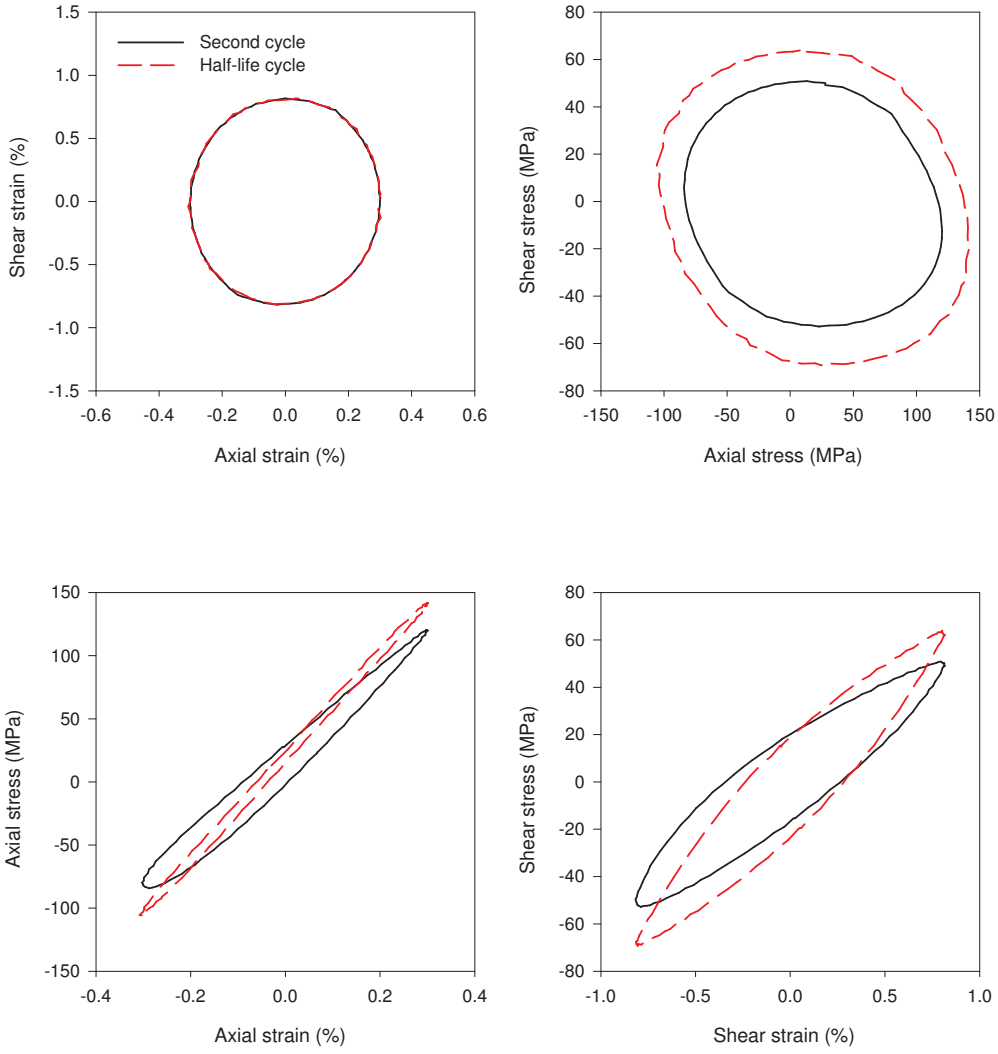

Test No.	ε_a (%)	γ_a (%)	φ (°)
BA-90-10	0.300	0.798	90.0
$2c$ (mm)	a (mm)	α (°)	N_f
1.66	0.62	32.195	2,800

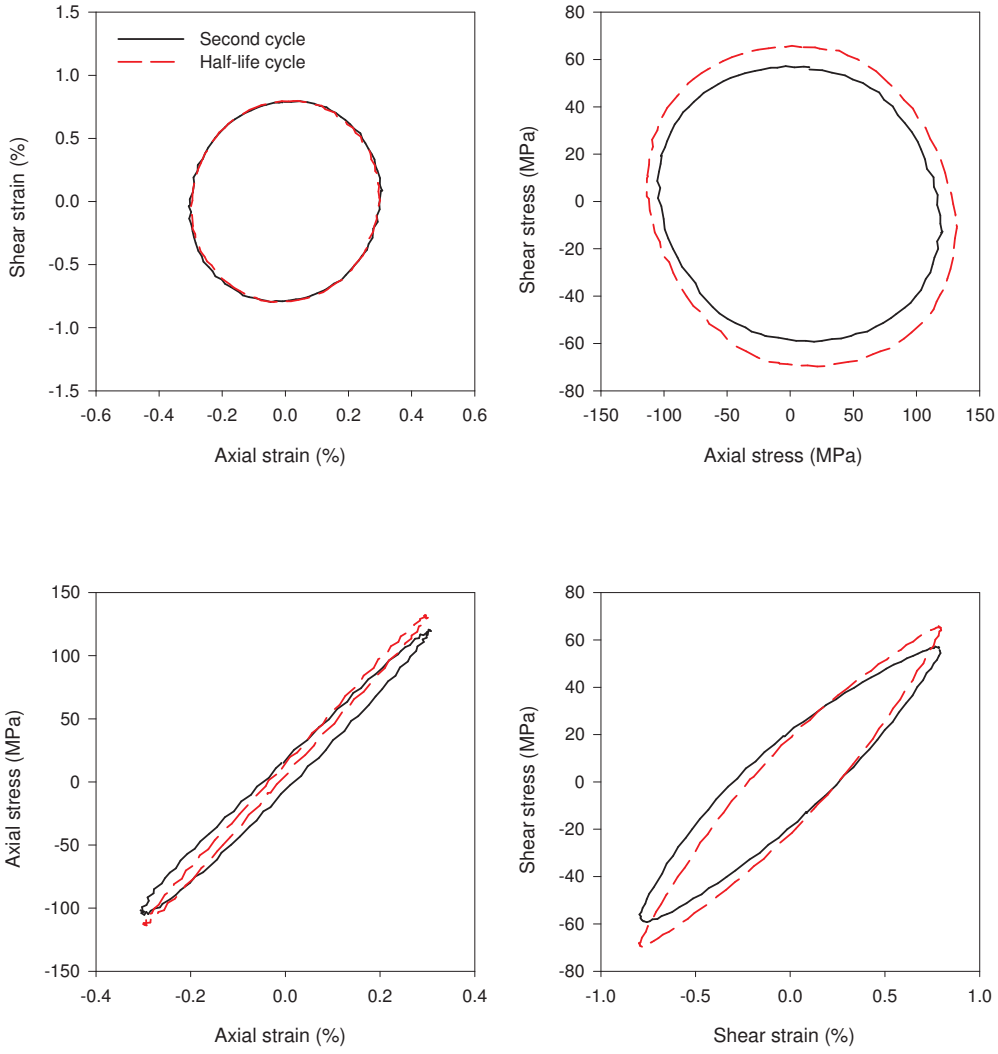

Test No.	ε_a (%)	γ_a (%)	φ (°)
BA-90-11	0.381	0.513	90.0
$2c$ (mm)	a (mm)	α (°)	N_f
2.04	0.725	10.14	3,215

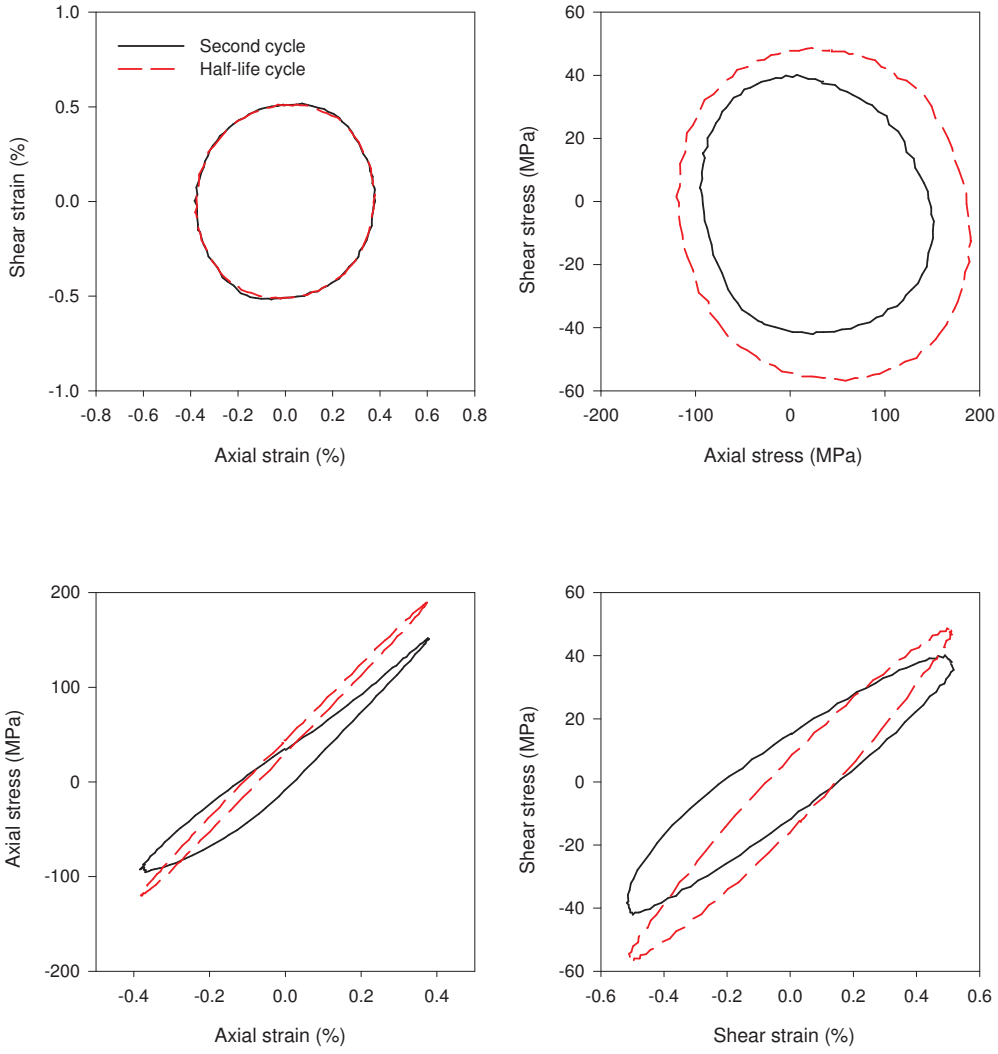

References

[1] M. L. Sharp, G. E. Nordmark, Menzemer, Fatigue design of aluminum components and structure.

[2] H. O. Fuchs, R. I. Stephens, Metal Fatigue in Engineering, Wiley, New York, 1980.

[3] W. S. Miller, L. Zhuang, J. Bottema, A. J. Wittebrood, P. D. H. A. Smet, A. Vieregge, Recent development in aluminium alloys for the automotive industry, Materials Science and Engineering A 280 (1) (2000) 37–49.

[4] C. Blawert, N. Hort, K. U. Kainer, Automotive applications of magnesium and its alloys, Trans. Indian Inst. Met. 57 (4) (2004) 397–408.

[5] H. Friedrich, S. Schumann, Research for a new age of magnesium in the automotive industry, Journal of Materials Processing Technology 117 (3) (2001) 276–281.

[6] B. L. Mordike, T. Ebert, Magnesium: Properties-applications-potential, Materials Science and Engineering: A 302 (1) (2001) 37–45.

[7] M. Kulekci, Magnesium and its alloys applications in automotive industry, The International Journal of Advanced Manufacturing Technology 39 (9) (2008) 851–865.

[8] H. Watarai, Trend of research and development for magnesium alloys-reducing the weight of structural materials in motor vehicles, Science and Technology Trends (18) (2006) 84–97.

[9] A. Luo, Magnesium: Current and potential automotive applications, JOM Journal of the Minerals, Metals and Materials Society 54 (2) (2002) 42–48.

[10] JMA, "the main projects for development of motor vehicles using magnesium" and "actual situation of mg alloy applications to motor vehicles", Tech. rep., The Japan Magnesium Association (2005).

[11] S. Hasegawa, Y. Tsuchida, H. Yano, M. Matsui, Evaluation of low cycle fatigue life in AZ31 magnesium alloy, International Journal of Fatigue 29 (2007) 1839–1845.

[12] D. W. Brown, A. Jain, S. R. Agnew, B. Clausen, Twinning and detwinning during cyclic deformation of Mg alloy AZ31B, Materials science forum 539-43 (2007) 3407–3413.

[13] H. Zenner, F. Renner, Cyclic material behaviour of magnesium die castings and extrusions, International Journal of Fatigue 24 (2002) 1255–1260.

[14] S. Hyuk Park, S.-G. Hong, B. Ho Lee, W. Bang, C. Soo Lee, Low-cycle fatigue characteristics of rolled Mg-3Al-1Zn alloy, International Journal of Fatigue 32 (11) (2010) 1835–1842.

[15] J. B. Jordon, J. B. Gibson, M. F. Horstemeyer, H. E. Kadiri, J. C. Baird, A. A. Luo, Effect of twinning, slip, and inclusions on the fatigue anisotropy of extrusion-textured AZ61 magnesium alloy, Materials Science and Engineering: A 528 (22-23) (2011) 6860–6871.

[16] C. M. Sonsino, K. Dieterich, Fatigue design with cast magnesium alloys under constant and variable amplitude loading, International Journal of Fatigue 28 (3) (2006) 183–193.

[17] L. Wu, S. R. Agnew, Y. Ren, D. W. Brown, B. Clausen, G. M. Stoica, H. R. Wenk, P. K. Liaw, The effects of texture and extension twinning on the low-cycle fatigue behavior of a rolled magnesium alloy, AZ31B, Materials Science and Engineering: A 527 (26) (2010) 7057–7067.

[18] A. Aluminum Automotive Extrusion Manual, Tech. rep., The Aluminum Association, Inc (1998).

[19] S. Begum, D. Chen, S. Xu, A. Luo, Low cycle fatigue properties of an extruded AZ31 magnesium alloy, International Journal of Fatigue 31 (2009) 726–735.

[20] L. Chen, C. Wang, W. Wu, Z. Liu, G. M. Stoica, L. Wu, P. K. Liaw, Low-cycle fatigue behavior of an as-extruded AM50 magnesium alloy, Metallurgical and Materials Transactions A 38 (2007) 2235–2241.

[21] S. H. Park, S.-G. Hong, W. Bang, C. S. Lee, Effect of anisotropy on the low-cycle fatigue behavior of rolled AZ31 magnesium alloy, Materials Science and Engineering: A 527 (2010) 417–423.

[22] Q. Yu, J. Zhang, Y. Jiang, Q. Li, Multiaxial fatigue of extruded AZ61A magnesium alloy, International Journal of Fatigue 33 (3) (2011) 437–447.

[23] F. Lv, F. Yang, Q. Q. Duan, Y. S. Yang, S. D. Wu, S. X. Li, Z. F. Zhang, Fatigue properties of rolled magnesium alloy (AZ31) sheet: Influence of specimen orientation, International Journal of Fatigue 33 (5) (2011) 672–682.

[24] F. Lv, F. Yang, S. X. Li, Z. F. Zhang, Effects of hysteresis energy and mean stress on low-cycle fatigue behaviors of an extruded magnesium alloy, Scripta Materialia 65 (1) (2011) 53–56.

[25] T. J. Luo, Y. S. Yang, W. H. Tong, Q. Q. Duan, X. G. Dong, Fatigue deformation characteristic of as-extruded AM30 magnesium alloy, Materials & Design 31 (3) (2010) 1617–1621.

[26] H. E. Kadiri, Y. Xue, M. F. Horstemeyer, J. B. Jordon, P. T. Wang, Identification and modeling of fatigue crack growth mechanisms in a die-cast AM50 magnesium alloy, Acta Materialia 54 (19) (2006) 5061–5076.

[27] J. B. Jordon, M. F. Horstemeyer, N. Yang, J. F. Major, K. A. Gall, J. Fan, D. L. McDowell, Microstructural inclusion influence on fatigue of a cast A356 aluminum alloy, Metallurgical and Materials Transactions: A 41 (2) (2010) 356–363.

[28] Y. Xue, H. El Kadiri, M. F. Horstemeyer, J. B. Jordon, H. Weiland, Micromechanisms of multistage fatigue crack growth in a high-strength aluminum alloy, Acta Materialia 55 (6) (2007) 1975–1984.

[29] G. Salerno, R. Magnabosco, C. d. Moura Neto, Mean strain influence in low cycle fatigue behavior of AA7175-T1 aluminum alloy, International Journal of Fatigue 29 (5) (2007) 829–835.

[30] H. C. Heikkenen, F.-S. Lin, E. A. Starke Jr, The low cycle fatigue behavior of high strength 7xxx-type aluminium alloys in the T7351 condition, Materials Science and Engineering 51 (1) (1981) 17–23.

[31] T. Srivatsan, The low-cycle fatigue and cyclic fracture behaviour of 7150 aluminium alloy, International Journal of Fatigue 13 (4) (1991) 313–321.

[32] American society for testing and materials in: Standard terminology relating to fatigue and fracture testing E1823-10a (2010).

[33] American society for testing and materials, in: Standard test methods for tension testing of metallic materials E8/E8M-09 (2009).

[34] American society for testing and materials, in: Standard test method for shear modulus at room temperature E143-02 (2008).

[35] R. I. Stephens, A. Fatemi, R. R. Stephens, H. O. Fuchs, Metal Fatigue in Engineering, 2nd edition, John Wiley and Sons, Inc, New Your, 2001.

[36] American society for testing and materials, in: Strain-controlled axial-torsional fatigue testing with thin walled tubular specimens E2207-08 (2008).

[37] American society for testing and materials, in: American society for testing and materials, in: Standard practice for strain-controlled fatigue testing E606-04 (2004).

[38] S. Manson, discussion on JF. Tavernelli and LF. Coffin "Experimental support for generalized equation predicting low cycle fatigue", Trans. ASME, J Basic Eng. 84 (4) (1962) 537.

[39] J. Tavernelli, L. Coffin, Experimental support for generalized equation predicting low cycle fatigue, Trans. ASME, J Basic Eng. 84 (4) (1962) 533.

[40] J. E. Shigley, C. R. Mischke, R. G. Budynas, Mechanical Engineering Design, seventh ed Edition, McGraw-Hill, New York, 2003.

[41] H. Neuber, Theory of stress concentration for shear-strained prismatical bodies with arbitrary non-linear stress-strain law, Journal of Applied Mechanics 28 (1961) 544–550.

[42] K. Molski, G. Glinka, A method of elastic-plastic stress and strain calculation at a notch root, Materials Science and Engineering 50 (1) (1981) 93–100.

[43] C. C. Chu, Incremental multiaxial neuber correction for fatigue analysis, Society of Automotive Engineers (950705).

[44] M. Hoffmann, T. Seeger, A generalized method for estimating multiaxial elastic-plastic notch stresses and strain. part I: Theory, Trans. ASME, J Eng Mater Tech 107 (1985) 250–254.

[45] Y. L. Lee, Y. J. Chiang, H. H. Wong, A constitutive model for estimating multiaxial notch strains, Journal of Engineering Materials and Technology 117 (1995) 33–40.

[46] A. Moftakhar, A. Buczynski, G. Glinka, Elastic-plastic stress-strain calculation in notched bodies subjected to nonproportional loading, International journal of fracture 70 (1995) 357–373.

[47] J. Morrow, Cyclic plastic strain energy and fatigue of metals, Internal Friction, Damping, and Cyclic Plasticity ASTM STP 378 (1965) 45.

[48] K. N. Smith, P. Watson, T. H. Topper, A stress-strain function for the fatigue of metals, J. Mater 5 (1970) 767–778.

[49] O. H. Basquin, The exponential law of endurance tests, Proc. ASTM 10 (Part 11) (1910) 625.

[50] F. Ellyin, A criterion for fatigue under multiaxial states of stress, in: Mechanics Research Conmmunications, Vol. 1, 1974, pp. 219–224.

[51] F. Ellyin, K. Golos, Multiaxial fatigue damage criterion, Journal of Engineering Materials and Technology 110 (1) (1988) 63–68.

[52] Y. S. Garud, A new approach to the evaluation of fatigue under multiaxial loadings, Journal of Engineering Materials and Technology 103 (1981) 118–126.

[53] J. Morrow, Internal friction, damping and cyclic plasticity, ASTM STP 378 (1965) 4587.

[54] G. Halford, The energy required for fatigue, Journal of Materials 1 (1) (1966) 318.

[55] H. Jahed, A. Varvani-Farahani, Upper and lower fatigue life limits model using energy-based fatigue properties, International Journal of Fatigue 28 (2006) 467–473.

[56] D. F. Socie, G. B. Marquis, Multiaxial Fatigue, Society of Automotive Engineers, Inc., Warrendale, Pa., 2000.

[57] M. W. Brown, K. J. Miller, A theory for fatigue failure under multiaxial stress-strain conditions, in: Proceedings of the Institute of Mechanical Engineers, Vol. 187, 1973, pp. 745–755.

[58] F. A. Kandil, M. W. Brown, K. J. Miller, Biaxial low cycle fatigue fracture of 316 stainless steel at elevated tempreature, Vol. Book 280, The Metals Society, 1982.

[59] D. Socie, Multiaxial fatigue damage models, Journal of Engineering Materials and Technology 109 (1987) 293.

[60] A. Fatemi, D. F. Socie, A critical plane approach to multiaxial fatigue damage including out-of-phase loading, Fatigue & Fracture of Engineering Materials and Structures 11 (3) (1988) 149–165.

[61] M. Barnett, Twinning and the ductility of magnesium alloys part I: Tension twins, Materials Science and Engineering: A 464 (2007) 1–7.

[62] S. Kleiner, P. Uggowitzer, Mechanical anisotropy of extruded Mg-6% Al-1% Zn alloy, Materials Science and Engineering: A 379 (2004) 258–263.

[63] Y. Uematsu, K. Tokaji, M. Kamakura, K. Uchida, H. Shibata, N. Bekku, Effect of extrusion conditions on grain refinement and fatigue behaviour in magnesium alloys, Materials Science and Engineering: A 434 (1-2) (2006) 131–140.

[64] Y. Wang, J. Huang, The role of twinning and untwinning in yielding behavior in hot-extruded MgAlZn alloy, Acta Materialia 55 (2007) 897–905.

[65] A. Staroselsky, L. Anand, A constitutive model for hcp materials deforming by slip and twinning: application to magnesium alloy AZ31B, International Journal of Plasticity 19 (10) (2003) 1843–1864.

[66] S. Suresh, Fatigue of materials, 2nd Edition, Cambridge University Press, 1998.

[67] R. Hertzberg, Deformation and fracture mechanics of engineering materials, 4th Edition, J. Wiley & Sons, 1996.

[68] R. Abbaschian, L. Abbaschian, R. E. Reed-Hill, Physical Metallurgy Principles, Cengage Learning, 2008.

[69] J. Koike, T. Kobayashi, T. Mukai, H. Watanabe, M. Suzuki, The activity of non-basal slip systems and dynamic recovery at room temperature in fine-grained AZ31B magnesium alloys, Acta materialia 51 (2003) 2055–2065.

[70] Y. Chino, K. Kimura, M. Hakamada, M. Mabuchi, Mechanical anisotropy due to twinning in an extruded AZ31 Mg alloy, Materials Science and Engineering: A 485 (2008) 311–317.

[71] R. Zhu, Y. J. Wu, W. Q. Ji, J. T. Wang, Cyclic softening of ultrafine-grained AZ31 magnesium alloy processed by equal-channel angular pressing, Materials Letters 65 (23-24) (2011) 3593–3596.

[72] W. Tang, S. Huang, S. Zhang, D. Li, Y. Peng, Influence of extrusion parameters on grain size and texture distributions of AZ31 alloy, Journal of Materials Processing Technology 211 (7) (2011) 1203–1209.

[73] J. Koike, R. Ohyama, Geometrical criterion for the activation of prismatic slip in AZ61 Mg alloy sheets deformed at room temperature, Acta Materialia 53 (7) (2005) 1963–1972.

[74] T. Obara, H. Yoshinga, S. Morozumi, $\{11\bar{2}2\} < \bar{1}123 >$ slip system in magnesium, Acta Metallurgica 21 (7) (1973) 845–853.

[75] J. Stohr, J. Poirier, Etude en microscopie electronique du glissement pyramidal $\{11\bar{2}2\} < 11\bar{2}3 >$ dans le magnesium, Phil Mag 25 (1972) 1313.

[76] H. Yoshinaga, R. Horiuchi., On the nonbasal slip in magnesium crystals, Trans JIM 5 (1963) 14.

[77] W. Sheerly, R. Nash, Mechanical properties of magnesium monocrystals, Trans Metall Soc AIME 218 (1960) 416.

[78] S. R. Agnew, O. Duygulu, Plastic anisotropy and the role of non-basal slip in magnesium alloy AZ31B, International Journal of Plasticity 21 (6) (2005) 1161–1193.

[79] A. Beer, M. Barnett, Influence of initial microstructure on the hot working flow stress of Mg3Al1Zn, Materials Science and Engineering: A 423 (2006) 292–299.

[80] M. Barnett, Twinning and the ductility of magnesium alloys part II. Contraction twins, Materials Science and Engineering: A 464 (2007) 8–16.

[81] X. Lou, M. Li, R. Boger, S. Agnew, R. Wagoner, Hardening evolution of AZ31B Mg sheet, International Journal of Plasticity 23 (2007) 44–86.

[82] J. Koike, N. Fujiyama, D. Ando, Y. Sutou, Roles of deformation twinning and dislocation slip in the fatigue failure mechanism of AZ31 Mg alloys, Scripta Materialia 63 (7) (2010) 747–750.

[83] C. H. Cáceres, T. Sumitomo, M. Veidt, Pseudoelastic behaviour of cast magnesium AZ91 alloy under cyclic loadingunloading, Acta Materialia 51 (20) (2003) 6211–6218.

[84] O. Muránsky, D. Carr, P. Šittner, E. Oliver, In situ neutron diffraction investigation of deformation twinning and pseudoelastic-like behaviour of extruded AZ31 magnesium alloy, International Journal of Plasticity 25 (2009) 1107–1127.

[85] G. Mann, T. Sumitomo, C. Caceres, J. Griffiths, Reversible plastic strain during cyclic loadingunloading of Mg and MgZn alloys, Materials Science and Engineering: A 456 (2007) 138–146.

[86] M. W. Barsoum, A. G. Zhou, S. Basu, Kinking nonlinear elasticity, damping and microyielding of hexagonal close-packed metals, Acta Materialia 56 (1) (2008) 60–67.

[87] S. Bentachfine, G. Pluvinage, L. S. Toth, Z. Azari, Biaxial low cycle fatigue under non-proportional loading of a magnesium-lithium alloy, Engineering Fracture Mechanics 54 (4) (1996) 513–522.

[88] K. Tokaji, M. Kamakura, Y. Ishiizumi, N. Hasegawa, Fatigue behaviour and fracture mechanism of a rolled AZ31 magnesium alloy, International Journal of Fatigue 26 (11) (2004) 1217–1224.

[89] Z. Y. Nan, S. Ishihara, T. Goshima, R. Nakanishi, Scanning probe microscope observations of fatigue process in magnesium alloy AZ31 near the fatigue limit, Scripta Materialia 50 (4) (2004) 429–434.

[90] S. Khan, Y. Miyashita, Y. Mutoh, Z. Sajuri, Influence of Mn content on mechanical properties and fatigue behavior of extruded Mg alloys, Materials Science and Engineering: A 420 (2006) 315–321.

[91] S. Ishihara, Z. Nan, T. Goshima, Effect of microstructure on fatigue behavior of AZ31 magnesium alloy, Materials Science and Engineering: A 468-470 (2007) 214–222.

[92] F. Yang, S. M. Yin, S. X. Li, Z. F. Zhang, Crack initiation mechanism of extruded AZ31 magnesium alloy in the very high cycle fatigue regime, Materials Science and Engineering: A 491 (1-2) (2008) 131–136.

[93] M. Matsuzuki, S. Horibe, Analysis of fatigue damage process in magnesium alloy AZ31, Materials Science and Engineering: A 504 (1-2) (2009) 169–174.

[94] S. Ishihara, A. J. McEvily, M. Sato, K. Taniguchi, T. Goshima, The effect of load ratio on fatigue life and crack propagation behavior of an extruded magnesium alloy, International Journal of Fatigue 31 (11-12) (2009) 1788–1794.

[95] S. Ishihara, T. Namito, S. Yoshifuji, T. Goshima, On fatigue lives of diecast and extruded Mg alloys, International Journal of Fatigue 35 (1) (2012) 56–62.

[96] Y. J. Wu, R. Zhu, J. T. Wang, W. Q. Ji, Role of twinning and slip in cyclic deformation of extruded Mg-3%Al-1%Zn alloys, Scripta Materialia 63 (11) (2010) 1077–1080.

[97] J. Zhang, Q. Yu, Y. Jiang, Q. Li, An experimental study of cyclic deformation of extruded AZ61A magnesium alloy 27 (5) (2011) 768–787.

[98] Q. Li, Q. Yu, J. Zhang, Y. Jiang, Effect of strain amplitude on tension-compression fatigue behavior of extruded Mg6Al1ZnA magnesium alloy, Scripta Materialia 62 (10) (2010) 778–781.

[99] S. H. Park, S.-G. Hong, C. S. Lee, Role of initial $\{10-12\}$ twin in the fatigue behavior of rolled Mg-3Al-1Zn alloy, Scripta Materialia 62 (9) (2010) 666–669.

[100] Q. Yu, J. Zhang, Y. Jiang, Fatigue damage development in pure polycrystalline magnesium under cyclic tension-compression loading, Materials Science and Engineering: A 528 (25-26) (2011) 7816–7826.

[101] Y. Jiang, A fatigue criterion for general multiaxial loading, Fatigue & Fracture of Engineering Materials & Structures 23 (1) (2000) 19–32.

[102] Y. Jiang, H. Sehitoglu, Fatigue and stress analysis of rolling contact, Tech. Rep. 161,UILU-ENG 92-3602, College of Engineering, University of Illinois at Urbana-Champaign (1992).

[103] Y. C. Lin, X.-M. Chen, G. Chen, Uniaxial ratcheting and low-cycle fatigue failure behaviors of AZ91D magnesium alloy under cyclic tension deformation, Journal of Alloys and Compounds 509 (24) (2011) 6838–6843.

[104] X. P. Zhang, S. Castagne, X. F. Luo, C. F. Gu, Effects of extrusion ratio on the ratcheting behavior of extruded AZ31B magnesium alloy under asymmetrical uniaxial cyclic loading, Materials Science and Engineering: A 528 (3) (2011) 838–845.

[105] F. Yang, F. Lv, X. M. Yang, S. X. Li, Z. F. Zhang, Q. D. Wang, Enhanced very high cycle fatigue performance of extruded Mg-12Gd-3Y-0.5Zr magnesium alloy, Materials Science and Engineering: A 528 (6) (2011) 2231–2238.

[106] M.-G. Lee, R. H. Wagoner, J. K. Lee, K. Chung, H. Y. Kim, Constitutive modeling for anisotropic/asymmetric hardening behavior of magnesium alloy sheets, International Journal of Plasticity 24 (4) (2008) 545–582.

[107] H. El Kadiri, A. Oppedal, A crystal plasticity theory for latent hardening by glide twinning through dislocation transmutation and twin accommodation effects, Journal of the Mechanics and Physics of Solids 58 (2010) 613–624.

[108] M. Li, X. Lou, J. Kim, R. Wagoner, An efficient constitutive model for room-temperature, low-rate plasticity of annealed Mg AZ31B sheet, International Journal of Plasticity 26 (2010) 820–858.

[109] T. Hama, H. Takuda, Crystal-plasticity finite-element analysis of inelastic behavior during unloading in a magnesium alloy sheet, International Journal of Plasticity 27 (7) (2011) 1072–1092.

[110] T. Shih, W. Liu, Y. Chen, Fatigue of as-extruded AZ61A magnesium alloy, Materials Science and Engineering A 325 (1-2) (2002) 152–162.

[111] K. Kainer, Magnesium alloys and technology, Wiley-VCH, 2003.

[112] X. Z. Lin, D. L. Chen, Strain controlled cyclic deformation behavior of an extruded magnesium alloy, Materials Science and Engineering: A 496 (1-2) (2008) 106–113.

[113] G. Eisenmeier, B. Holzwarth, H. W. Höppel, H. Mughrabi, Cyclic deformation and fatigue behaviour of the magnesium alloy AZ91, Materials Science and Engineering: A 319-321 (0) (2001) 578–582.

[114] M. F. Horstemeyer, N. Yang, K. Gall, D. McDowell, J. Fan, P. Gullett, High cycle fatigue mechanisms in a cast AM60B magnesium alloy, Fatigue & Fracture of Engineering Materials & Structures 25 (11) (2002) 1045–1056.

[115] M. H. Yoo, Slip, twinning, and fracture in hexagonal close-packed metals, Metallurgical Transactions A 12 (1981) 409–418.

[116] C. Guillemer, M. Clavel, G. Cailletaud, Cyclic behavior of extruded magnesium: Experimental, microstructural and numerical approach, International Journal of Plasticity 27 (12) (2011) 2068–2084.

[117] S. Choi, H. Kim, S. Hong, Y. Shin, G. Lee, H. Kim, Evaluation and prediction of the forming limit of AZ31B magnesium alloy sheets in a cross-shaped cup deep drawing process, Metals and Materials International 15 (4) (2009) 575–584.

[118] H. Somekawa, T. Mukai, Effect of texture on fracture toughness in extruded AZ31 magnesium alloy, Scripta Materialia 53 (2005) 541–545.

[119] H. Wang, P. D. Wu, M. A. Gharghouri, Effects of basal texture on mechanical behaviour of magnesium alloy AZ31B sheet, Materials Science and Engineering: A 527 (15) (2010) 3588–3594.

[120] A. Serra, D. J. Bacon, Computer simulation of screw dislocation interactions with twin boundaries in H.C.P. metals, Acta Metallurgica et Materialia 43 (12) (1995) 4465–4481.

[121] A. Lopes, F. Barlat, J. Gracio, J. Ferreiraduarte, E. Rauch, Effect of texture and microstructure on strain hardening anisotropy for aluminum deformed in uniaxial tension and simple shear, International Journal of Plasticity 19 (2003) 1–22.

[122] A. Eshraghi, H. Jahed, S. Lambert, A lagrangian model for hardening behaviour of materials at finite deformation based on the right plastic stretch tensor, Materials & Design 31 (2010) 2342–2354.

[123] P. Šittner, P. Lukáš, V. Novák, M. R. Daymond, G. M. Swallowe, In situ neutron diffraction studies of martensitic transformations in NiTi polycrystals under tension and compression stress, Materials Science and Engineering: A 378 (1-2) (2004) 97–104.

[124] K. N. Melton, O. Mercier, Fatigue of NiTi thermoelastic martensites, Acta Metallurgica 27 (1) (1979) 137–144.

[125] H. Tobushi, Y. Shimeno, T. Hachisuka, K. Tanaka, Influence of strain rate on superelastic properties of TiNi shape memory alloy, Mechanics of Materials 30 (2) (1998) 141–150.

[126] G. Eggeler, E. Hornbogen, A. Yawny, A. Heckmann, M. Wagner, Structural and functional fatigue of NiTi shape memory alloys, Materials Science and Engineering: A 378 (1-2) (2004) 24–33.

[127] W. Predki, M. Klönne, A. Knopik, Cyclic torsional loading of pseudoelastic NiTi shape memory alloys: Damping and fatigue failure, Materials Science and Engineering: A 417 (1-2) (2006) 182–189.

[128] L. Wu, S. R. Agnew, D. W. Brown, G. M. Stoica, B. Clausen, A. Jain, D. E. Fielden, P. K. Liaw, Internal stress relaxation and load redistribution during the twinningdetwinning-dominated cyclic deformation of a wrought magnesium alloy, ZK60A, Acta Materialia 56 (14) (2008) 3699–3707.

[129] J. Koike, Enhanced deformation mechanisms by anisotropic plasticity in polycrystalline Mg alloys at room temperature, Metallurgical and Materials Transactions A 36 (2005) 1689–1696.

[130] S. Begum, D. Chen, S. Xu, A. A. Luo, Strain-controlled low-cycle fatigue properties of a newly developed extruded magnesium alloy, Metallurgical and Materials Transactions A 39 (2008) 3014–3026.

[131] T. Itoh, M. Sakane, M. Ohnami, D. F. Socie, Nonproportional low cycle fatigue criterion for type 304 stainless steel, Journal of Engineering Materials and Technology 117 (3) (1995) 285–292.

[132] X. Chen, S. Xu, D. Huang, A critical plane-strain energy density criterion for multiaxial low-cycle fatigue life under non-proportional loading, Fatigue & Fracture of Engineering Materials & Structures 22 (8) (1999) 679–686.

[133] F. Ellyin, K. Golos, Z. Xia, In-phase and out-of-phase multiaxial fatigue, Journal of Engineering Materials and Technology 113 (1) (1991) 112–118.

[134] H. Jahed, R. Dubey, An axisymmetric method of elastic-plastic analysis capable of predicting residual stress field, Journal of pressure vessel technology 119 (1997) 264–273.

[135] H. Jahed, A. Varvani-Farahani, M. Noban, I. Khalaji, An energy-based fatigue life assessment model for various metallic materials under proportional and non-proportional loading conditions, International Journal of Fatigue 29 (2007) 647–655.

[136] H. Tobushi, T. Nakahara, Y. Shimeno, T. Hashimoto, Low-cycle fatigue of TiNi shape memory alloy and formulation of fatigue life, Journal of Engineering Materials and Technology 122 (2) (2000) 186–191.

[137] J. J. F. Bonnen, T. H. Topper, The effect of bending overloads on torsional fatigue in normalized 1045 steel, International Journal of Fatigue 21 (1) (1999) 23–33.

[138] J. P. Strizak, H. Tian, P. K. Liaw, L. K. Mansur, Fatigue properties of type 316LN stainless steel in air and mercury, Journal of Nuclear Materials 343 (1-3) (2005) 134–144.

[139] L. Reis, B. Li, M. De Freitas, Analytical and experimental studies on fatigue crack path under complex multi-axial loading, Fatigue & Fracture of Engineering Materials & Structures 29 (4) (2006) 281–289.

[140] J. A. Araújo, D. Nowell, R. C. Vivacqua, The use of multiaxial fatigue models to predict fretting fatigue life of components subjected to different contact stress fields, Fatigue & Fracture of Engineering Materials & Structures 27 (10) (2004) 967–978.

[141] A. Varvani-Farahani, T. H. Topper, Closure-free biaxial fatigue crack growth rate and life prediction under various biaxiality ratios in SAE 1045 steel, Fatigue & Fracture of Engineering Materials & Structures 22 (8) (1999) 697–710.

[142] M. Firat, U. Kocabicak, Analytical durability modeling and evaluation complementary techniques for physical testing of automotive components, Engineering Failure Analysis 11 (4) (2004) 655–674.

[143] B. Wilczynski, Z. Mróz, Optimal design of machine components using notch correction and plasticity models, Computers and structures 85 (2007) 1382–1398.

[144] Y.-Y. Wang, W.-X. Yao, Evaluation and comparison of several multiaxial fatigue criteria, International Journal of Fatigue 26 (1) (2004) 17–25.

[145] Y. Jiang, O. Hertel, M. Vormwald, An experimental evaluation of three critical plane multiaxial fatigue criteria, International Journal of Fatigue 29 (8) (2007) 1490–1502.

[146] K. Shiozawa, J. Kitajima, T. Kaminashi, T. Murai, T. Takahashi, Low-cycle fatigue deformation behavior and evaluation of fatigue life on extruded magnesium alloys, Procedia Engineering 10 (2011) 1244–1249.